U.S.G.S. Award Number: G09AP00010

Project Dates: 12/01/08 – 12/31/11

Seismic Assessment of Earth Structures overlying Potentially Liquefiable Soils

Michelle Shriro[1] and Jonathan D. Bray[2]

[1]Doctoral Candidate and [2]Professor
University of California, Berkeley

Principal Investigator:
Professor Jonathan D. Bray
Department of Civil and Environmental Engineering
University of California, Berkeley
453 Davis Hall, MC-1710
Berkeley, CA 94720-1710
Tel. (510) 642-9843
Fax. (510) 642-7476
bray@ce.berkeley.edu
URL: http://www.ce.berkeley.edu/~bray/

Final Technical Report

September 28, 2011

U.S.G.S. Award Number: G09AP00010

Seismic Assessment of Earth Structures overlying Potentially Liquefiable Soils

Michelle Shriro and Jonathan D. Bray
University of California, Berkeley

ABSTRACT

Soil liquefaction presents a significant hazard to the built environment. The seismically induced permanent displacement of earth levees, embankments, and earth-fill slopes resulting from liquefaction below these earth structures is not well captured in current seismic design practice. Ground remediation can be employed to reduce the hazards resulting from soil liquefaction for cases where the analytical tools predict poor seismic performance. There are not sufficient funds to repair all vulnerable levees in the system. Robust analytical procedures are required to evaluate sections of levees where liquefiable foundation materials have been identified which may lead to significant damage.

Inertially driven ground movements of intermediate levels are the primary focus of this study. In these cases, the post-liquefaction static stability of the earth slope is greater than one, and seismically induced permanent displacements result primarily from earthquake shaking after liquefaction is triggered. “Limited” lateral spreads involving liquefaction of medium dense sand can produce seismic displacements on the order of several centimeters to a meter or more. These levels of seismic displacements are sufficient to severely damage levees. The most commonly employed simplified method for evaluation of seismic deformation at these intermediate levels relies on the concept post-liquefaction residual shear strength. For many practical cases, residual shear strength is ill-defined due to the ever changing resistance provided by soils that undergo repetitive dilative responses during cyclic loading. Where liquefied soils are sufficiently strong to resist flow failures, engineers lack satisfactory tools to evaluate the seismic performance of earth structures that overlie liquefiable soils.

In this study, a promising, popular nonlinear soil constitutive model (UBCSAND), which was developed by Professor Byrne and implemented in the widely available finite difference program FLAC is employed to evaluate seismic deformations of earth structures resulting from liquefaction-induced lateral movements. Analyses of one-element laboratory tests were performed first to develop trends within the UBCSAND soil model calibration parameters. The trends identified are implemented in the back-analysis of several case histories, and the ability of the UBCSAND model within the program FLAC to capture observed deformations is evaluated. The numerical simulations of seismic performance at Moss Landing Marine Laboratory and Monterey Bay Aquarium Research Institute during the 1989 Loma Prieta Earthquake and at the Juvenile Hall Facility during the 1971 San Fernando Earthquake are shown to capture well the key features of these case histories.

After incorporating the lessons learned from the previous phases of the study, a sensitivity study is carried out to investigate the seismic performance of earthen levees built atop potentially liquefiable soils. Generalized levee systems are analyzed, wherein key characteristics, such as the thickness of the liquefiable layer and its relative density, are systematically varied to develop useful insights. A suite of nine near-fault, forward-directivity, fault-normal soil ground motions and seven intermediate-field soil earthquake ground motions are used to reflect the seismic hazards most likely to control the design of levees within the San Joaquin-Sacramento delta region of California. Trends in the simulated seismic performances of levees affected by liquefaction-induced ground deformations within their foundations are presented, and key findings are provided.

Acknowledgements

Research supported by the U. S. Geological Survey (U.S.G.S.), Department of Interior, under USGS award number G09AP00010. The views and conclusions contained in this document are those of the authors and should not be interpreted as necessarily representing the official policies, either expressed or implied, of the U.S. Government. The financial support of the USGS is gratefully acknowledged. We would like to thank Dr. Shideh Dashti, Dr. Ben Mason, Katherine Jones for their efforts in the early stages of this project as well as their support and collaboration throughout. We would also like to thank Professor Nicholas Sitar, Roozbeh Grayeli, Gabriel Candida and Nick Oettle for their collaborative efforts. Their input and assistance is greatly appreciated.

BIBLIOGRAPHY

[No publications have been produced by this research at the time of this report]

TABLE OF CONTENTS

ABSTRACT 2

BIBLIOGRAPHY 3

1. INTRODUCTION 5

1.1. STUDIES MOTIVATING RESEARCH 6
1.2. OBJECTIVE AND SCOPE 9
1.3. UBCSAND CONSTITUTIVE MODEL 10
1.4. UBCSAND MODEL CALIBRATION PARAMETERS 12
1.4.1. RELATIVE DENSITY INDEX 12
1.4.2. ELASTIC STIFFNESS PARAMETERS 12
1.4.3. PLASTIC SHEAR STIFFNESS PARAMETERS 13
1.4.4. STRENGTH AND FLOW RULE 14
1.4.5. FITTING PARAMETERS 14

2. MODEL CALIBRATION WITH CSS LABORATORY TEST MODELING 15

2.1. SELECTED CSS TEST SET 15
2.2. SAND – FLAT GROUND CSS TESTS 17
2.3. SAND – SLOPING GROUND CSS TESTS 19
2.4. UBCSAND CALIBRATION CURVES 21
2.4.1. M_HFAC1 AND M_HFAC2 21
2.4.2. M_HFAC3 23
2.4.3. M_HFAC4 24
2.5. SILT – FLAT AND SLOPING GROUND 26

3. MODEL CALIBRATION WITH BACK ANALYSIS 27

3.1. MOSS LANDING MBARI/SANDHOLDT ROAD – LOMA PRIETA 1989 27
3.2. MOSS LANDING MARINE LABORATORY (MLML) – LOMA PRIETA 1989 35
3.3. JUVENILE HALL FACILITY – SAN FERNANDO 1971 42

4. SENSITIVITY STUDY USING CALIBRATED UBCSAND MODEL 48

4.1. INTRODUCTION 48
4.2. SENSITIVITY OF RESULTS TO VARIATIONS IN $(N_1)_{60}$ 49
4.3. SENSITIVITY OF RESULTS TO VARIATIONS IN MODEL GEOMETRY 50
4.3.1. LAYER THICKNESS 52
4.3.2. EMBANKMENT HEIGHT 56
4.4. SENSITIVITY OF RESULTS TO VARIATIONS IN EARTHQUAKE GROUND MOTIONS 59

5. SUMMARY AND CONCLUSIONS 62

6. REFERENCES 64

APPENDIX A: GROUND MOTION DATA 69

APPENDIX B: SENSITIVITY ANALYSIS X-DISPLACEMENT DATA 87

Seismic Assessment of Earth Structures overlying Potentially Liquefiable Soils

1. INTRODUCTION

The liquefaction of soils presents a significant hazard to the built environment. Whereas much attention has been devoted over the past four decades towards developing liquefaction triggering procedures to evaluate the likelihood of liquefaction occurring, relatively less attention has been devoted to understanding liquefaction-induced ground movements. In particular, the seismically induced permanent displacement of earth levees, embankments, and fill slopes due to liquefaction below these earth structures is not well captured in current seismic design practice (e.g., EERI 2003, Seed et al. 2003).

There are several levee systems that are potentially vulnerable to liquefaction-induced ground failure. This project is particularly important to the new studies of the seismic fragility of the levees in the San Joaquin-Sacramento delta region. This levee system provides drinking water for over 66% of Californians as well as water for agriculture, recreation, and environmental purposes (CADWR 2007). Unacceptable liquefaction-induced deformations to this system could lead to devastating consequences. However, there is not sufficient funding available currently to repair all vulnerable levees in the San Joaquin-Sacramento Delta.

Many of the prevalent procedures for evaluating liquefaction are discussed in the document "Recommended Procedures for Implementation of DMG Special Publication 117: Guidelines for Analyzing and Mitigating Liquefaction Hazards in California" edited by Martin and Lew (1999). This important guidance document separates liquefaction-related slope movement hazards into two categories:

1. Flow slides wherein the post-liquefaction static factor of safety (FS) is below unity so that large displacements that are greater than a few meters occur after the cessation of earthquake shaking; and
2. "Limited" lateral spreads of the order of a meter or so triggered and sustained by the earthquake ground shaking."

Flow slides could potentially be the most catastrophic liquefaction-induced slope movement. The expected range of displacement for a flow slide (i.e., post-liquefaction FS < 1) is typically large and current prediction methods are well suited to predict their occurrence. Once identified, these levee or embankment sections would require remediation in most cases as the amount of permanent ground displacement that could occur would be too large. As summarized in Finn (1990), large liquefaction-induced levee crest settlements on the order of several meters are possible as the post-liquefaction factor of safety approaches a value of about 0.8. However, Finn also indicates that crest settlements of a meter or so are possible when the post-liquefaction factor of safety is slightly greater than one. Movements of a meter or so can produce significant damage to earth structures, so reliable procedures for estimating seismic displacements within this range of movements are also required.

"Limited" lateral spreads involving liquefaction of moderately dense clean sand or silty sands can produce seismic displacements in earth levees, earth embankments, and earth slopes on the order of several centimeters to a meter or more. These levels of seismically induced displacements are sufficient to damage water retention structures in the following ways:

- Deformations can cause cracking that can lead to piping of water through the structure.
- Deformations resulting in a loss of freeboard can lead to overtopping.

The post-liquefaction static stability of the earth slopes for these cases are greater than unity; therefore, significant deviatoric-induced seismic displacements are not expected after the cessation of ground shaking. The seismically induced permanent displacement for these cases occurs primarily during earthquake shaking but after liquefaction is triggered. Hence, there are three important aspects of the problem to capture: (1) the point in which liquefaction is triggered; (2) the seismic response of the sliding mass during continued shaking; and (3) the post-liquefaction cyclic response of these soils.

These are not easy aspects of nonlinear soil response to capture. Robust analytical procedures are required to evaluate sections of levees where liquefiable foundation materials exist to evaluate:

1. If large flow slides will occur, which will require relatively expensive remediation;
2. If negligible seismic displacements will occur, which will require no expenditures; or
3. If intermediate seismic displacements will occur, which may require some level of remediation depending on the consequences of the estimated level of seismic displacement.

To meet this objective, we have employed a promising, popular nonlinear soil constitutive model (UBCSAND) that has been implemented in a widely available finite difference program (FLAC) for evaluating seismic deformations of earth structures resulting from liquefaction-induced lateral movements focusing on ground conditions that lead to inertially driven ground movements of intermediate levels. The results of this research will also be applicable to earth structures other than San Joaquin-Sacramento Delta levees. It is our hope that with these improved analytical tools, earthquake losses can be reduced through effective screening and remediation of those earth slopes that would likely perform poorly in a future seismic event.

1.1. Studies Motivating Research

A prime motivator for this proposed research project is a recently completed study that developed a simplified probabilistic method for evaluating the effects of liquefaction-induced lateral spreading of piled bridge foundations that included the “pile-pinning” effect (i.e., Ledezma and Bray, 2007). The testbed bridge soil profile for this project is shown in Figure 1.1.1. The problematic soil layer, which is labeled as “Loose Sand,” is actually a loose to medium dense normally consolidated sand deposit with overburden corrected, clean sand Standard Penetration Test (SPT) blow counts, $(N_1)_{60\text{-}CS}$, of 15 at the left abutment and only 13 for the thicker sand deposit at the right abutment.

The sand layer liquefies at significant levels of ground shaking, and with reasonable undrained residual shear strengths, the embankment slopes have post-liquefaction static factors of safety slightly greater than one. Yet, both slopes displace inward excessively. As we developed a probabilistically based liquefaction-induced lateral spread method that incorporated the “pile-pinning” effect as described in the MCEER/ATC-49-1 bridge design document (ATC/MCEER Joint Venture, 2003), we realized that the prevailing use of a Newmark sliding block method was questionable. In practice, the Newmark method is applied using a yield acceleration based on the slope’s geometry and the post-liquefaction residual strength of the liquefied material of the critical layer. However, use of a constant value of post-liquefaction residual strength does not

capture the soil response depicted in Figure 1.1.2. From this it became clear that the profession needs a relatively straightforward Newmark-type liquefaction-induced deformation prediction method that is calibrated to account for a non-constant post-liquefaction residual strength.

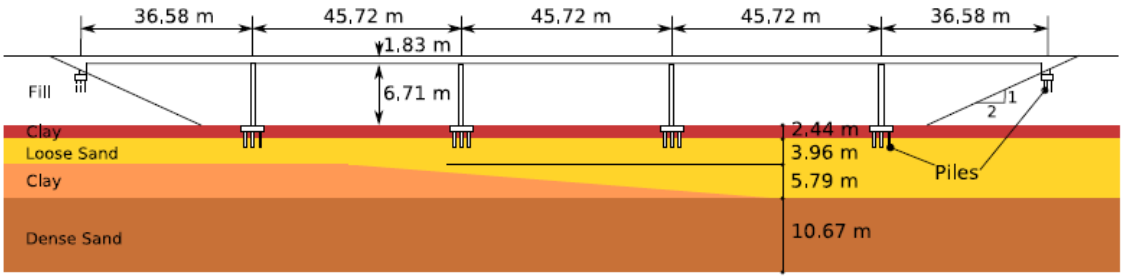

Figure 1.1.1. Pacific Earthquake Engineering Research Center Liquefaction Testbed Bridge Soil Profile (Ledezma and Bray 2007).

To highlight some of the difficulties in defining the post-liquefaction residual strength of this dilative liquefied material, consider the response of a representative cyclic simple shear test on a medium dense sand specimen. The medium dense to dense Monterey sand specimens tested by Kammerer et al. (2002), which are summarized in Seed et al. (2003), were tested at low to intermediate confining stresses, which represent soil conditions appropriate for soils underlying small levees and earth embankments, eventually undergo dilation during shearing, leading to the development of "banana-shaped" loops in each half cycle of loading in the stress versus strain plots, such as that shown in the plot to the right (normalized shear stress vs. shear strain) shown in Figure 1.1.2. More sophisticated soil models and numerical procedures are required to capture this complex phenomenon in cases where soil resistance is changing throughout cyclic loading.

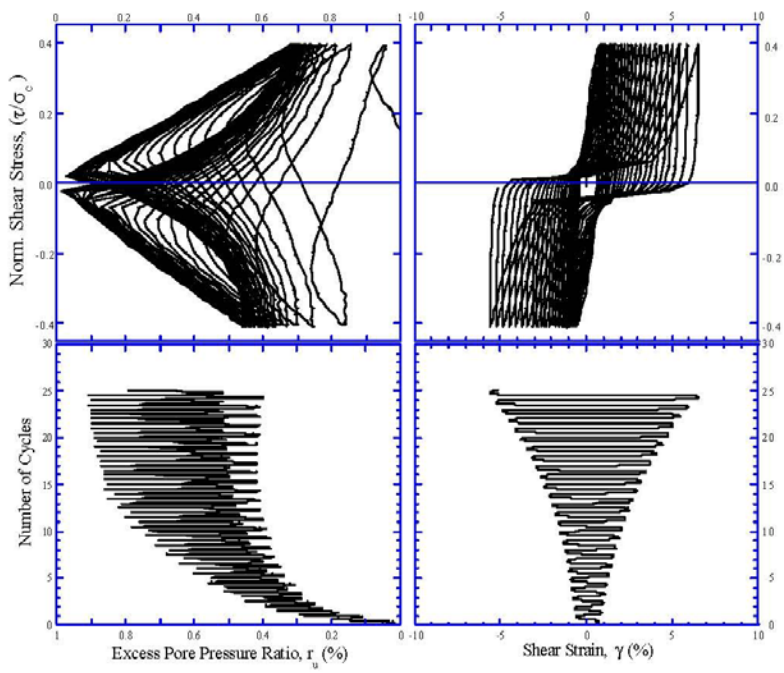

Figure 1.1.2. Undrained cyclic simple shear test on medium dense Monterey #30/0 sand (D_r = 75%, σ'_{vo} = 85 kPa, CSR = 0.4, and α = 0) [from Seed et al. 2003].

Post-liquefaction static stability analyses of potential flow slides are complicated by the fact that results of the slope stability analyses depend greatly on the selection of the undrained residual shear strength of the liquefied soil. Several recent studies provide procedures to estimate the residual strength of liquefied soil for post-liquefaction stability analyses (e.g., Olson and Stark 2002; Idriss and Boulanger 2008).

Analytical procedures for evaluating the effects of potential liquefaction-induced flow slides on overlying earth structures are discussed in papers such as Finn (1998), Finn (2000a), and Finn (2000b). In these cases, seismic displacement, such as levee crest settlement, depends significantly on the post-liquefaction static factor of safety as illustrated by Finn (1990).

Currently, liquefaction-induced lateral deformations (both flow slides and “limited” lateral spreads) are evaluated using four different approaches: (1) empirical methods; (2) analytical methods using advanced soil constitutive models; (3) physical modeling; and (4) a combination of one or more of the previous three methods.

Empirical methods (e.g., Hamada et al. 1986, Rauch and Martin 2000, Bardet et al. 2002, and Youd et al. 2002) are developed using regression techniques with data from lateral spreading case histories. These relationships are straight-forward to use, but only have an accuracy range within a factor of about two. For a large flow slide, if the best deformation estimate is 12 m, a method predicting 6 to 24 m may provide an acceptable level of accuracy as remediation will be required once a tolerable threshold of deformation is surpassed. For “limited” lateral spreads, however, using these methods to predict seismic deformation is more problematic, as an estimated displacement of 30 cm might be acceptable for a given earthen structure, while an estimated displacement of 120 cm might not (i.e., best estimate is 60 cm for this example).

Additionally, it is often difficult to apply these methods to specific cases such as an embankment or earth levee atop a particular subsurface stratigraphy that is not captured in the databases used to develop the empirical correlations. Moreover, the empirical methods also do not directly consider the complex phenomena that underlie liquefaction-induced displacements – such as the complex soil behavior exhibited in Fig. 1.1.2. More recent empirical models (e.g., Zhang et al. 2004 and Faris et al. 2006) have attempted to incorporate model parameters that capture these complex responses, but these methods still do not directly address the seismic performance of levees that are situated atop potentially liquefiable soils.

Analytical models often employ a Newmark-type rigid block analysis (Newmark 1965) to calculate lateral spreading displacements. In this method, the seismically induced permanent displacement is calculated by double integrating the acceleration-time history once the ground acceleration exceeds the yield acceleration of the sliding block (i.e., the horizontal acceleration that leads to a factor of safety equal to one for a limit equilibrium analysis) until the velocities of the sliding block and ground coincide. Yegian et al. (1991) and Baziar et al. (1992) employed these “Newmark” type analyses to develop prediction methods; however, their methods are limited by the assumption that the sliding soil mass is rigid. More recently, other researchers (e.g., Rathje and Bray 2000) improved the “Newmark” sliding block analysis by eliminating the original assumptions that the deformable sliding mass is rigid and that the seismic response of the deformable mass is decoupled from sliding of the block atop the base soil. This work led to more robust estimates of seismic displacements for the cases specified (e.g., Bray and Travasarou 2007). However, most of these methods warn that they should not be used when liquefaction occurs.

Advanced effective stress constitutive models (e.g., Byrne et al. 2004 and Yang et al. 2003) can also be used to predict liquefaction-induced lateral displacements with reasonable accuracy. The Byrne et al. (2004) “UBCSAND” model was used to accurately predict liquefaction-induced lateral displacements of a full-scale field tested embankment and of an embankment tested in a centrifuge (Puebla et al. 1997); and the Elgamal et al. (2002) “Pressure-Independent-Multi-Yield (PIMY)” model was used to accurately predict the response of an earth dam modeled in four centrifuge tests (Yang et al. 2003; and Yang et al. 2004). The strength of well-calibrated effective stress constitutive modeling is the ability to capture complex soil behavior phenomena seen in Figure 1.1.2 that eludes both empirical and simpler analytical methods. The limitation of using advanced numerical analysis to evaluate lateral spreading is the extensive calibration and knowledge required to use the soil models properly. Some of the soil constitutive model input parameters, for instance, are unfamiliar to practicing engineers. However, the results from a comprehensive set of sound analyses can provide useful insights and guidance to design engineers in practice.

Physical models, such as centrifuge experiments and full-scale field tests, can also be used to capture the seismic performance of an earthen structure. These physical models, if properly built and tested, can yield the most realistic indications of seismic performance. This technology is typically used by researchers as a means to calibrate or gain understanding about effective stress constitutive models (e.g., Puebla et al. 1997, and Yang et al. 2003). These techniques are rarely used in practice, however, because of the costs, time, and expertise required.

Combinations of the three aforementioned methods usually lead to the most robust methods for predicting lateral spreading displacements, as they draw from the strengths of the methods and bypass some of the weaknesses. One such “combined” procedure has been advanced by Finn (1998), Finn (2000a), and Finn (2000b). Professor Finn used a calibrated numerical model to make forward predictions of the displacements of levees exposed to seismic excitation and then developed a simple analytical expression based on the results. Notably, this method was concerned with large, flow-like lateral displacements. In this procedure, seismic displacement, such as levee crest settlement, depends significantly on the post-liquefaction static factor of safety as illustrated by Finn (1990). Large liquefaction-flow-type ground movements are possible when the post-liquefaction FS < 1. However, ground movements on the order of centimeters to a meter or so can still occur when the post-liquefaction FS > 1, and this level of movement can produce significant damage to earth structures. Thus, reliable procedures for estimating seismic displacements within this range of movements are required.

Researchers at the University of Washington (e.g., Baska 2002) have also proposed another “combined” method for calculating liquefaction-induced lateral spreading. These researchers calibrated a constitutive model (“UWSand”; Arduino et al. 2001) by back-analyzing case histories, made forward predictions of ground displacements by varying key parameters (e.g., thickness and relative density of the liquefiable layer), determined the sensitivity that the key parameters have on predicted displacements, and then regressed an equation for predicting lateral displacements based on key input parameters. However, this work focused on lateral spreading events that occur on gently sloping ground and at a free face. The work did not specifically address the case of earthen structures such as levees.

1.2. Objective and Scope

A promising soil constitutive model that is implemented in a widely used finite difference program is employed to analyze seismic deformations of levees resulting from liquefaction-

induced lateral movements in foundation soils. It is important to note that the cases to be analyzed will have post-liquefaction static slope stability factors of safety greater than unity, so inertially driven “limited” lateral spreads is this study’s focus. An assessment of this commonly employed advanced seismic displacement model is required to evaluate its ability to capture inertially driven liquefaction-induced lateral deformation effects. One such timely application is the high priority seismic vulnerability studies of the earth levees in the San Joaquin-Sacramento delta region of California.

The solution of complex, geographical distributed problems such as the levee system in the San Joaquin-Sacramento Delta requires a significant effort to characterize the project-specific seismic hazard and geologic/hydraulic conditions. Simplified assessment methodologies will be required to screen long sections of the levees to identify those cases requiring advanced analysis. Following adequate characterization and screening assessment, for some sites it will be sufficiently clear that remediation is required. In cases that pass the screening assessment, it will be clear that little, if anything, needs to be done. In some cases additional analyses based on an enhanced characterization of the site will be advantageous. Those latter cases are addressed in this study. It is our hope to advance reliable finite difference methods for cases in which refined assessments are required to evaluate seismic performance.

The scope of the study is divided into four phases: (1) perform analyses of one-element laboratory tests to demonstrate proficiency with the FLAC/UBCSAND numerical simulations; (2) perform back-analyses of key case histories to calibrate the numerical model; (3) conduct a systematic numerical sensitivity study of a simplified case; and (4) development of findings and dissemination of results.

The objective of this study is to advance the capabilities of numerical methods toward the solution of problems involving limited lateral spreads. Characterization of the seismic hazard and the geotechnical conditions at a particular site will always remain critical factors. No amount of sophistication in the analytical method employed can compensate for shortcomings in one’s understanding of the local site conditions and the seismic hazard at a site. However, there are cases where advanced analyses based on an enhanced characterization of the site will be required. The goal is to advance a reliable numerical method for cases in which refined assessments are required to evaluate seismic performance.

1.3. UBCSAND Constitutive Model

In the “limited” lateral spread cases examined in the proposed study, the liquefied soils undergo cyclic mobility with limited strain potential. Medium dense to dense sands and silty sands often undergo this type of cyclic response when at relatively low to intermediate effective confining stresses (e.g., Seed 1979; Seed and Idriss 1982). During the initial cycles of undrained loading, excess pore water pressures develop and the soil softens and may liquefy in terms of developing excess pore water pressures close to the effective confining stresses acting on the soil initially. However, as the soil deforms in undrained shear, the soil’s tendency to dilate in drained shear is manifested through a sudden drop in the excess pore water pressure and a rapid stiffening of the soil. This is the soil response depicted in the cyclic simple shear test that was shown in Figure 1.1.2. As noted previously, the concept of a specified post-liquefaction residual strength of the liquefied soil is a gross simplification to what is inherently a complex phenomenon. The engineering profession has analytical methods available to address this phenomenon, but these methods are still not well calibrated or accepted. To advance the state-of-the-practice, this needs to be rectified.

Soil constitutive models have been developed in attempts to capture the cyclic response of soils undergoing cyclic mobility with limited strain potential in numerical simulations. A promising nonlinear effective stress soil model is UBCSAND by Professor Peter Byrne and his colleagues (e.g., Beaty and Byrne 1998, Byrne et al. 2004, and Park and Byrne 2004). The UBCSAND soil model is employed in this study, because it is well documented, available for researchers and practitioners, implemented in the widely used finite difference programs, and offers potentially important insights into this phenomenon.

UBCSAND is implemented in the finite difference computer program FLAC (Itasca 2005), which is described at: http://www.itascacg.com/flac.html. It is relatively straightforward model that is noteworthy because it was developed to capture the undrained deviatoric response of liquefied soil and has been used to evaluate seismic displacements on several projects (e.g., Byrne and Seid-Karbasi 2003, and Seid-Karbasi and Byrne 2004). Some of its capabilities are shown in Figure 1.3.1. It is able to capture the cyclic build-up of excess pore water pressure and the softening and dilation of soil as it repeatedly crosses the phase transformation line during undrained cyclic shearing. Hence, it can capture the “banana-shaped” loops that occur during cyclic mobility with limited strain potential.

The UBCSAND constitutive model is a nonlinear stress-dependent effective stress model that captures the build-up of excess pore water pressure during cyclic loading and the development of “banana loops” in the shear stress versus shear strain plot once liquefaction occurs as is observed in countless laboratory experiments. Realistic soil responses are obtained by independently controlling the accumulation of permanent shear strains and volumetric strains in the model. It is one of the most popular nonlinear effective stress soil models used in engineering practice for evaluating liquefaction-induced deformation problems. Although the UBCSAND soil constitutive model is promising for evaluating liquefaction-induced lateral deformation, every nonlinear soil model has its inherent strengths and weaknesses. An evaluation of its ability to capture inertially driven liquefaction-induced lateral spreads is required before practicing engineers can apply it confidently to study the seismic performance of earth structures situated atop potentially liquefiable soils, such as the kilometers of earth levees in the San Joaquin-Sacramento delta region of California.

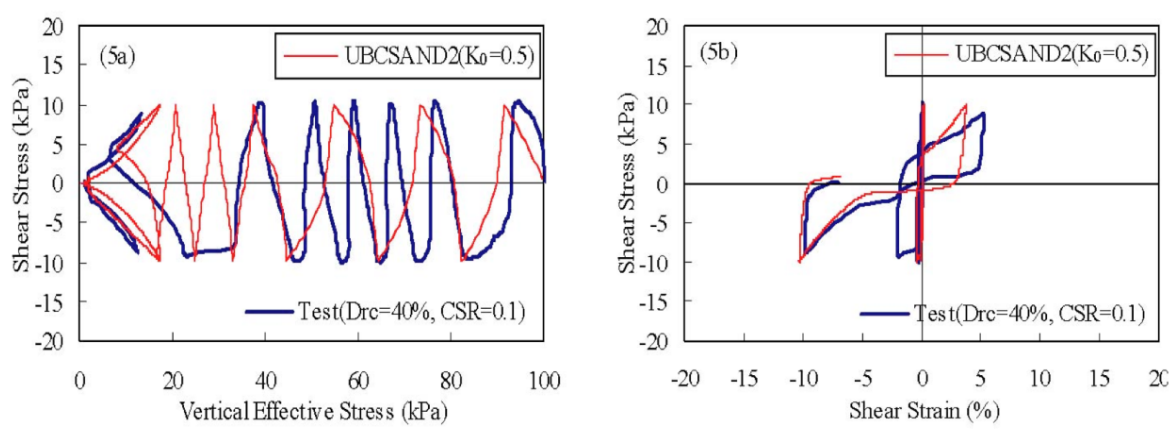

Figure 1.3.1. Predicted and measured stress paths and stress-strain responses for a sand with relative density of 40% at low CSR = 0.1 using UBCSAND (from Park and Byrne 2004).

1.4. UBCSAND Model Calibration Parameters

Several versions of UBCSAND currently exist and the model is evolving continually. Thus, calibration of the UBCSAND model may vary with changes made to the model. The version of UBCSAND employed in this study is UBCSANDCheck1 (Byrne 2009). The model input includes parameters modeling elastic stiffness, plastic shear stiffness, strength, flow rule, relative density, and four fitting parameters. Through our correspondence with Peter Byrne, the model developer, generic recommended values and relationships are provided for all but the corrected standard penetration test (SPT) blow count value, referred to as $(N_1)_{60}$, and four fitting parameters controlling triggering and post-triggering dilation. For this study, the generic correlations were not modified, and the model was evaluated for its ability to capture and predict deformations by limiting required user input to SPT blow count and the four fitting parameters discussed below.

1.4.1. Relative Density Index

The input parameter accounting for the relative density of the soil is the corrected SPT blow count, or $(N_1)_{60}$ value. This parameter is in wide use in industry, though laboratory testing on which model calibrations are frequently based are typically performed using the measure of relative density. A common equation used to relate relative density with $(N_1)_{60}$ blow count is:

$$D_R = \sqrt{\frac{(N_1)_{60}}{C_d}}$$

As summarized in Idriss and Boulanger (2008), the value of C_d has been evaluated by Meyerhof (1957), Skempton (1986), Cubrinovsky and Ishihara (1999) and found to range between 35 and 65 for clean sands. A consistent conversion methodology was desirable to evaluate trends in the fitting parameters. A value of C_d of 46 was used by Idriss and Boulanger (2008) in their SPT relationship, and this value falls within a reasonable range when considering the above studies. Initial modeling showed this to be a value that could capture response of the majority of tests while allowing sufficient range in the curve fitting parameters such that they could be used in fine adjustments of the response. A C_d value of 46 was selected and used to relate relative density and $(N_1)_{60}$ blow count for this effort.

1.4.2. Elastic Stiffness Parameters

Elastic stiffness parameters include the elastic shear stiffness number (m_kGe), the bulk stiffness number (m_kb), and the stress exponents m_ne and m_me. These parameters are related in these generic equations as provided by the model developer Peter Byrne:

- m_kge = 21.7 * 15 * $((N_1)_{60})^{0.333}$
- Max. Shear Modulus = G_{max} = m_kge * P_{atm} * $(\sigma'_m/P_{atm})^{m_ne}$
- m_kb = m_kge * 0.916 (assumes a small strain Poisson's ratio of 0.125)
- Bulk Modulus = K = m_kb * P_{atm} * $(\sigma'_m/P_{atm})^{m_me}$
- m_me = 0.5
- m_ne = 0.5

A plot showing the variation of normalized bulk and shear modulii with $(N_1)_{60}$ blow count is shown in Figure 1.4.1.

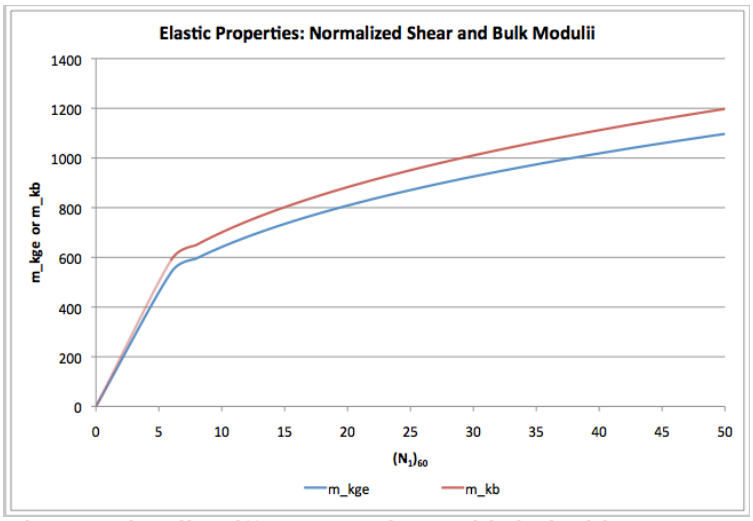

Figure 1.4.1. Elastic Shear and Bulk Stiffness Numbers with $(N_1)_{60}$ blow count.

1.4.3. Plastic Shear Stiffness Parameters

- Plastic shear stiffness parameters include the plastic shear modulus number (m_kgp), the plastic shear modulus stress exponent, anisotropy parameter, and the failure ratio (m_rf). Generic correlation equations provided by the model developer were used in our analysis and are described below and plotted on Figure 1.4.2. The anisotropy parameter varies linearly between 0.333 for loose pluviated soils and 1.0 for isotropic stress conditions.

- m_kgp = m_kge* $((N_1)_{60})^2$ * 0.003) + 100
- Shear Modulus = G = m_kge * P_{atm} * $(\sigma'_m/P_{atm})^{m_ne}$
- m_np = 0.4
- Failure Ratio = m_rf = 1.0 – m_n160/100
    - 0.5 < m_rf < 0.99
- Anisotropy parameter = m_anisofac = 0.0166 * $(N_1)_{60}$)
    - 0.333 (loose pluviated) < m_anisofac < 1.0 (isotropic)

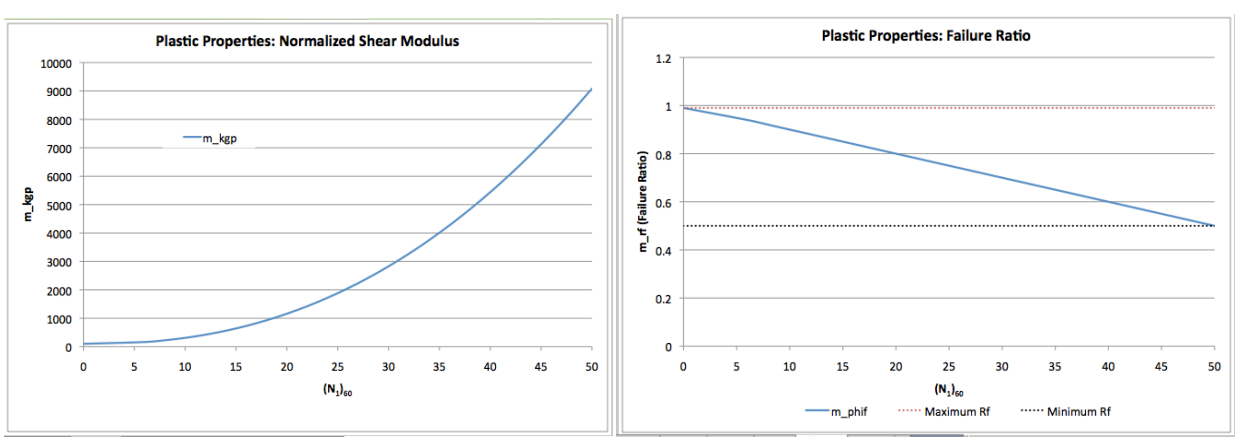

Figure 1.4.2. Plastic Shear Modulus Number and Failure Ratio vs. $(N_1)_{60}$ blow count.

1.4.4. Strength and Flow Rule

The constant volume friction angle is the parameter controlling the flow rule. Volumetric strain is calculated as a function of dilation angle. The dilation angle is calculated from the difference between peak friction angle and constant volume friction angle. The generic value of the constant volume friction angle is 33 degrees where the peak friction angle is calculated as a function of constant volume friction angle and blow count. Generic equations used in this study are provided below, and Figure 1.4.5 shows peak and constant volume friction angles plotted against blow count.

- m_phicv = 33
- m_phif = m_phicv + $((N_1)_{60})/5.0$

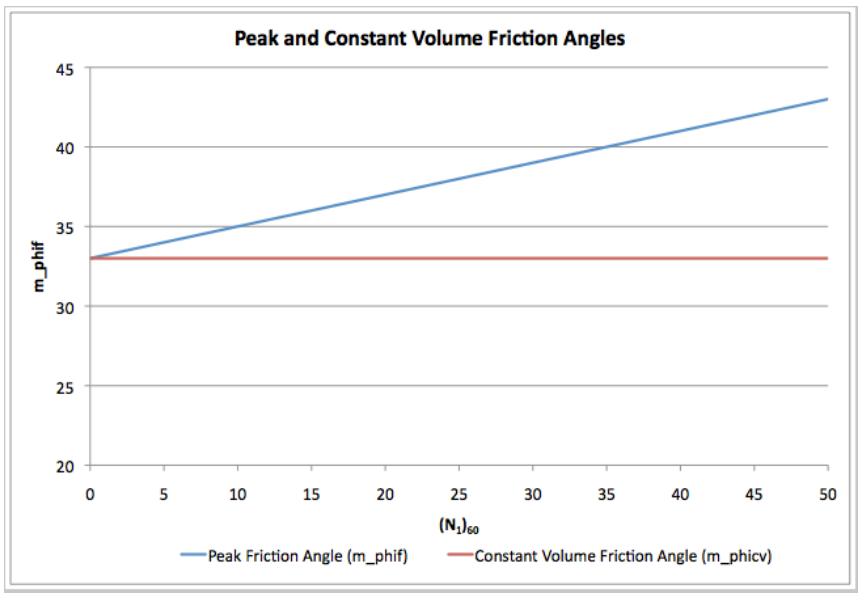

Figure 1.4.5. Peak and Constant Volume Friction Angles with $(N_1)_{60}$ blow count.

1.4.5. Fitting Parameters

Four fitting parameters are available within the UBCSANDCheck1 (Byrne, 2009) version of UBCSAND. The parameters and their listed function are provided below:

- m_hfac1 – Primary hardener that controls number of cycles to trigger liquefaction
- m_hfac2 – Secondary hardener that is reported to refine shape of pore water pressure rise with cycles.
- m_hfac3 – Dilation hardener, controls post-trigger response. This parameter can be set to 1 when running the model wet.
- m_hfac4 – This parameter reduces dilation after triggering.

2. MODEL CALIBRATION WITH CSS LABORATORY TEST MODELING

2.1. Selected CSS Test Set

As discussed previously, some of the difficulty the profession has had in developing simplified methods for evaluating lateral spreading is in capturing the complex phenomenon where soil resistance is changing throughout cyclic loading. Soils with low to intermediate confining stresses, which represent soil conditions appropriate for soils underlying small levees and earth embankments, eventually undergo dilation during shearing, leading to the development of "banana-shaped" loops in each half cycle of loading in the stress versus strain plots

Representative cyclic simple shear (CSS) laboratory tests were selected and modeled using a single-element numerical simulation to evaluate the proficiency of the UBCSAND soil model. Laboratory CSS tests were selected from data sets performed by Wu (2002) and Kammerer et al. (2002) on Monterey sand specimens and Nevada sand specimens, respectively. These clean sand tests were used to evaluate the ability of the model to capture the cyclic pore water pressure increase and corresponding cyclic strain response in clean sand soils. The laboratory tests listed in Tables 2.1.1 and 2.1.2 were selected to represent flat and sloping ground conditions, and UBCSAND was then evaluated in terms of its ability to capture the seismic response of these test specimens under a range of densities, cyclic stress ratios, and initial static shear stresses.

Table 2.1.1. Laboratory CSS test specimens selected to represent flat ground conditions in clean sand soils.

Test Name*	α ($=\tau/\sigma_v'$)	D_r	σ_v'	CSR
MS22J	0.005	40	85	0.099
MS24J	-0.001	43	85	0.136
MS42J	0.002	44	83	0.162
MS17J	0.003	48	40	0.164
MS16J	-0.003	59	85	0.166
MS21J	0	34	82	0.174
MS43J	-0.001	31	82	0.181
MS15J	0.004	54	95	0.195
MS23J	0.006	43	81	0.2
MS59J	0.004	58	98	0.223
MS48J	0.016	33	39	0.226
MS36J	0.004	70	80	0.227
MS28J	-0.005	56	85	0.247
MS20J	-0.004	45	85	0.249
MS60J	-0.002	56	40	0.258
MS124	0	49	81	0.312
MS19J	-0.01	55	80	0.323
MS7j	-0.004	58	33	0.324
MS25J	-0.002	56	85	0.339
MS30J	0.01	77	77	0.364
MS32J	0.018	82	80	0.401
MS125	0.012	64	79	0.429

* Tests beginning with the MS designation are from Wu (2002) and were performed on Monterey Sand 0/30.

Table 2.1.2. Laboratory CSS test specimens selected to represent sloping ground conditions in clean sand soils.

Test Name*	α (=τ/σ_v')	D_r	σ_v'	CSR
NS13	0.05	47	38	0.17
NS17	0.05	50	30	0.22
MS118J	0.06	60	85	0.175
MS39J	0.07	45	81.4	0.22
MS117J	0.08	46	86.2	0.139
NS11	0.08	90	44	0.22
NS16b	0.08	48	43	0.24
MS111J	0.09	66	81.4	0.173
MS113J	0.09	64	81.4	0.253
NS12	0.09	93	36	0.53
NS16	0.1	48	44	0.1
MS116J	0.1	44	81.4	0.168
NS4	0.1	68	40	0.24
MS122	0.11	48	76.6	0.127
NS10	0.11	90	95	0.26
MS123J	0.12	48	81.4	0.138
MS119J	0.13	61	81.4	0.154
MS120J	0.14	47	71.8	0.166
NS3	0.14	62	39	0.24
NS18	0.16	51	40	0.25
MS114J	0.17	60	82	0.24
NS19	0.19	51	41	0.24
NS9	0.21	90	102	0.24

* Tests with MS designation were performed on Monterey Sand Specimens by Wu (2002). Test names beginning with NS were performed on Nevada Sand specimens by Kammerer et al. (2002)

A range of representative silt CSS tests were selected from data sets by Sancio (2003) and a set of CSS laboratory tests performed on non-plastic Bonnie Silt by UC Davis as part of the Verification of Liquefaction Analysis by Centrifuge Studies (VELACS) project (Arulmoli et al., 1992). These laboratory tests were evaluated through single element numerical simulations in UBCSAND to evaluate the ability of the constitutive model to capture silt behavior. The test specimens listed in Table 2.1.3 were utilized in this study.

Table 2.1.3. Laboratory CSS test Specimens selected to represent silt soils.

Test Name*	α (=τ/σ_v')	Void Ratio (e)	σ_1' (kPa)	σ_3' (kPa)	σ_m' (kPa)	CSR	Plasticity Index
CSSBS-07	0.035	0.678	80	-	-	0.213	NP
A5P9B3	0	1.08	133	82	99	0.27	11
G4P3-6	0.2	1.09	136.5	82	100	0.27	14
G4P3-2	0.193	0.9	133.7	79	97	0.23	0

** All tests are from Sancio (2003) except test CSSBS-07 which is from Arulmoli et al., 1992.*

2.2. Sand – Flat Ground CSS Tests

Figures 2.2.1 through 2.2.3 show representative 4-way plots of shear stress vs. shear strain (upper left corner), shear stress vs. effective vertical stress (upper right corner), pore water pressure increase as a ratio of initial vertical effective stress vs. cycles of shear (lower left), and pore water pressure as a function of shear strain (lower right) for several CSS tests. In general, flat ground cases are well matched. Damping is generally overestimated as can be seen by the difference in shapes of the 'banana loops' shown in the shear stress vs. shear strain plots.

Based on the tests modeled in this study, pore water pressures were typically overestimated by UBCSAND resulting in difficulty matching strains over a range of cycles (i.e., a range of approximately 5 to 20 cycles would represent typical earthquake scenarios possible in California). As an example of this, Figure 2.2.2 shows an overlay of predicted vs. actual laboratory results for Monterey Sand test MS23J. As a result of overestimation of pore water pressures, softening of soils occurs earlier in the time record than observed in the actual laboratory test. Looking at plots of shear stress vs. shear strain and effective vertical stress (the two upper plots), one can see that when sufficient softening has occurred to trigger yielding in the soil under cyclic loading, the initial predicted lateral yield is larger than measured but with additional cycles the strain increment is reduced relative to measured and a match can be achieved. The range of cycles over which a suitable match to measured strains can be achieved varies with relative density, CSR, initial static shear, plasticity, and other factors as discussed in subsequent sections of this report.

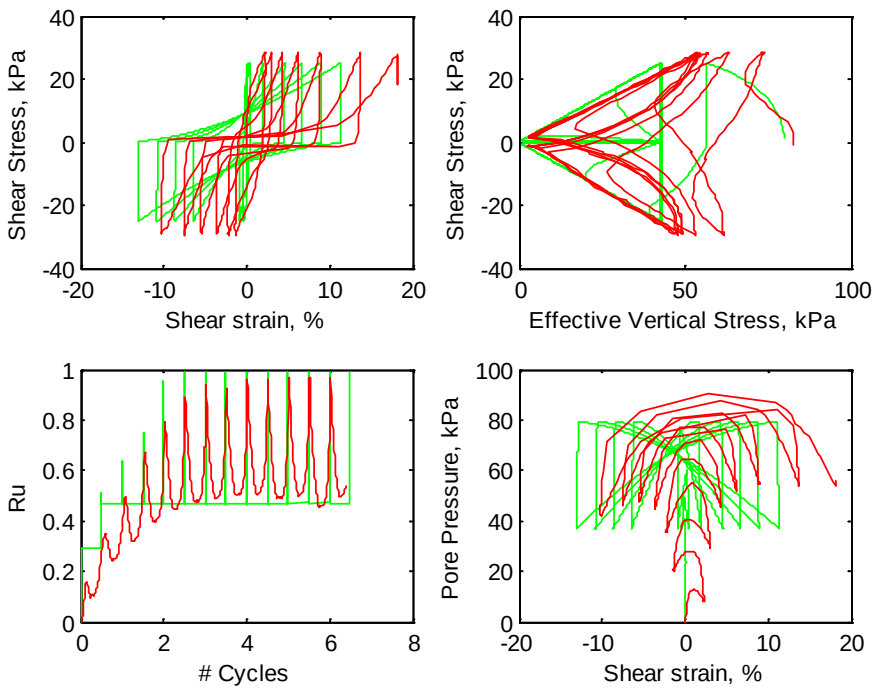

Figure 2.2.1. Test MS19J: α=-0.01; Dr=55%; CSR=.24 (Wu, 2002). Test data in red and UBCSAND output in green.

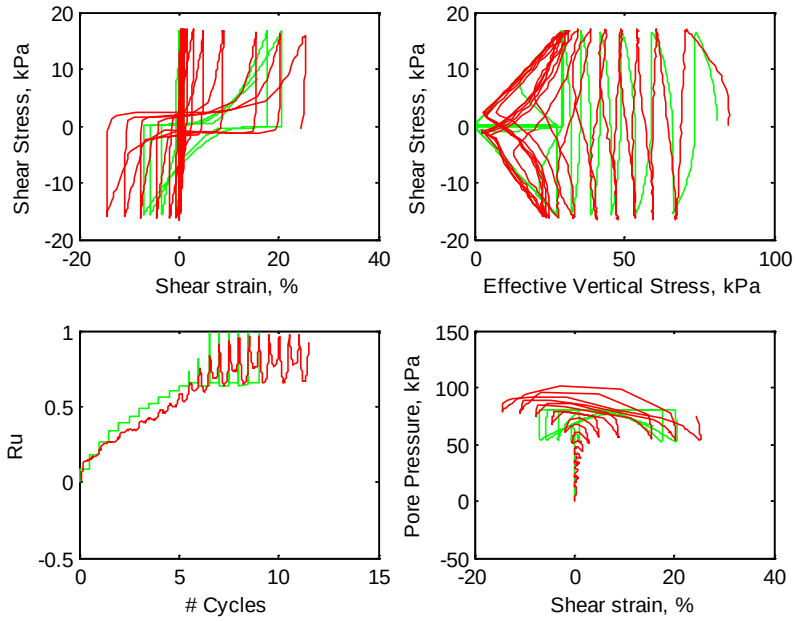

Figure 2.2.2. Test MS23J: α=0.006; Dr=81%; CSR=0.20 (Wu, 2002). Test data in red and UBCSAND output in green.

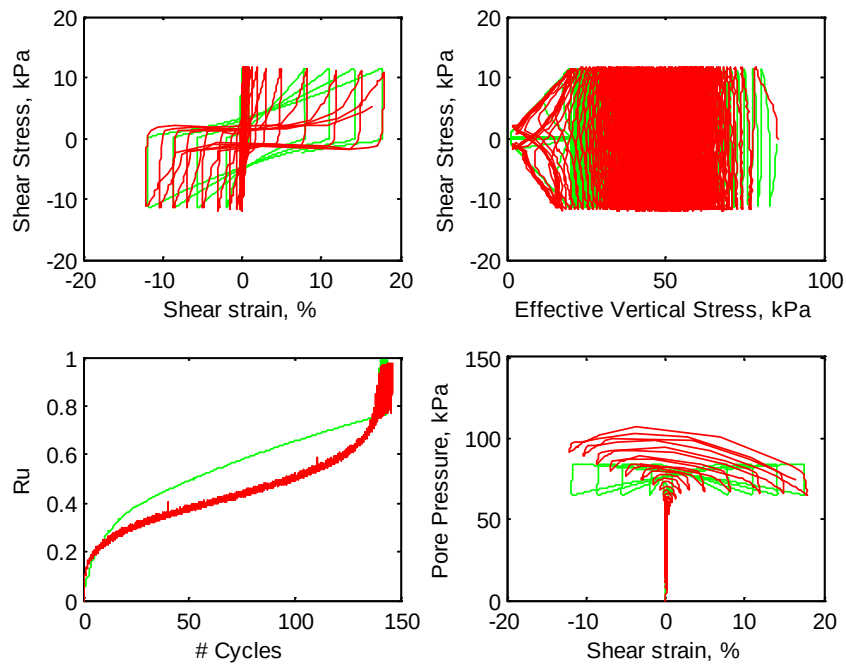

Figure 2.2.3. Test MS24J: α=-0.001; Dr=43%; CSR=0.136 (Wu, 2002). Test data in red and UBCSAND output in green.

2.3. Sand – Sloping Ground CSS Tests

Figures 2.3.1 through 2.3.4 show examples of calculated vs. measured response of clean sand Specimens of Monterey and Nevada Sands under initial static loading conditions and subjected to cyclic loading in simple shear. The UBCSAND model can capture many key aspects of soil response. However, it has a few limitations, which will be the focus of this discussion.

Shear strain is typically not matched in both the forward and reverse directions. Instead, it is matched in only the forward direction as can be seen for tests NS3 (Figure 2.3.1), MS118J (Figure 2.3.3), and MS11J (Figure 2.3.4). Further, the model is unable to calculate accurately the significant shear strains that sometimes occur due to the static shear loading prior to the triggering of flow liquefaction but during the incremental building of pore water pressures. Laboratory test specimens NS9 and MS11J are excellent examples of this (Figures 2.3.2 and 2.3.4, respectively). Specimen NS9 does not liquefy during the test and strains are not well captured. Similarly, Specimen MS11J exhibits cyclic mobility with limited strain potential as well as incremental movements in the downslope direction (the direction of the initial static shear stress). Looking at the plot of pore water pressure with shear strain (lower right corner) of Figure 2.3.4, the UBCSAND model can capture the deformation well once pore water pressures have incrementally increased to a pore water pressure ratio (Ru) of greater than about 50%. The UBCSAND model has not captured the effects of cyclic mobility with limited strain potential or the 'creeping' movements in the downslope direction driven by the initial static shear.

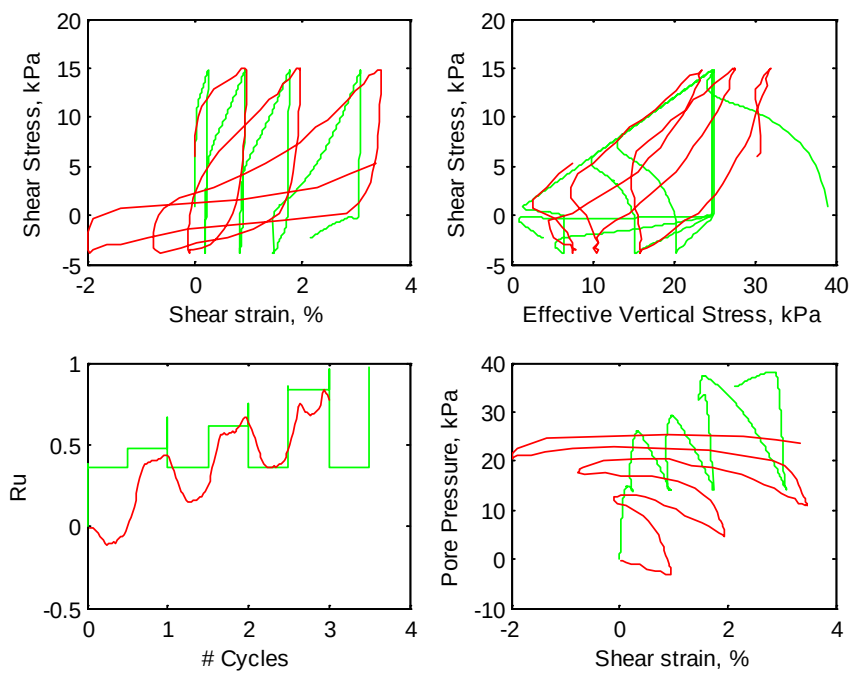

Figure 2.3.1. Test NS3: α=0.14; Dr=62%; CSR=0.24 (Kammerer, 2002). Test data in red and UBCSAND output in green.

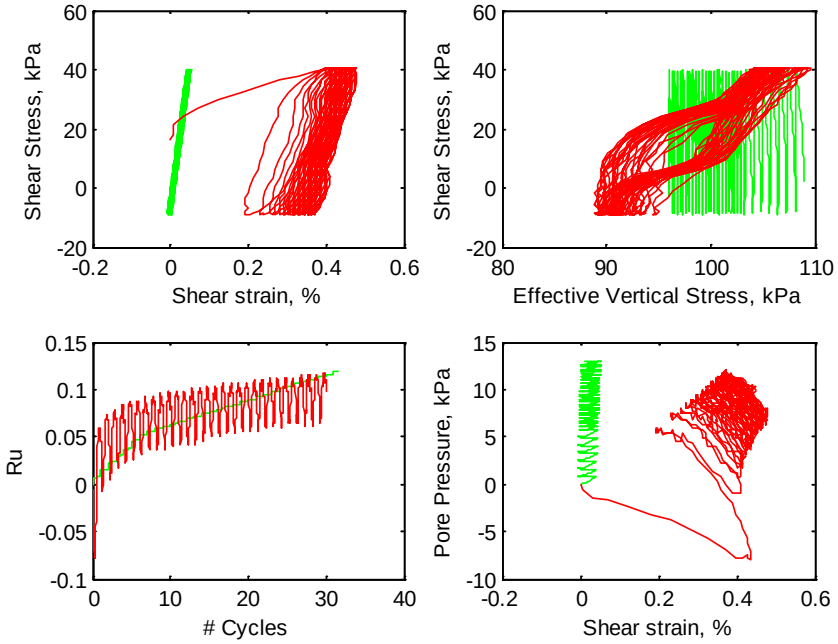

Figure 2.3.2. Test NS9: α=-0.21; Dr=90%; CSR=0.24 (Kammerer, 2002). Test data in red and UBCSAND output in green.

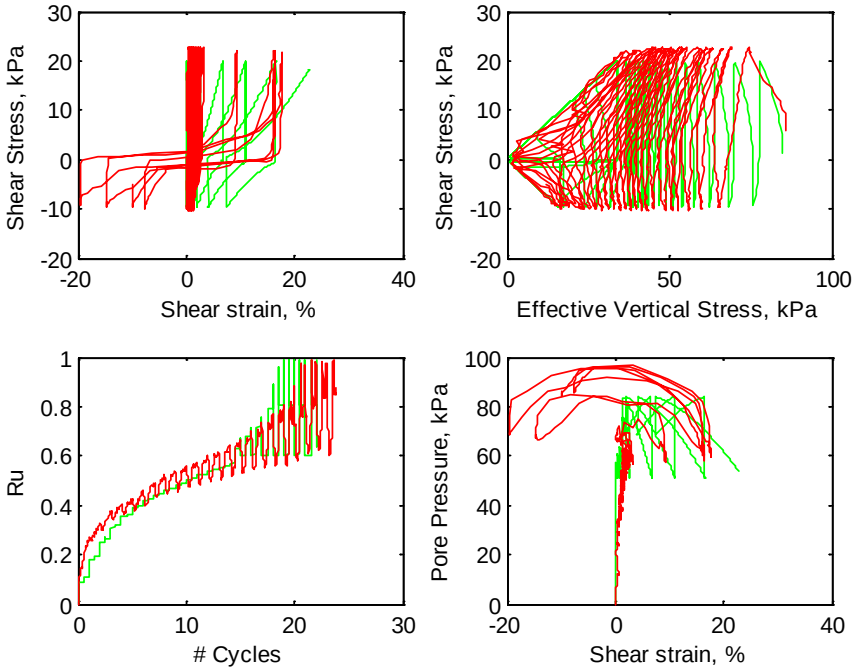

Figure 2.3.3. Test MS118J: α=0.06; Dr=60%; CSR=0.175 (Wu, 2002). Test data in red and UBCSAND output in green.

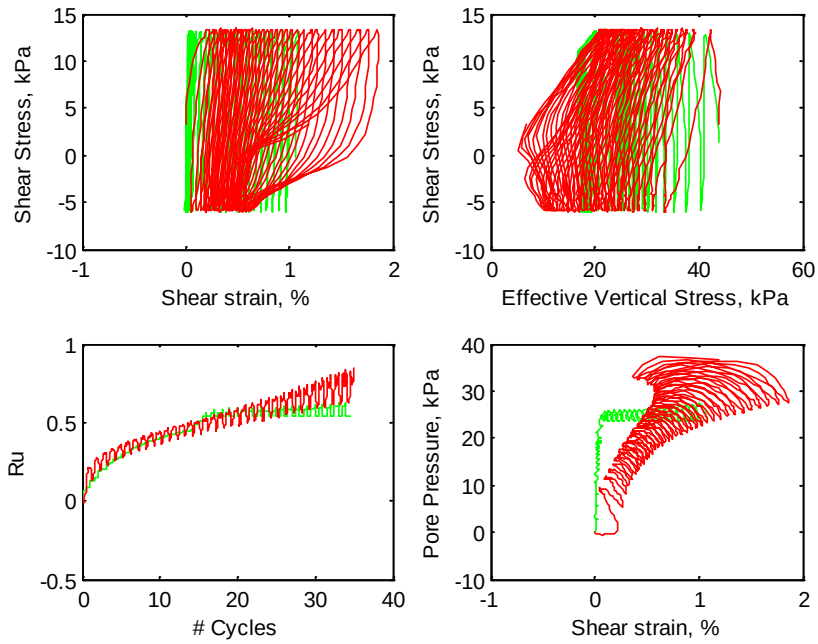

Figure 2.3.4. Test NS11J: α=0.08; Dr=90%; CSR=0.22 (Kammerer, 2002). Test data in red and UBCSAND output in green.

2.4. UBCSAND Calibration Curves

2.4.1. M_HFAC1 and M_HFAC2

Though different functions are listed for these two parameters, we found that m_hfac1 and m_hfac2 have similar function as both affect the number of cycles to triggering. We were unable to achieve variation in the rate of pore water pressure rise with cycles through variation of the m_hfac2. In our studies we found that varying both parameters added unnecessary complication to the analysis and found best results obtained by matching m_hfac2 to m_hfac1 and treating the two parameters as a single parameter. Personal communication with the model developer, Professor Byrne, confirmed that this was an acceptable strategy. Subsequent plots refer to m_hfac1 and m_hfac2 with the assumption that the parameters were equal to one another.

Figure 2.4.1 shows how the m_hfac1 and m_hfac2 parameters vary with relative density (D_r). In general, we found that tests with lower initial static shear stress required slightly lower values of the m_hfac1 and 2 while specimens with higher initial static shear stress required higher values of these fitting parameters to achieve the best match with laboratory testing values. Specimens with higher initial static shear stress exhibited greater variation in the m_hfac1 and 2 parameters to capture the response. Larger values of the m_hfac1 and 2 fitting parameters reduce the rate of pore water pressure rise with cycles and increase the number of cycles to liquefaction.

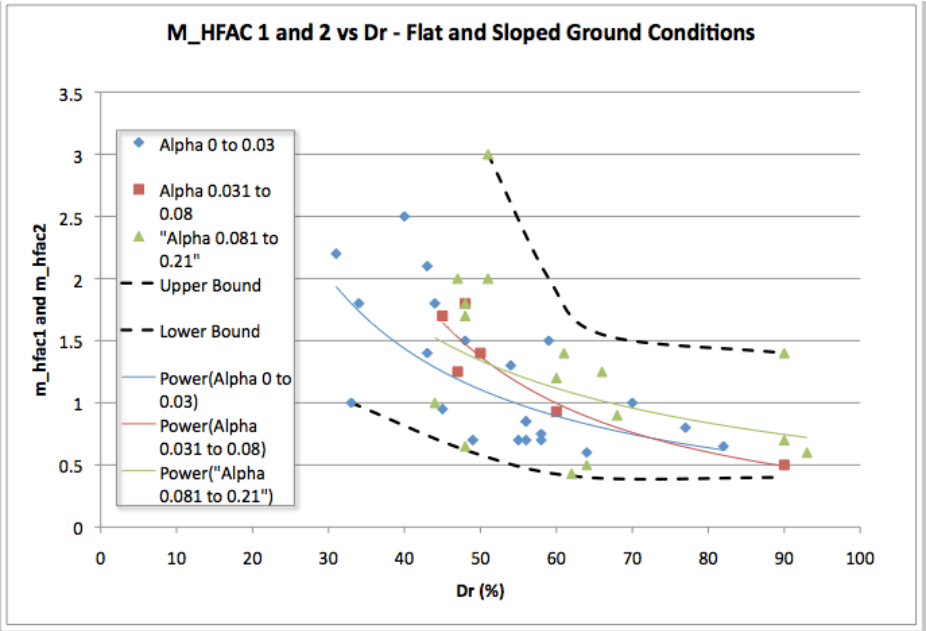

Figure 2.4.1. Triggering Parameters m_hfac1 and m_hfac2 vs. Relative Density (Dr).

Trends of m_hfac1 and 2 with CSR are plotted on Figure 2.4.2 for the flat ground condition and Figure 2.4.3 for sloping and flat ground conditions. A clear trend is seen with CSR for the flat ground condition. It should be noted that affects of relative density were not separated out in Figures 2.4.2 and 2.4.3 and laboratory specimens prepared with a low relative density tend to be tested at low CSR, while those prepared at higher relative density tend to be tested at higher CSR in order to trigger liquefaction.

It is clear from Figure 2.4.3 that sloping ground conditions do not exhibit the same trend with CSR seen with flat ground specimens. The triggering parameters used to capture the liquefaction response for specimens with larger initial static shear stress exhibit trends with density as opposed to CSR. Both Figures 2.3.2 and 2.4.3 were used in determining the values of fitting parameters m_hfac1 and m_hfac2 for use in back analysis of case histories as well as forward modeling of the simplified cases of our sensitivity study. Parameter selection for these models will be discussed in subsequent sections of this report.

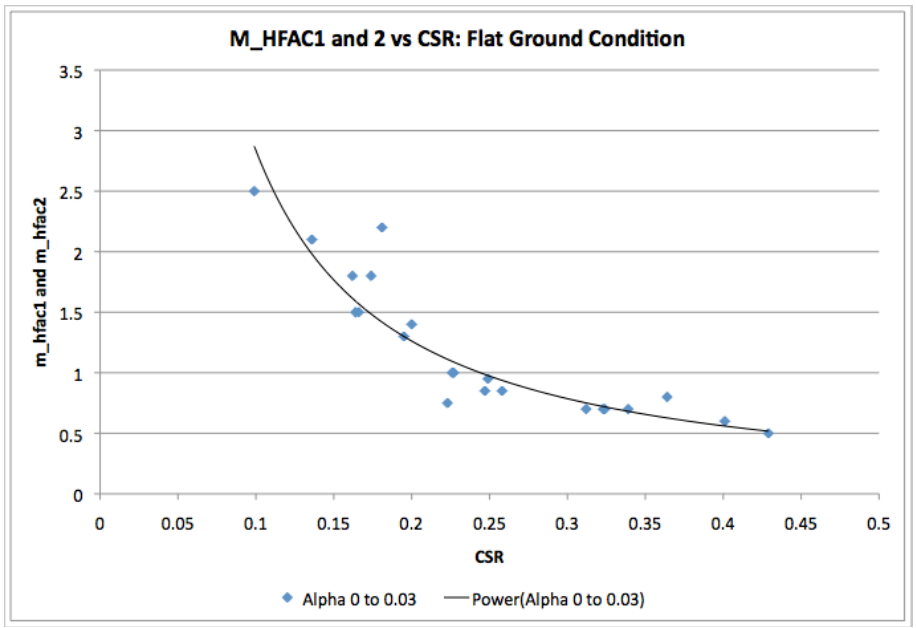

Figure 2.4.2. Triggering Parameters m_hfac1 and 2 vs. CSR – Flat Ground Condition.

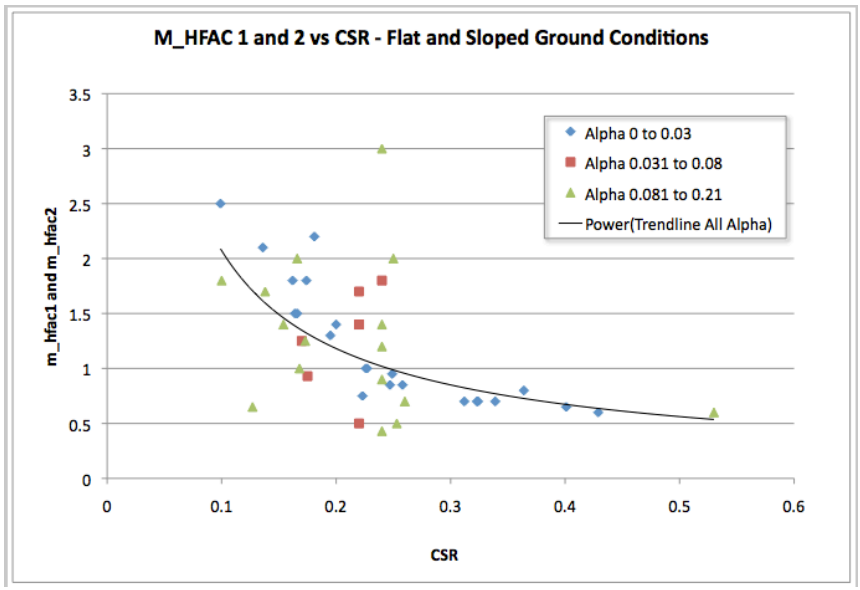

Figure 2.4.3. Triggering Parameters m_hfac1 and 2 vs. CSR – Flat and Sloping Ground Conditions.

2.4.2. M_HFAC3

The parameter m_hfac3 was not varied, but rather was set to 1.0 for analyses where the model was to be run wet. Layers above the groundwater table were modeled with the Mohr-Coulomb model.

2.4.3. M_HFAC4

The dilation reduction parameter m_hfac4 was varied between 0.5 and 2.7 to capture the post-triggering shear strains of clean sand and silt specimens. Silts will be discussed in a separate section, and we will discuss clean sand trends as they vary with relative density, CSR and initial static shear stress.

Figures 2.4.4 and 2.4.5 show the value of m_hfac4 that was used to capture the level of shear strain in clean sand specimens with varying CSR and D_r respectively for a flat ground case. The data were divided into groups of low CSR (equal to 0.2 or less) and higher CSR (greater than 0.2). Specimens subjected to higher CSR values showed a weak trend with CSR and no noticeable trend with D_r. The value of m_hfac4 increases with increasing CSR. Increasing m_hfac4 reduces dilation after triggering and increases incremental strains. Specimens subjected to lower CSR did not show a trend with increasing CSR, but rather exhibited a weak trend with Dr. As soils became looser, the value of m_hfac4 was decreased to match strains. Decreasing m_hfac4 increases dilation after triggering and limits the overestimation of shear strains.

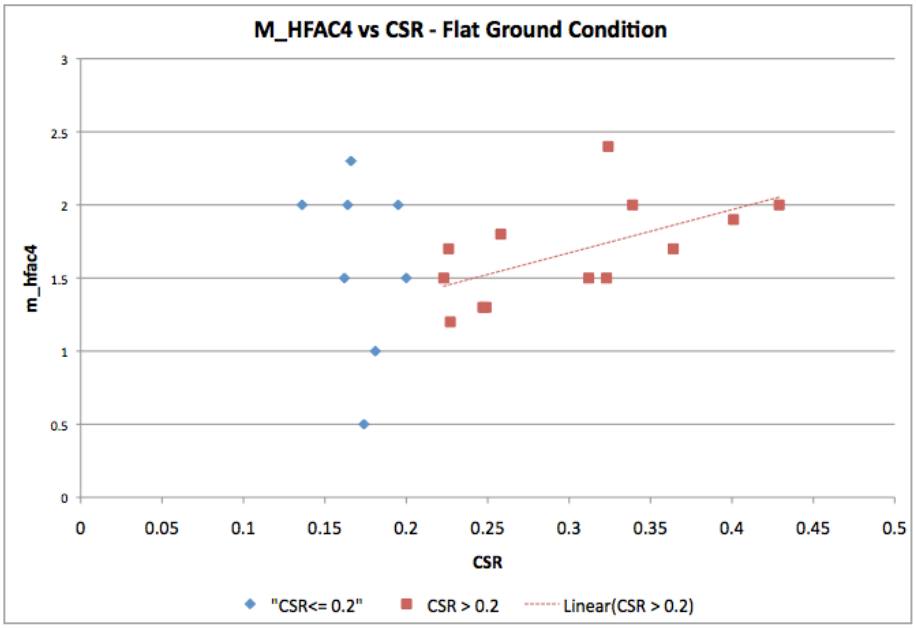

Figure 2.4.4. Dilation reduction parameter, m_hfac4 vs. CSR – Flat Ground Case. A weak trend with CSR is visible for values of CSR greater than 0.2. No trend is observed at CSR values of 0.2 or less.

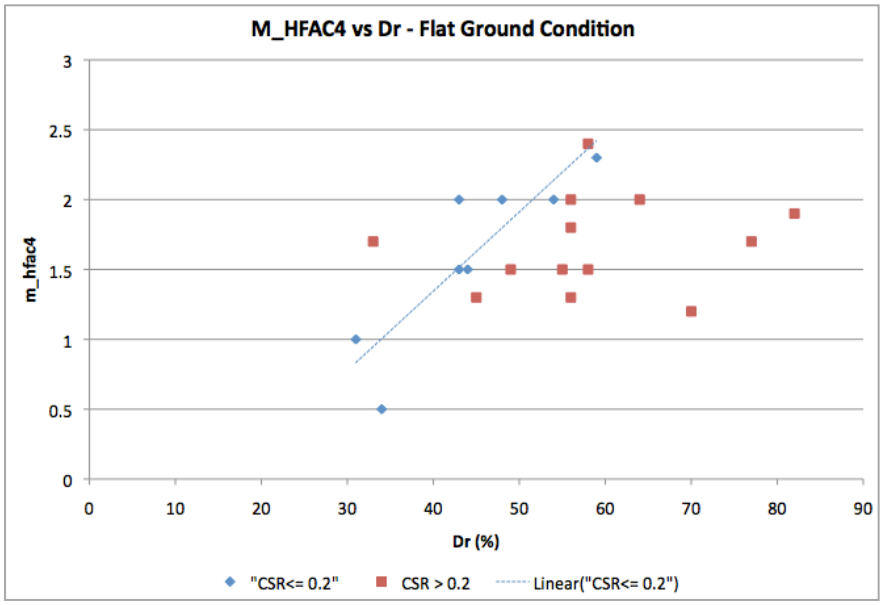

Figure 2.4.5 Dilation reduction parameter, m_hfac4 vs. D_r – Flat Ground Case. A weak trend is visible with D_r at values of CSR of 0.2 or less.

Figures 2.4.6 and 2.4.7 show plots of both sloping and flat ground condition cases against relative density and CSR. A weak trend with D_r can still be seen in the specimens subjected to CSR values of 0.2 or less (Figure 2.4.6). No trend is visible with CSR (Figure 2.4.7), though values typically range between 1.5 and 2.0.

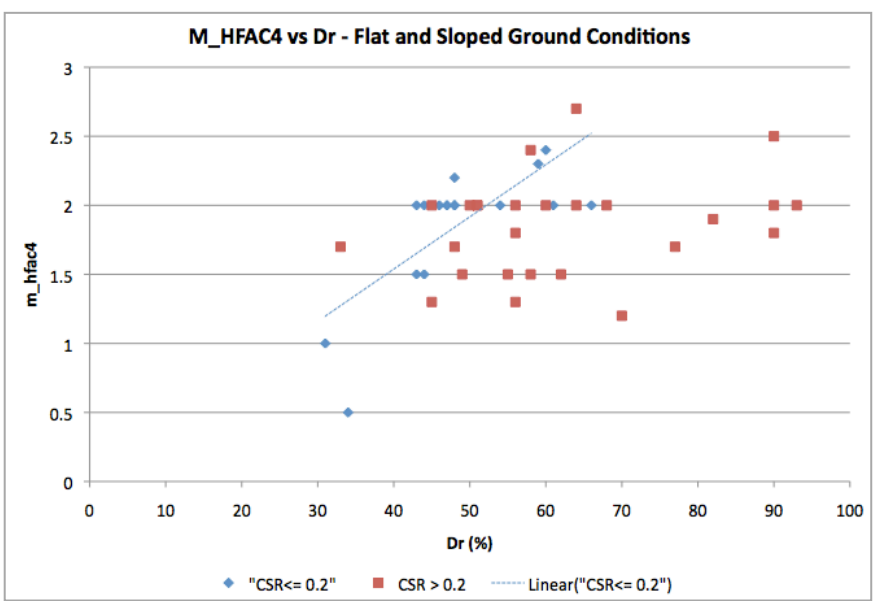

Figure 2.4.6. Dilation reduction parameter, m_hfac4 vs. D_r – Sloping and Flat Ground Cases. A weak trend is visible with D_r at values of CSR of 0.2 or less.

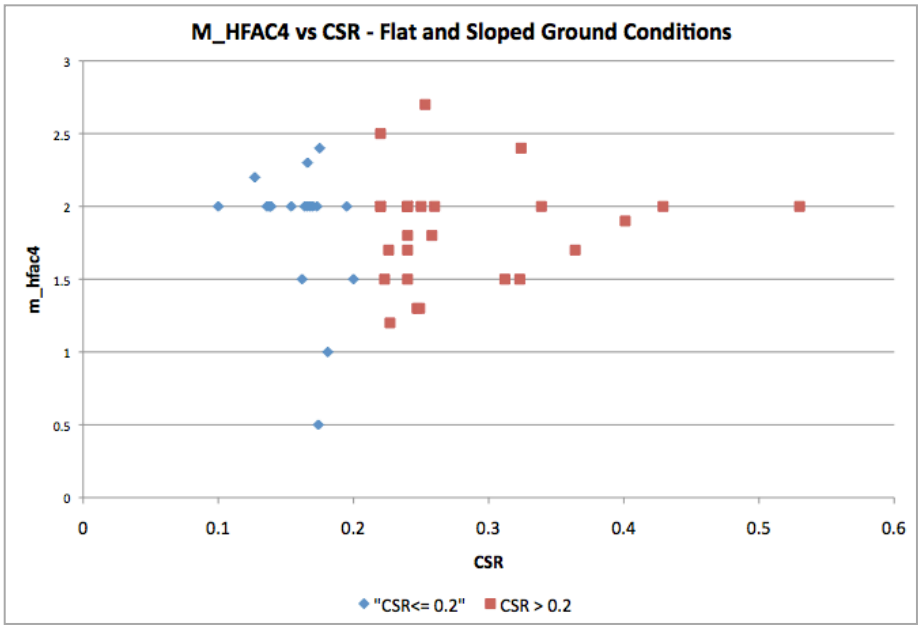

Figure 2.4.7. Dilation reduction parameter, m_hfac4 vs. CSR – Sloping and Flat Ground Cases.

2.5. Silt – Flat and Sloping Ground

Parameters used for modeling silts were developed by modeling laboratory tests using a series of blow count values within UBCSAND to determine a value that yielded a realistic fit to laboratory data. In general, values of m_hfac1 and m_hfac2 selected were found to be slightly higher for silts than sands of zero initial static shear stress but were found to follow a similar trend when considering the void ratio of the sample as a relative measure of blow count. Figure 2.5.1 shows a plot of m_hfac1 and 2 for the 4 laboratory tests considered against the selected value of blow count. The data are plotted with previously reported sand data for comparison. The values selected for m_hfac4 were lower than those selected for sands of similar fines corrected $(N_1)_{60}$ blow count. For higher void ratio silts, a value of m_hfac4 of 0.5 was found to be appropriate. For silts of lower void ratio as well as silty sands, we selected a value of m_hfac4 of 1.5.

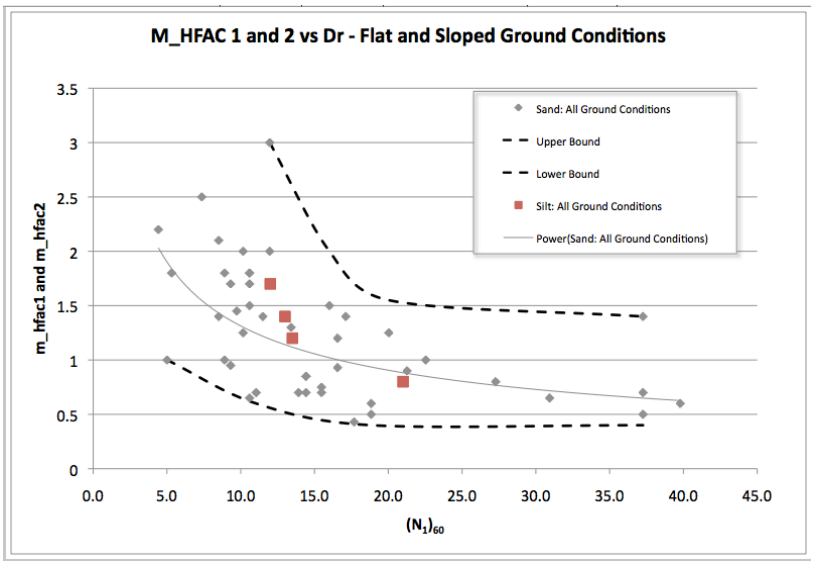

Figure 2.5.1. Selected values of m_hfac1 and m_hfac2 found to yield a fit to the laboratory data.

3. MODEL CALIBRATION WITH BACK ANALYSIS

A few important case histories of "limited" lateral spreads, as defined by Martin and Lew (1999), will be performed to calibrate the numerical tools discussed previously. Excellent descriptions of lateral spread case histories are contained in Bardet et al. (1999) and Faris (2004). These descriptions will be relied upon in this study.

Due to their relatively excellent documentation and range of liquefaction-induced lateral spread displacements, these case histories will be used in this study:

- Juvenile Hall lateral spread with a maximum displacement of 2.4 m during the 1971 San Fernando Earthquake
- Moss Landing Marine Laboratory lateral spread with a maximum displacement of 1.4 m during the 1989 Loma Prieta Earthquake
- Monterey Bay Aquarium Research Institute lateral spread with a maximum displacement of 0.3 m during the 1989 Loma Prieta Earthquake

Each of these case histories will be back-analyzed with the UBCSAND model as implemented in FLAC to ensure that the analytical methods being employed in this research project provides reliable insights.

3.1. Moss Landing MBARI/Sandholdt Road – Loma Prieta 1989

Moss Landing and the surrounding region was the site of numerous examples of ground failure due to liquefaction and lateral spreading associated with ground shaking of the 1989 Loma Prieta earthquake. One such site is located along Sandholdt Road about 300 feet north of the western approach of an existing timber access bridge crossing the Old Salinas River on the Moss Landing spit in the vicinity of the Monterey Bay Aquarium Research Institute (MBARI). Sandholdt Road runs in a north/south direction and functions as the primary access road for MBARI complex (Figure 3.1.1).

Site damage, subsurface stratigraphy, and a summary of available reports and information surrounding the case study were well documented and summarized in a comprehensive report by Boulanger et al. (1995). Inclinometers had been installed and monitored prior to the Loma Prieta earthquake and captured lateral movements with depth at three locations within the zone of lateral spreading. Section A-A' of Figure 3.1.1 was selected for our analysis as a soil boring and two cone penetration tests (CPT) were performed along this section.

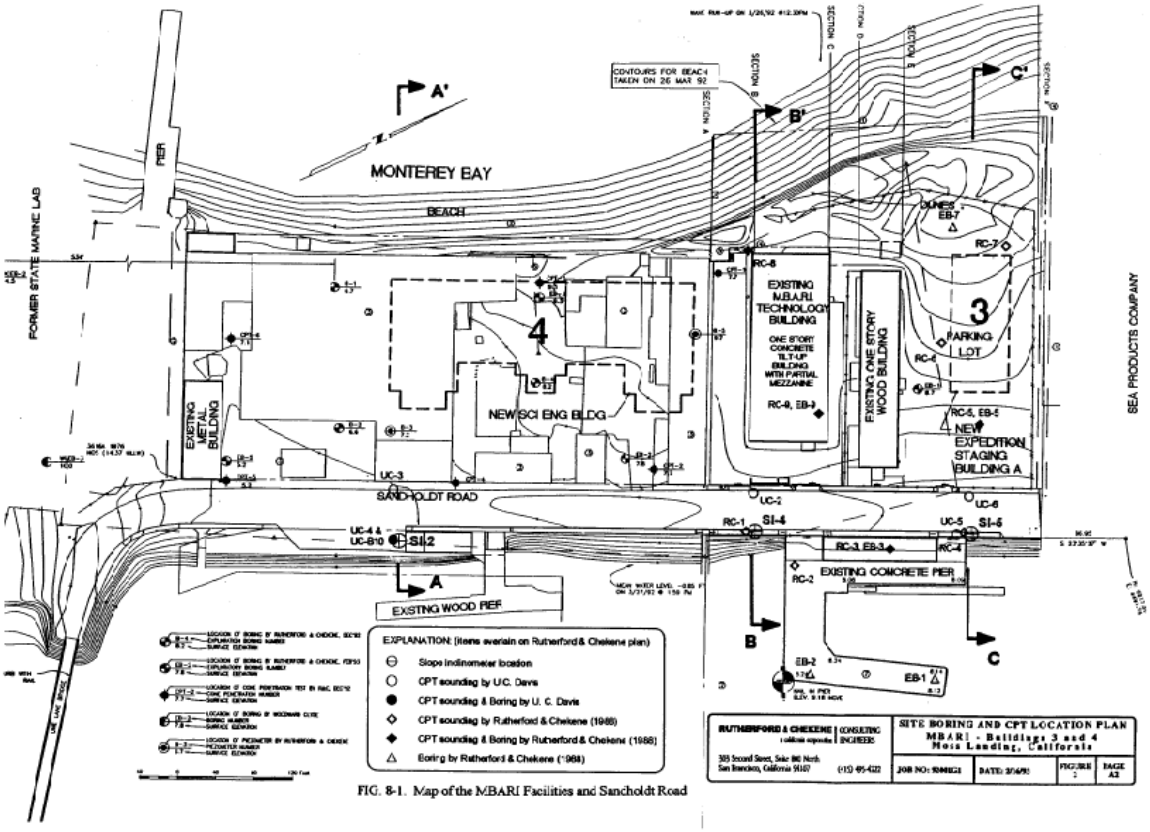

Figure 3.1.1. Site plan showing Sandholdt Road, the MBARI complex, waterfront piers, and the former State Marine Lab site discussed in Section 3.2.

Figure 3.1.2 shows a cross section of the subsurface stratigraphy at Section A-A'. Inclinometer S-2 is located adjacent to boring UC-B10 and CPT UC-4. Based on Boulanger et al. (1995) the large crack within Sandholdt Road was considered to be the limit of primary deformation as shown in the photograph included in Figure 3.1.3. Figure 3.1.4 shows inclinometer S-2 data plotted with the soil profile created using soil boring B10 and CPT UC-4. Blow count data are overlain with CPT tip resistance. Inclinometer S-2 shows lateral displacements of up to approximately 27 cm at the surface. Deformations extended to a depth of approximately 4.6 meters from the surface and stopped at the transition between the thin sand layer and the clayey silt layer below. The movement occurred gradually over a zone extending from a depth of approximately 1.5 m to a depth of 4.6 m rather than sliding as a block on a single slide plane as would be assumed by post-liquefaction stability analysis methods using residual strength assumptions.

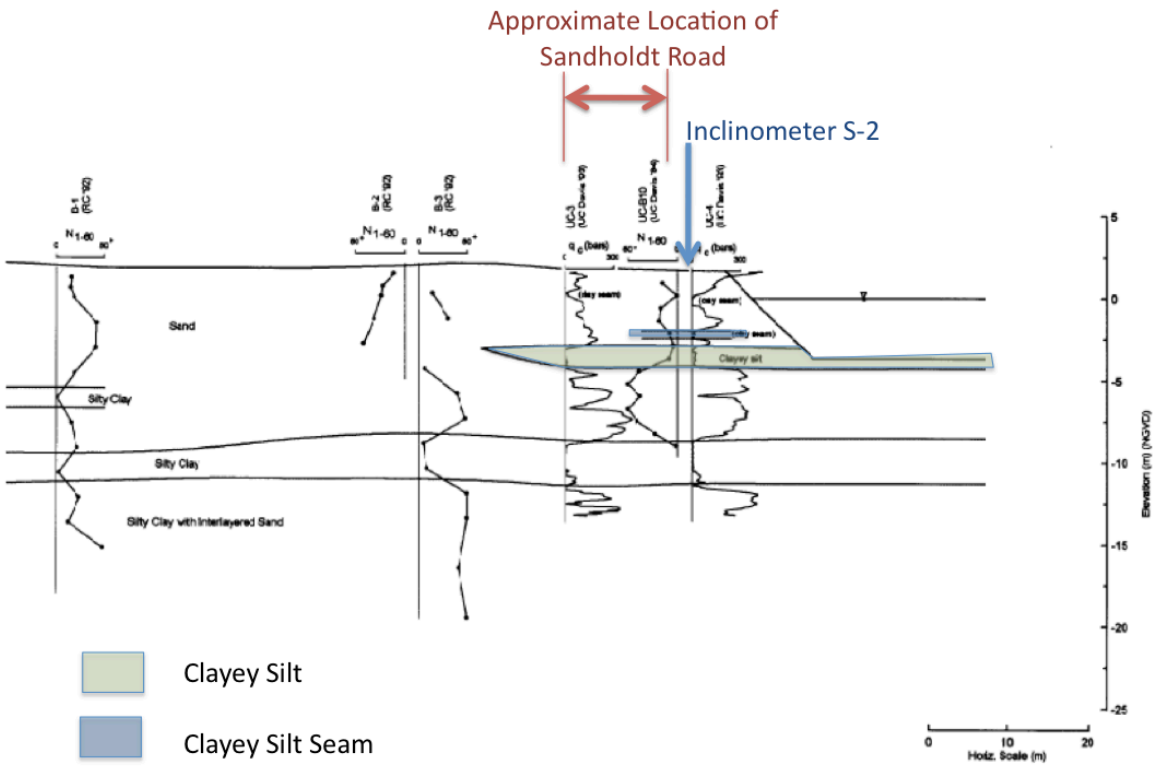

Figure 3.1.2. Subsurface stratigraphy at Section A-A'. The thin seam shown in blue will be referred to as a clayey silt seam to be consistent with available boring logs and laboratory test data from UC-B10.

Figure 3.1.3. Cracking along Sandholdt Road (looking north just south of MBARI pier; from Boulanger et al. 1995).

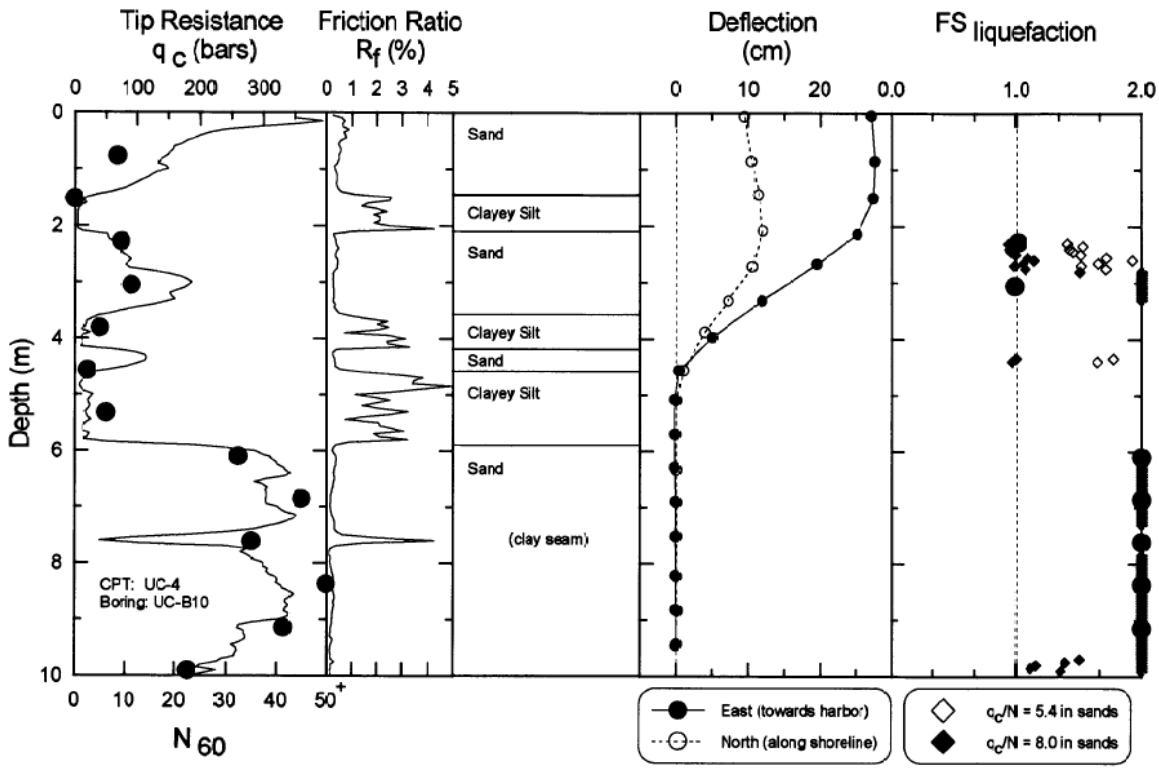

Figure 3.1.4. Inclinometer S-2 measured deformation data. Data is plotted with subsurface stratigraphy from boring UC-B10 and CPT UC-4 (from Boulanger et al. 1995).

Two silt layers are labeled on Figure 3.1.2 as ‘clayey silt’ and ‘clayey silt seam’ for the purpose of this discussion. Based on Figure 3.1.4, inclinometer data shows that movement occurred within the ‘silt seam’ but not within the ‘clayey silt’ layer below it. The ‘clayey silt seam’ may be so thin that it deformed with sand layers above and below or that the inclinometer pipe stiffness ‘averaged’ the deformations across thin seams of sand and silt. In deciding whether to model each silt layer with the UBCSAND or Mohr-Coulomb models, available CPT, boring, and laboratory data were evaluated in detail for each layer.

Both the ‘clayey silt seam’ and ‘clayey silt’ layers exist at the location of inclinometer S-2 and both appear in soil boring UC-B10 and CPT UC-4. Gradation testing performed on the ‘clayey silt seam’ found fines content to be 74% passing the number 200 sieve with 18% finer than 5 microns. Similar testing on the ‘clayey silt’ found a fines content of 80% and 14 percent smaller than 5 microns. Atterberg limits testing was performed only on the ‘clayey silt seam’ and was found to have a plasticity index (PI) of 7% and a liquid limit of 32%.

Cone penetration data (UC-4 and UC-3) are available on either side of Sandholdt road as indicated on Figures 3.1.1 and 3.1.2. The ‘clayey silt’ layer appears in both CPTs, while the ‘clayey silt seam’ appears only in UC-4, adjacent to inclinometer S-2. A comparison of CPT data yielded an inconclusive result as to whether the ‘clayey silt’ layer at the toe of slope should be modeled as a potentially liquefiable layer with the UBCSAND model or with the Mohr-Coulomb model. Thus, both cases were considered, and the results compared. In Model A, the ‘clayey silt’ layer at the toe of slope is modeled as a cohesive soil with the Mohr-Coulomb model. Figure 3.1.6 shows the mesh and layers used to model the site. As summarized in Boulanger et al.

(1995), the ground motion driving the observed lateral spread deformation was estimated to have a peak ground acceleration (PGA) of approximately 0.2 to 0.3 g using a bedrock motion of 0.15 g. The report concluded that 0.25 g would likely represent a median or slightly lower estimate of Loma Prieta earthquake. The Salinas ground motion record (PGA = 0.15 g) was identified as having similar soil conditions at depth and was scaled to 0.25 g. This ground motion was used as input in our analysis.

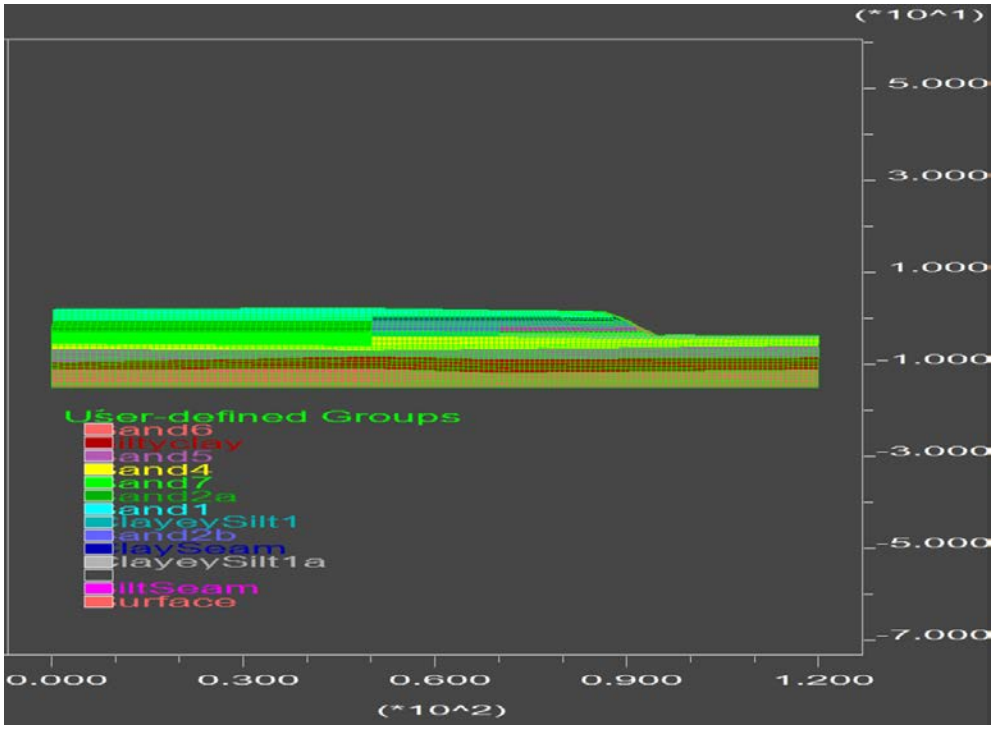

Figure 3.1.6. Mesh and soil groups at the site of the MBARI/Sandholdt Road lateral spread.

Figures 3.1.7 and 3.1.9 show the resulting lateral deformations from each model. Figure 3.1.8 and 3.1.10 show vectors of deformation showing both horizontal and vertical movements for Models A and B, respectively. Figure 3.1.11 shows the resulting deformations for each model plotted with measured inclinometer data. It can be seen that when the 'Clayey Silt' layer is modeled with the Mohr-Coulomb model, estimated deformations closely match observations. When the UBCSAND model is used to model the 'Clayey Silt' layer, the simulation calculates deformations in this layer that were not observed and as a consequence, the deformations are overestimated by a factor of about 2. As discussed previously, numerical models are not a substitute for detailed subsurface characterization as the model may be improved significantly with increased understanding of the subsurface conditions.

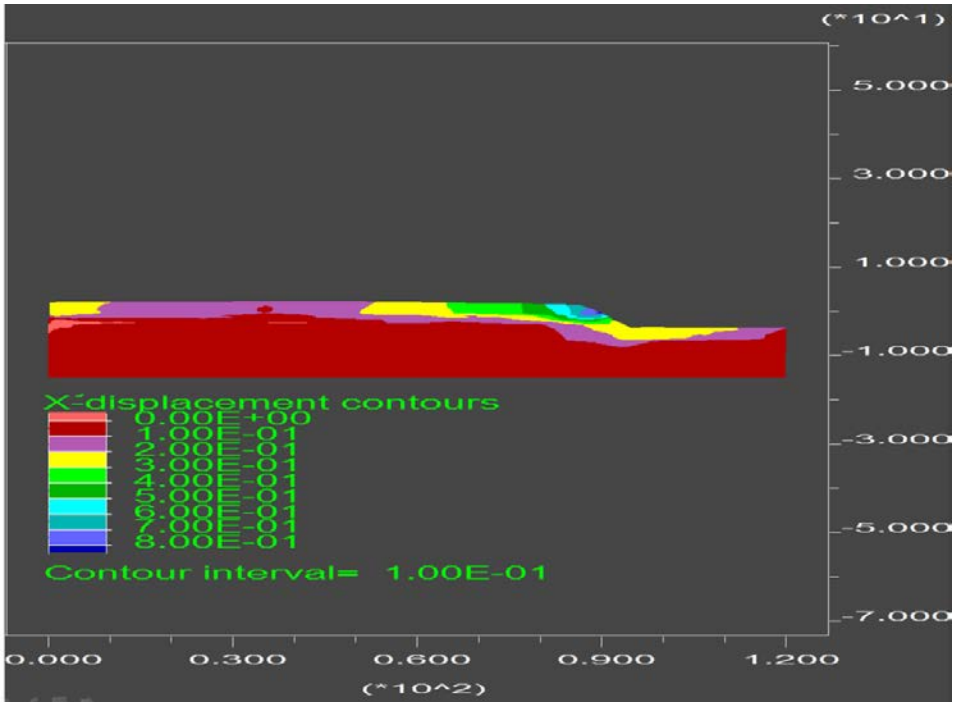

Figure 3.1.7. Predicted lateral displacements at MBARI/Sandholdt Road Section A-A' as predicted by Model A.

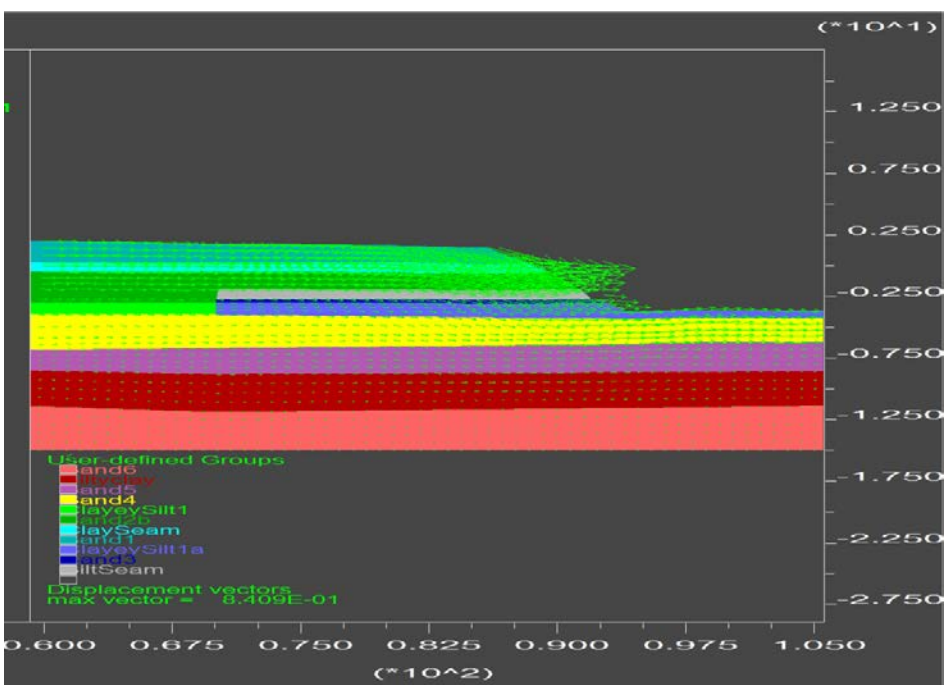

Figure 3.1.8. Predicted displacement vectors plotted with soil type at MBARI/Sandholdt Road Section A-A' as predicted by Model A.

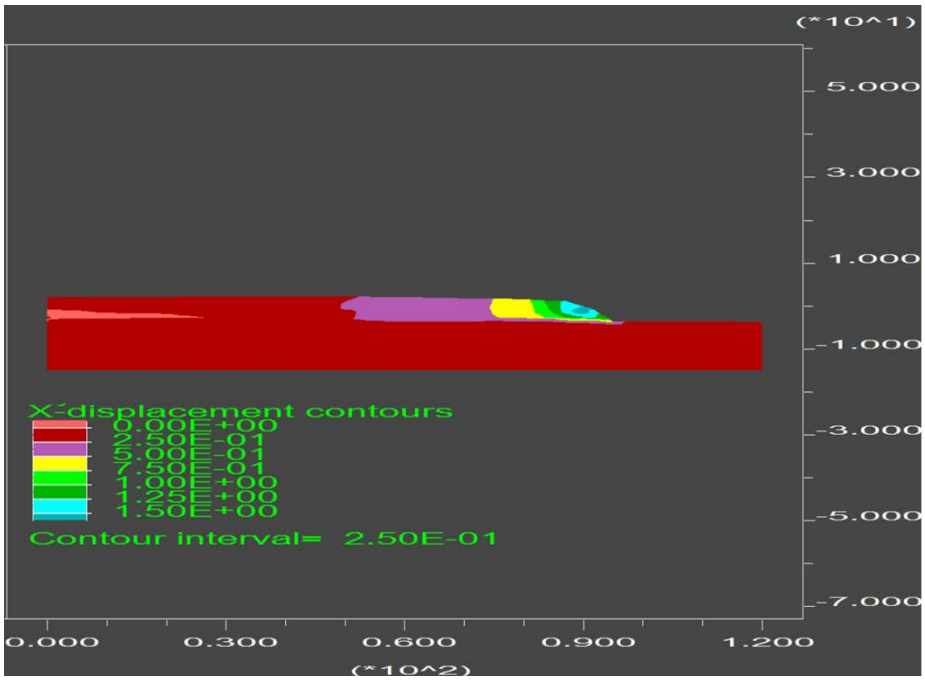

Figure 3.1.9. Predicted lateral displacements at MBARI/Sandholdt Road Section A-A' as predicted by Model B.

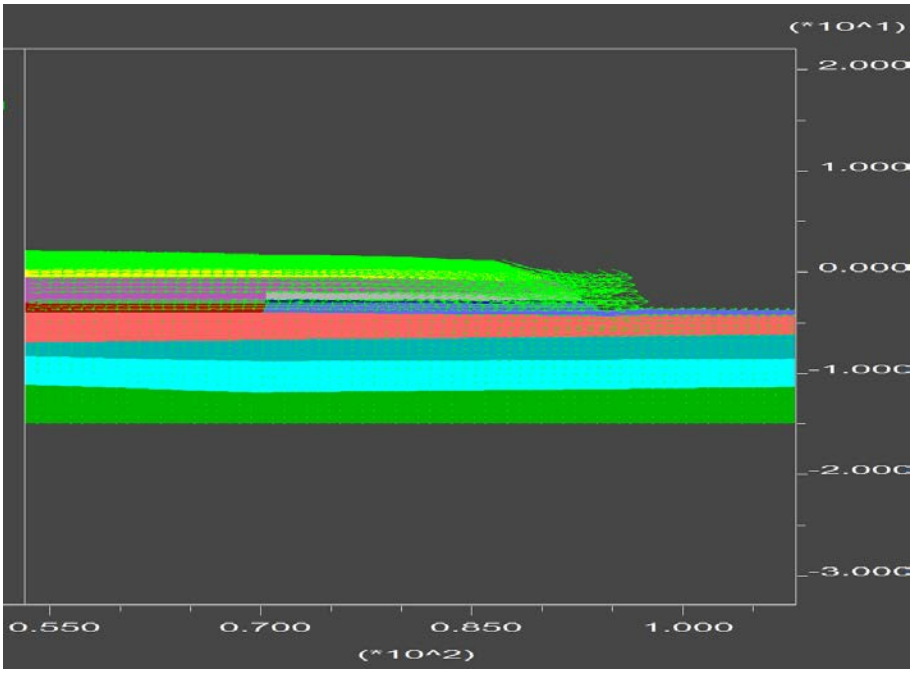

Figure 3.1.10. Predicted displacement vectors plotted with soil type at MBARI/Sandholdt Road Section A-A' as predicted by Model B.

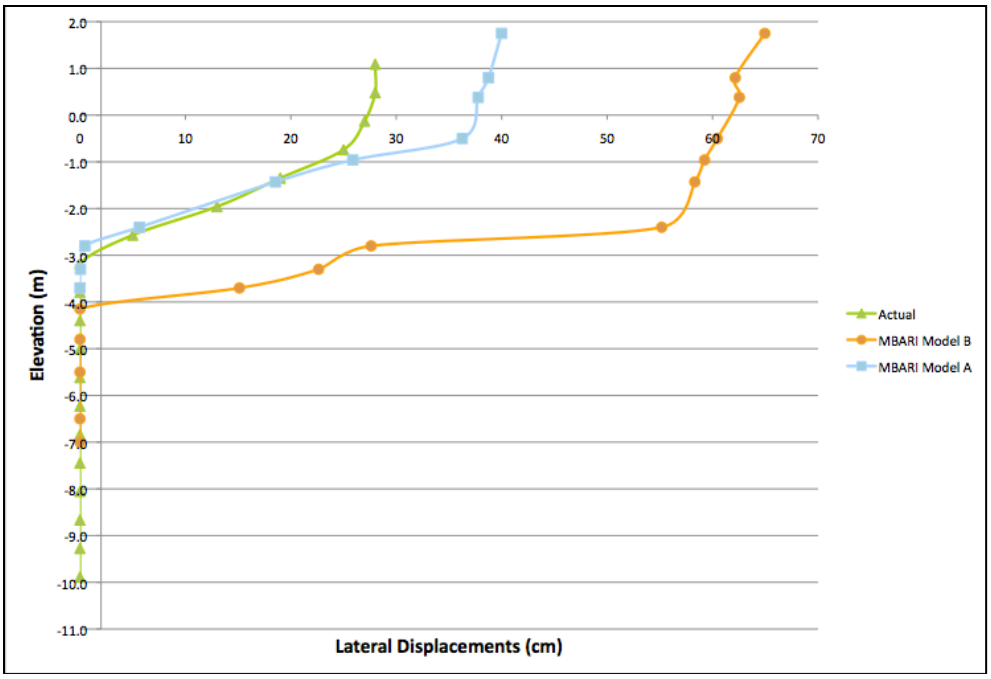

Figure 3.1.11. Measured and predicted lateral displacements at MBARI/Sandholdt Road. Deformations predicted by Models A and B as well as measured values are compared with depth.

3.2. Moss Landing Marine Laboratory (MLML) – Loma Prieta 1989

The Moss Landing Marine Laboratory (MLML) is located on the West side of Sandholdt road just south of the timber access bridge crossing the Old Salinas River. The location is shown on Figure 3.1.1 and is approximately 330 meters southwest of the MBARI/Sandholdt road case study discussed in Section 3.1. The complex is shown on Figure 3.2.1 along with photographs of racking of one of the structures and sand boil ejecta from an area just south of the structures. The MLML facility consisted of three 1 to 2 story wood frame structures supported on spread footings constructed surrounding a center courtyard with appurtenant surface parking and a volleyball court to the south.

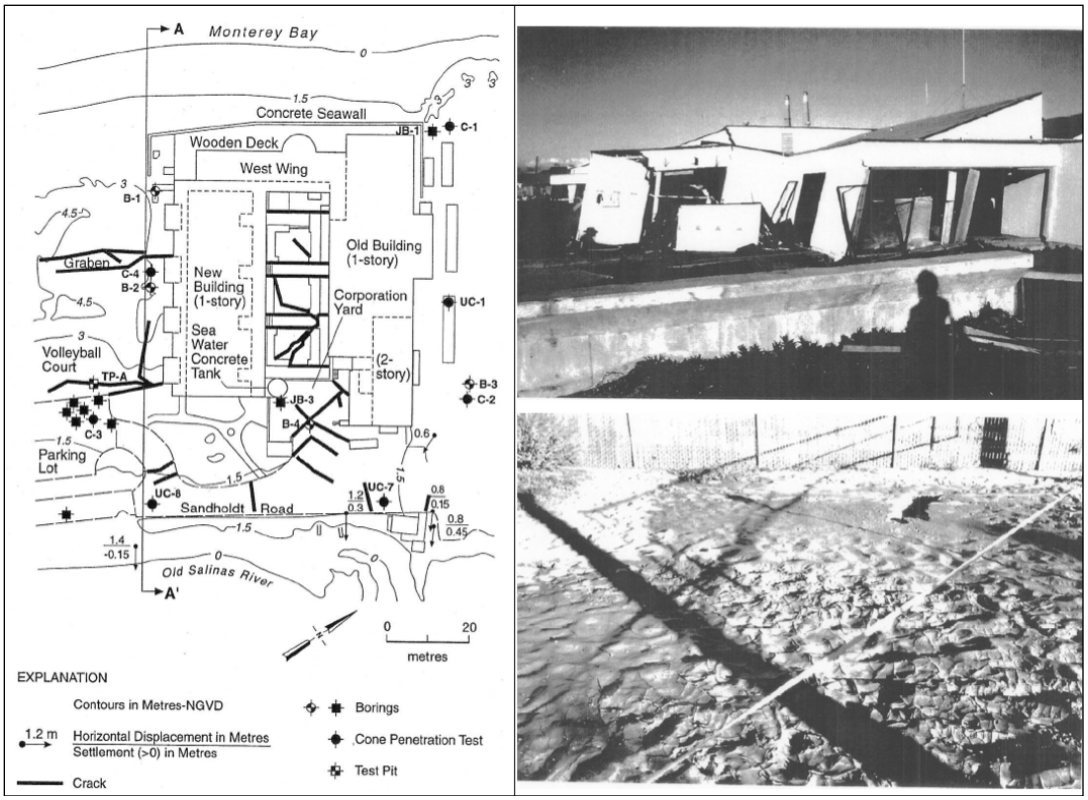

Figure 3.2.1. Lateral spreading damage at the Moss Landing Marine Laboratory. To the left is a map of observed cracking and deformations as well as subsurface exploratory points. Upper right shows damage to the MLML structure. Lower left photo shows sand boil ejecta at the volleyball court just south of the facility (Boulanger et al. 1995).

According to the UC Davis investigation by Boulanger et al. (1995), sand boils were observed to have ejecta shooting several feet into the air for approximately 45 minutes after ground shaking associated with the Loma Prieta earthquake had ceased. Liquefaction and lateral spreading at the site had torn the structure apart, though it did not collapse. Lateral and vertical deformations were estimated in a post-earthquake survey by Brian Kangas Foulk and summarized in Boulanger et al. (1995). A post-earthquake reconnaissance report was performed at the site by Woodward-Clyde Consultants (WCC) in 1990. Geologic cross sections were prepared as part of the Davis investigation and included subsurface data performed by WCC. Figure 3.2.2 shows the subsurface stratigraphy and a summary of geologic information for Section A-A', just south

of the MLML facility. Similarly, Figure 3.2.3 details available subsurface information north of the facility.

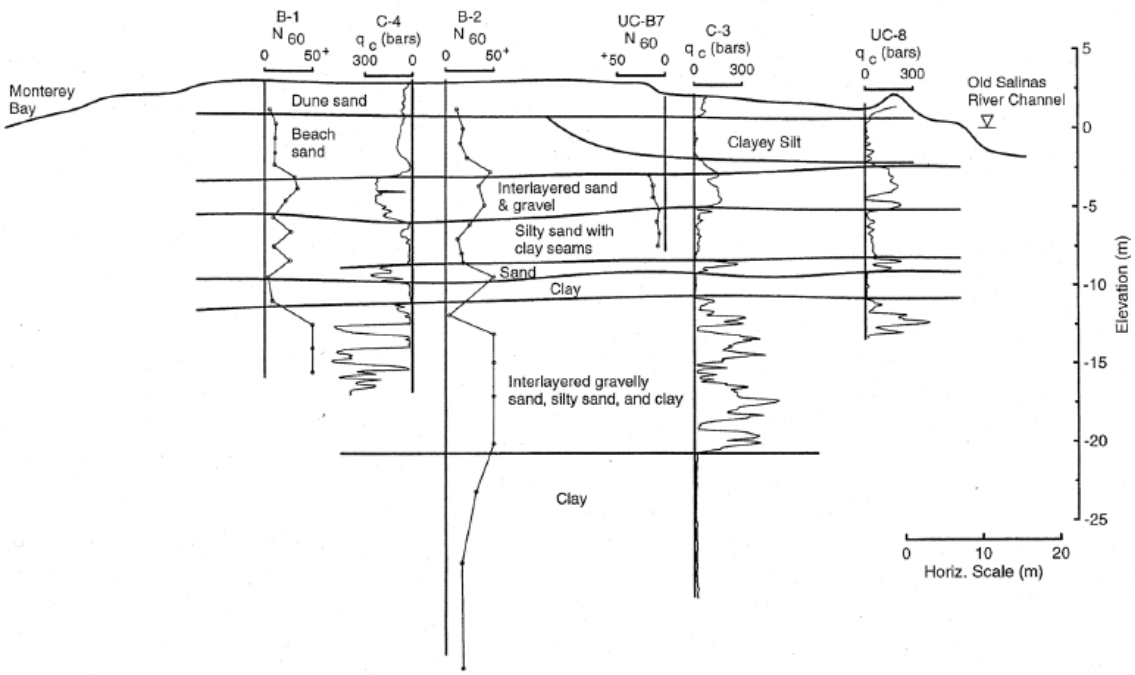

Figure 3.2.2. Geologic section south of MLML facility (Section A-A' of Figure 3.2.1) (Boulanger et al. 1995).

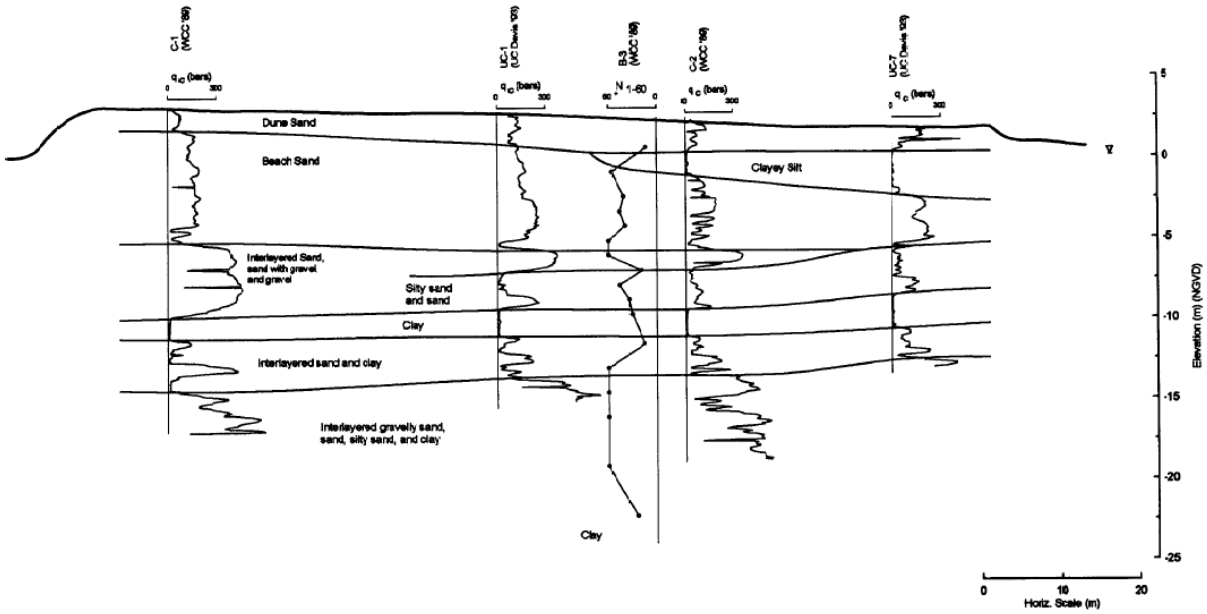

Figure 3.2.3. Geologic section south of MLML facility (Section A-A' of Figure 3.2.1) (Boulanger et al. 1995).

Lateral spreading on the order of 0.75 m was estimated in the western direction, toward the Monterey Bay. Lateral spreading to the east toward the Old Salinas River was estimated to be 0.45 m at the structure and 0.8 to 1.4 meters east of Sandholdt Road (Figure 3.2.1). Overall, Boulanger et al. (1995) estimates spreading of the Moss Landing spit at the MLML facility to be about 1.4 m on the north side of the structure and 2.1 m on the south side of the structure. Vertical settlements were estimated at 0.35 m on the west side of the structure and 0.3 m on the east side. Some areas of heave were also observed at the site and are detailed on Figure 3.2.1 (site plan).

As with the MBARI facility previously discussed in Section 3.1, the Salinas ground motion record (scaled to a PGA of 0.25 g) was used to simulate ground motions at Moss Landing during the Loma Prieta earthquake. Figures 3.2.4 and 3.2.7 show the mesh and layers used to model sections A-A and B-B to the south and north of the facility, respectively. Figures 3.2.5 and 3.2.6 show the horizontal and vertical displacement respectively as predicted at Section A-A'. Figures 3.2.8 and 3.2.9 show contours of lateral and vertical displacement predicted for Section B-B', north of the MLML structure. A plan view summary showing contours of predicted lateral displacement extrapolated from Sections A-A' and B-B' is provided as Figure 3.2.10. Overall, lateral displacements were captured well as the calculated lateral spread displacements of the Moss Landing spit is approximately 2.25 m on the south side of the structure and 0.85 m on the north side of the structure. Calculated vertical displacements ranged from approximately 10 to 60 cm. Measured values of vertical displacements generally fall into this range.

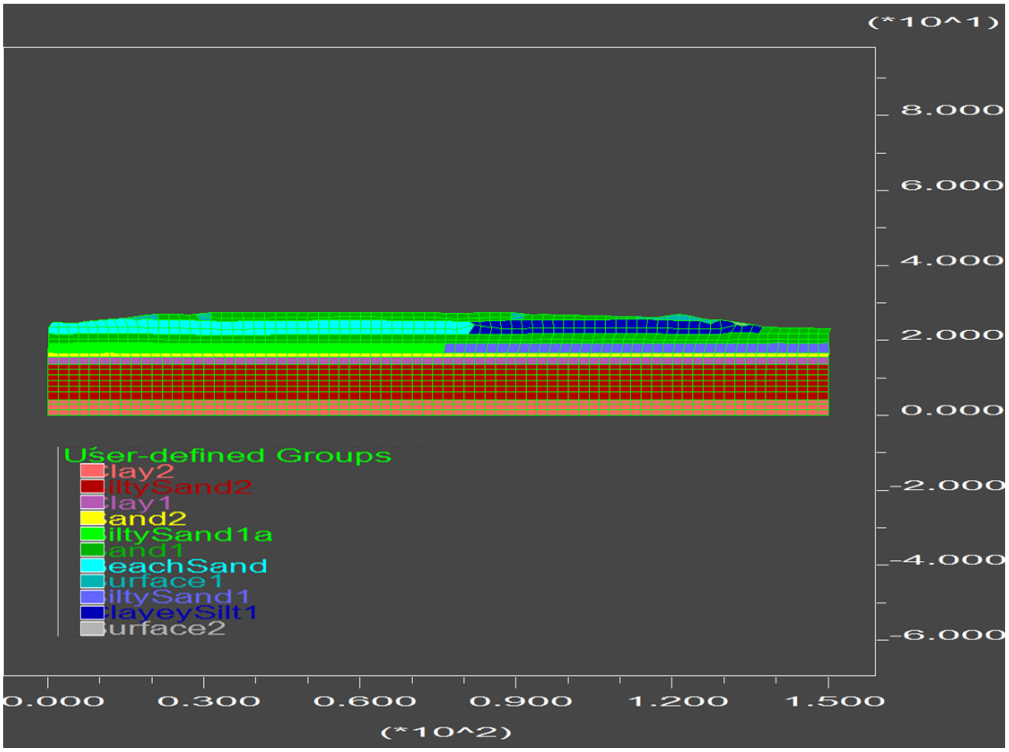

Figure 3.2.4. Mesh and soil types south of MLML facility (Section A-A' of Figure 3.2.1).

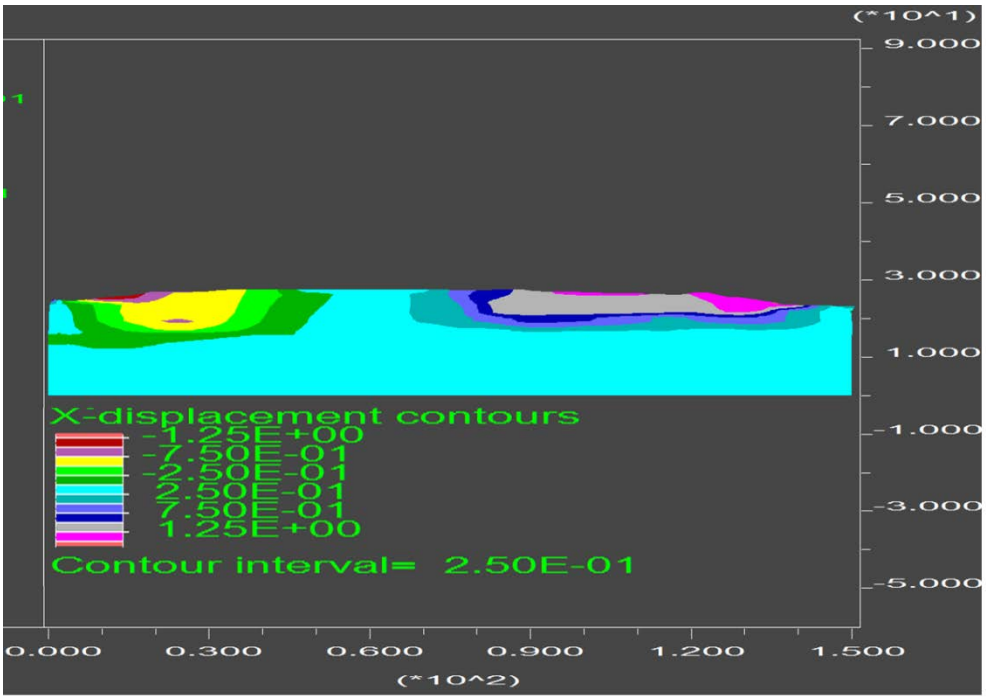

Figure 3.2.5. Predicted lateral displacements south of MLML facility (Section A-A' of Figure 3.2.1).

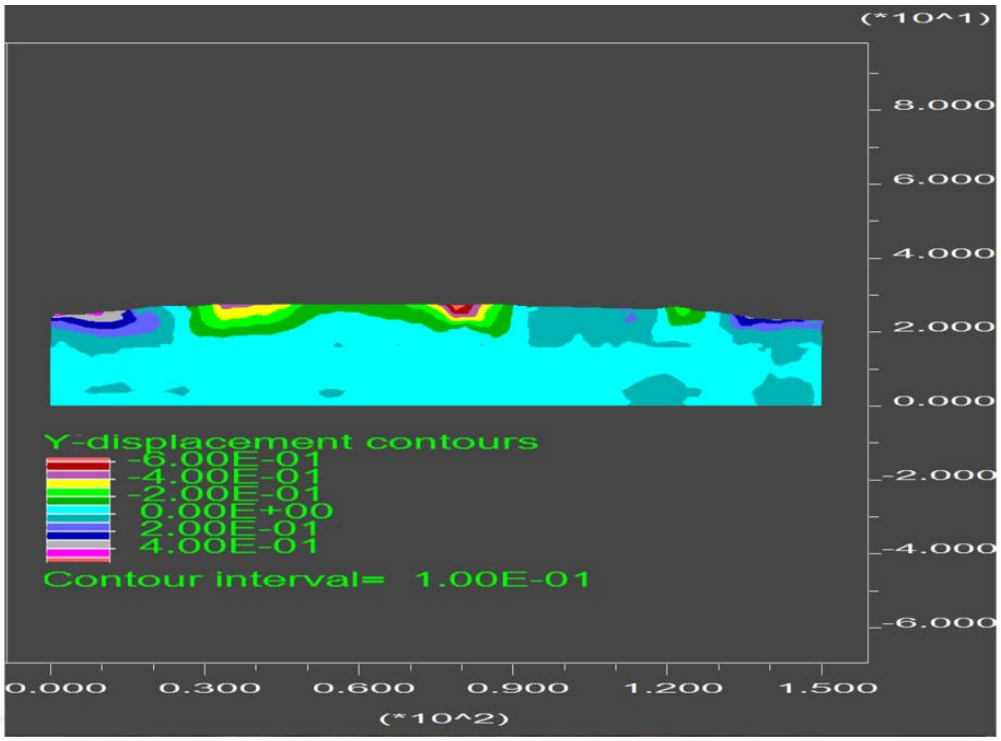

Figure 3.2.6. Predicted vertical displacements south of MLML facility (Section A-A' of Figure 3.2.1).

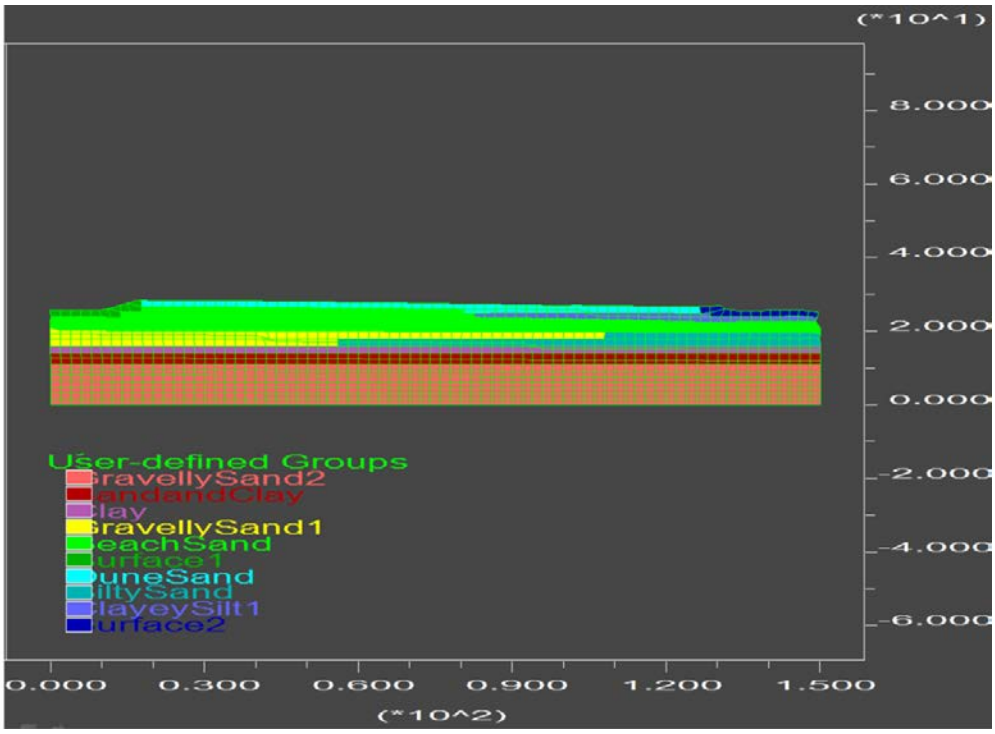

Figure 3.2.7. Mesh and soil types north of MLML facility (Section B-B' of Figure 3.2.1).

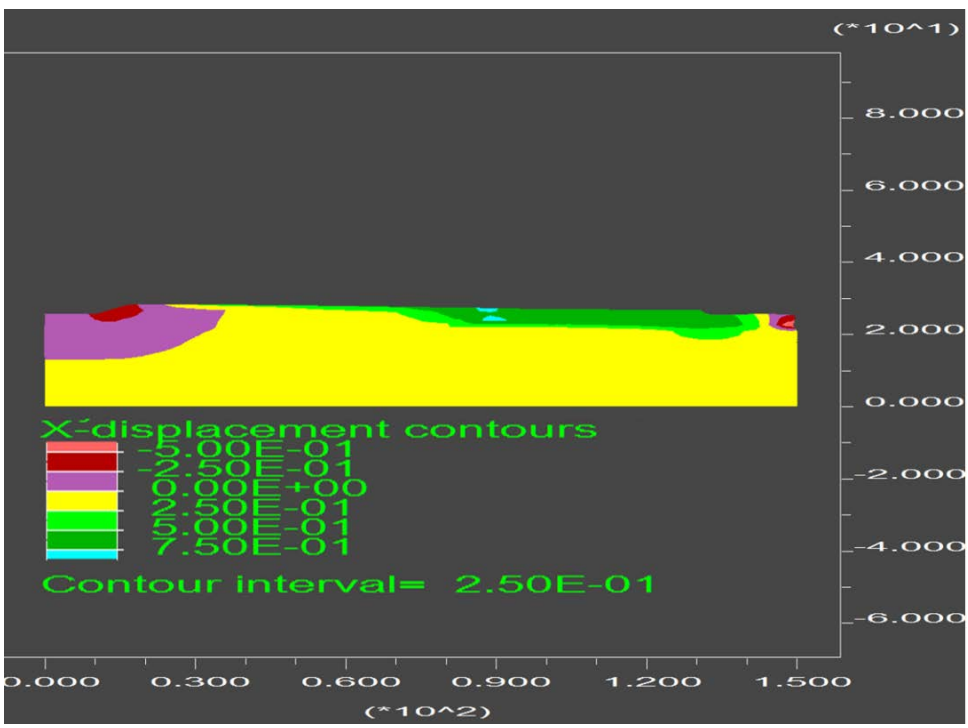

Figure 3.2.8. Predicted lateral displacements north of MLML facility (Section B-B' of Figure 3.2.1).

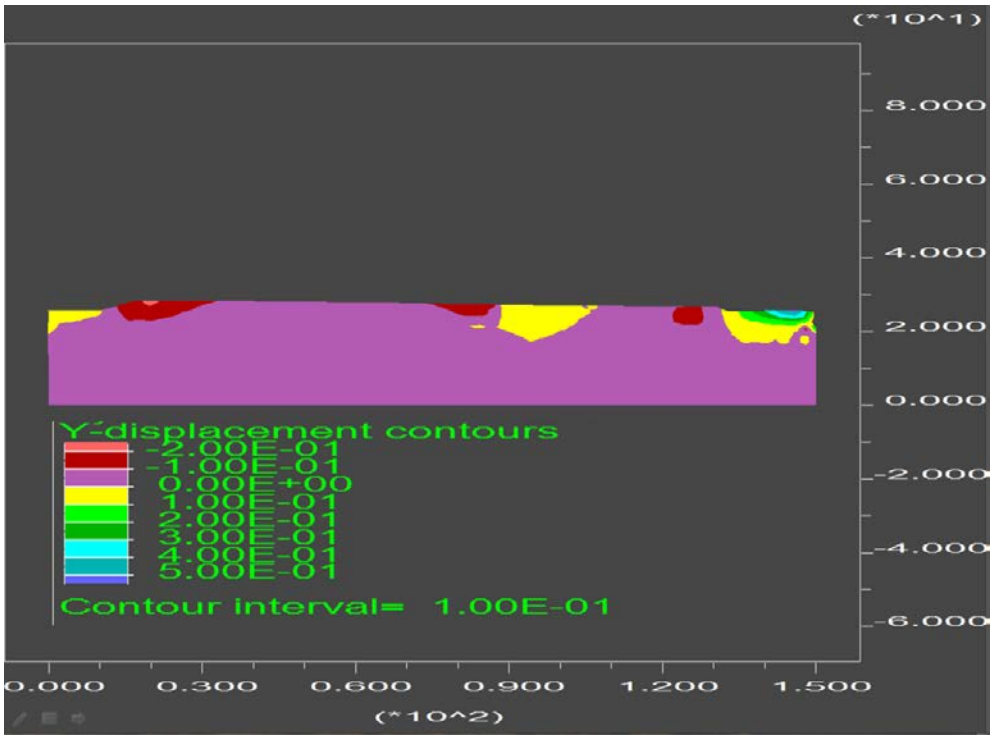

Figure 3.2.9. Predicted vertical displacements north of MLML facility (Section B-B' of Figure 3.2.1).

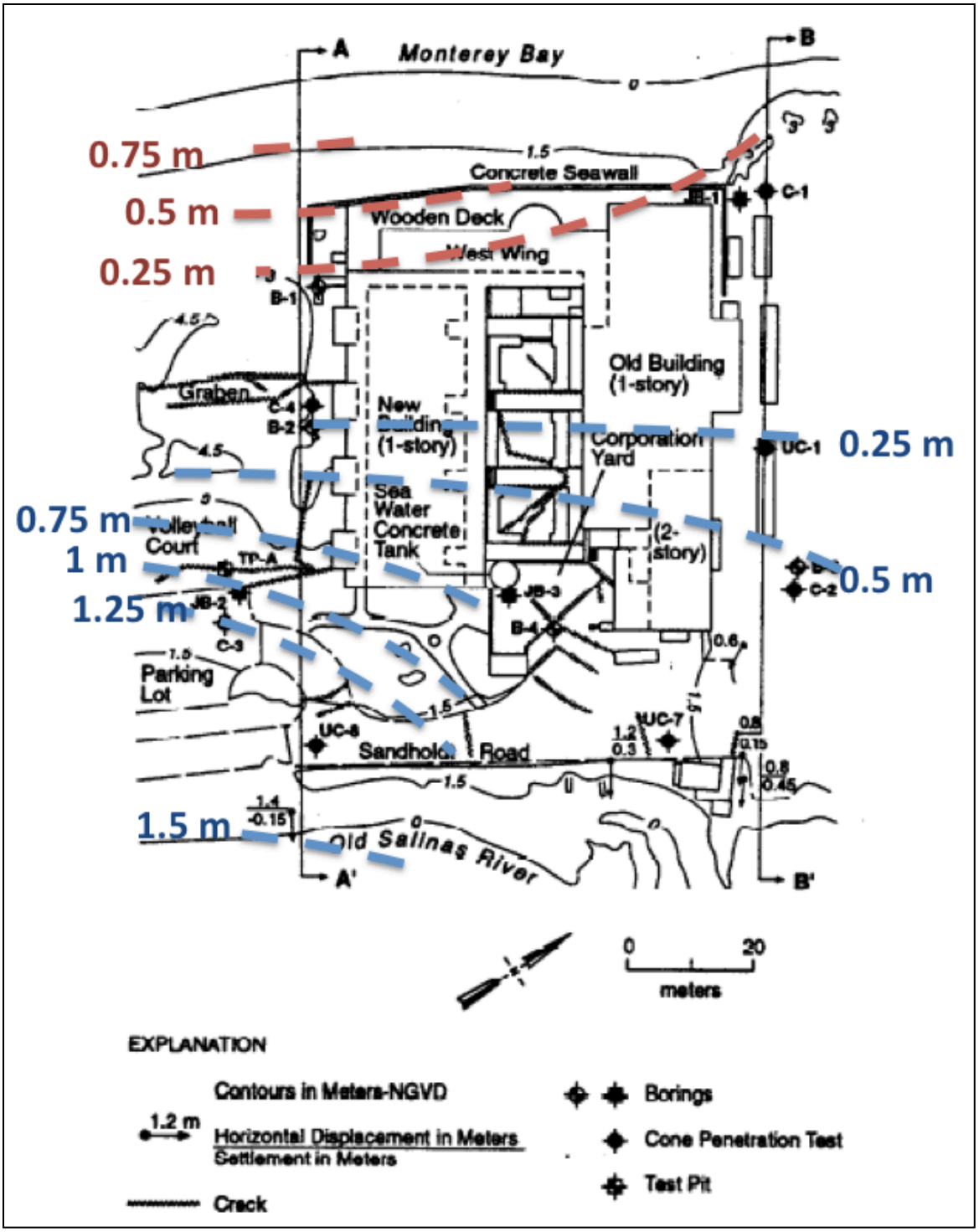

Figure 3.2.10. Measured and predicted lateral deformations at the MLML Facility during the Loma Prieta Earthquake in 1989. Blue contours represent movement to the east toward the Old Salinas River. Red contours represent movement to the west toward the Monterey Bay. Prediction contours based on extrapolations from models performed at Sections A and B.

3.3. Juvenile Hall Facility – San Fernando 1971

The Los Angeles County Juvenile Hall site is located at the junction of Interstate 5 and the Foothill Freeway (210) east of the Van Norman Reservoir complex in the Sylmar region of Los Angeles, California. During the 1971 San Fernando earthquake (moment magnitude of 6.6 centered as shown on Figure 3.3.1), the Juvenile Hall facility experienced lateral deformations on the order of 2 meters. Displacement vectors were plotted by O'Rourke et al. (1992) and are included as Figure 3.3.2. A map of cracking associated with the lateral spread by Fallgren and Smith (1973) is included as Figure 3.3.3. Subsurface exploratory data point locations are provided on Figure 3.3.4 (O'Rourke et al., 1992). Subsurface data were interpreted by Bennett (1989) and summarized on Figures 3.3.5 and 3.3.6. A complete summary of the Juvenile Hall case study is available in Faris (2004). Faris (2004) performed a liquefaction analysis of the subsurface soils at the site and a portion of the analysis is included as Figure 3.3.7.

Four alluvium units, labeled A through D are shown in subsurface profiles on Figures 3.3.5 and 3.3.6. Unit A consists of a 2-7 m layer of poorly sorted, loose to medium-dense silty sand located above the groundwater table. Underlying Unit A is Unit B, 2-5 m layer of very loose to loose, poorly sorted silty sand to silt. Unit C consists of medium-dense to dense, poorly sorted silty sand, while Unit D consists of stiff clayey silt. Liquefaction initiation analyses performed by Faris (2004) confirmed that the loose, saturated silty sand and sandy silt within Unit B was likely to have liquefied during the event. The precise locations of the geologic sections shown on Figures 3.3.5 and 3.3.6 were not included in Faris (2004). The approximate location of the section was interpreted from the topographic map included as Figure 3.3.2 and the exploratory point locations shown on Figure 3.3.4.

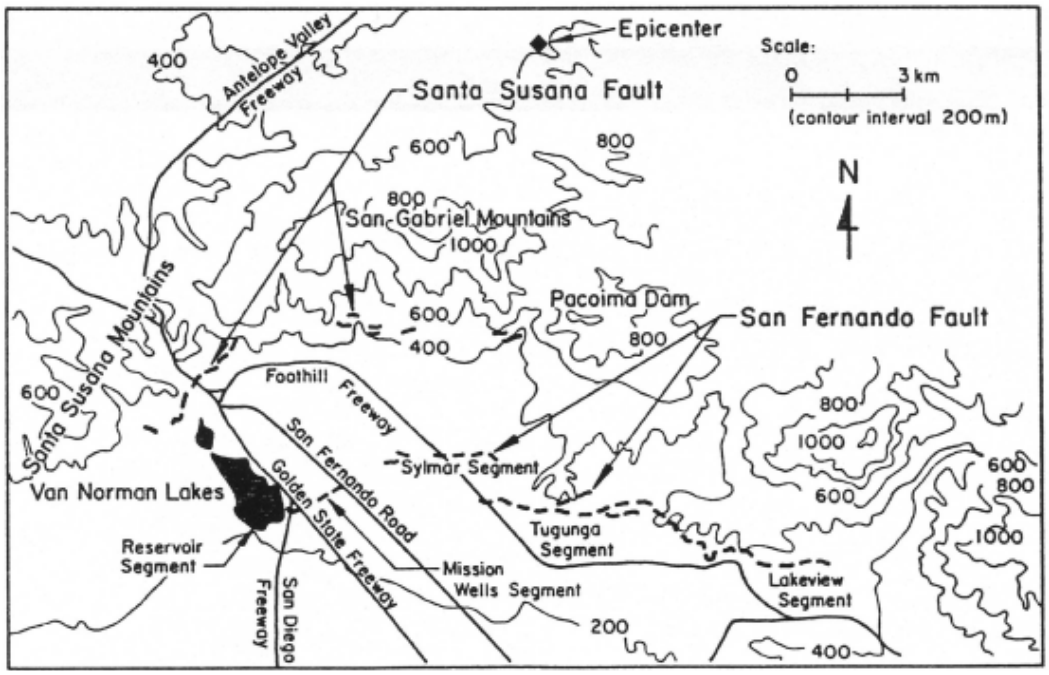

Figure 3.3.1. Epicenter and fault map showing Juvenile Hall site vicinity. The site is located east of the Van Norman Reservoir in the San Fernando Valley northeast of I-5 (modified from O'Rourke et al. 1992).

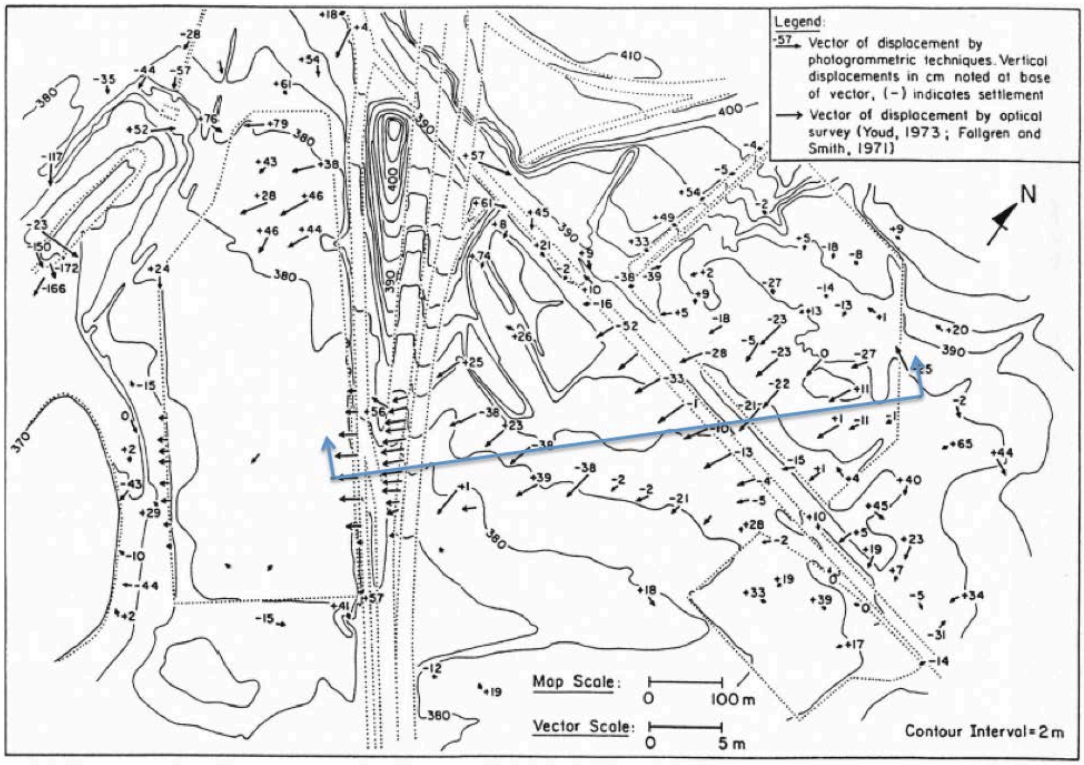

Figure 3.3.2. Estimated vectors of displacement at the Juvenile Hall facility during the San Fernando earthquake of 1971 (O'Rourke et al. 1992).

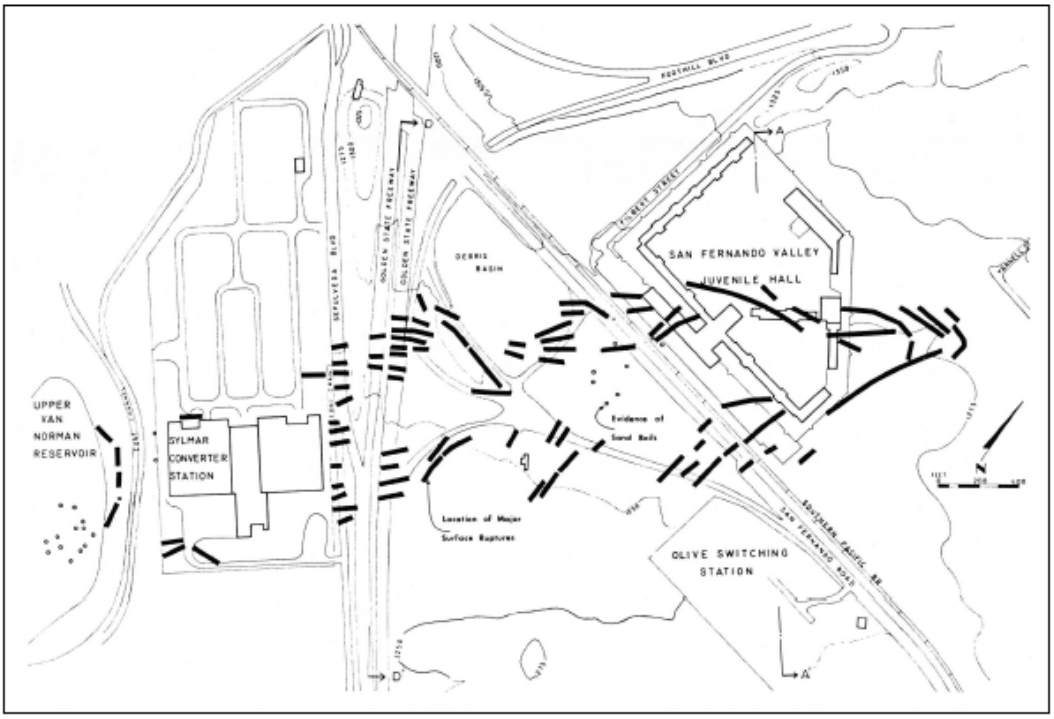

Figure 3.3.3. Locations of ground cracks at Juvenile Hall facility after 1971 San Fernando earthquake (Fallgren and Smith, 1973).

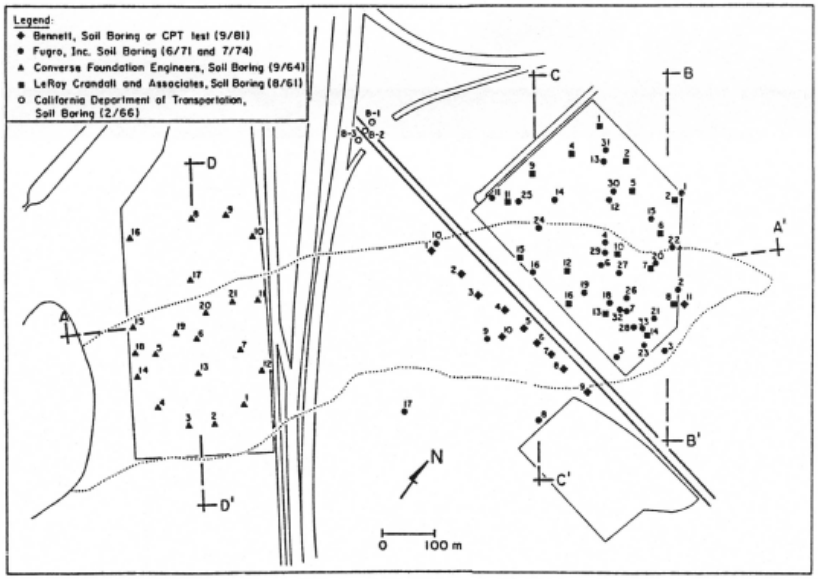

Figure 3.3.4. Location of subsurface exploratory points at the Juvenile Hall Facility (O'Rourke et al., 1992).

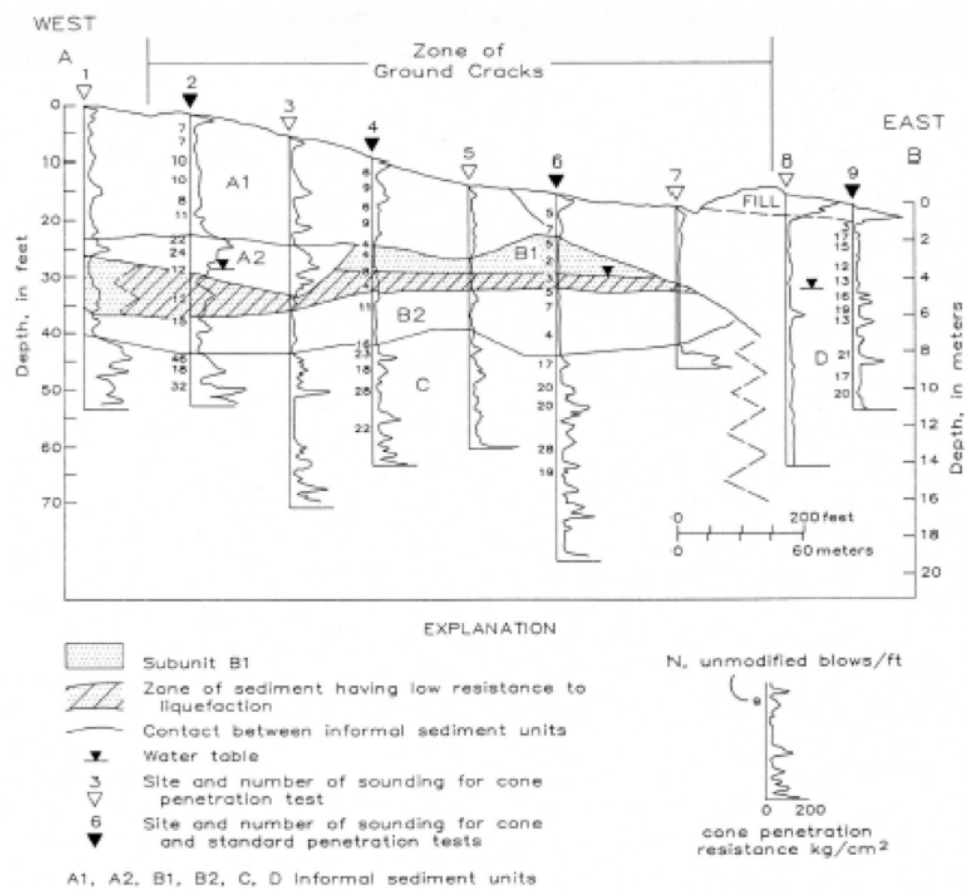

Figure 3.3.5. Subsurface profile at Juvenile Hall (Bennett, 1989).

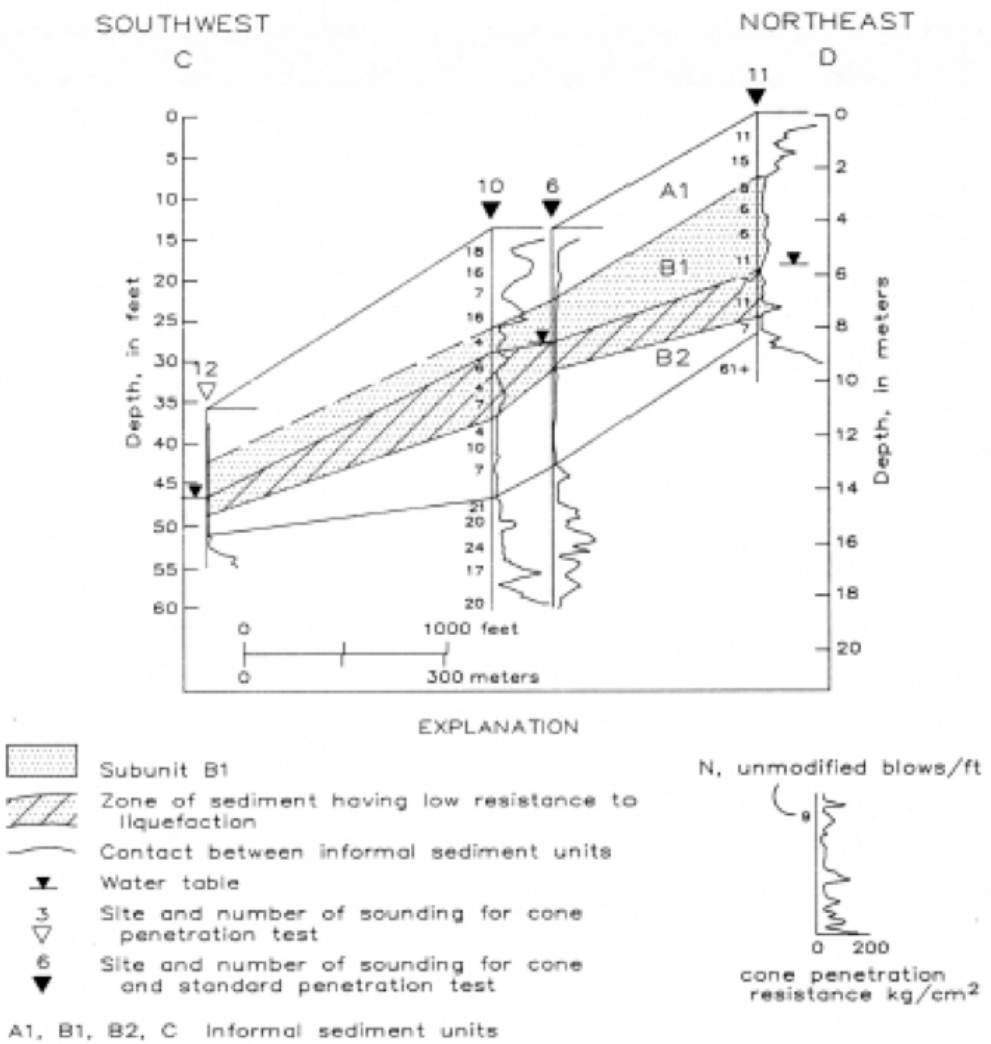

Figure 3.3.6. Subsurface profile at Juvenile Hall (Bennett, 1989).

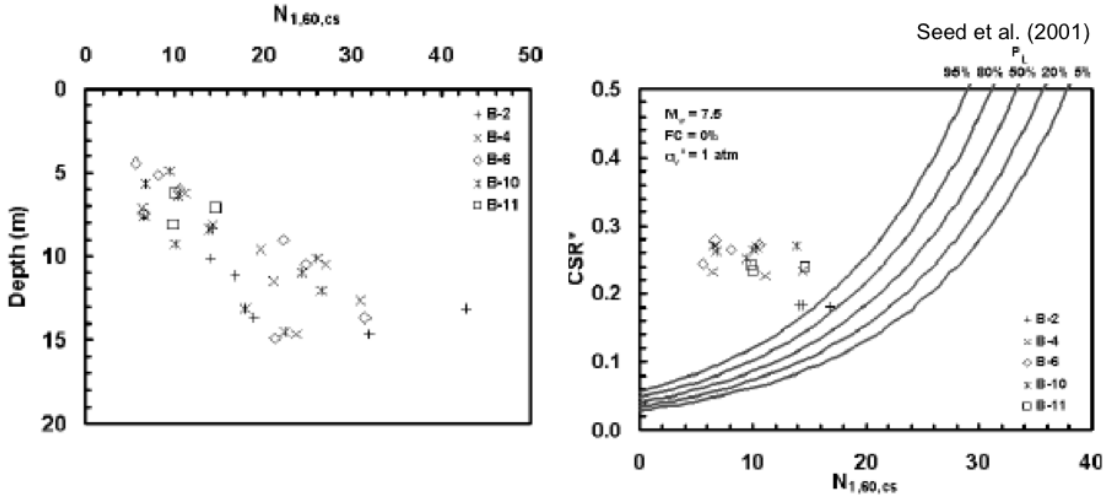

Figure 3.3.7. Liquefaction analysis for Juvenile Hall by Faris (2004).

No ground motion instruments were present at the site at the time of the San Fernando earthquake. Cetin (2000) estimated that the peak ground acceleration at the site was approximately 0.45 g. A limited number of ground motion recordings are available in this area for this earthquake. Ground motion records at the Upper Pacoima Dam are available for both the 1971 San Fernando earthquake and the 1994 Northridge earthquake with PGAs of 1.23 g and 1.53 g, respectively. The instrument at Lower Pacoima Dam recorded only the 1994 Northridge earthquake with a PGA of 0.45 g. Using this information, a PGA of 0.36 g was estimated for Lower Pacoima Dam during the 1971 San Fernando earthquake, and it was used as the rock input motion in SHAKE to generate a ground motion for the lower Juvenile hall site. The shear wave velocity profile of a nearby site, Olive View Community Hospital, was studied previously by Chang (1996). An idealized profile for Olive View hospital is shown on Figure 3.3.8. A within soil motion with a PGA of 0.45 g was the output of this analysis. Based on the agreement with estimates by Cetin (2000), this motion was used in our study.

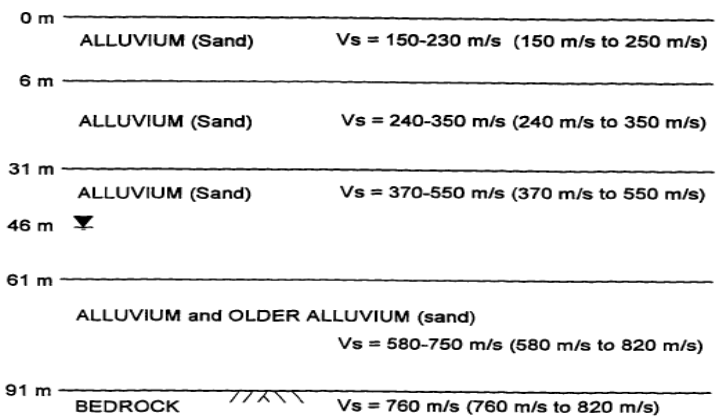

Figure 3.3.8. Idealized soil profile for Olive View/Sylmar County Hospital (Chang, 1996).

In general, the model was able to capture the magnitude of the liquefaction-induced lateral displacement. The contours of lateral displacement are provided on Figure 3.3.9. Measured lateral displacements at the site range between approximately 0.5 and 2 m (Figure 3.3.2). The model predicted lateral displacements near the lower part of the site (nearest the I-5 freeway) to be on the order of 1.5 m. Soils near the top of the movement area were calculated to displace 0.5 m to 2 m relative to the competent base materials. Measured values are consistent with calculated values as shown on Figure 3.3.10. Figure 3.3.10 shows the values of lateral displacements plotted together on an interpreted geologic cross section by Bennett (1989). Where there are large areas lacking in initial shear stress, the model calculates smaller displacements, whereas measured displacements do not show this trend. This indicates the sensitivity of the UBCSAND model to small amounts of initial static shear stress and the need for slightly increased values of m_hfac1 and 2 under initial shear. Judgment is required in this regard.

Measured vertical displacements as shown on Figure 3.2.2 were variable across the failure area and typically ranged from 2 to 20 cm (sometimes varying this much in adjacent measurements) of settlement with localized pockets settling as much as 38 cm along the modeled section. Calculated values were similarly erratic with typical values of settlement on the order of 5 cm and values of up to 35 cm predicted near the top of slope (the areas of largest horizontal movement).

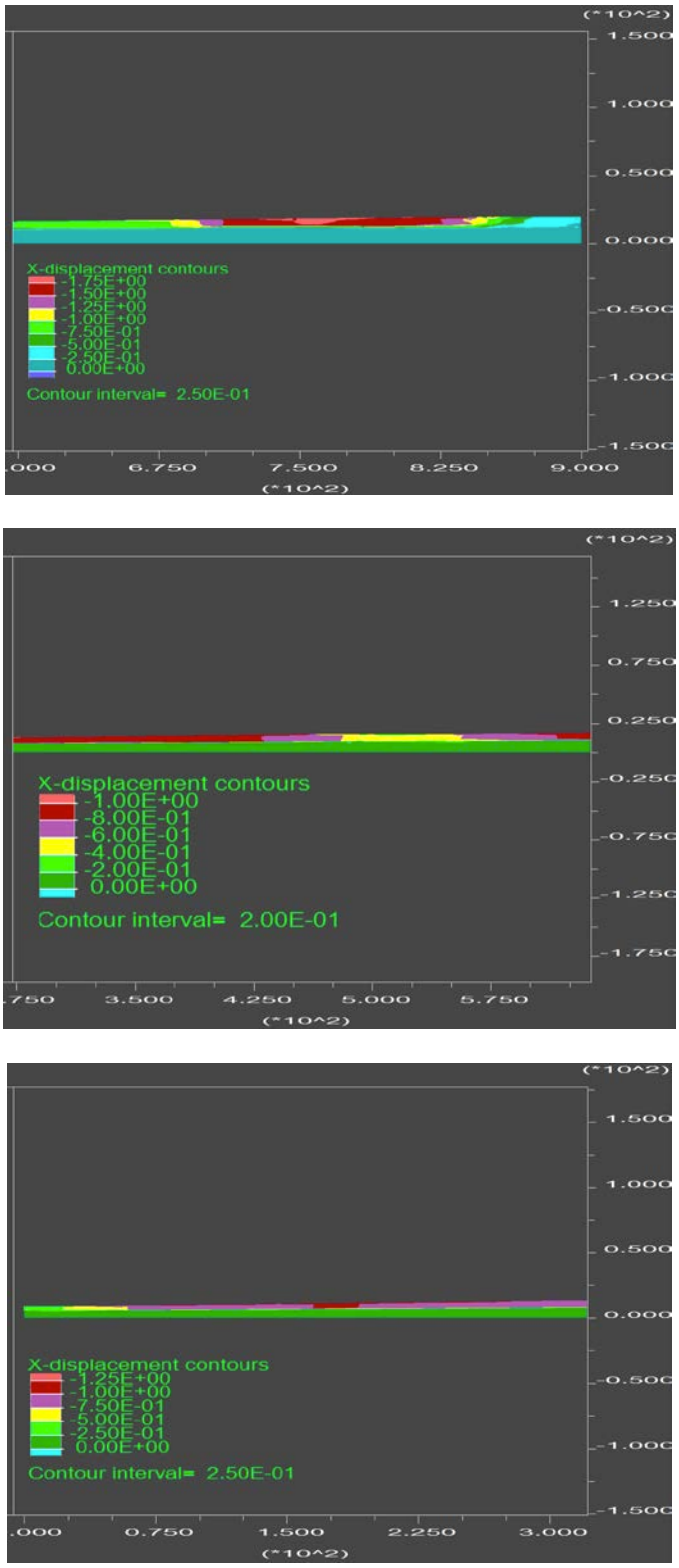

Figure 3.3.9. Contours of predicted lateral deformation. The deformation was on the order of 900 m in length, while liquefiable soils were located approximately 6 m below the surface. To better view the predicted deformations, the site was divided into the toe segment of 0 to 300 m (bottom), the central section of 300 to 600 m (center) and the top segment of 600 to 900 m (top).

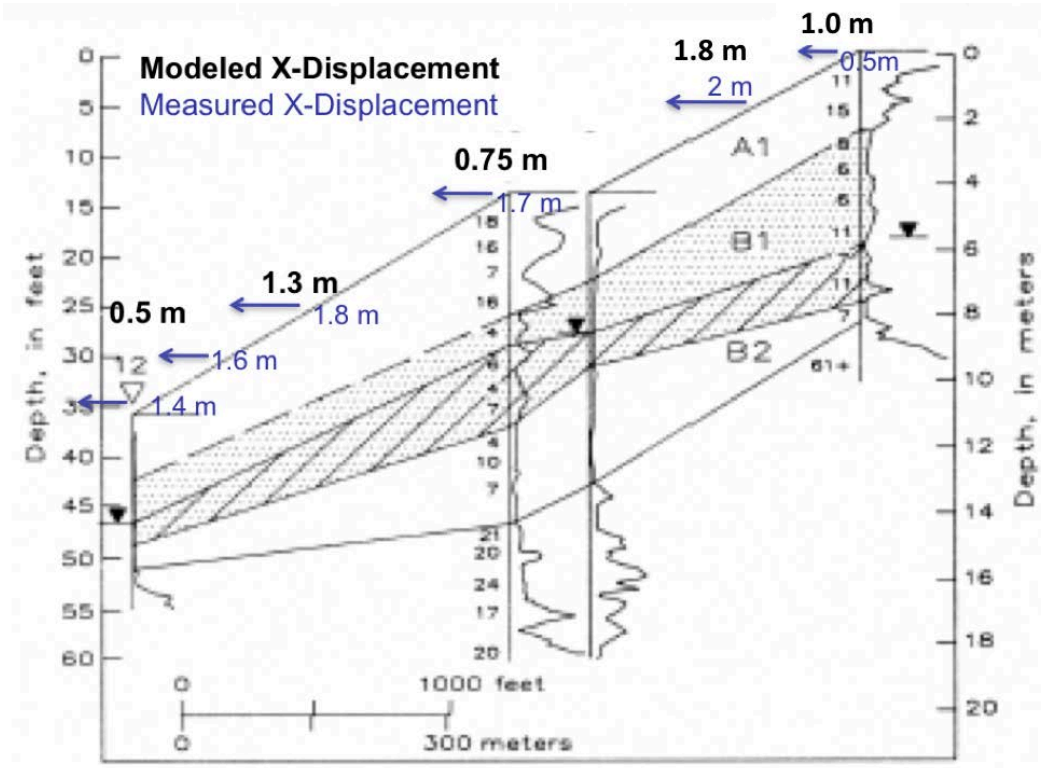

Figure 3.3.10. Measured and predicted lateral deformations at Juvenile Hall following the San Fernando earthquake of 1971 (modified from Bennett,1989).

4. SENSITIVITY STUDY USING CALIBRATED UBCSAND MODEL

4.1. Introduction

After the back-analyses of the aforementioned case histories were performed, forward modeling of a simplified embankment section allowed for the use of the calibrated FLAC/UBCSAND model in calculating liquefaction-induced deformations under seismic loading in a limited lateral spread condition. The simplified baseline model is shown in Figure 4.1.1.

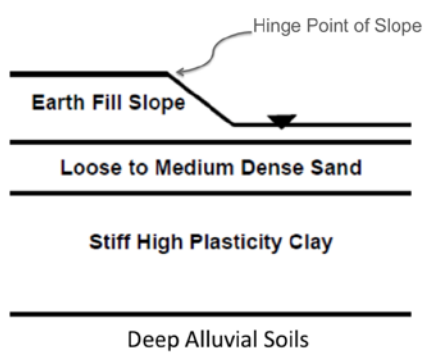

Figure 4.1.1. Simplified Embankment Model.

The intent is to analyze relatively simple geometries wherein key parameters, such as the thickness of the liquefiable layer and its relative density, can be systematically varied to develop useful insights. The results of the analyses will show trends in the response of liquefaction-induced lateral spreading ground. These trends were generally explored using two ground motions: 1) the 1992 Landers Joshua Tree motion was selected to represent a backward-directivity motion, and 2) the 1994 Northridge Sylmar Converter Station motion was selected to represent a forward-directivity near-fault motion. A series of additional ground motions were selected to evaluate the sensitivity of the results of a single model to a variety of motions to explore the effects of ground motion.

4.2. Sensitivity of Results to Variations in $(N_1)_{60}$

A simplified model was created in a series of configurations, varying the thickness of the liquefiable layer as well as the embankment height (discussed in subsequent sections). To explore the effects of variations in the liquefiable sand's relative density, the corrected blow count (i.e., $(N_1)_{60}$ value) was varied while embankment height and thickness of liquefiable layer were held constant. An embankment height of 9 m over a liquefiable layer thickness of 8 m was selected for the baseline model for this phase of the study. Figure 4.2.1 shows predicted displacement values at a distance of approximately 2 m behind the hinge point of the slope with $(N_1)_{60}$ values ranging from 8 to 25. The hinge point of a slope is defined here as the top of slope, or the location of a dramatic change in slope near the top of the embankment (Figure 4.1.1). The backward-directivity motion shows significantly less lateral displacement for this case, especially at a blow count of 8. Figure 4.2.2 shows the variation in calculated lateral displacement at this point for two values of $(N_1)_{60}$ for the cases wherein the liquefiable soil is a clean sand or a low plasticity silt. For this model, the variation in lateral displacement is modest.

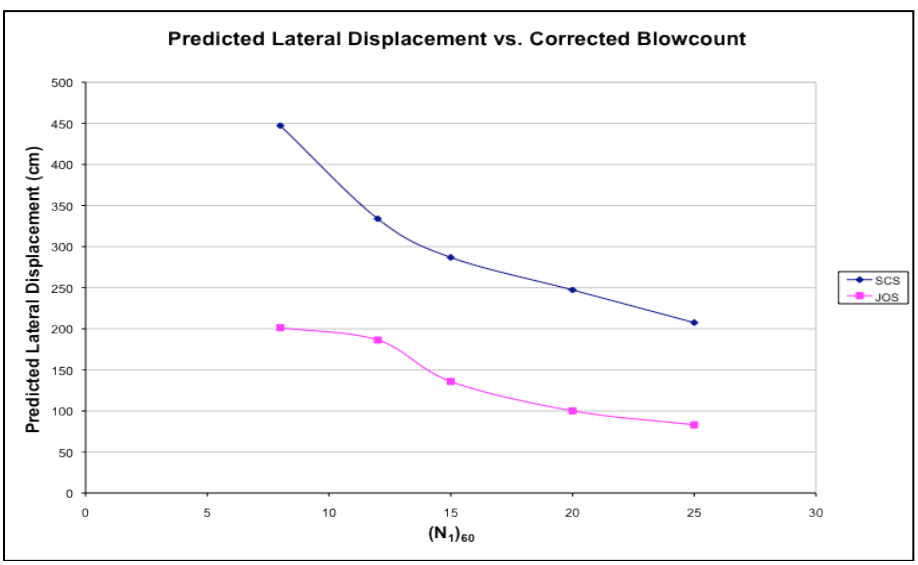

Figure 4.2.1. Comparisons of predicted response of 'clean sand' over similar blow count range but loaded with different ground motions. Data points marked 'SCS' were calculated using the 1994 Northridge Sylmar Converter Station motion (blue) and those labeled 'JOS' were calculated using the 1992 Landers Joshua Tree motion (pink).

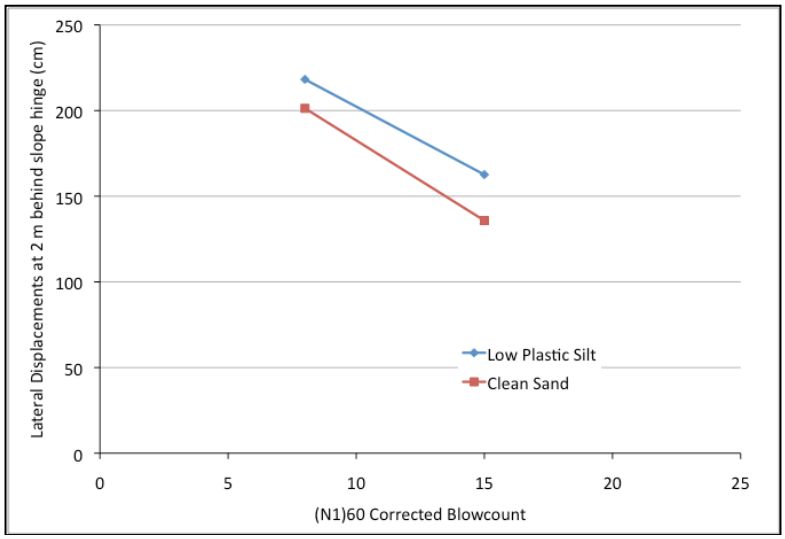

Figure 4.2.2. Predicted Lateral Displacement of 'low plasticity silt' and 'clean sand' as a function of blow count. Data was calculated using the 1992 Landers Joshua Tree motion.

4.3. Sensitivity of Results to Variations in Model Geometry

The configuration of the simplified soil model was varied to explore the effects of different embankment heights and thicknesses of the underlying liquefiable layer. Embankment heights of 6, 9, and 12 feet were modeled overlying loose to medium dense sands of 3, 8, and 12 feet in thickness. The lateral and vertical displacements were plotted against the distance from the slope hinge point. Figures 4.3.1 and 4.3.2 show the range in lateral and vertical displacement data resulting from the variation in geometry using the 1992 Landers Joshua Tree motion and the 1994 Northridge Sylmar Converter Station Motion, respectively. N8 indicates a corrected blow count of 8, E6 indicates an embankment height of 6, T3 indicates a loose to medium dense sand layer of 3 m in thickness, and 'j' or 's' at the end indicates the ground motion used (i.e., 'j' stands for 1992 Landers Joshua Tree motion while 's' stands for 1994 Northridge Sylmar Converter Station motion). The geometry was modeled assuming an $(N_1)_{60}$ blow count value of either 8 or 15 for the loose to medium dense sand.

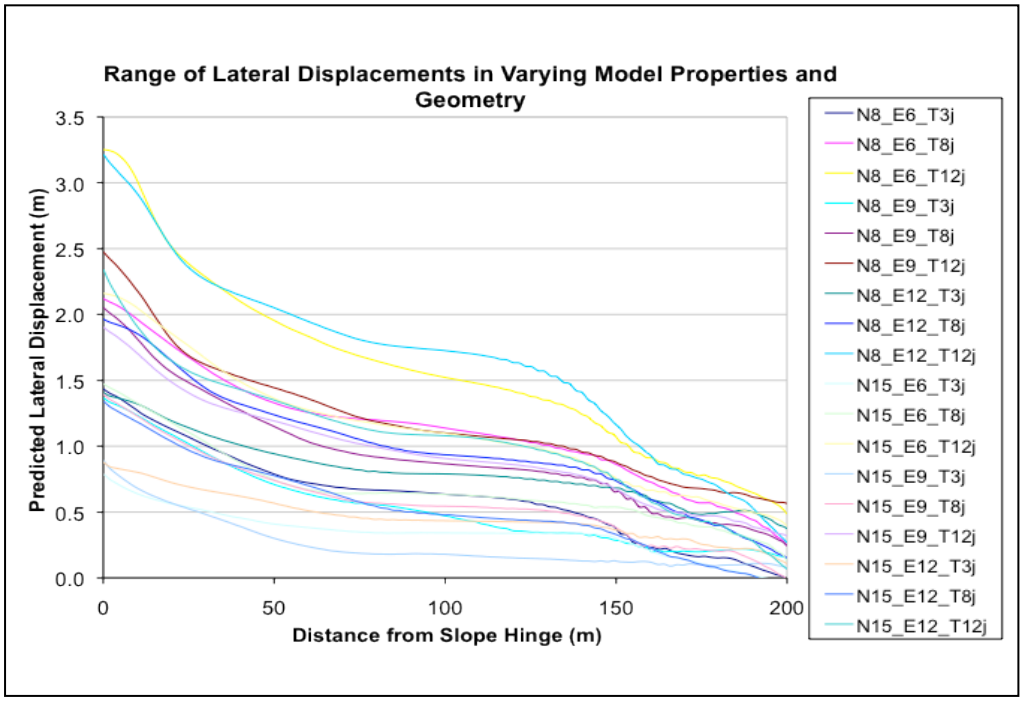

Figure 4.3.1. Range in liquefaction-induced lateral displacement with distance from the slope hinge point for the 1992 Landers Joshua Tree ground motion.

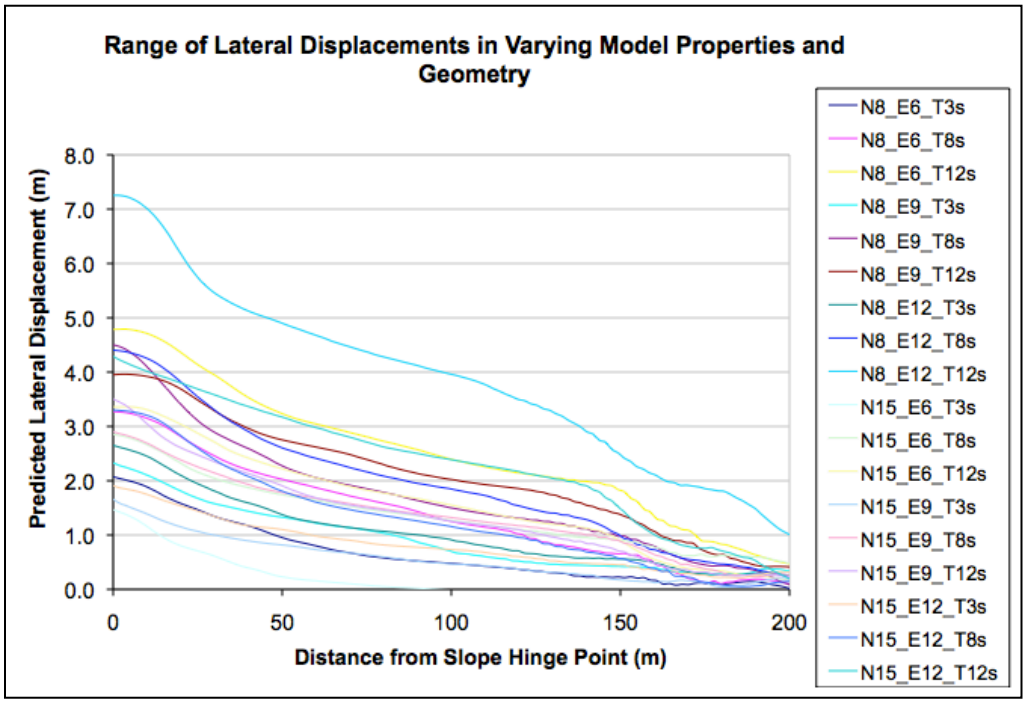

Figure 4.3.2. Range in liquefaction-induced lateral displacement with distance from the slope hinge point for the 1994 Northridge Sylmar Converter Station ground motion.

For the looser sandy foundation layers, the entire embankment slid as a block on the liquefied sand in several of the simulations as shown in Figure 4.3.3. The loose to medium dense sand layers were densified near the edges (5 m from the edge on the downslope side of the model and 15 m on the upslope side) to minimize boundary modeling errors in the program FLAC. These zones prevented the model from deforming excessively at the edge of the 300 meter long model. The simplified model is limited in that actual soils typically have a higher degree of heterogeneity in layer geometry, density, fines content, and other factors. The absence of heterogeneity built into the model may result in an unrealistic lateral extent of spreading.

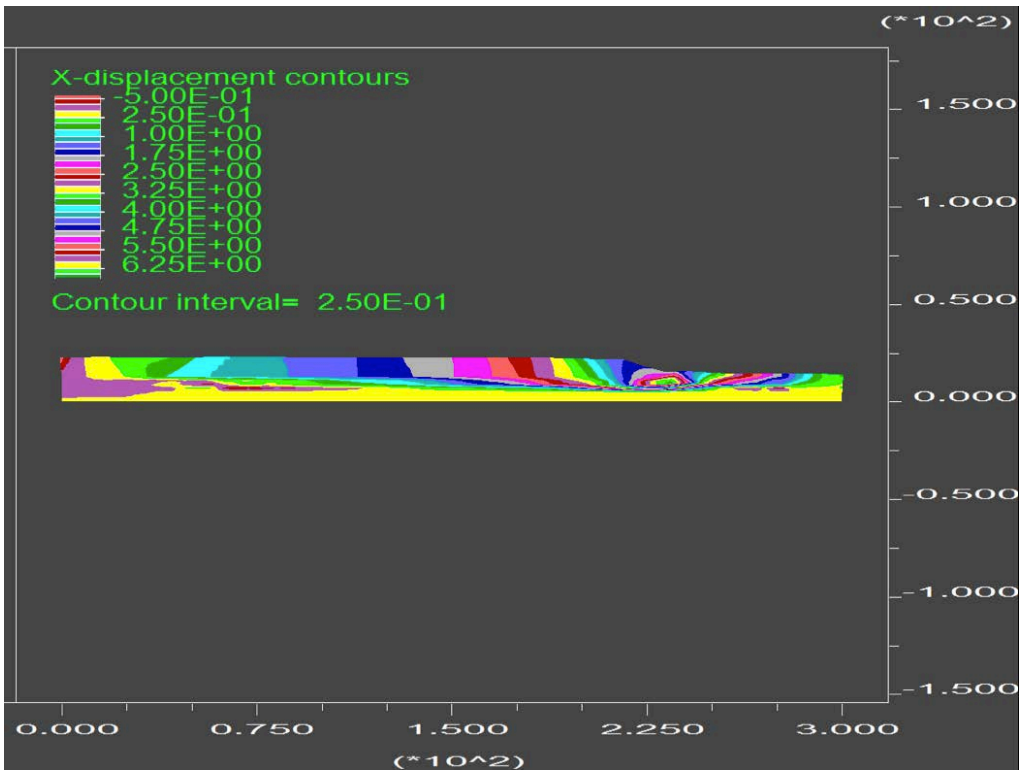

Figure 4.3.3. Example of predicted embankment deformation extending over 200 meters from slope hinge point. Model used in this example is a 9 foot embankment height and an 8 foot thick layer of sand with corrected $(N_1)_{60}$ blow count of 8 for the Sylmar Converter Station ground motion.

4.3.1. Layer Thickness

Layer thickness was found to have a significant impact on deformations. Figures 4.3.4 through 4.3.9 show comparisons of models with the same embankment height and density of loose to medium dense sand, but with different thicknesses of liquefiable sand. The effects of increasing the layer thickness of the liquefiable soils can be significant. For example, increasing layer thickness while decreasing blow count can increase deformations to over 7 m as shown on Figure 4.3.4.

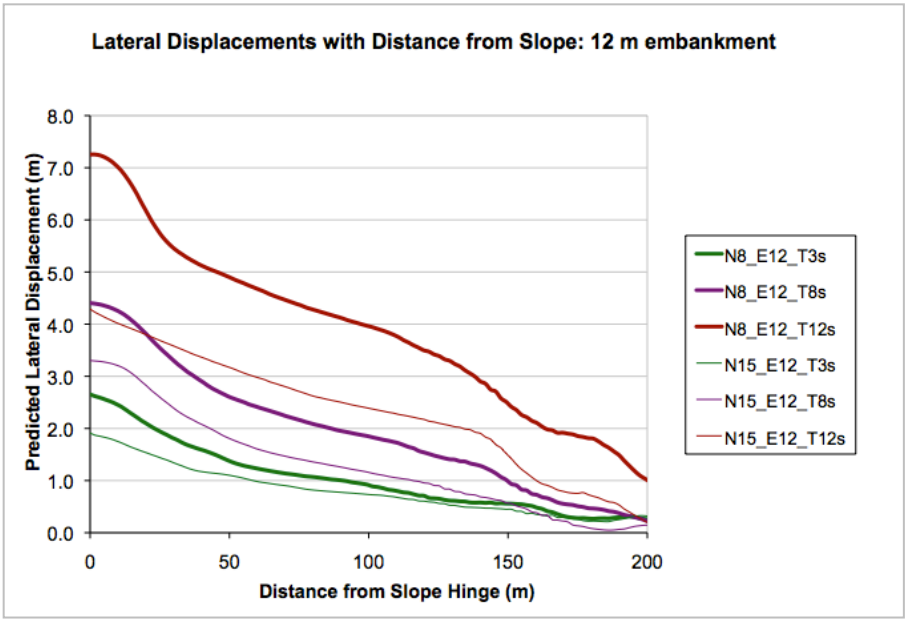

Figure 4.3.4. Calculated lateral displacements with distance from a slope hinge point for an embankment 12 m high founded on a sand layer of variable thickness and with $(N_1)_{60}$ blow count value of 8 and 15. (Ground Motion: 1994 Northridge Sylmar Converter Station)

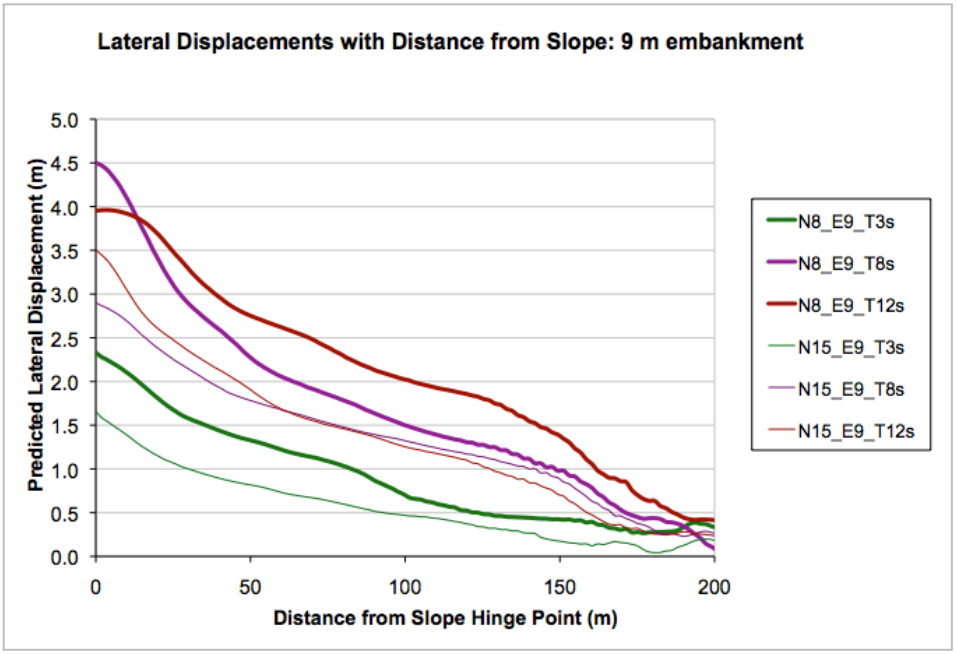

Figure 4.3.5. Calculated lateral displacements with distance from a slope hinge point for an embankment 9 m high founded on a sand layer of variable thickness and with $(N_1)_{60}$ blow count value of 8 and 15. (Ground Motion: 1994 Northridge Sylmar Converter Station)

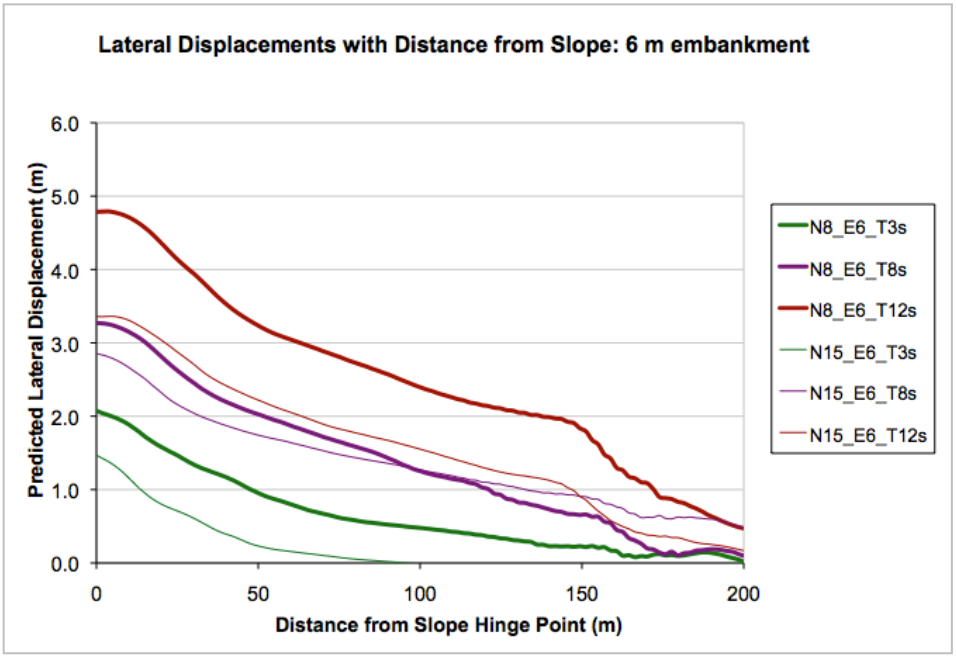

Figure 4.3.6. Calculated lateral displacements with distance from a slope hinge point for an embankment 6 m high founded on a sand layer of variable thickness and with $(N_1)_{60}$ blow count value of 8 and 15. (Ground Motion: 1994 Northridge Sylmar Converter Station)

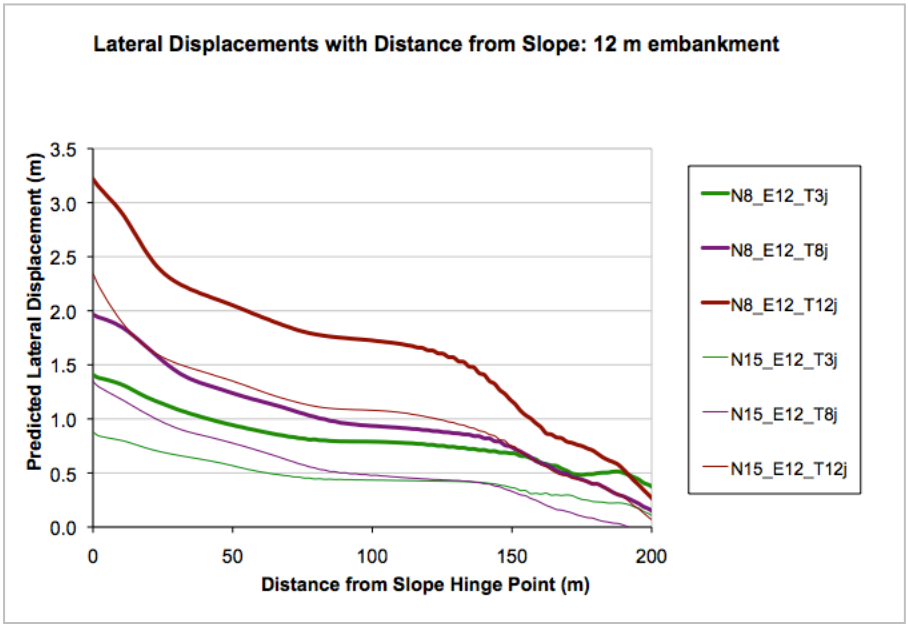

Figure 4.3.7. Calculated lateral displacements with distance from a slope hinge point for an embankment 12 m high founded on a sand layer of variable thickness and with $(N_1)_{60}$ blow count value of 8 and 15. (Ground Motion: 1992 Landers Joshua Tree)

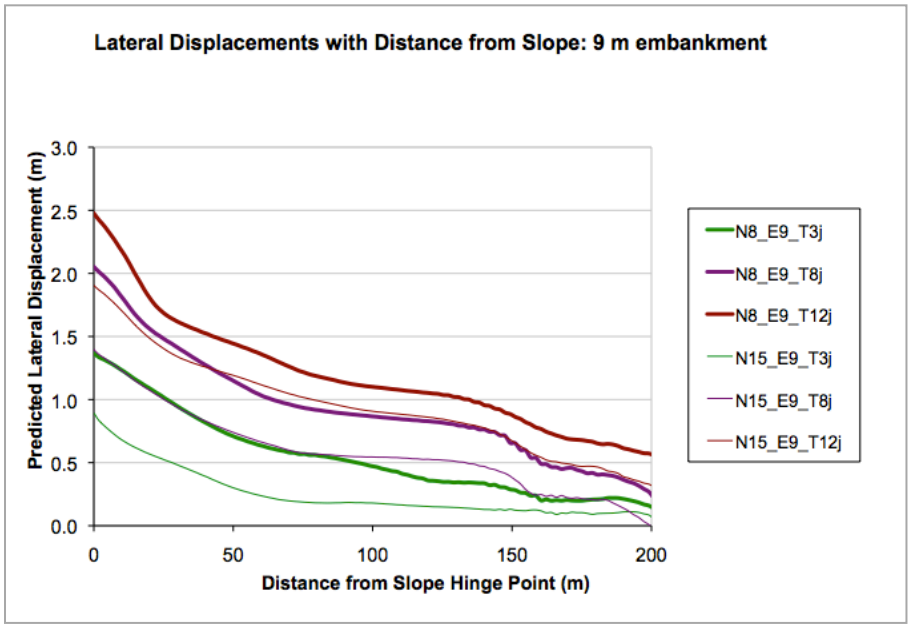

Figure 4.3.8. Calculated lateral displacements with distance from a slope hinge point for an embankment 9 m high founded on a sand layer of variable thickness and with $(N_1)_{60}$ blow count value of 8 and 15. (Ground Motion: 1992 Landers Joshua Tree)

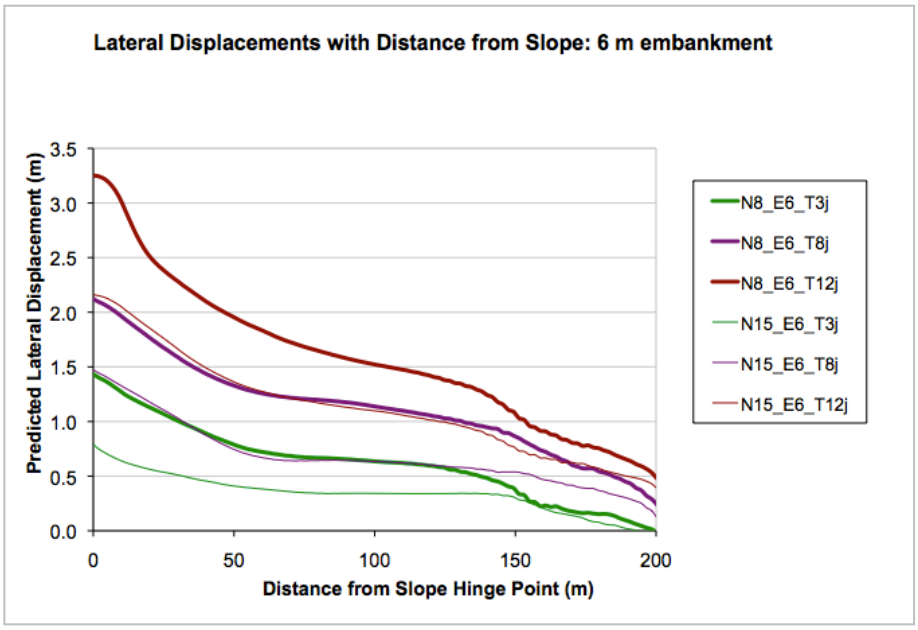

Figure 4.3.9. Calculated lateral displacements with distance from a slope hinge point for an embankment 6 m high founded on a sand layer of variable thickness and with $(N_1)_{60}$ blow count value of 8 and 15. (Ground Motion: 1992 Landers Joshua Tree)

4.3.2. Embankment Height

The embankment height of the model was found to have a relatively minor effect on the calculated seismic displacement, though the effect becomes more pronounced when combined with a thicker zone of liquefiable foundation soils. Results are shown in Figures 4.3.10 - 4.3.15.

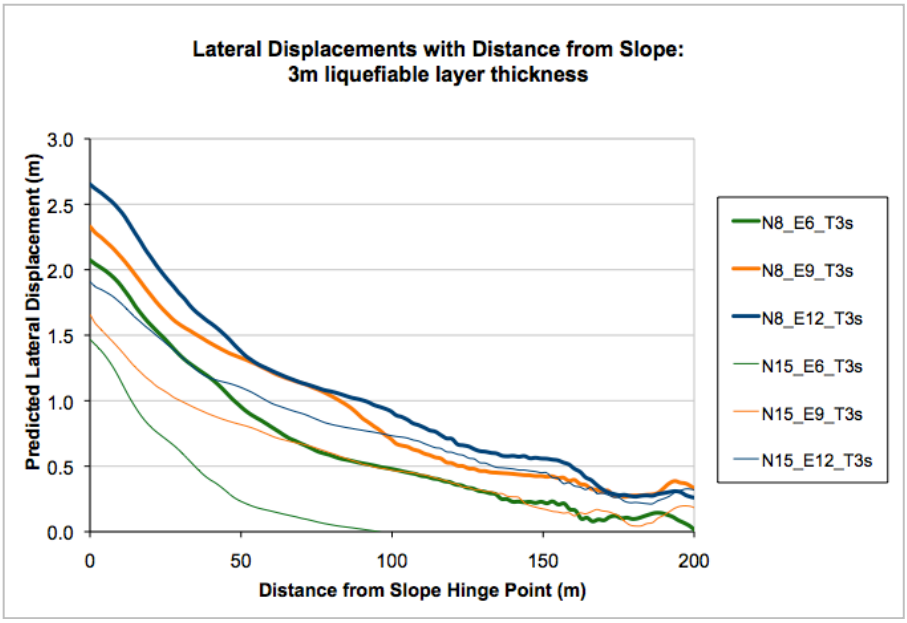

Figure 4.3.10. Calculated lateral displacements with distance from a slope hinge point for a variable height embankment over 3 m of liquefiable foundation soils with $(N_1)_{60}$ blow count value of 8 and 15. (Ground Motion: 1994 Northridge Sylmar Converter Station)

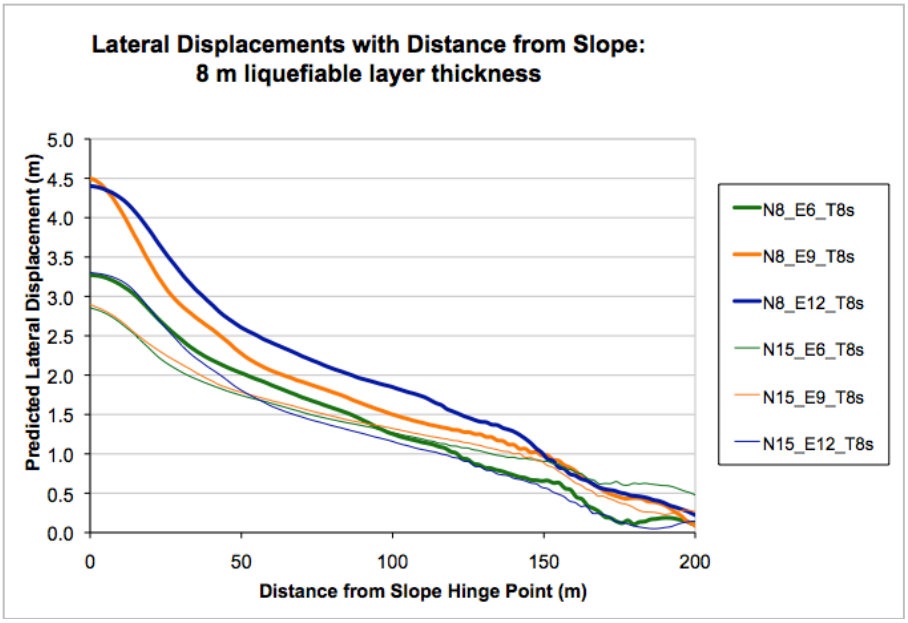

Figure 4.3.11. Calculated lateral displacements with distance from a slope hinge point for a variable height embankment over 8 m of liquefiable foundation soils with $(N_1)_{60}$ blow count value of 8 and 15. (Ground Motion: 1994 Northridge Sylmar Converter Station)

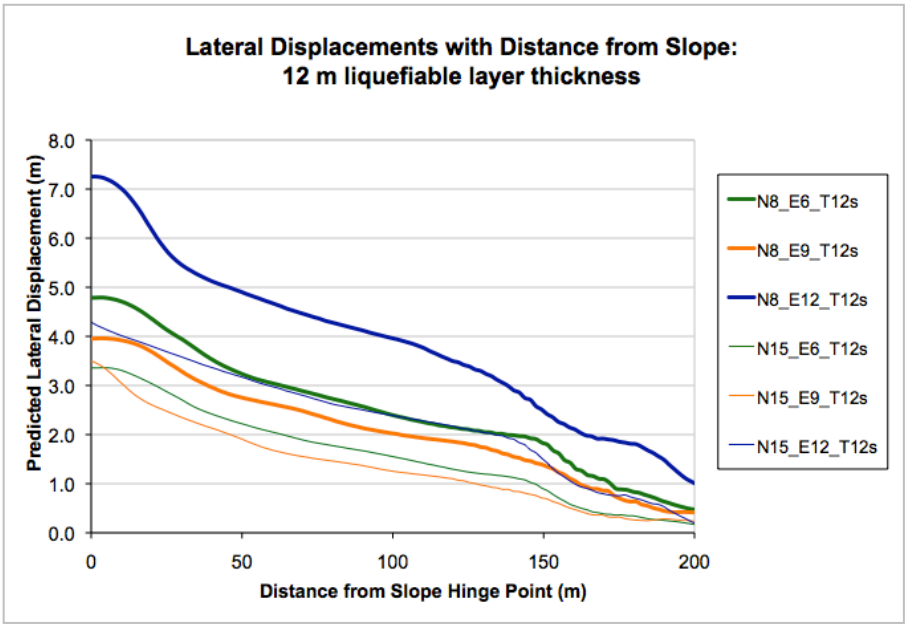

Figure 4.3.12. Calculated lateral displacements with distance from a slope hinge point for a variable height embankment over 12 m of liquefiable foundation soils with $(N_1)_{60}$ blow count value of 8 and 15. (Ground Motion: 1994 Northridge Sylmar Converter Station)

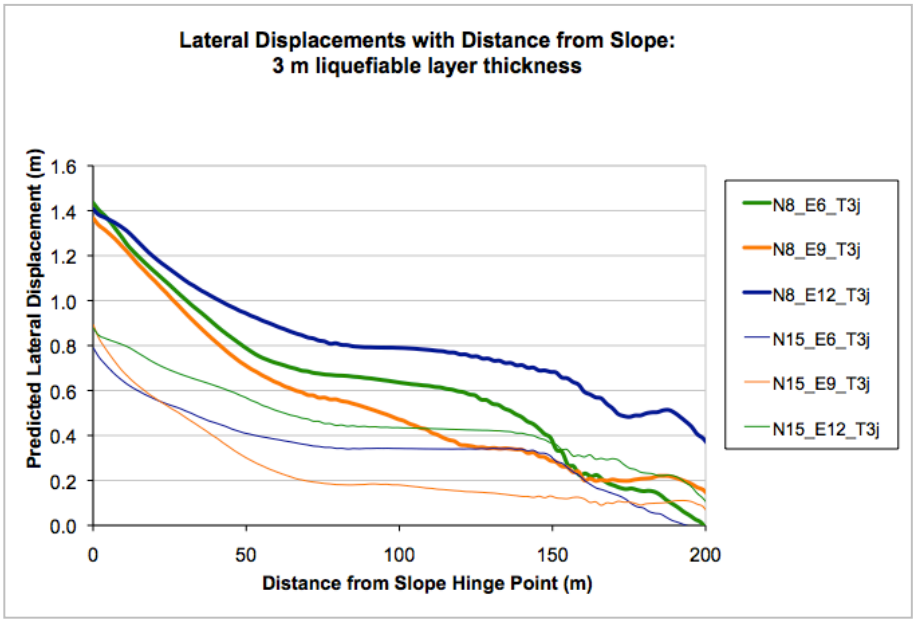

Figure 4.3.13. Calculated lateral displacements with distance from a slope hinge point for a variable height embankment over 3 m of liquefiable foundation soils with $(N_1)_{60}$ blow count value of 8 and 15. (Ground Motion: 1992 Landers Joshua Tree)

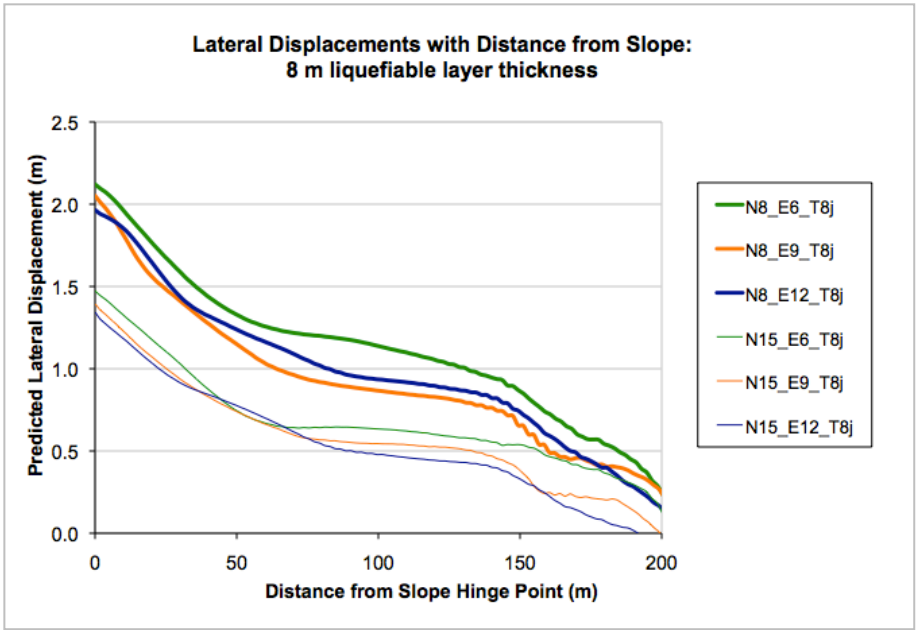

Figure 4.3.14. Calculated lateral displacements with distance from a slope hinge point for a variable height embankment over 8 m of liquefiable foundation soils with $(N_1)_{60}$ blow count value of 8 and 15. (Ground Motion: 1992 Landers Joshua Tree)

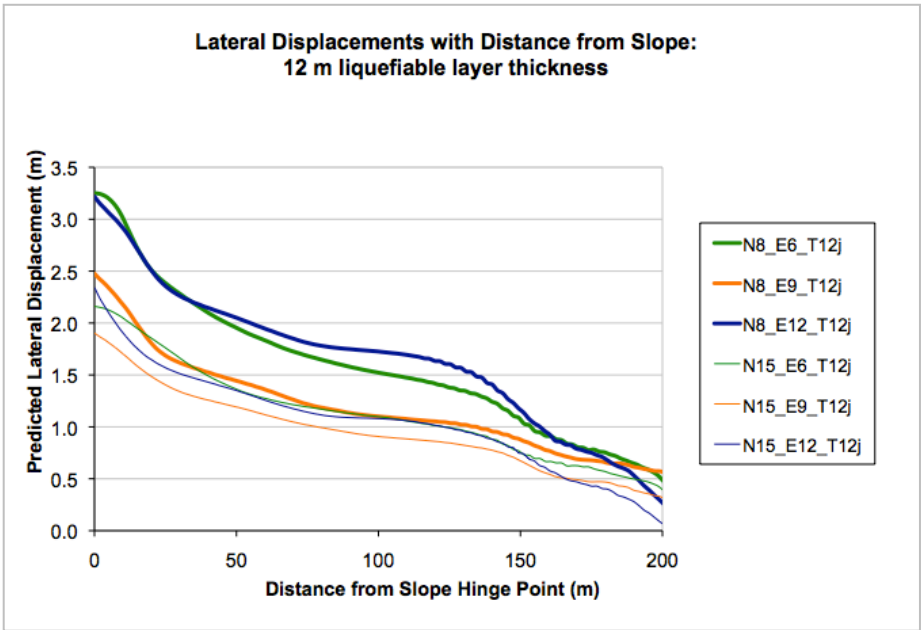

Figure 4.3.15. Calculated lateral displacements with distance from a slope hinge point for a variable height embankment over 12 m of liquefiable foundation soils with $(N_1)_{60}$ blow count value of 8 and 15. (Ground Motion: 1992 Landers Joshua Tree)

4.4. Sensitivity of Results to Variations in Earthquake Ground Motions

Earthquake ground motions for these analyses were selected from the PEER ground motion database: http://peer.berkeley.edu/nga/search.html. A suite of nine near-fault, forward-directivity, fault-normal ground motions (Table 4.1.1) and seven intermediate field ground motions (Table 4.1.2) were selected for comparisons in the sensitivity analysis. Selections were made based on a suite of motions used by Mason (2011). Ground motions were selected to reflect the seismic hazards most likely to control the design of levees within the San Joaquin-Sacramento delta region of California. Plots that describe the ground motions are provided in Appendix A.

Tables 4.4.1 and 4.4.2 provide additional information for each ground motion. Table 4.4.3 presents the calculated lateral and vertical displacements at a distance of approximately 2 m behind the slope hinge point for each ground motion. Arias intensity proved to correlate well with predicted displacement, as shown in Figure 4.4.1. Peak ground acceleration (PGA) was found to have a weaker correlation with the predicted displacements, as shown in Figure 4.4.2. Figure 4.2.3 and 4.2.4 show calculated displacements plotted with the peak ground velocity (PGV) and the square of the PGV. Arias intensity provides the best fit with displacement as can be seen below.

Table 4.4.1. Selected near-fault, forward directivity, fault-normal deep soil ground motions

Station	Scale	Earthquake	Mw	PGA (g)	PGV (m/s)	I_a (m/s)	Tm (sec)
Brawley Airport	1	79 Imperial Valley	6.5	0.128	3.357	23	1.15
Saratoga WV Coll 270	1	89 Loma Prieta	7	0.293	5.766	97.9	0.99
Newhall - W Pico Cany 046	1	94 Northridge	6.7	0.421	0.843	126.6	1.57
Sylmar - Conv Sta 052	0.5	94 Northridge	6.7	0.264	5.282	115.4	1.16
Sylmar - Conv Sta 052	1	94 Northridge	6.7	0.543	10.646	478.8	1.15
Sylmar - Conv Sta 052	1.25	94 Northridge	6.7	0.684	13.32	752.2	1.15
LGPC 090	1	Loma Prieta	7	0.468	4.697	239.3	0.59
Rinaldi R Sta 228	1	94 Northridge	6.7	0.747	15.226	595.3	0.75
Lucern 260	1	92 Landers	7.3	0.536	13.876	332.5	0.5

Table 4.4.2. Selected intermediate field ground motions

Station	Scale	Earthquake	Mw	PGA (g)	PGV (m/s)	I_a (m/s)	Tm (sec)
TCU078 270 (E)	1	99 Chi Chi	7.6	0.354	3.59	424.6	0.45
LA Hollywood Stor Lot 180	1	71 San Fernando	6.6	0.133	1.333	26.1	0.42
Parachute T S 315	1	87 Superstition Hills	6.6	0.328	4.062	135	0.69
Joshua Tree 090	0.75	92 Landers	7.3	0.192	2.792	101.6	0.79
Joshua Tree 090	1	92 Landers	7.3	0.256	3.873	185.4	0.78
Joshua Tree 090	1.5	92 Landers	7.3	0.386	6.129	428.7	0.78
Superstition Mtn Cam 045	1	87 Superstition Hills	6.6	0.489	2.896	261.9	0.35

Table 4.4.3. Calculated lateral and vertical displacements for a 9 m-high embankment founded on an 8 m-thick layer of loose to medium dense sands for the suite of 16 selected ground motions

			$(N_1)_{60}$ = 8		$(N_1)_{60}$ = 15	
Station	**Scale**	**Earthquake**	**X-displacement at 2m from Hinge Point (cm)**	**Y-displacement at 2m from Hinge Point (cm)**	**X-displacement at 2m from Hinge Point (cm)**	**Y-displacement at 2m from Hinge Point (cm)**
Brawley Airport	1	79 Imperial Valley	2	2	1	-1
Saratoga WV Coll 270	1	89 Loma Prieta	153	-22	74	-16
Newhall - W Pico Cany 046	1	94 Northridge	186	-34	89	-30
Sylmar - Conv Sta 052	0.5	94 Northridge	209	-32	144	-27
Sylmar - Conv Sta 052	1	94 Northridge	447	-133	287	-63
Sylmar - Conv Sta 052	1.25	94 Northridge	514	-77	411	-66
LGPC 090	1	Loma Prieta	136	30	105	-24
Rinaldi R Sta 228	1	94 Northridge	268	-29	221	-55
Lucern 260	1	92 Landers	105	-14	168	-12
TCU078 270 (E)	1	99 Chi Chi	300	-36	180	-24
LA Hollywood Stor Lot 180	1	71 San Fernando	3	-3	2	-2
Parachute T S 315	1	87 Superstition Hills	81	-22	59	-19
Joshua Tree 090	0.75	92 Landers	132	-25	94	-14
Joshua Tree 090	1	92 Landers	205	-42	136	-23
Joshua Tree 090	1.5	92 Landers	333	-58	333	-58
Superstition Mtn Cam 045	1	87 Superstition Hills	106	-42	94	-40

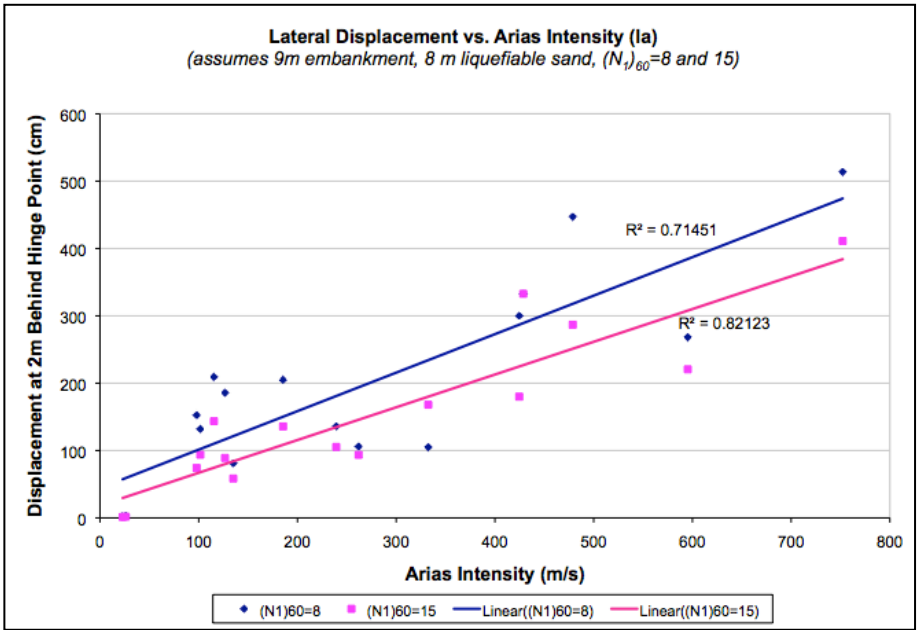

Figure 4.4.1. Calculated liquefaction-induced lateral displacement (cm) as a function of the Arias Intensity of the input earthquake ground motion.

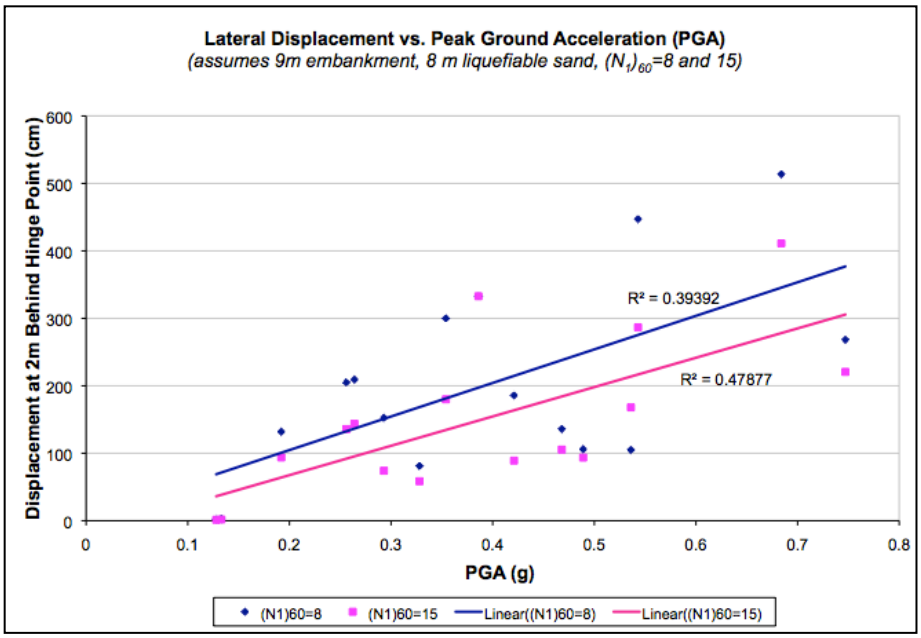

Figure 4.4.2. Calculated liquefaction-induced lateral displacement as a function of the peak ground acceleration of the input earthquake ground motion.

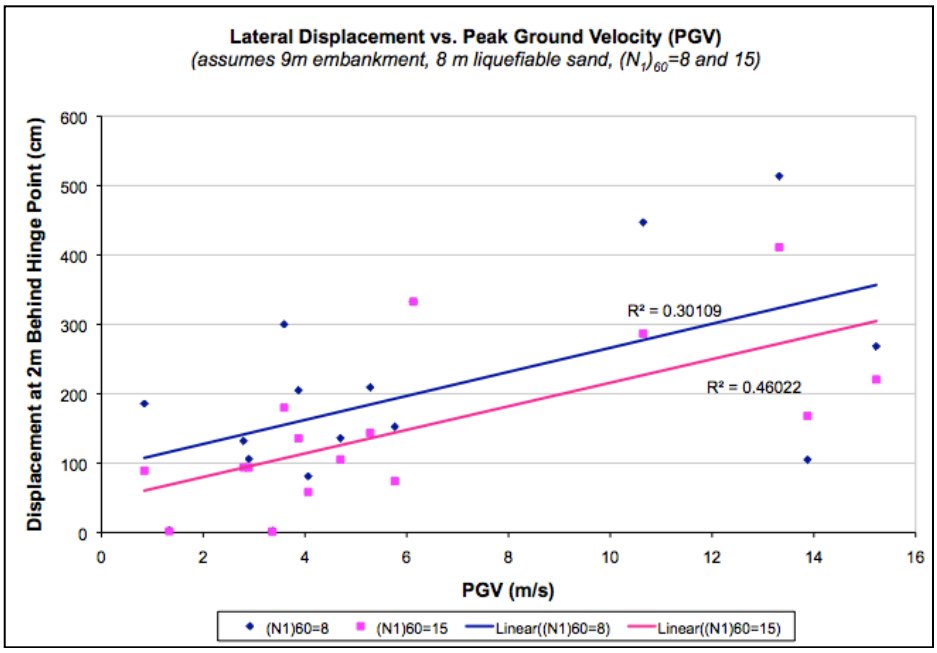

Figure 4.4.3. Calculated liquefaction-induced lateral displacement as a function of the peak ground velocity of the input earthquake ground motion.

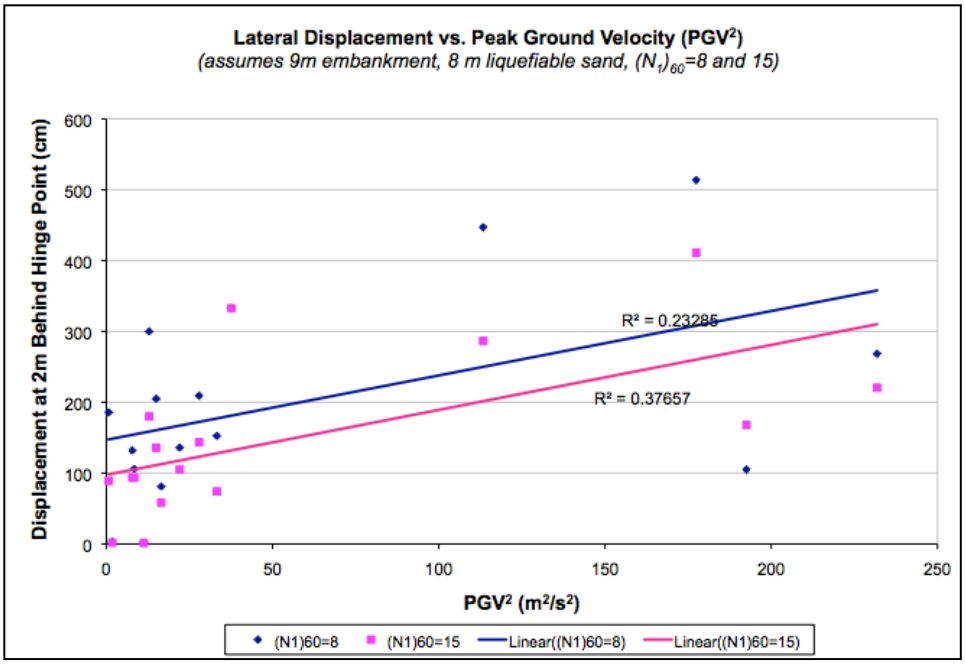

Figure 4.4.4. Calculated liquefaction-induced lateral displacement as a function of the square of the peak ground velocity of the input earthquake ground motion.

5. SUMMARY AND CONCLUSIONS

Calibration of the fully nonlinear effective stress UBCSAND soil model using CSS test results established trends in the variation of its model parameters that prove useful for employing the UBCSAND model in practice. The CSS-based model parameter calibration led to the development of UBCSAND model parameterizations that were found to capture the observed performance of three well documented liquefaction-induced displacement case histories. These back-analyses of case histories demonstrate the robustness of the UBCSAND model as implemented in the computer program FLAC for this application. Thus, the proposed model calibration procedure can be employed by engineers in the development of UBCSAND model parameters for liquefaction-induced deformation analysis.

In addition, to the UBCSAND model parameters that depend on conventional geotechnical characterizations (e.g., $(N_1)_{60}$), there are four “fitting” parameters that are available for use in UBCSAND. In this study, only two of these “fitting” parameters were used (i.e., m_fac1 and m_fac4). The model parameters m_hfac1 and m_hfac2 were found to serve a similar function. Best results were obtained by setting the parameters equal to each other. These parameters are used to model the number of cycles to liquefaction and their value has an effect on the rate of pore water pressure rise with cyclic loading. Values of 0.5 to 2.0 were typical values used in our analyses, though values can be higher and lower than this range of values. For the case of sand at very low relative density, the value of m_hfac1 (which is the same as m_hfac2 for our study) must be increased to match liquefaction triggering response in CSS laboratory test results data. Increases in the initial static shear stress acting on the soil yielded a weak trend of a corresponding increase in m_hfac1 (and similarly, m_hfac2). The effect is most evident for

sand at low relative density. Non-plastic or low plasticity silts were found to follow a similar trend as that for clean sands, though these materials required a slightly higher value of m_hfac1 (and m_hfac2) to capture their measured cyclic response. The UBCSAND m_hfac3 parameter was not used in this study. Lastly, the UBCSAND m_hfac4 parameter was found to vary between approximately 0.5 and 2.5 for sands with typical values being between 1.5 and 2.0. The m_hfac4 parameter was moderately influenced by the relative density of the sand at low CSR (i.e., CSR ≤ 0.2) and by the value of the earthquake-induced CSR at higher CSR (i.e., CSR ≥ 0.2). For silty soils, a value of 0.5 was selected for cases where the soil had a higher void ratio, and a value of 1.5 was selected for lower void ratio silty soils.

The calibrated UBCSAND model was used to estimate liquefaction-induced embankment deformations with varying foundation soil properties, layer thicknesses, as well as a range of embankment heights and ground motions. In this study, the liquefiable soils were present in the foundations of earth levees. The range of calculated displacement values for all configurations modeled with the intense forward-directivity 1994 Northridge Sylmar Converter Station motion was approximately 1.5 m to 7.5 m. The displacement resulting from the same models but with the lower intensity backward-directivity 1992 Landers Joshua Tree motion yielded displacements ranging from 0.75 m to 3.25 m, which is approximately half those values calculated using the Sylmar Converter Station motion. The intensity of the earthquake appears to be the key factor as the calculated liquefaction-induced displacements increased significantly as the input motion's value of Arias intensity increased. The rate of increase of the calculated liquefaction-induced displacement with increasing Arias intensity was roughly linear for these embankment configurations for the complete suite of earthquake ground motions. The rate of increase in the calculated liquefaction-induced displacement increased as the relative density of the liquefied sand decreased.

The thickness of the liquefiable foundation layer impacted displacements in a non-linear pattern where displacement increased more rapidly as the liquefiable material layer thickness increases significantly. As would be expected, looser foundation soils led to increased amounts of displacement of the overlying embankment. Additionally, for the cases analyzed in this study, higher embankments displaced more when strongly shaken. Combinations of thicker deposits of liquefiable foundation soils combined with higher embankments yielded the maximum displacement of the cases analyzed in this study, especially when shaken with the intense forward-directivity 1994 Northridge Sylmar Converter Station ground motion.

Therefore, the UBCSAND model as implemented in FLAC proved to be a reliable tool for evaluating the effects of liquefaction in the foundation of earth levees. With some initial calibration effort to understand trends in the model parameters, it was able to capture the performance of three case histories well. Our hope is that this independent evaluation of the capabilities of this soil constitutive model to capture inertially driven liquefaction-induced lateral spreads will enable practicing engineers to employ this model with confidence in evaluations of the seismic performance of earth structures situated atop potentially liquefiable soils.

6. REFERENCES

Arduino, P., Kramer, S. and Baska, D. (2001). “UW-Sand: a simple constitutive model for liquefiable soils.” In: Book of Abstracts, 2001 Mechanics and Materials Summer Conference, 27-29 June, San Diego, CA. pg. 108

Arulmoli, K., K. K. Muraleetharan, M. M. Hossain, and L.S. Fruth, 1992, “VELACS: Verification of Liquefaction Analysis by Centrifuge Studies. Laboratory Testing Program. Soil Data Report,” The Earth Technology Corporation, Long Beach, CA, report for the National Science Foundation.

Bardet, J.P., Hu, J., Tobita, T., and Mace, N. (1999) “Database of case histories on liquefaction-induced ground deformation,” Univ. of Southern California, Department of Civil Engineering, A Report to PEER/PG&E, Task 4A, Phase 2, October 16.

Bardet, J.P., Tobita, T., Mace, N., and Hu, J. (2002) “Regional model of liquefaction-induced ground de-formation.” *Earthquake Spectra*. 18(1): 19-46.

Baska, D.A. (2002). “An analytical/empirical model for prediction of lateral spread displacements.” Ph.D. thesis, Dept. of Civil & Environ. Engineering, Univ. of Washington, Seattle.

Baziar, M.H., Dobry, R., and Elgamal, A. (1992). “Engineering evaluation of permanent ground deformations due to seismically-induced liquefaction.” Technical Report NCEER-92-0007, National Center fo Earth-quake Engineering Research (NCEER), Buffalo, NY.

Beaty, M. and Byrne, P.M. (1998) “An effective stress model for predicting liquefaction behavior of sand,” Geotechnical Earthquake Engineering and Soil Dynamics III, ASCE Spec. Pub. No. 75, Edited by Dakoulos, Yegian and Holz, ASCE, Reston, VA, Vol. 1, pp. 766-777.

M.J. Bennett. Liquefaction analysis of the 1971 ground failure at the San Fernando Valley Juvenile Hall, California. Bulletin of the Association of Engineering Geologists, XXVI (2):209 – 226, 1989.

R.W. Boulanger, I.M. Idriss, and L.H. Mejia. Investigation and evaluation of liquefaction related ground displacements at Moss Landing during the 1989 Loma Prieta earthquake. Technical Report UCD/CGM-95/02, UC Davis Center for Geotechnical Modeling, UC Davis, Davis, California, 1995.

Boulanger R.W., Mejia L.H. and Idriss I.M. (1997) “Liquedaction at Moss Landing During Loma Prieta Earthquake,” *Journal of Geotechnical and Geoenvironmental Engineering*. Vol. 123(5): 453-467.

Bray, J.D. and Stewart, J.P., coordinators (2000). “Damage patterns and foundation performance in Ada-pazari.” Kocaeli, Turkey Earthquake of August 17, 1999 Reconnaissance Report, T.L. Youd, J.P. Bardet, and J.D. Bray, eds., *Earthquake Spectra*, Supplement A to Vol. 16, 163-189.

Bray, J. D., R. B. Sancio, H.T. Durgunoglu, A. Onalp, R. B. Seed, J. P. Stewart, T. L. Youd, M. B. Batu-ray, K.O. Cetin, C. Christensen, T. Karadayilar, and C. Emrem, (2001) “Ground Failure In Adapaza-ri, Turkey,” in Proc., Earthquake Geotechnical Engineering Satellite Conf. of the XVth International Conference on Soil Mechanics & Geotechnical Engineering, Istanbul, Turkey, August 24-25.

Bray, J.D., Sancio, R.B., Riemer, M.F. and Durgunoglu, T. (2004a) “Liquefaction Susceptibility of Fine-Grained Soils,” *11th International Conf. On Soil Dynamics and Earthquake*

Engineering and 3rd In-ternational Conf. On Earthquake Geotechnical Engineering, Doolin, Kammerer, Nogami, Seed and Towhata, Eds., Berkeley, CA, Jan. 7-9, 2004, V.1, pp. 655-662.

Bray, J. D., R. B. Sancio, H.T. Durgunoglu, A. Onalp, T. L. Youd, J. P. Stewart, R. B. Seed, O.K. Cetin, E. Bol, M. B. Baturay, C. Christensen, and T. Karadayilar (2004b) "Subsurface Characterization at Ground Failure Sites in Adapazari, Turkey," Journal of Geotechnical and Geoenvironmental Engi-neering, ASCE, Vol. 130, No. 7, July, pp. 673-685.

Bray, J.D., and Sancio, R.B. (2006) "Assessment of the Liquefaction Susceptibility of Fine-Grained Soils," J. of Geotechnical and Geoenvironmental Engineering, ASCE, Vol. 132, No. 9, Sept., pp. 1165-1177.

Bray, J.D. and Travasarou, T. (2007) "Simplified Procedure for Estimating Earthquake-Induced Deviatoric Slope Displacements," J. of Geotechnical and Geoenvironmental Engineering, ASCE, Vol. 133, No. 4, April, pp. 381-392.

Byrne, P.M., Park, S-S., Beaty, M., Sharp, M., Gonzalez, L., and Abdoun, T. (2004) "Numerical modeling of liquefaction and comparison with centrifuge tests," Canadian Geotechnical Journal, Vol. 41, pp. 193-211.

Byrne, P.M., and Seid-Karbasi, M. (2003) "Seismic stability of impoundments," 17th Annual Symposium of VGS, Canada (http://www.civil.ubc.ca/liquefaction/Publications/VGS12R.pdf).

California Department of Water Resources. (2007). Delta Risk Management Strategy Technical Memorandum: Levee Vulnerability, Draft 2. Sacramento, CA Available online at:
< http://www.drms.water.ca.gov/Updated2007/>.

Center for Earthquake Engineering Research Center. Woodward-Clyde Consultants. Phase i - geotechnical study, Marine Biology Laboratory, California State University, Moss Landing, California. Technical report, California State University, San Jose, California, 1990.

S.W. Chang. Seismic Response of Deep Stiff Soil Deposits, Ph.d. disseration, University of California, Berkeley, 1996.

K.O. Cetin. Reliability-Based Assessment of Seismic Soil Liquefaction Initiation Hazard. Ph.D. dissertation, University of California, Berkeley, 2000.

Earthquake Engineering Research Institute (2003) "Securing Society Against Catastrophic Earthquake Losses: A Research and Outreach Plan in Earthquake Engineering."

Electric Power Research Institute (1990), Manual on Estimating Soil Properties for Foundation Design, EPRI EL-6800, August 1990.

Elgamal, A., Yang, Z., and Parra, E. (2002) "Computational Modeling of Cyclic Mobility and Post-Liquefaction Site Response," Soil Dynamics and Earthquake Engineering, ASCE, V. 22, pp. 259-271.

R.B. Fallgren and J.L. Smith. Ground displacement at San Fernando Valley Juvenile Hall during San Fernando earthquake. In The San Fernando, California, Earthquake of February 9, 1971, volume 3, pages 189 – 196. National Oceanic and Atmospheric Administration, 1973.

Faris, A.T. (2004) "Probabilistic models for engineering assessment of liquefaction-induced lateral spreading displacements," Ph.D. thesis, Dept. of Civil & Environ. Engineering, Univ. of California, Berkeley, Fall.

Faris, A.T., Seed, R.B., Kayen, R.E., and Wu. J. (2006) "A semi-empirical model for estimation of maximum horizontal displacement due to liquefaction-induced lateral spreading," Proc. 8th US Nat. Conf. EQ Engrg., 100th Anniversary Earthquake Conference Commemorating the 1906 San Francisco Earthquake, EERI, April.

Finn, W.D. Liam (1990) “Analysis of Post-Liquefaction Deformations in Soil Structures,” Proc. H. Bolton Seed Memorial Symposium, Univ. of Calif., Berkeley, Editor J.M. Duncan, Bi-Tech Publishers, Vancouver, Canada, Vol. 2, pp. 291-311.

Finn, W.D. Liam (1998) “Seismic safety of embankment dams developments in research and practice 1988-1998,” Geotechnical Earthquake Engineering and Soil Dynamics III, ASCE Spec. Pub. No. 75, Edited by Dakoulos, Yegian and Holz, ASCE, Reston, VA, Vol. 2, pp. 812-853.

Finn, W.D. Liam (2000a) “State-of-the-art of geotechnical earthquake engineering practice,” Soil Dynamics and Earthquake Engineering, Vol. 20, pp. 1-15.

Finn, W.D. Liam (2000b) “Post-liquefaction flow deformations,” ASCE Geotechnical Engineering Spec. Pub. No. 107, Proceedings of GeoDenver 2000, pp. 108-122.

Hamada, M., Yasuda, S., Isoyama, R., and Emoto, K. (1986) “Study on liquefacton induced permanent ground displacements,” Report for the Association for the Development of Earthquake Prediction.

Holzer, T.L., Bennett, M.J., Ponti, D.J., and Tinsley, J.C. (1999) “Liquefaction and Soil Failure During 1994 Northridge Earthquake,” *Journal of Geotechnical and Geoenvironmental Engineering*. Vol. 125(6): 438-452.

Idriss, I.M., and Boulanger, R.W. (2008) Soil Liquefaction During Earthquakes, EERI Monograph, Oakland, California (draft available to selected persons; 2nd Edition to be published soon).

Itasca Consulting Group, Inc. (2005). FLAC, version 5.0. Itasca Consulting Group, Inc.: Minneapolis, Minnesota.

Kammerer, A., Pestana, J., and Seed, R. (2002). “Undrained Response of 0/30 Sand Under Multidirec-tional Cyclic Simple Shear Loading Conditions.” Geotechnical Engineering Research Report No. UCB/GT/02-01, University of California, Berkeley, July.

Ledezma, C. and Bray, J.D. (2006) “A Probabilistic Design Procedure that Incorporates the Pile-Pinning Effect in Bridge Foundations Undergoing Liquefaction-Induced Lateral Spreading,” Proc. 5th Nat. Seismic Conf. on Bridges & Highways, San Francisco, CA, Sept. 18-20.

Ledezma, C. and Bray, J.D. (2007) “Performance-Based Earthquake Engineering Design Evaluation Pro-cedure for Bridge Foundations Undergoing Liquefaction-Induced Lateral Spreading,” PEER Report 2007/xx, Pacific Earthquake Engineering Research Center, College of Engineering, University of California, Berkeley, November.

Martin, G.R. and Lew, M., eds. (1999) “Recommended Procedures for Implementation of DMG Special Publication 117: Guidelines for Analyzing and Mitigating Liquefaction Hazards in California,” Southern California Earthquake Center, Univ. of Southern Calif., March.

Mason, H. B. (2011). Seismic Performance Assessment in Dense Urban Environments. PhD dissertation, Department of Civil & Environmental Engineering, University of California, Berkeley.

Newmark, N.M. (1965). “Effects of earthquakes on dams and embankments.” *Geotechnique*. 15(2): 139-160.

Olson, S.M. and Stark, T.D. (2002) “Liquefied strength ratio from liquefaction flow failure case histo-ries,” Canadian Geotechnical Journal, Vol. 39, pp. 629-647.

T.D. O’ Rourke, B.L. Roth, and M. Hamada. Large ground deformation and their effects on lifeline facilities: 1971 San Fernando Earthquake. In T.D. O’Rourke and M. Hamada, editors,

Case studies of liquefaction and lifeline performance during past earthquakes, volume 2 of NCEER-92-0002, Buffalo, N.Y., 1992b. National Center for Earthquake Engineering Research.

Park, S.-S. and Byrne, P.M. (2004) “Stress densification and its evaluation,” Canadian Geotechnical Journal, Vol. 41, pp. 181-186.

Puebla, H., Byrne, P.M., and Phillips, R. (1997). “Analysis of CANLEX liquefaction embankments: pro-totype and centrifuge models.” *Canadian Geotechnical Journal*. 34: 641-657.

Rathje, E.M. and Bray, J.D. (2000). “Nonlinear coupled seismic sliding analysis of earth structures.” *Journal of Geotechnical and Geoenvironmental Engineering*. 126(11): 1002-1014.

Rauch, A.F. and Martin, J.R. (2000) “EPOLLS model for predicting average displacements on lateral spreads.” *Journal of Geotechnical and Geoenvironmental Engineering*. 126(4): 360-371.

Robertson, P.K., and Robertson, K.L. (2006) Guide to Cone Penetration Testing and it’s Application to Geotechnical Engineering. *Gregg Drilling and Testing, Inc.* 126(4): 360-371.

Rutherford and Chekene. Geotechnical investigation: Moss Landing Facility (Technology Building), Monterey Bay Aquarium Research Institute. Technical report, Monterey Bay Aquarium Research Institute, 1988.

R.B. Sancio. Ground Failure and Building Performance in Adapazari, Turkey. Ph.d. dissertation, University of California, Berkeley, 2003.

Seed, H.B. (1979) “Soil Liquefaction and Cyclic Mobility Evaluation for Level Ground During Earth-quakes,” J. of the Geotechnical Engineering Div., Vol. 105, No. GT2, pp. 201-255.

Seed, H. B.; Idriss, I. M. (1982) Ground Motions and Soil Liquefaction During Earthquakes. EERI Mo-nograph, Berkeley, California, 134 pages.

Seed, R.B., Cetin, K.O., Moss, R.E.S., Kammerer, A.M., Wu, J., Pestana, J.M., Riemer, M.F., Sancio, R.B., Bray, J.D., Kayen, R.E., and Faris, A. (2003) “Recent Advances in Soil Liquefaction Engineering: A Uni-fied and Consistent Framework,” 26th Annual ASCE Los Angeles Geotechnical Spring Seminar, Keynote Presentation, Long Beach, Calif., April 30.

Seid-Karbasi, M., and Byrne, P.M. (2004) “Embankment dams and earthquakes,” J. Hydropower & Dams, Vol. 11(2), pp. 96-102.

J.C. Tinsley, III and W.R. Dupre. Liquefaction hazard mapping, depositional faces, and lateral spreading ground failure in the Monterey Bay Area, Central California, during the 10/17/89 Loma Prieta Earthquake. In Proceedings from the Fourth U.S.-Japan Workshop on Earthquake Resistant Design of Lifeline Facilities and Countermeasures Against Soil Liquefaction, volume I of NCEER-92-0019, pages 71 – 85, Buffalo, N.Y., 1992. National

J. Wu. Liquefaction Triggering and Post Liquefaction Deformations of Monterey 0/30 Sand under Uni-Directional Cyclic Simple Shear Loading. Ph.d. dissertation, University of California, Berkeley, 2002.

Yang, Z., Elgamal, A., Adalier, K., and Sharp, M.K. (2004). “Earth dam on liquefiable foundation and remediation: numerical simulation of centrifuge experiments.” *Journal of Engineering Mechanics*. 130(10): 1168-1176.

Yang, Z., Elgamal, A. and Parra, E. (2003). “A computational model for cyclic mobility and associated shear deformation.” *Journal of Geotechnical and Geoenvironmental Engineering*. 129(12): 1119-1127.

Yegian, M.K., Marciano, E.A., and Ghahraman, V.G. (1991). “Earthquake-induced permanent deforma-tion: probabilistic approach. *Journal of Geotechnical Engineering*. 117(1): 35-50.

Youd, T.L., Bardet, J.P., and Bray, J.D. (2000). Kocaeli, Turkey Earthquake of August 17, 1999 Recon-naissance Report, in *Earthquake Spectra* Journal, Suppl. A to Vol. 16, EERI.

Youd T.L., Idriss I.M., Andrus R.D., Arango I., Castro G., Christian J.T., Dobry R., Finn W.D.L., Harder Jr. L.F., Hynes M.E., Ishihara K., Koester J.P., Liao S.S.C., Marcuson III W.F., Martin G.R., Mitchell J.K., Moriwaki Y., Power M.S., Robertson P.K., Seed R.B., & Stokoe II K.H., 2001. Liquefaction resistance of soils: summary report from the 1996 NCEER and 1998 NCEER/NSF workshops on evaluation of liquefaction resistance of soils. *Journal of Geotechnical and Geoenvironmental Engineering*. Vol. 127(10): 817-903.

Youd, T.L., Hansen, C.M., and Bartleet, S.F. (2002) “Revised multilinear regression equations for prediction of lateral spread displacement,” *Journal of Geotechnical and Geoenvironmental Engineering*. Vol. 128(12): 1007-1017.

Woodward-Clyde Consultants. Phase i - geotechnical study, Marine Biology Laboratory, California State University, Moss Landing, California. Technical report, California State University, San Jose, California, 1990.

Zhang, G., Robertson, P.K., and Brachman, R.W.I. (2004). “Estimating liquefaction-induced lateral spread displacements using the standard penetration test or cone penetration test.” *Journal of Geotechnical and Geoenvironmental Engineering*. 130(8): 861-871.

APPENDIX A: GROUND MOTION DATA

1979 Imperial Valley, Brawley Airport 225

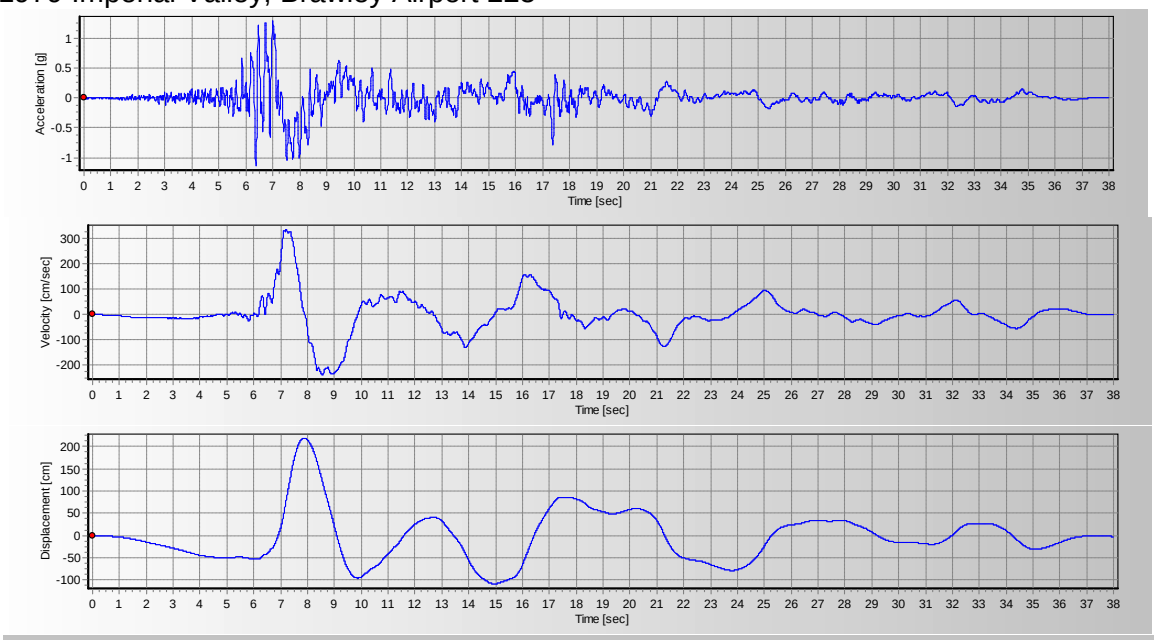

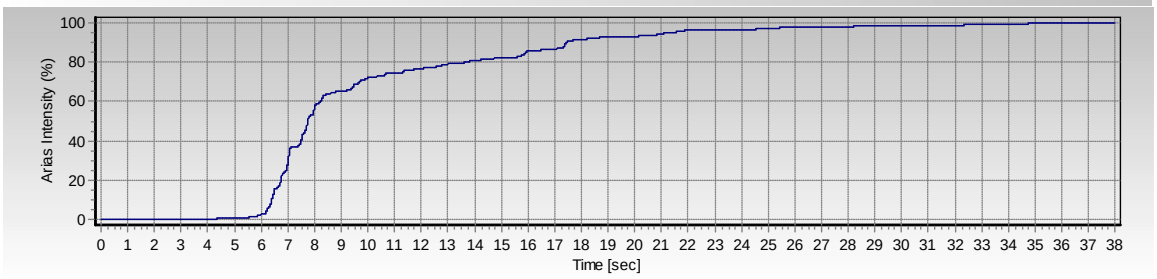

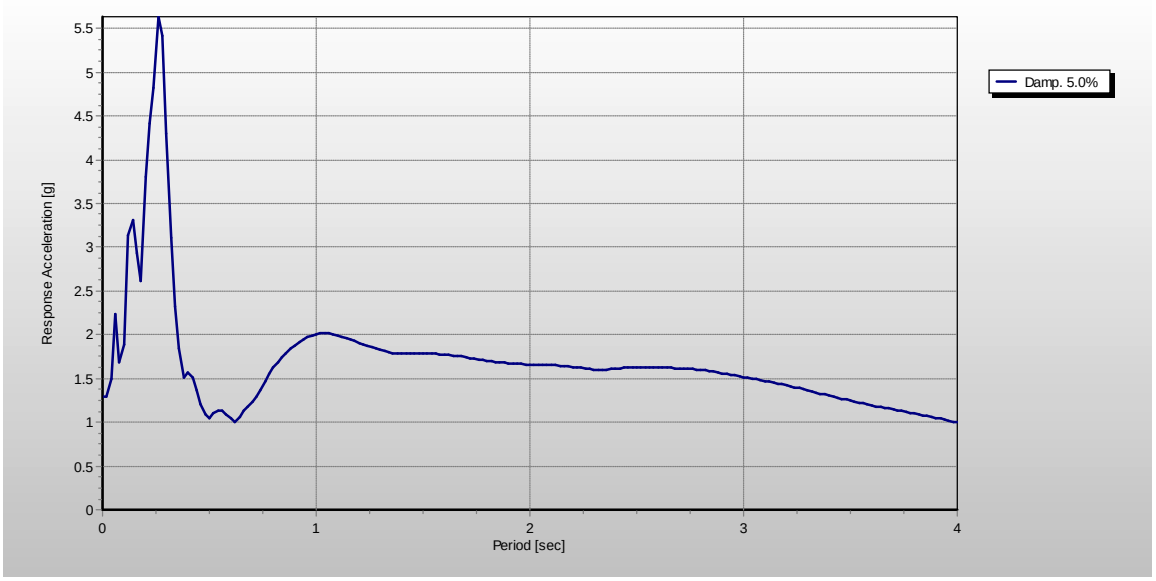

1994 Northridge, Sylmar – Conv Sta 052 scaled to 1.25x

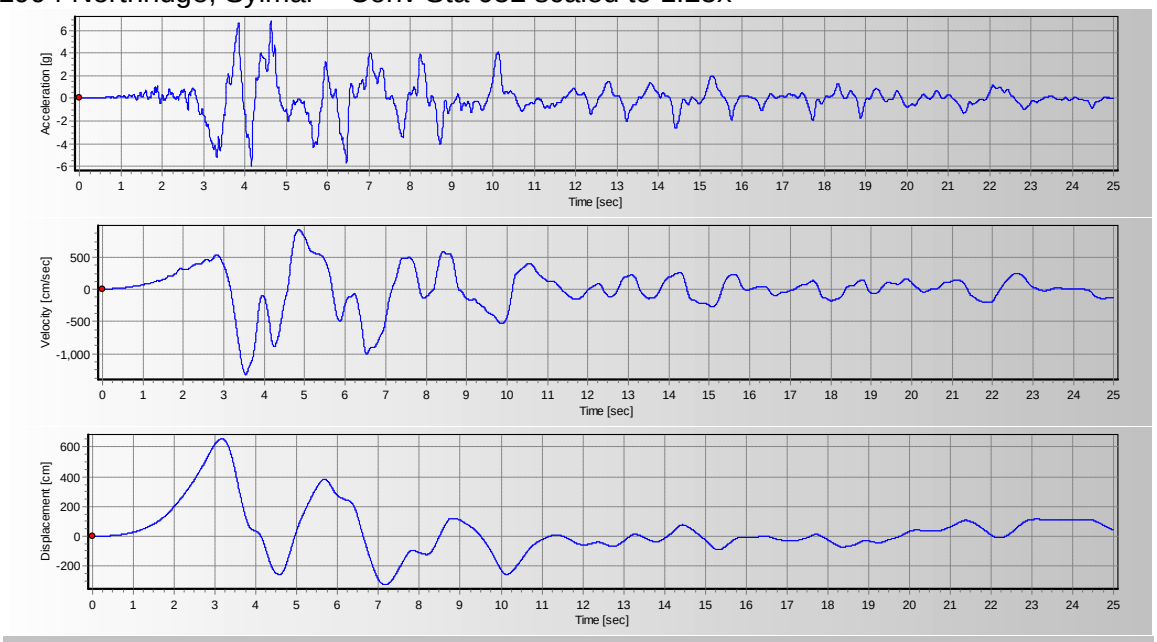

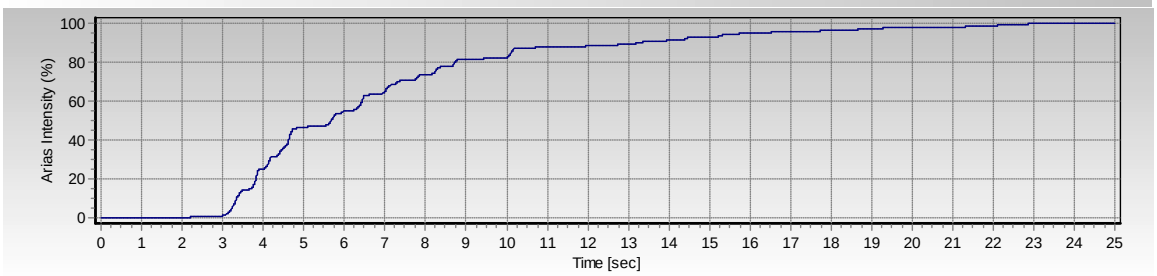

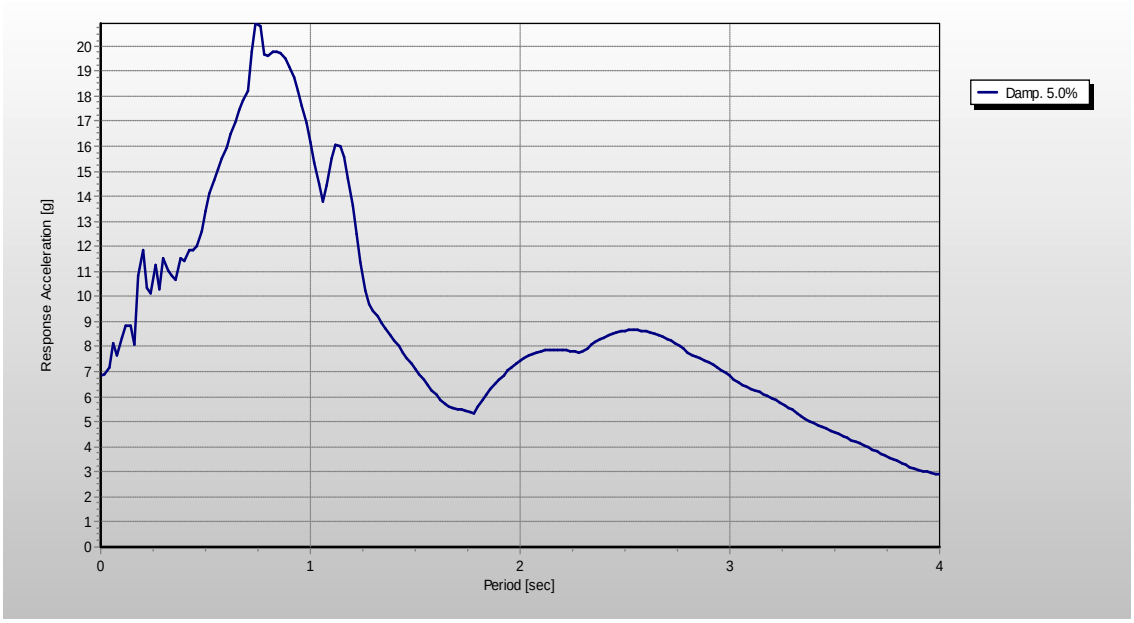

1987 Superstition Hills, Superstition Mountain Camera 045

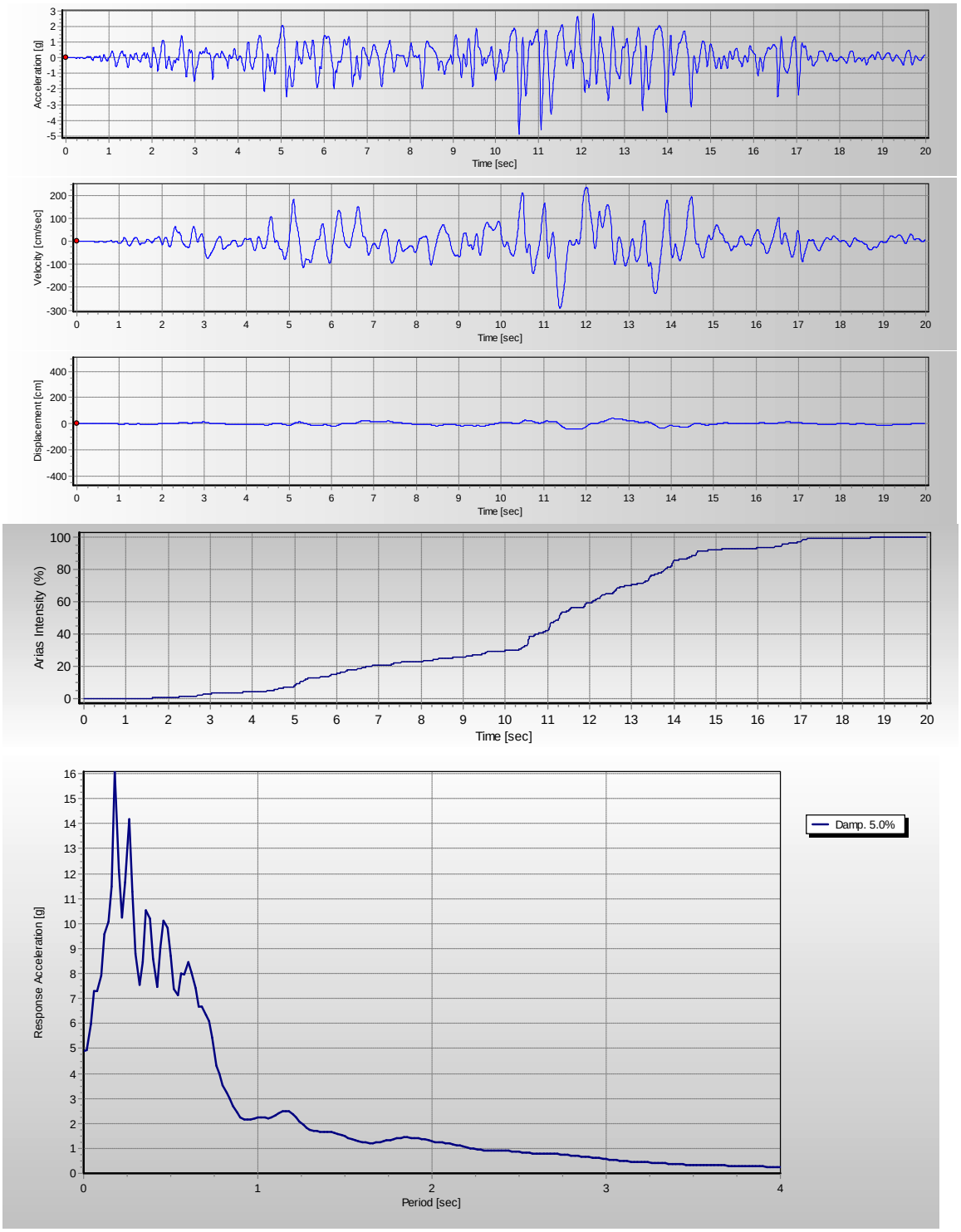

92 Landers, Joshua Tree 090 – Scaled by 0.75x

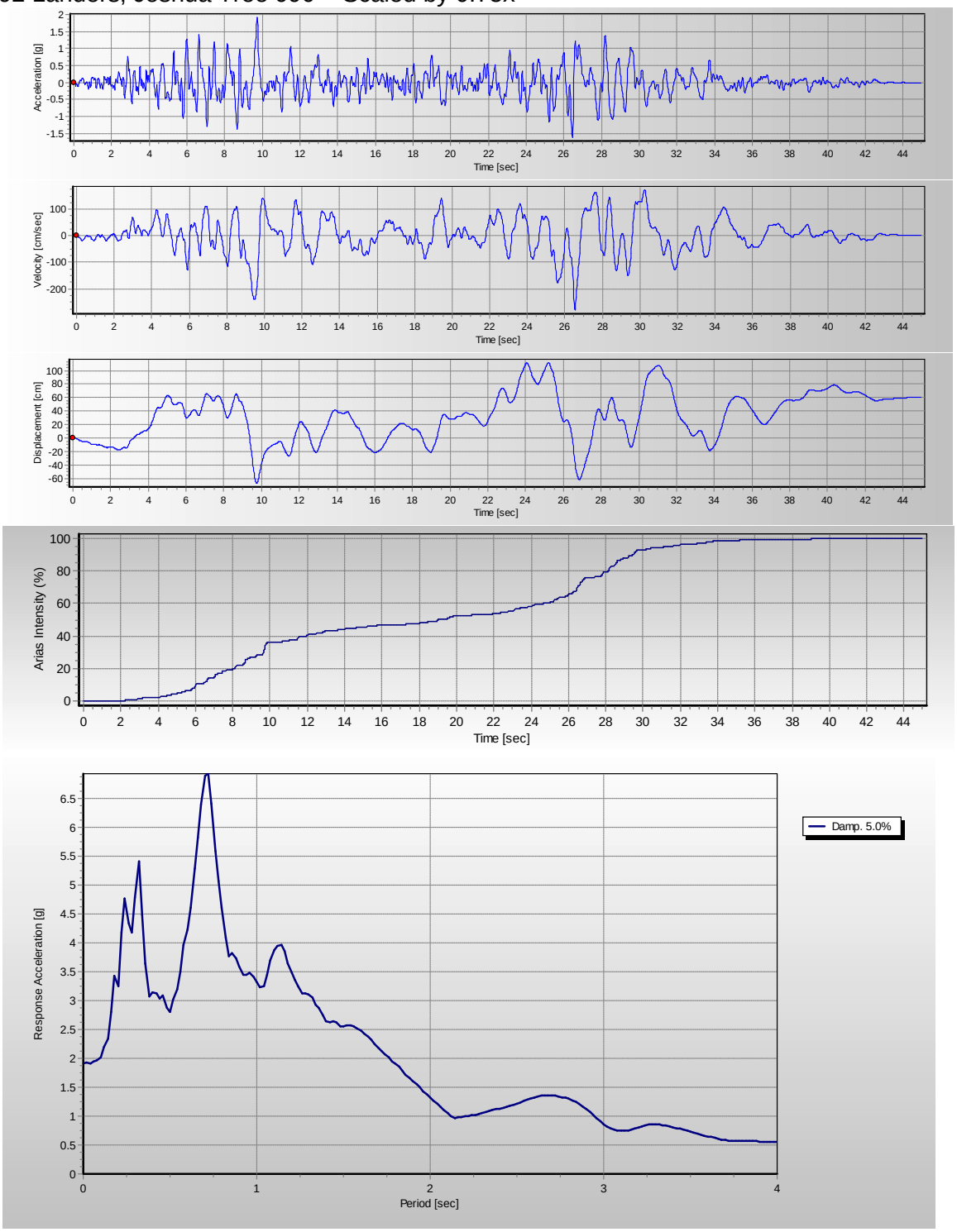

92 Landers, Joshua Tree 090 – Scaled by 1.0x

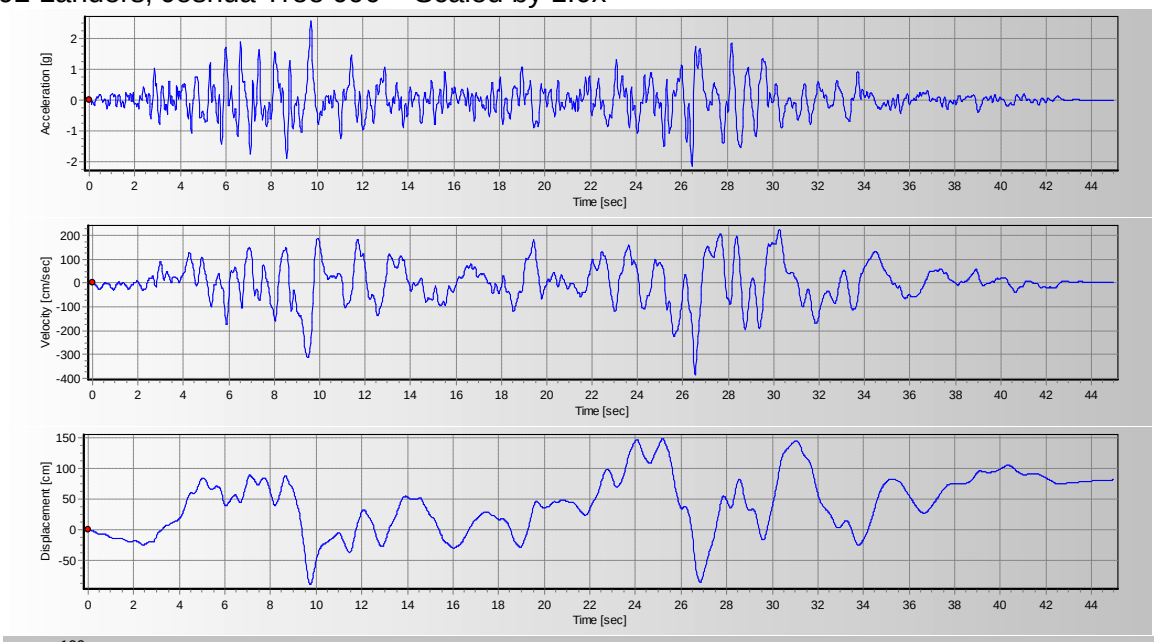

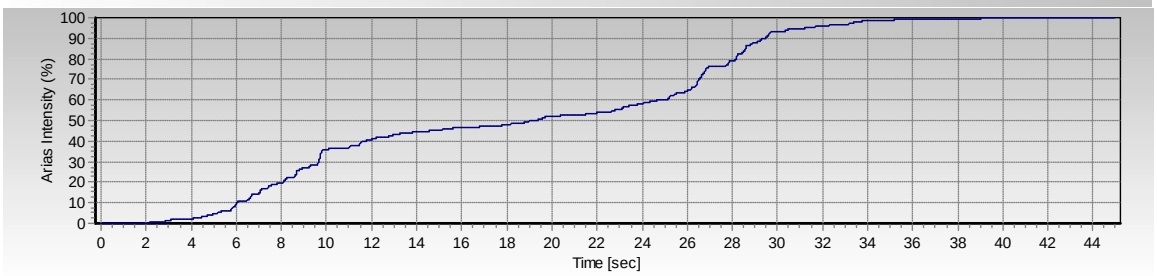

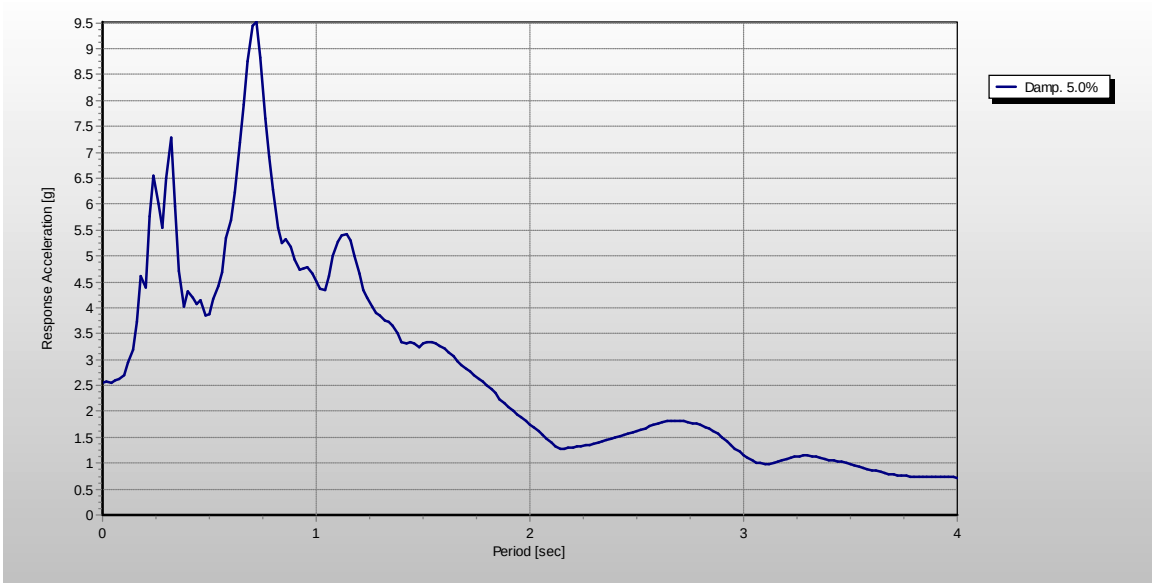

92 Landers, Joshua Tree 090 – Scaled by 1.5x

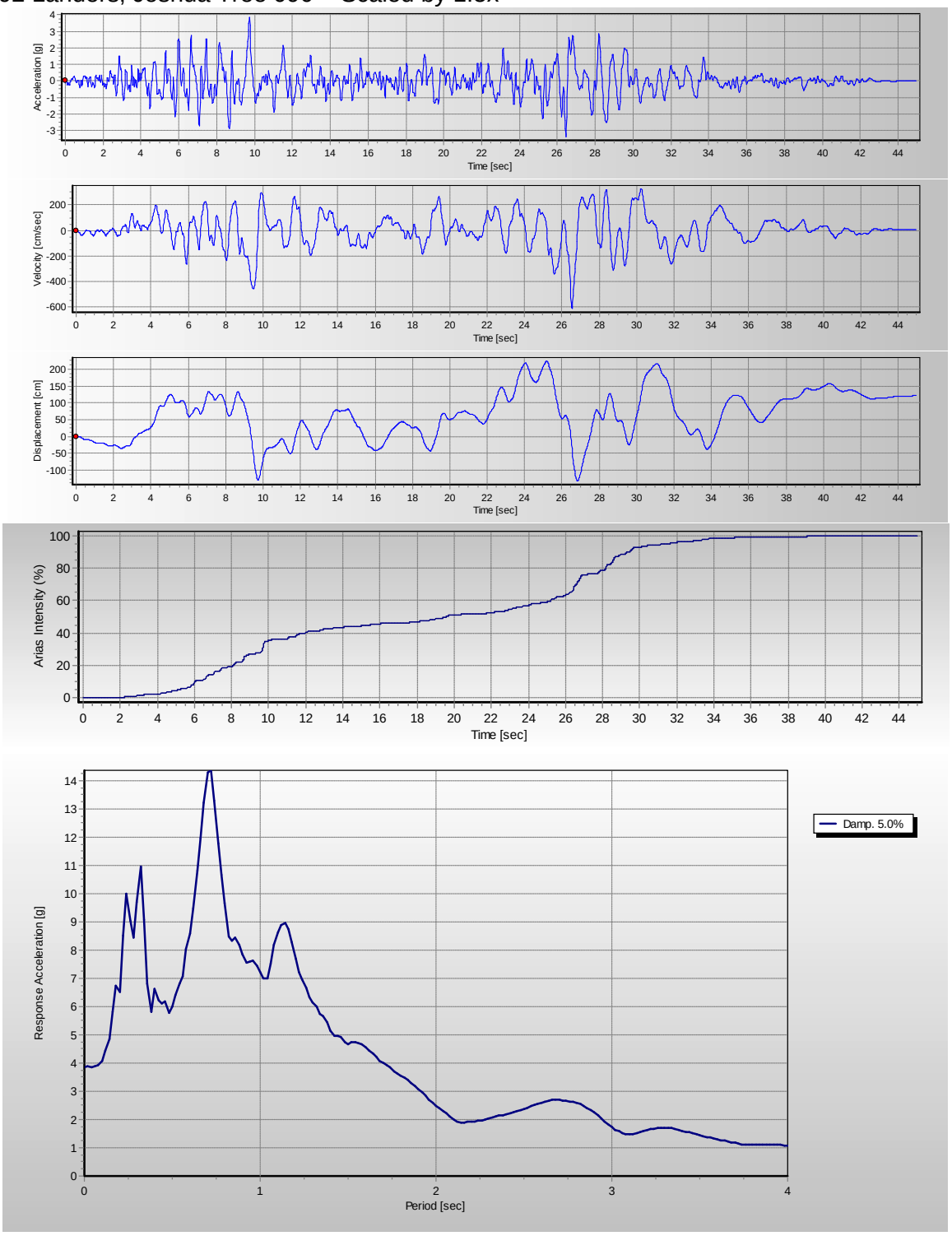

1992 Landers, Lucerne 260

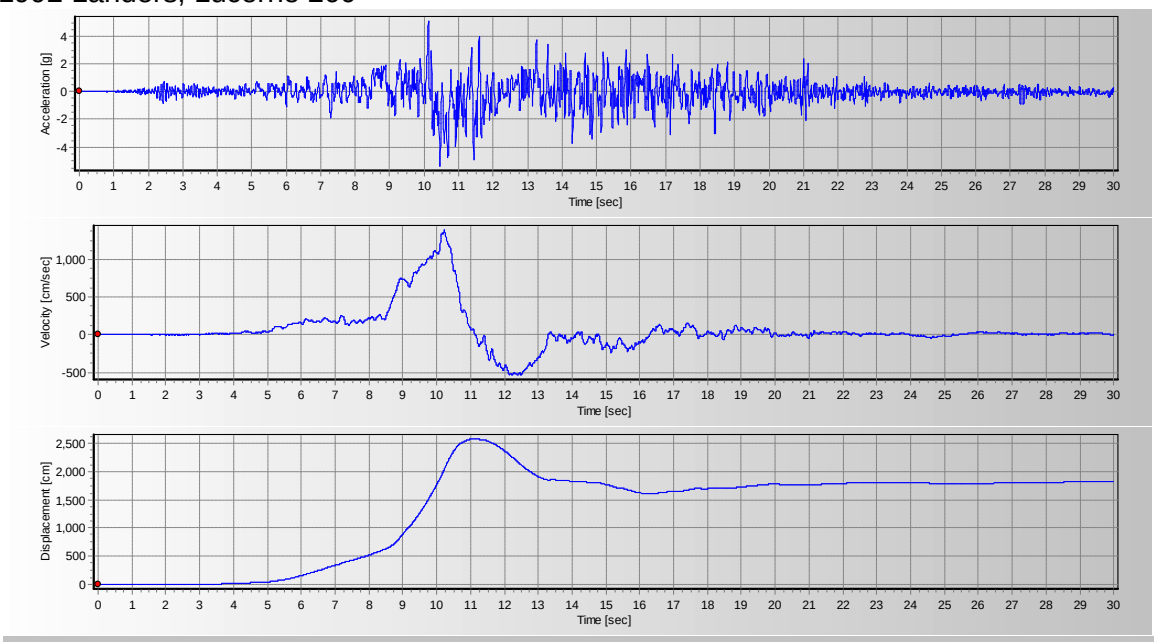

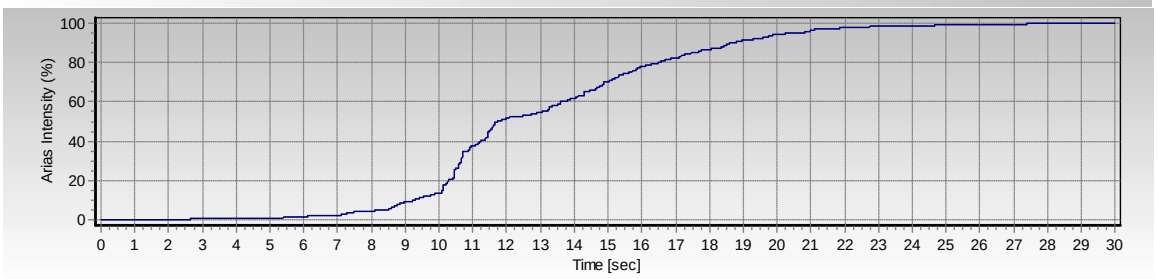

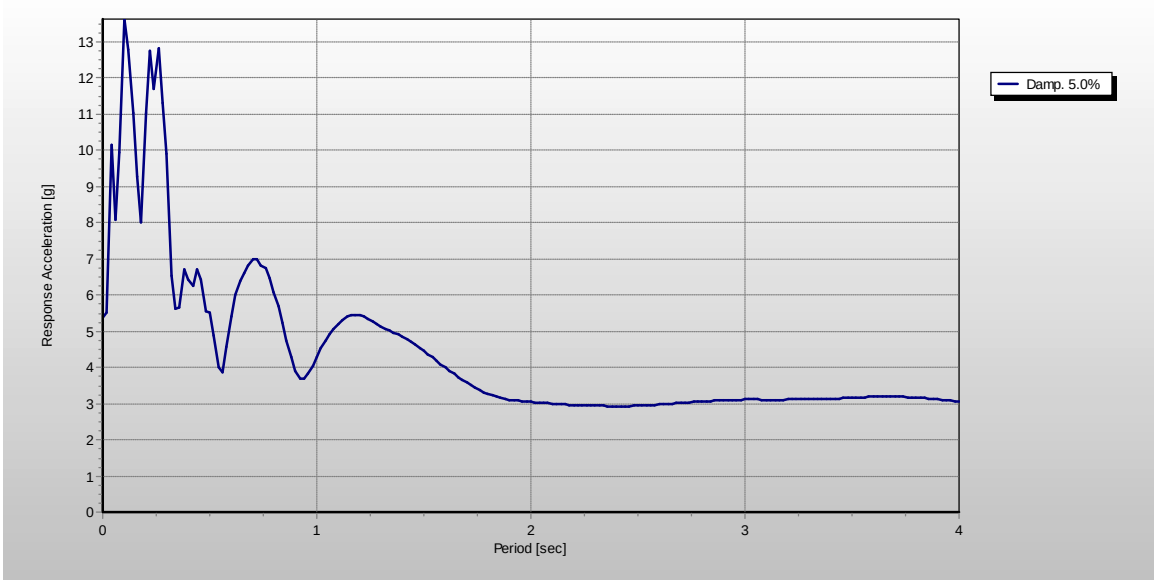

1989 Loma Prieta EQ, LGP

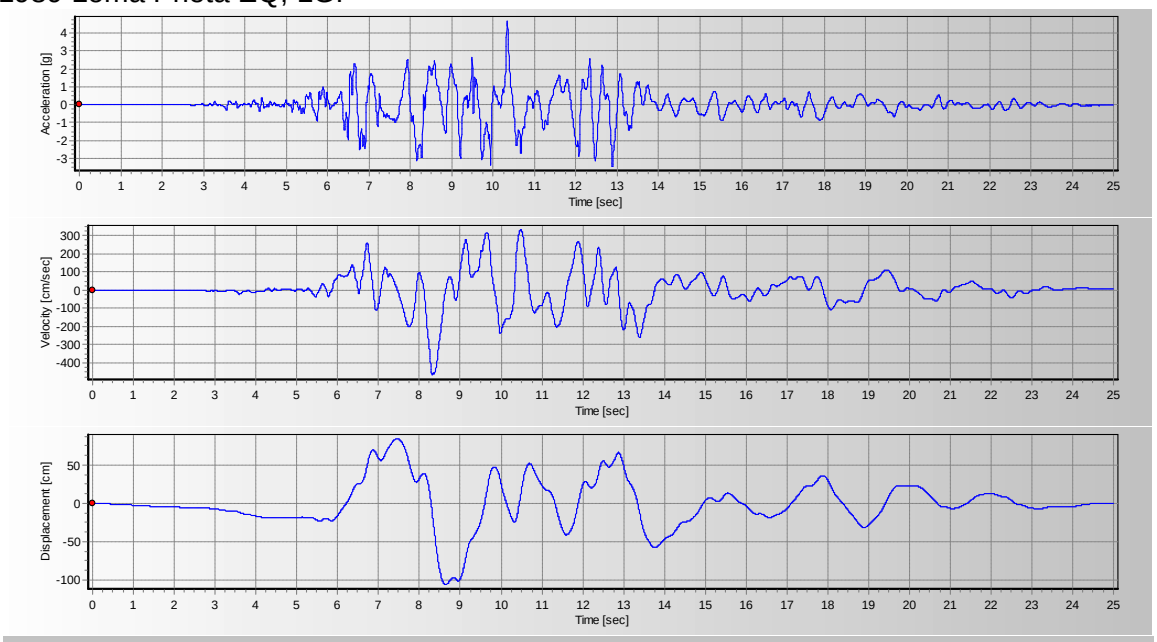

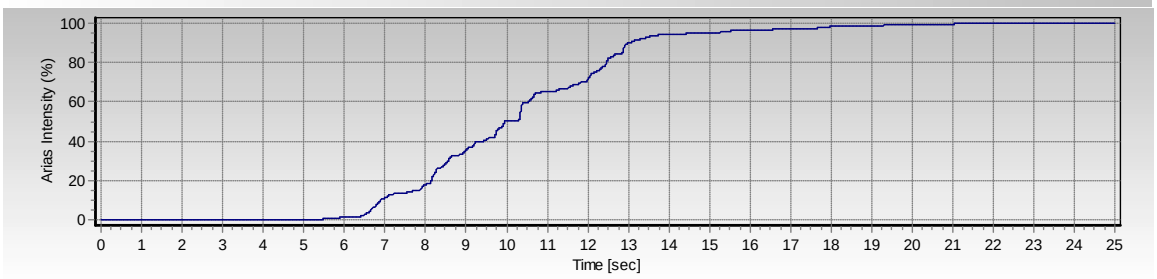

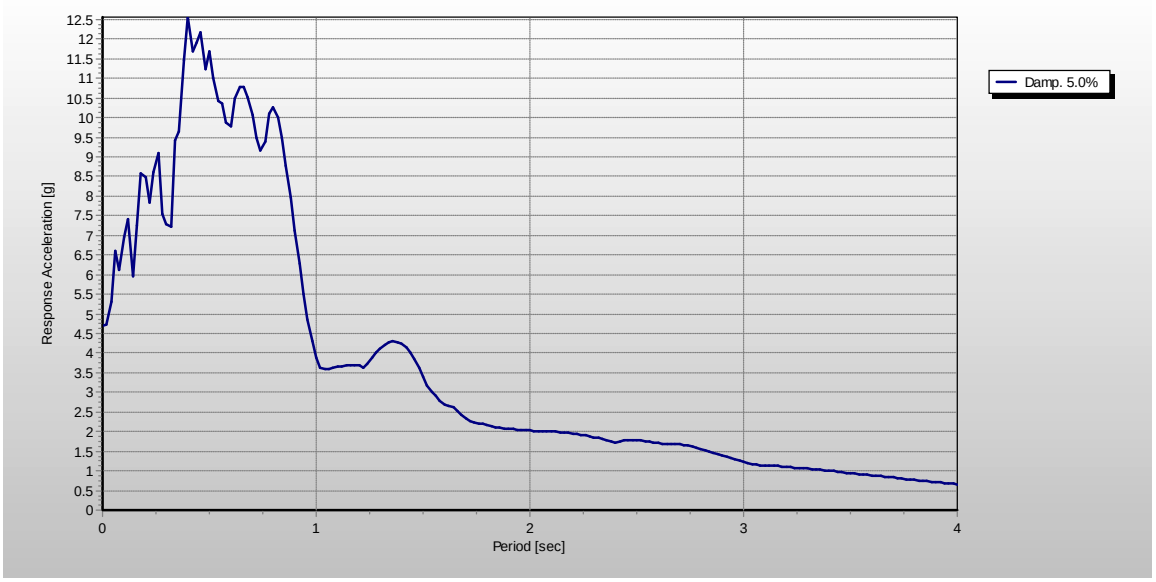

1971 San Fernando EQ, Hollywood Storage Facility,

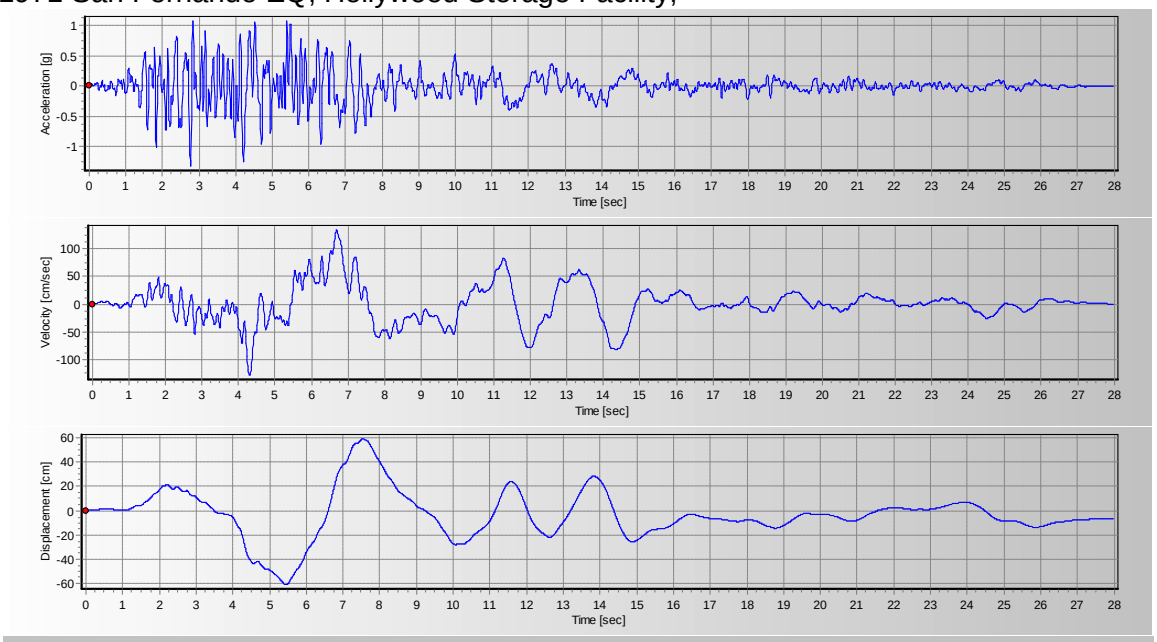

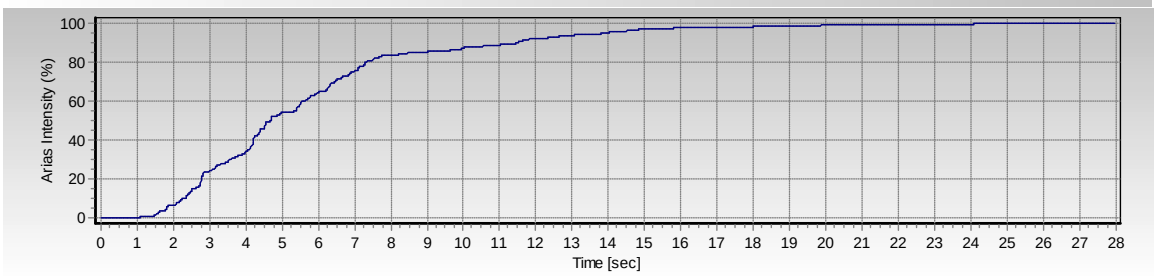

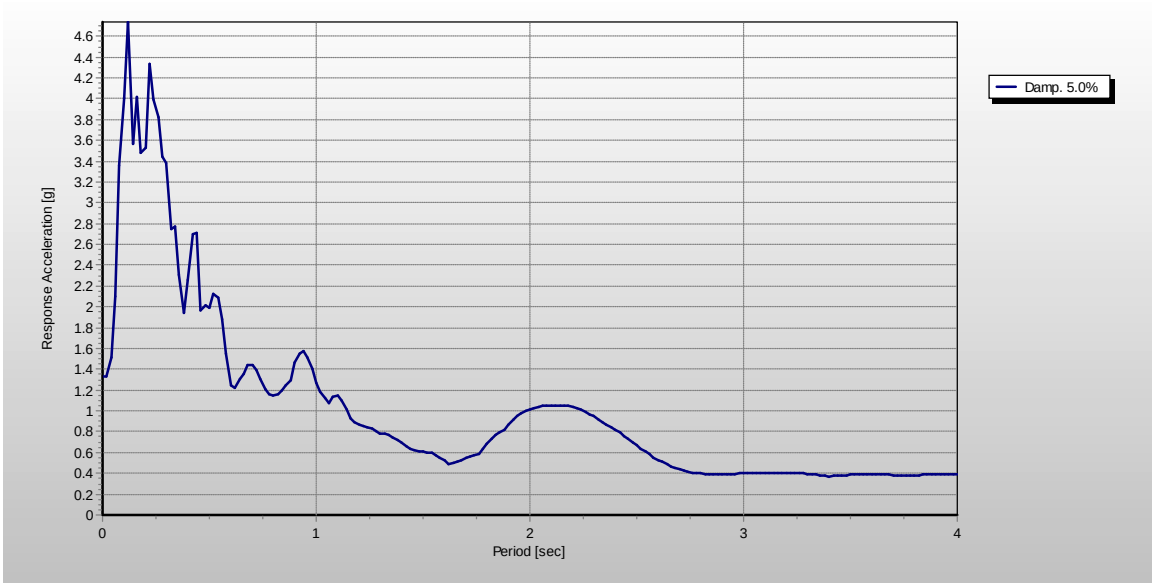

Superstition Hills, Parachute T S

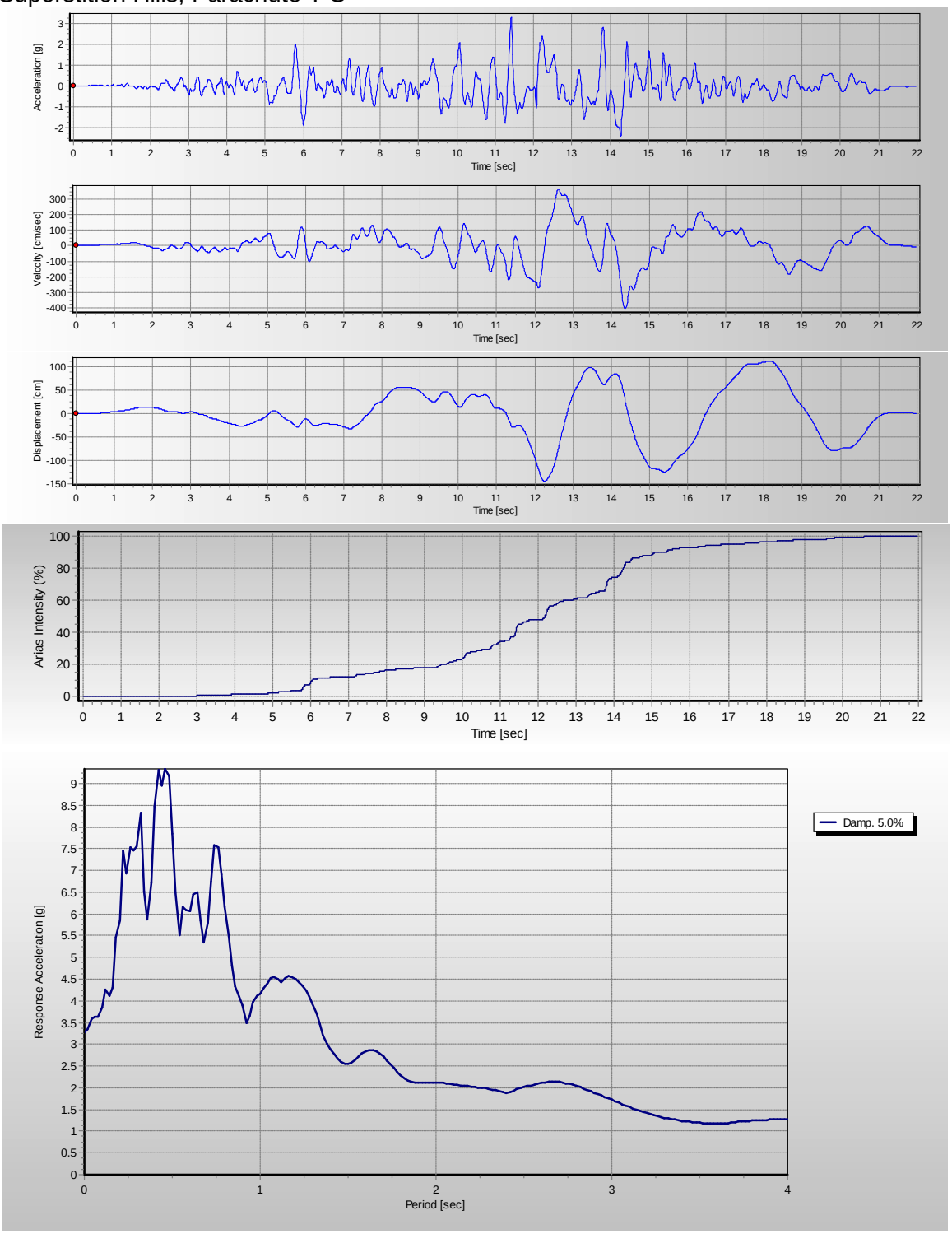

1994 Northridge, Rinaldi R Sta 228

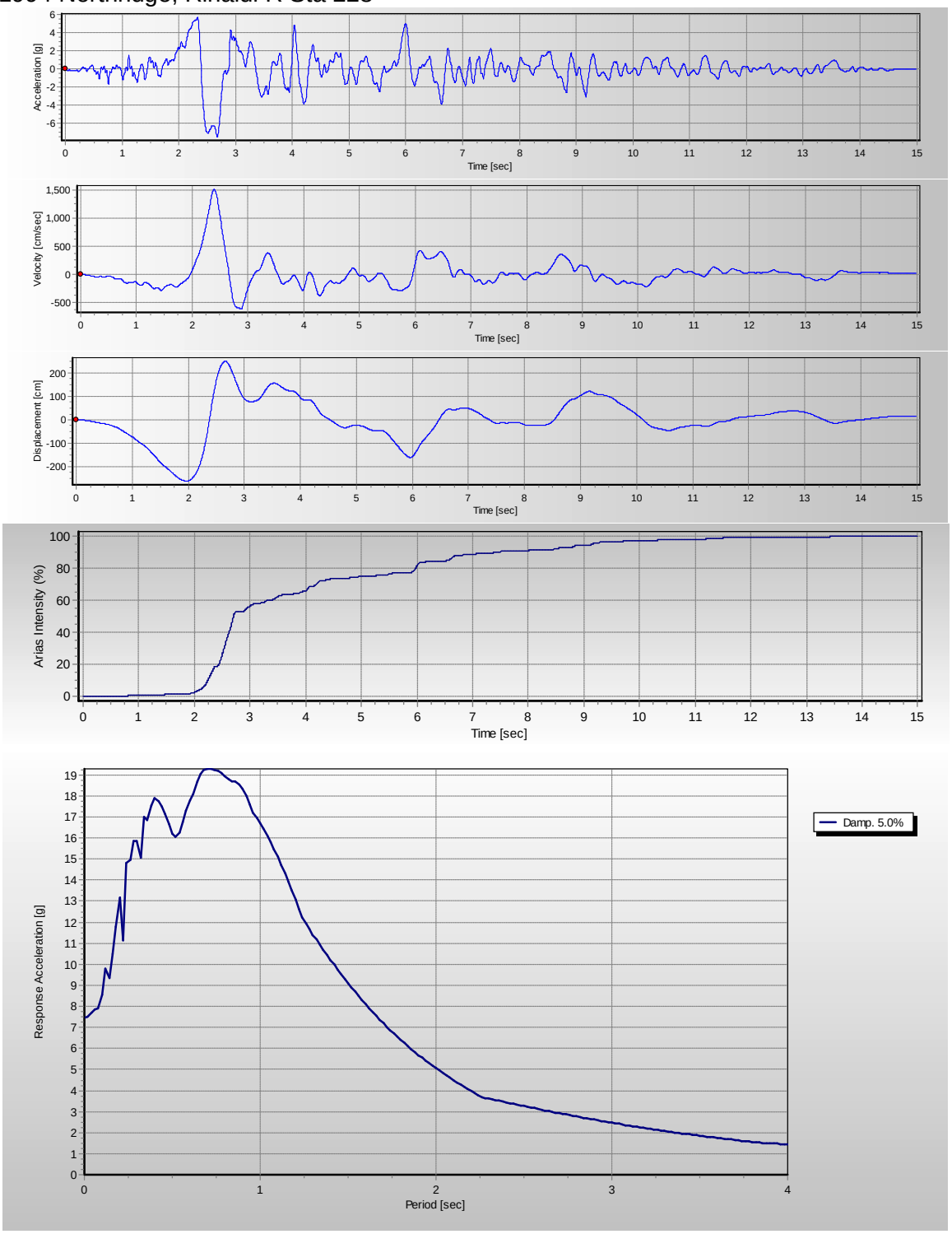

1994 Northridge, Sylmar – Conv Sta 052 scaled to 0.5x

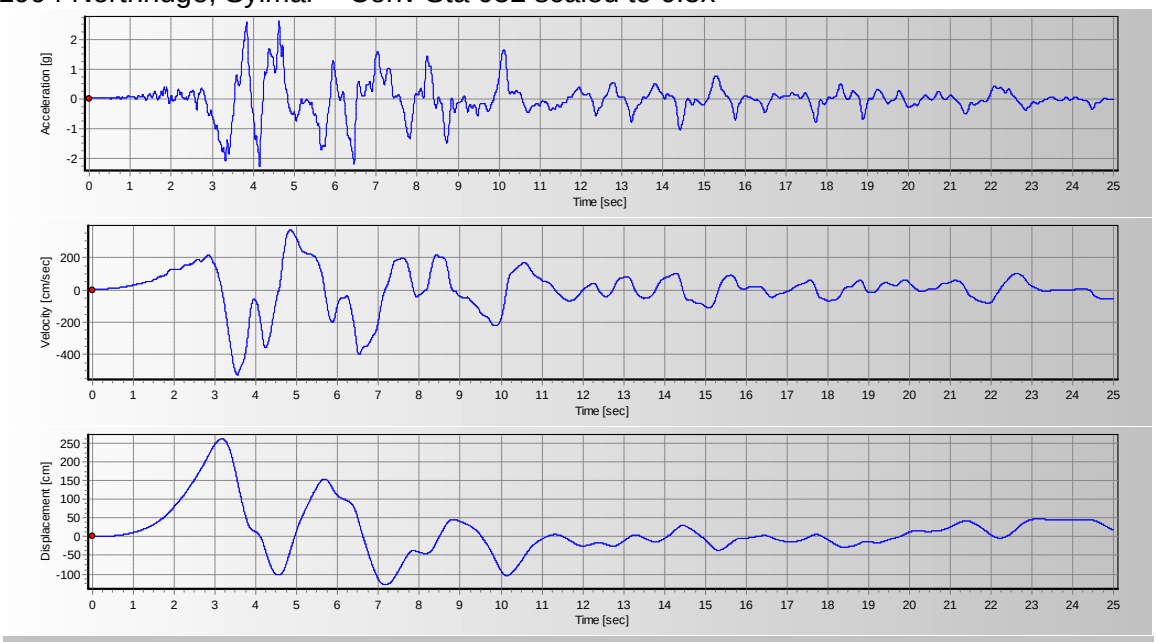

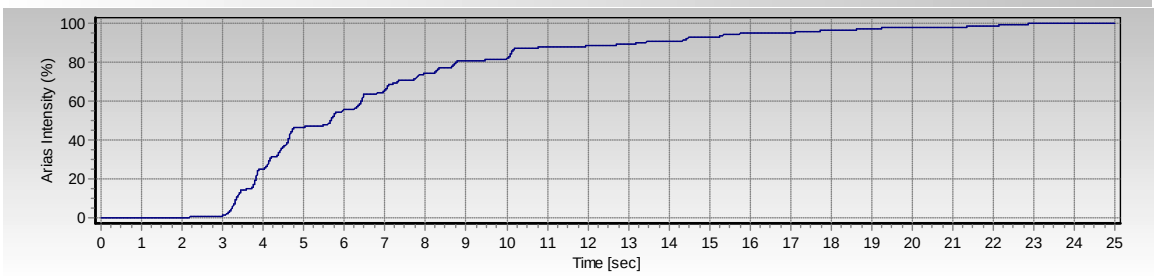

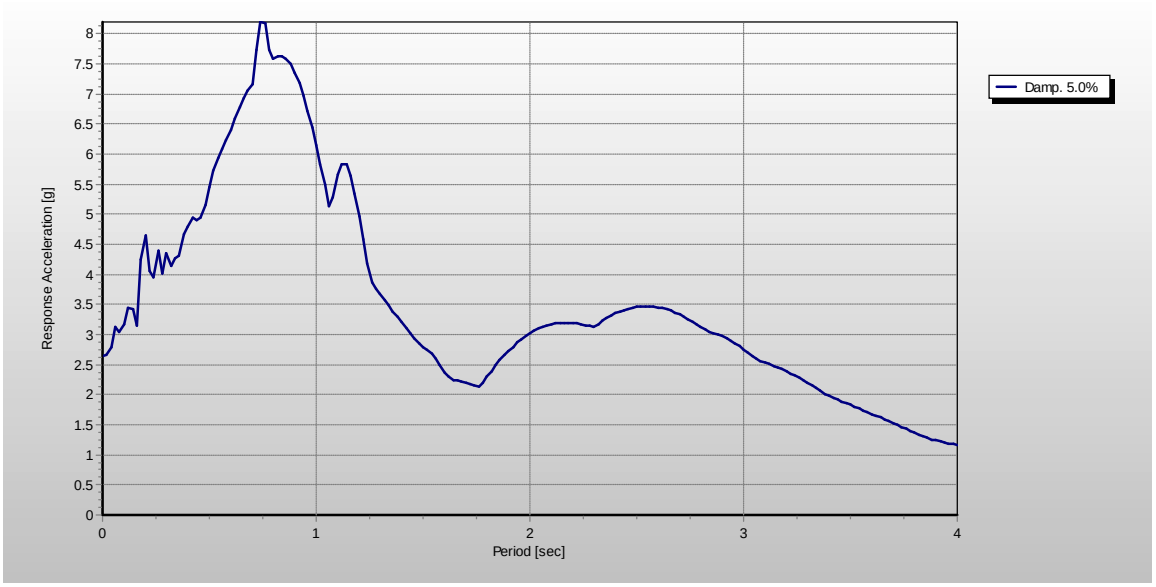

1994 Northridge, Sylmar – Conv Sta 052 scaled to 1.0x

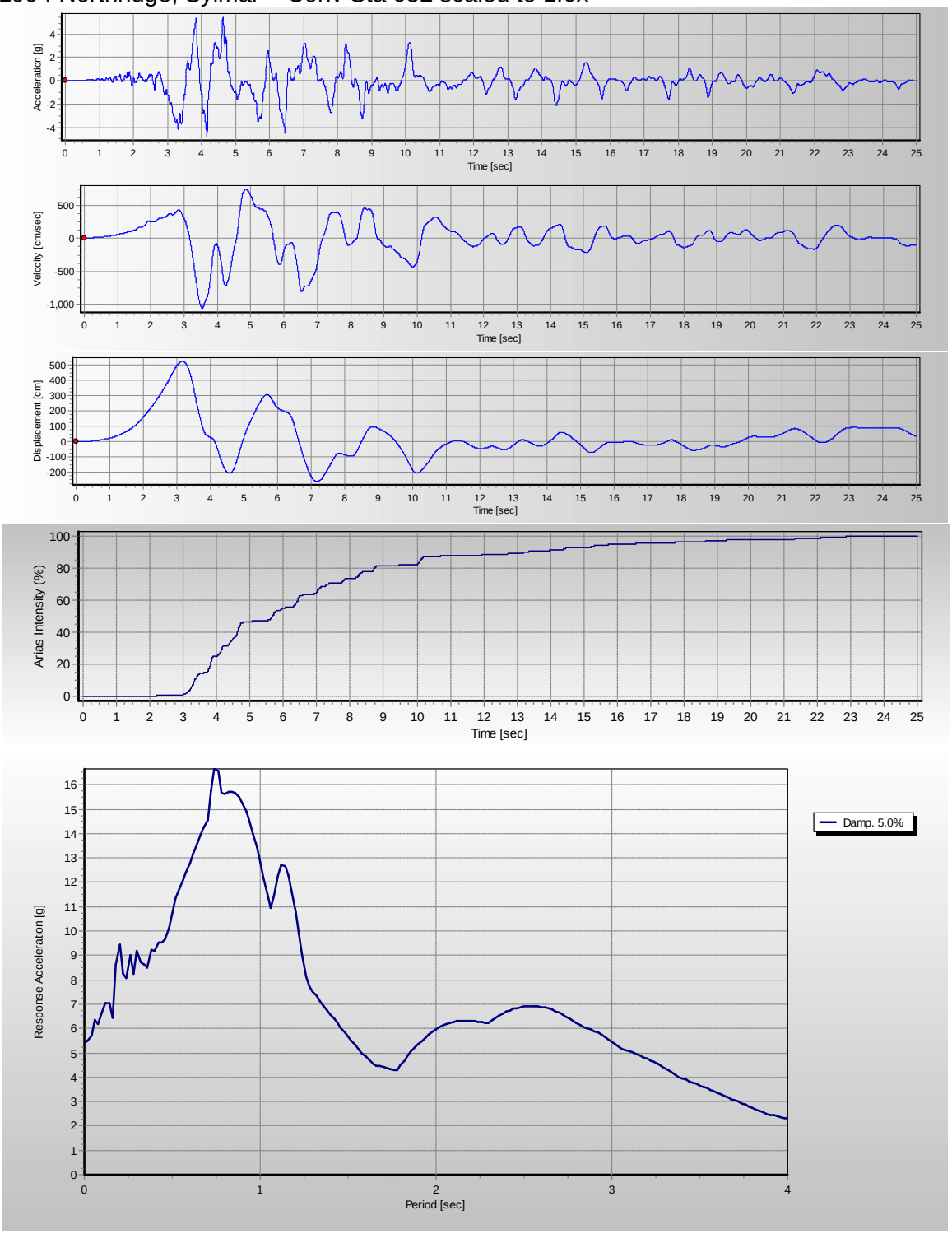

1994 Northridge, Sylmar – Conv Sta 052 scaled to 1.25x

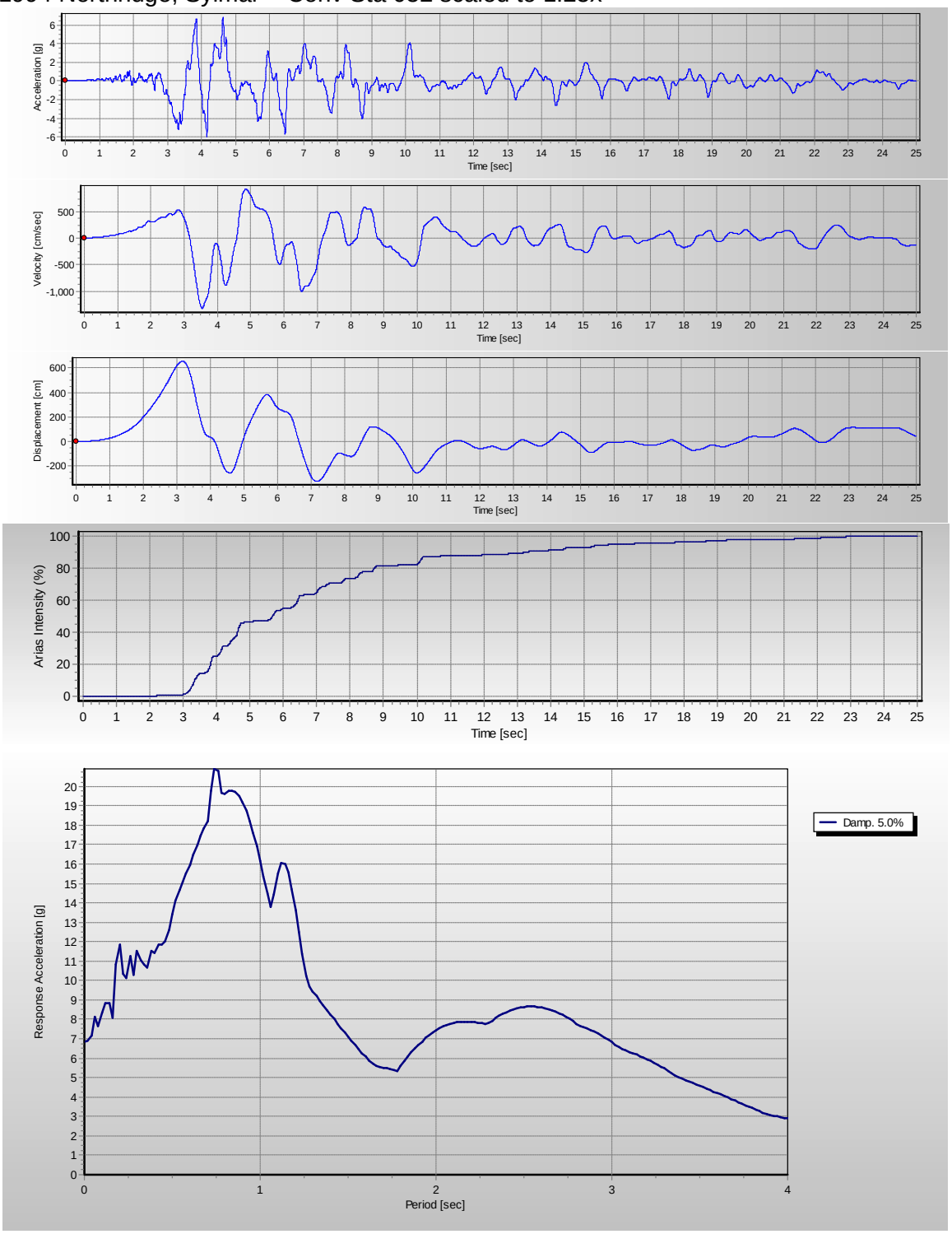

TCU078, 1999 Chi-Chi, Taiwan Earthquake

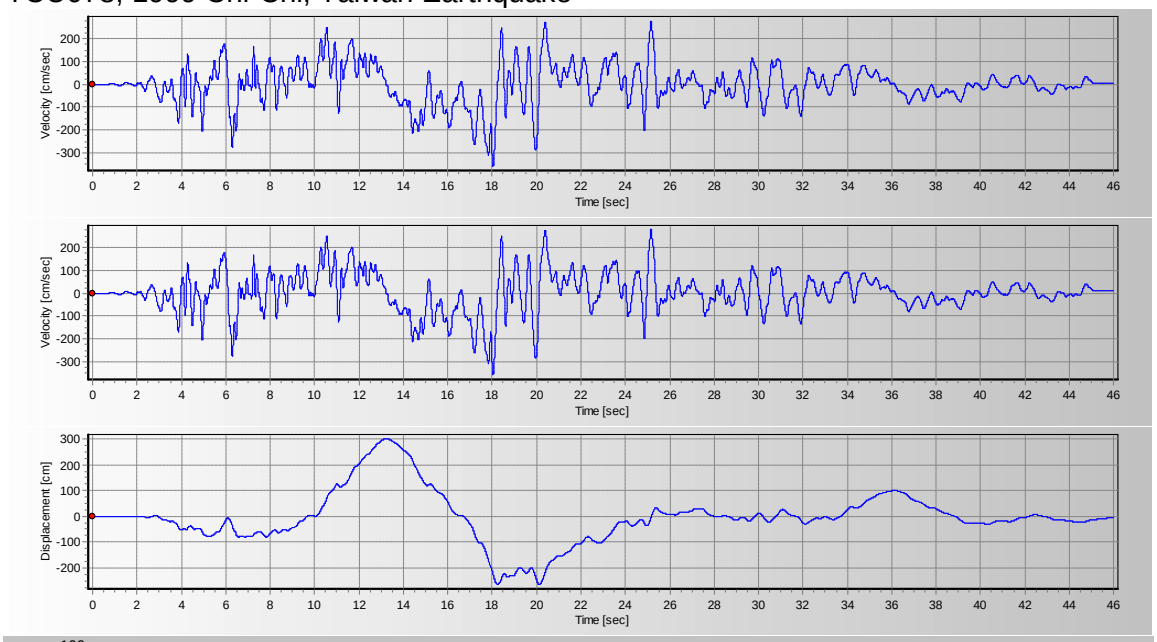

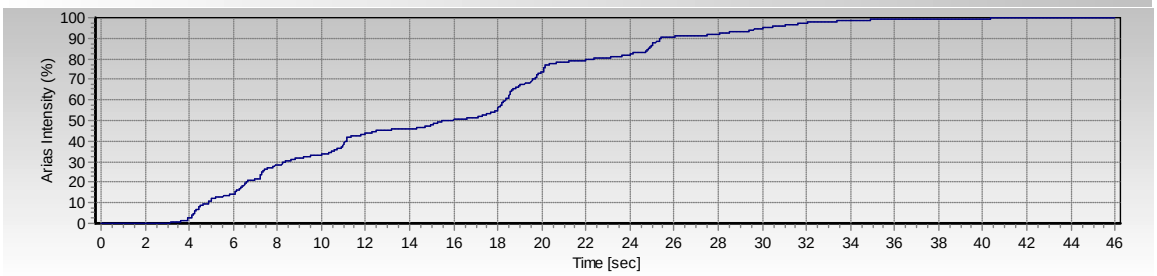

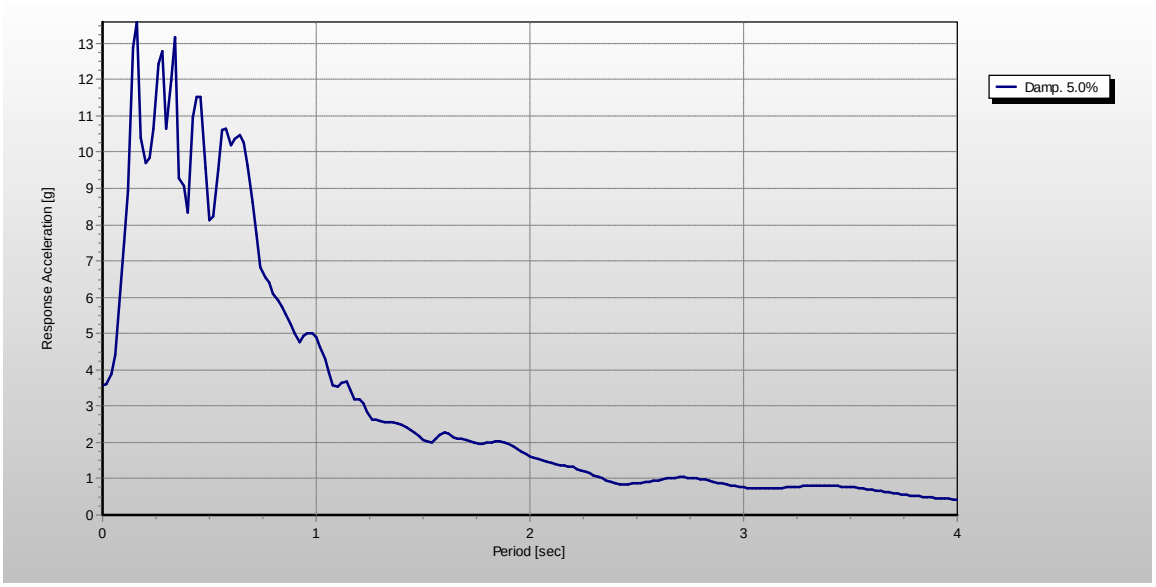

1994 Northridge EQ, Newhall W. Pico Canyon 046

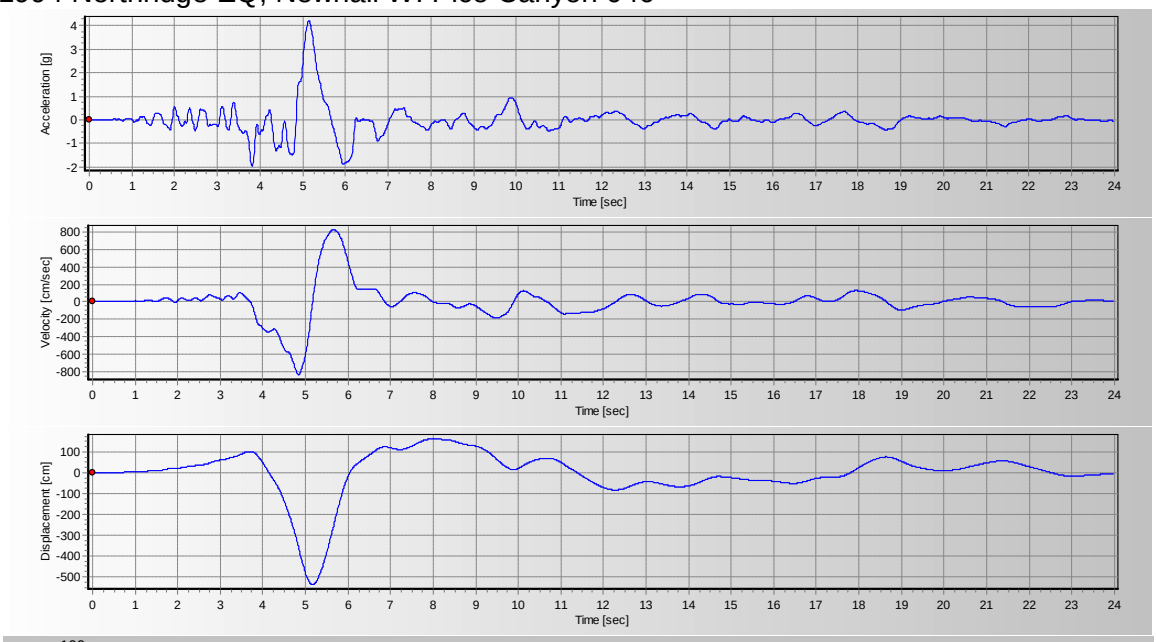

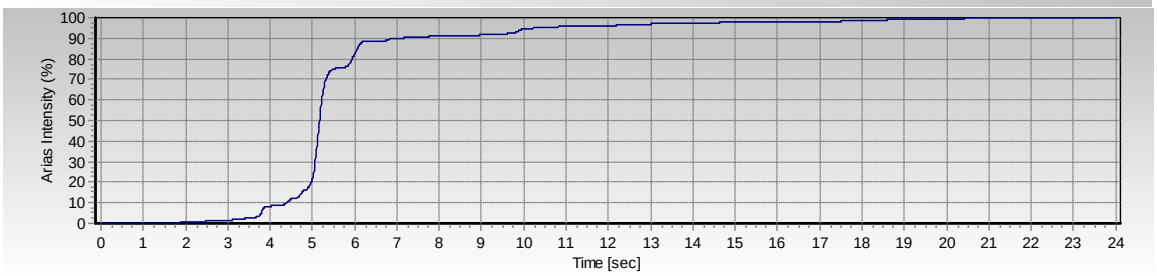

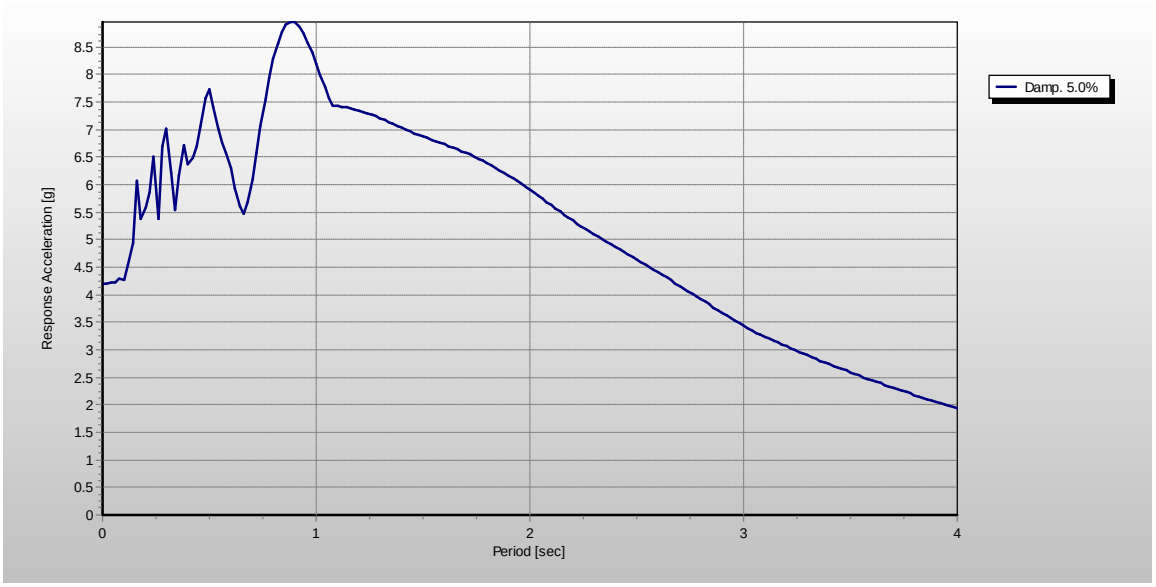

1989 Loma Prieta EQ, Saratoga WV Coll 270

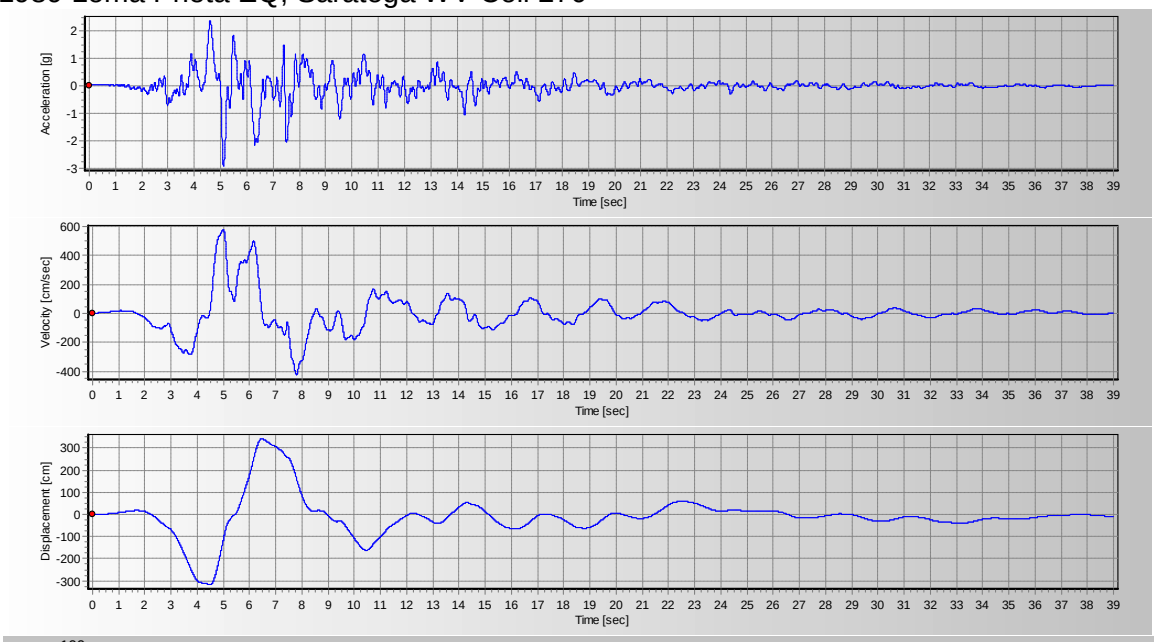

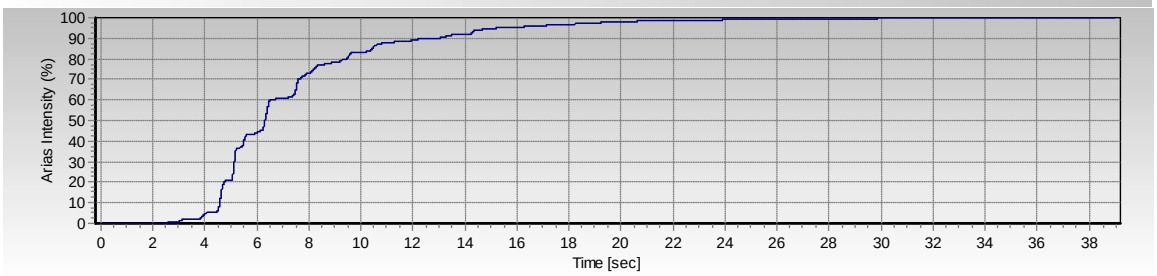

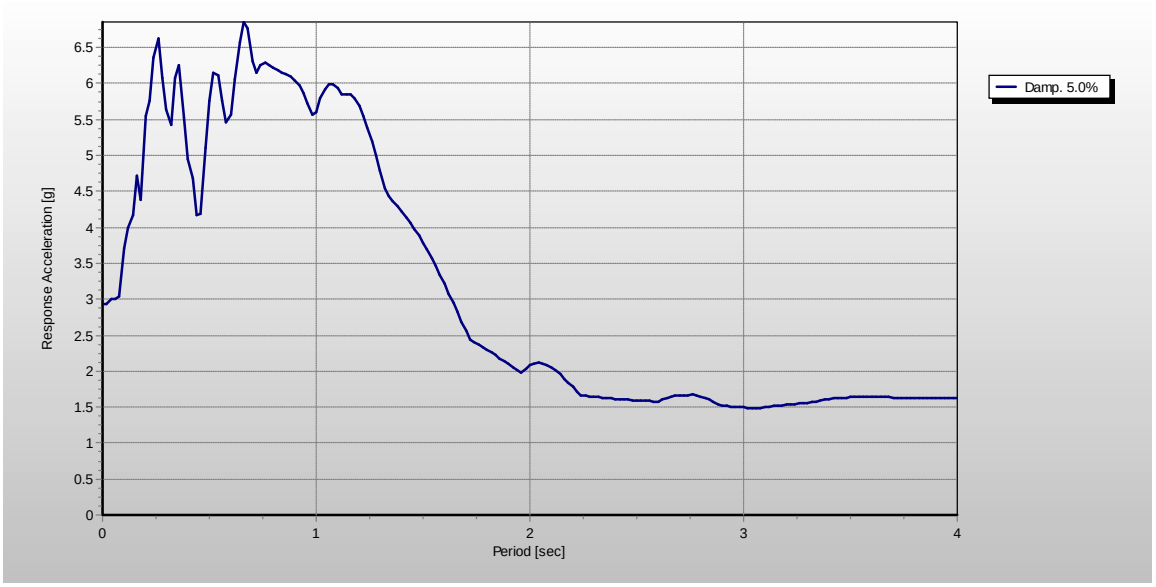

APPENDIX B: SENSITIVITY ANALYSIS X-DISPLACEMENT DATA

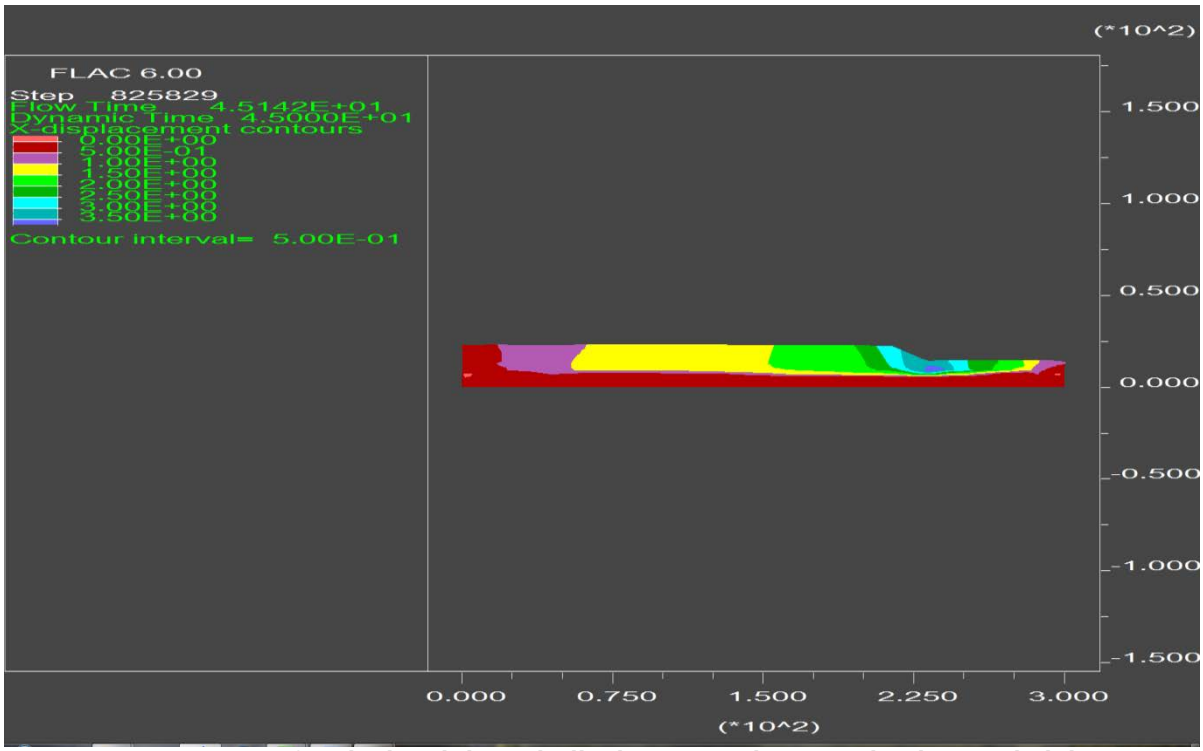

Figure B.1. Contours of calculated lateral displacement (9 m embankment height, 8 meter liquefiable silt layer, clean sand corrected $(N_1)_{60\text{-}cs}$ blow count of 8, ground motion = 92 Landers Joshua Tree 090 Scale 1.0x).

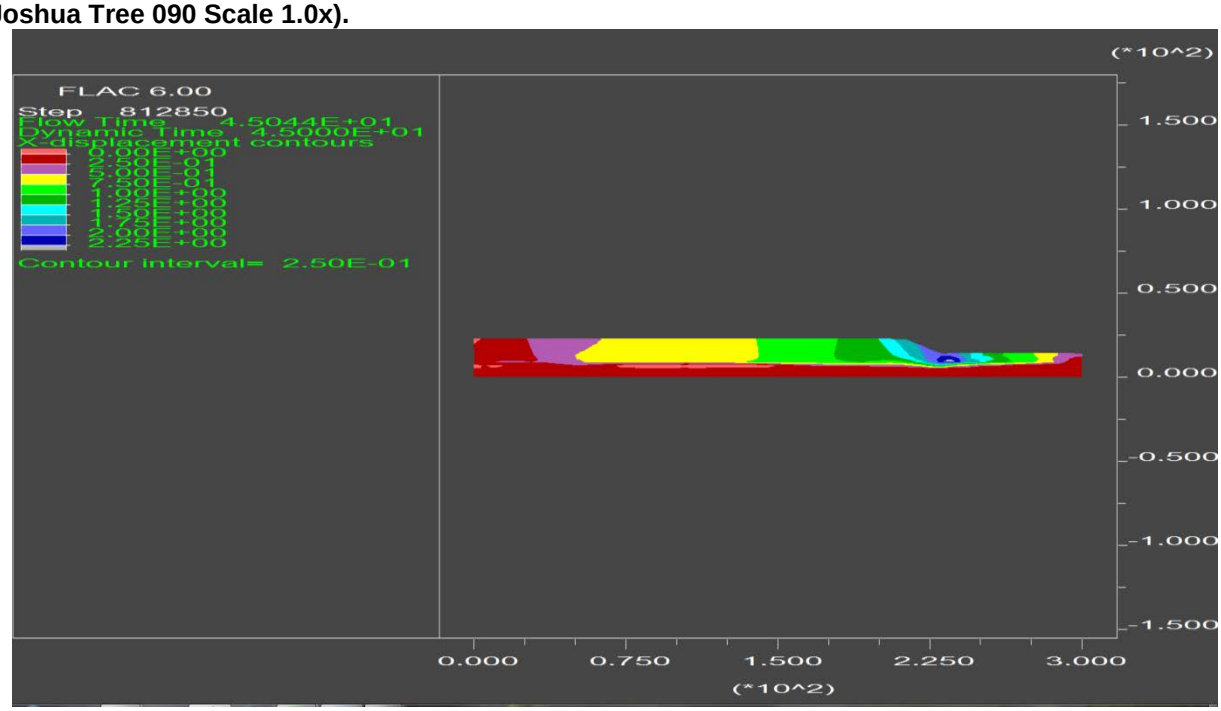

Figure B.2. Contours of calculated lateral displacement (9 m embankment height, 8 meter liquefiable silt layer, clean sand corrected $(N_1)_{60\text{-}cs}$ blow count of 15, ground motion = 92 Landers Joshua Tree 090 Scale 1.0x).

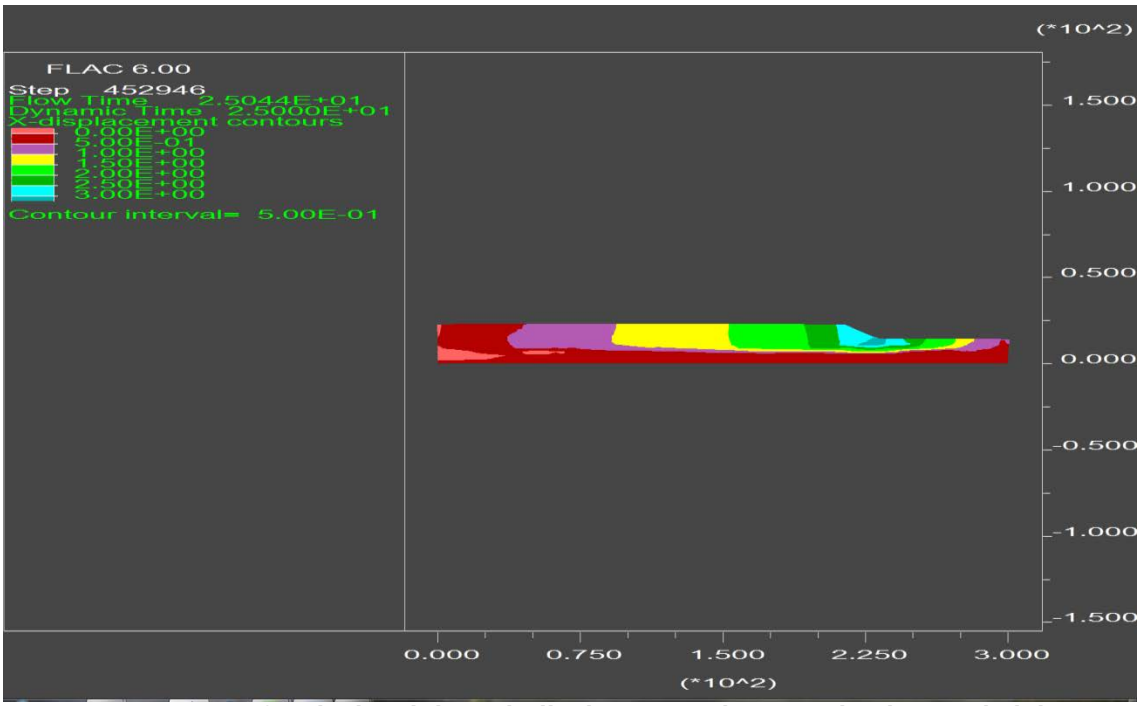

Figure B.3. Contours of calculated lateral displacement (9 m embankment height, 8 meter liquefiable silt layer, clean sand corrected $(N_1)_{60\text{-}cs}$ blow count of 15, ground motion = 94 Northridge Sylmar - Conv Sta 052 Scale 1.0x).

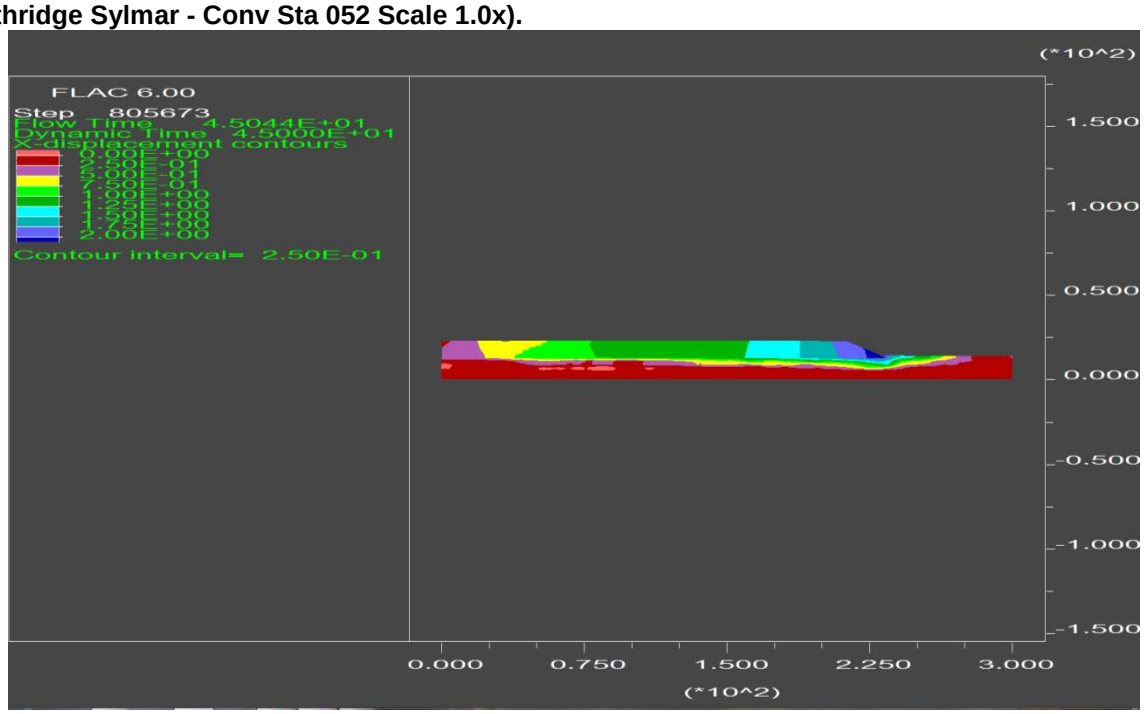

Figure B.4. Contours of calculated lateral displacement (9 m embankment height, 8 meter liquefiable sand layer, corrected $(N_1)_{60}$ blow count of 12, ground motion = 92 Landers Joshua Tree 090 Scale 1.0x).

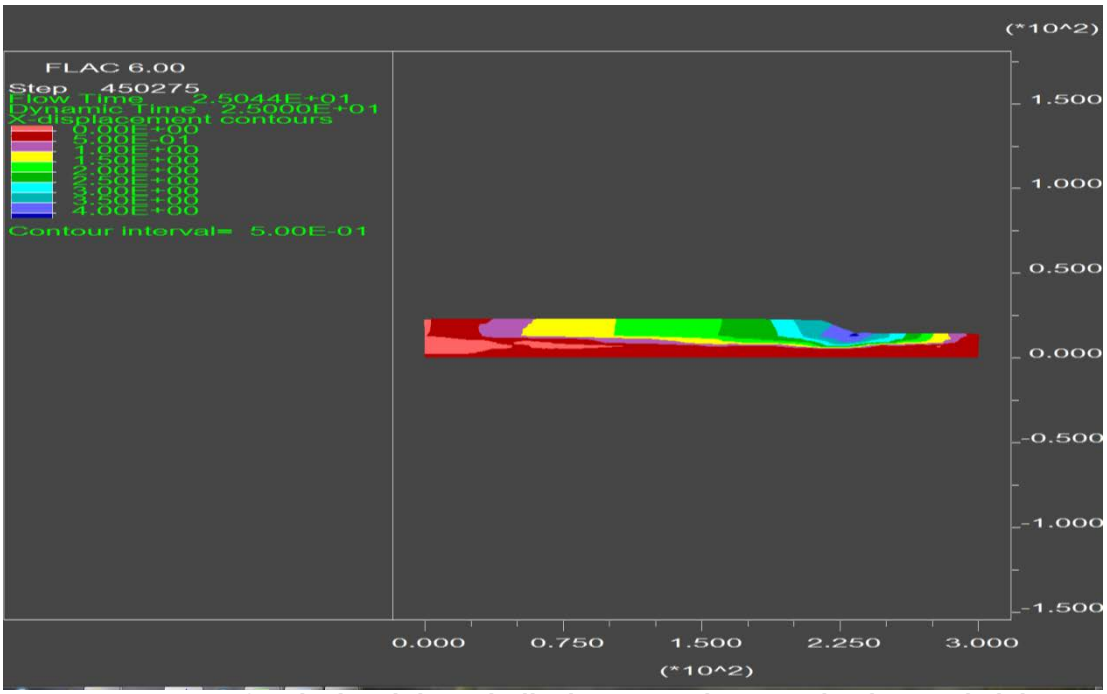

Figure B.5. Contours of calculated lateral displacement (9 m embankment height, 8 meter liquefiable sand layer, corrected $(N_1)_{60}$ blow count of 12, ground motion = 94 Northridge Sylmar - Conv Sta 052 Scale 1.0x).

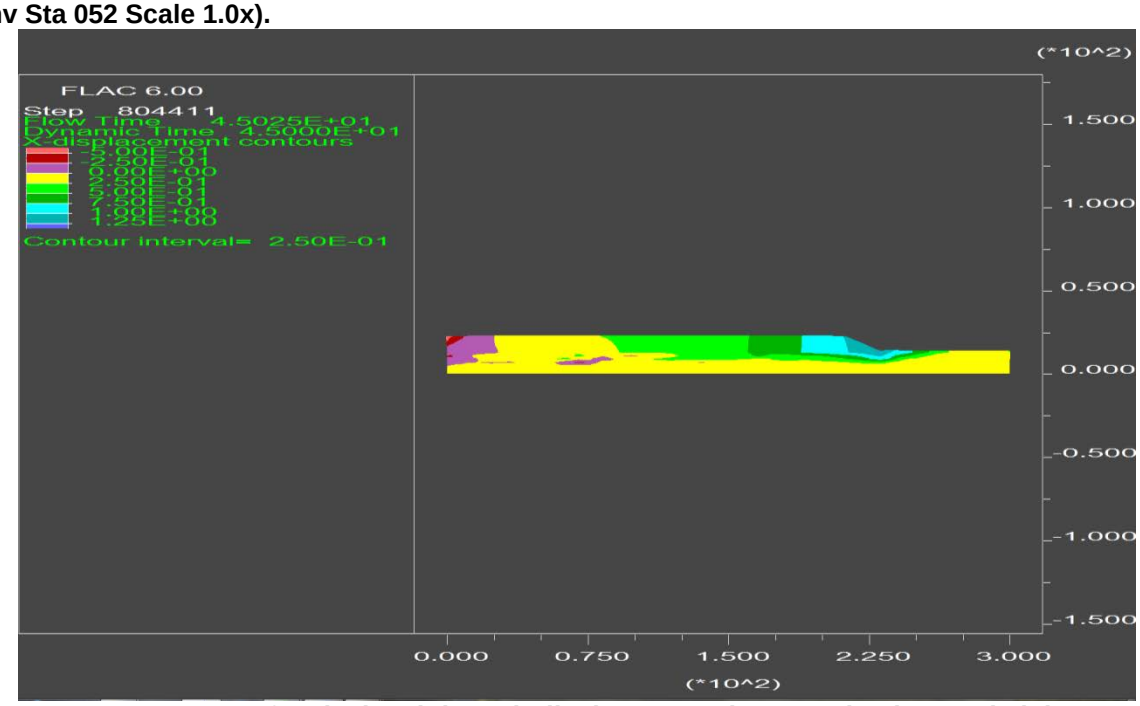

Figure B.6. Contours of calculated lateral displacement (9 m embankment height, 8 meter liquefiable sand layer, corrected $(N_1)_{60}$ blow count of 20, ground motion = 92 Landers Joshua Tree 090 Scale 1.0x).

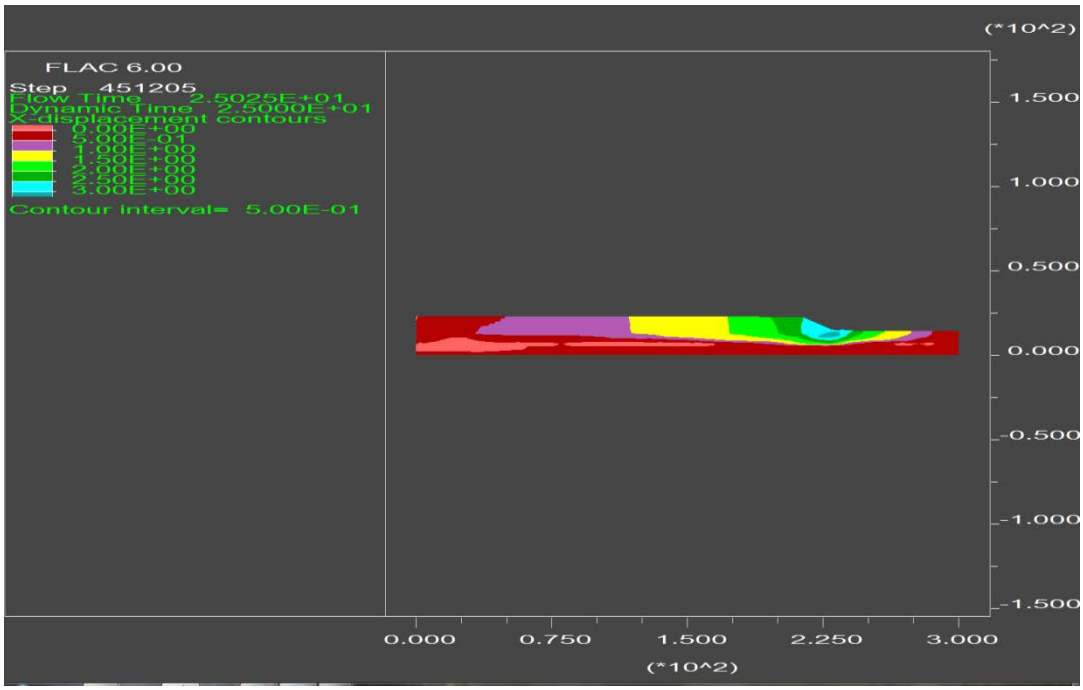

Figure B.7. Contours of calculated lateral displacement (9 m embankment height, 8 meter liquefiable sand layer, corrected $(N_1)_{60}$ blow count of 20, ground motion = 94 Northridge Sylmar - Conv Sta 052 Scale 1.0x).

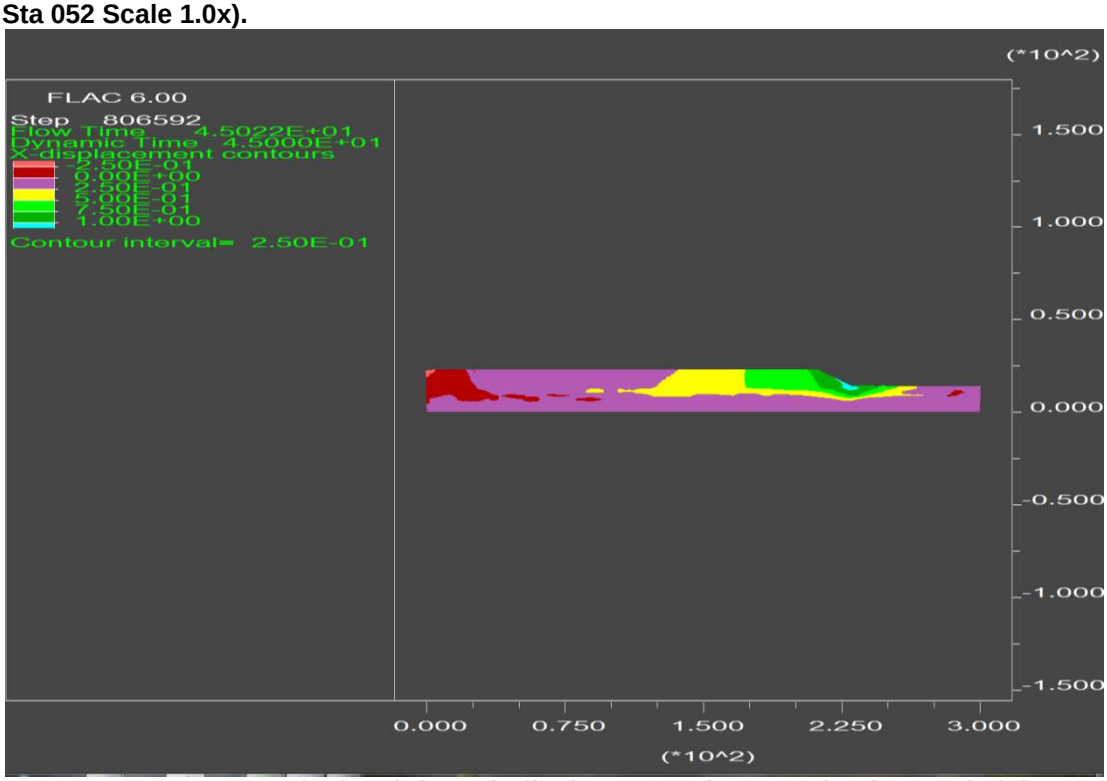

Figure B.8. Contours of calculated lateral displacement (9 m embankment height, 8 meter liquefiable sand layer, corrected $(N_1)_{60}$ blow count of 25, ground motion = 92 Landers Joshua Tree 090 Scale 1.0x).

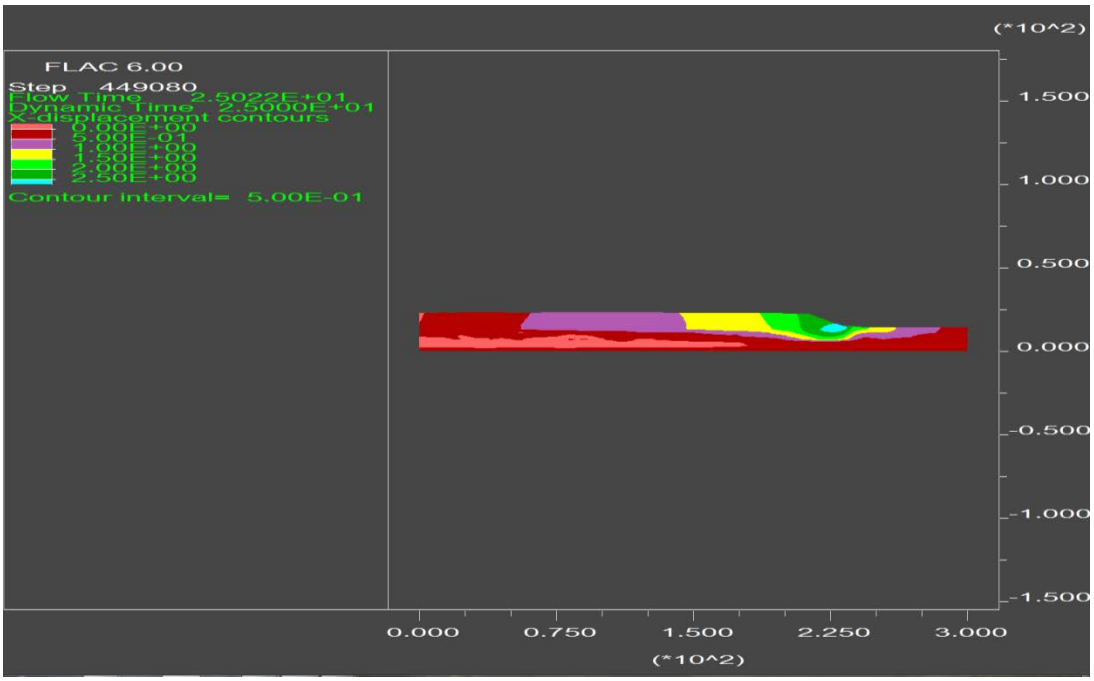

Figure B.9. Contours of calculated lateral displacement (9 m embankment height, 8 meter liquefiable sand layer, corrected $(N_1)_{60}$ blow count of 25, ground motion = 94 Northridge Sylmar - Conv Sta 052 Scale 1.0x).

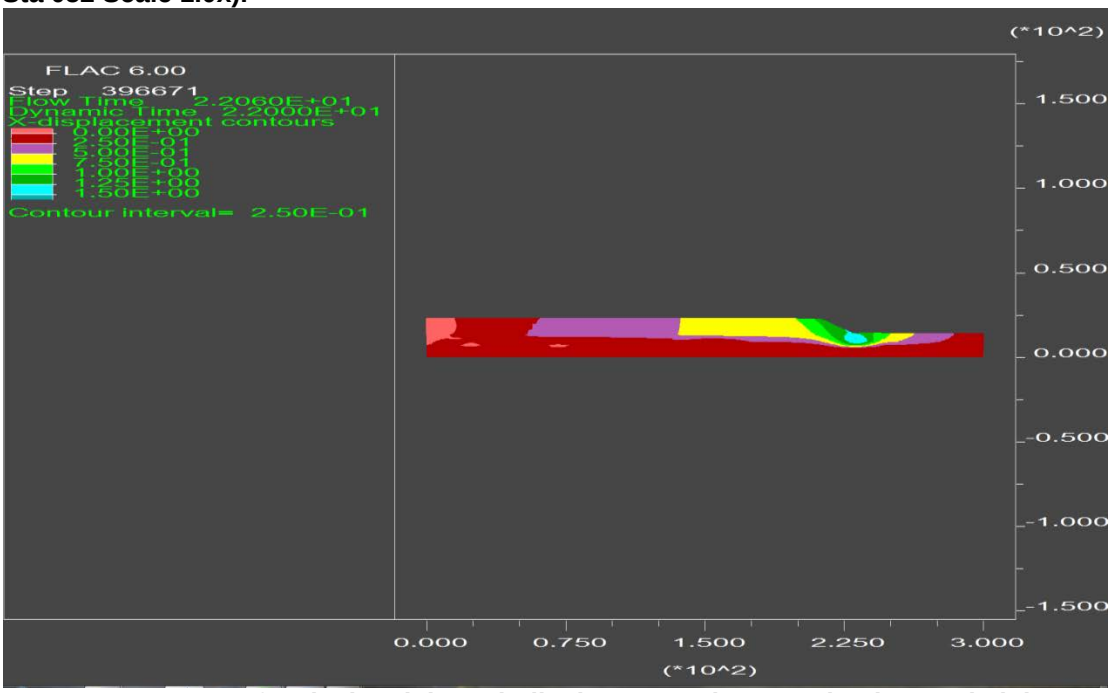

Figure B.10. Contours of calculated lateral displacement (9 m embankment height, 8 meter liquefiable sand layer, corrected $(N_1)_{60}$ blow count of 8, ground motion = 87 Superstition Hills Superstition Mtn Cam 045)

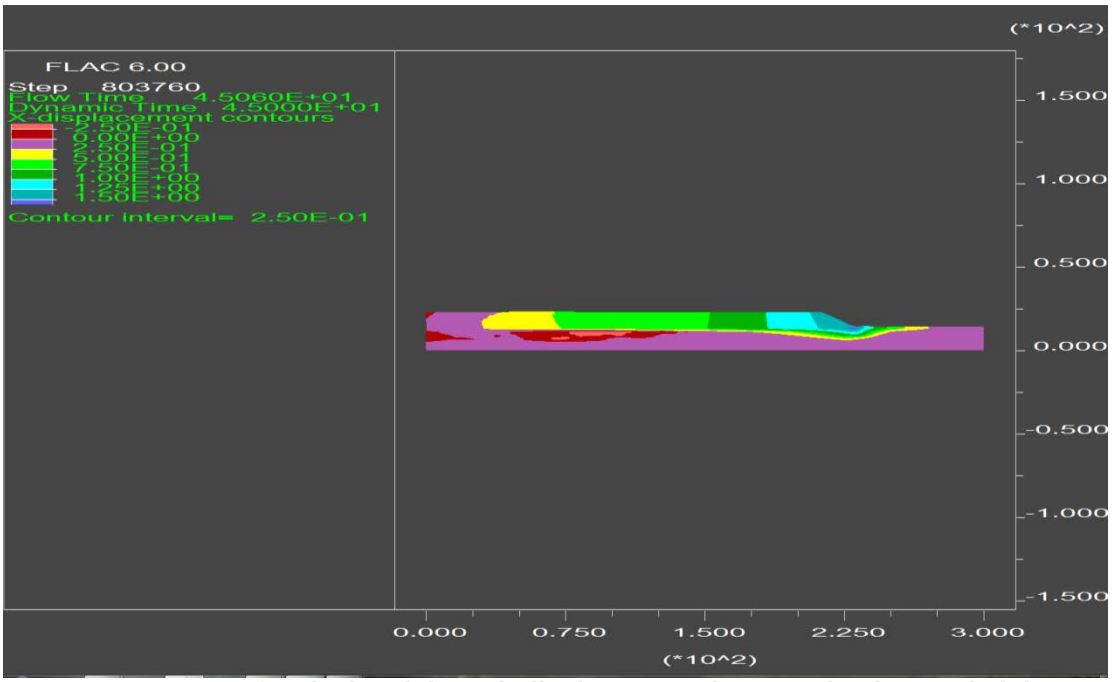

Figure B.11. Contours of calculated lateral displacement (9 m embankment height, 8 meter liquefiable sand layer, corrected $(N_1)_{60}$ blow count of 8, ground motion = 92 Landers Joshua Tree 090 Scale 0.75x).

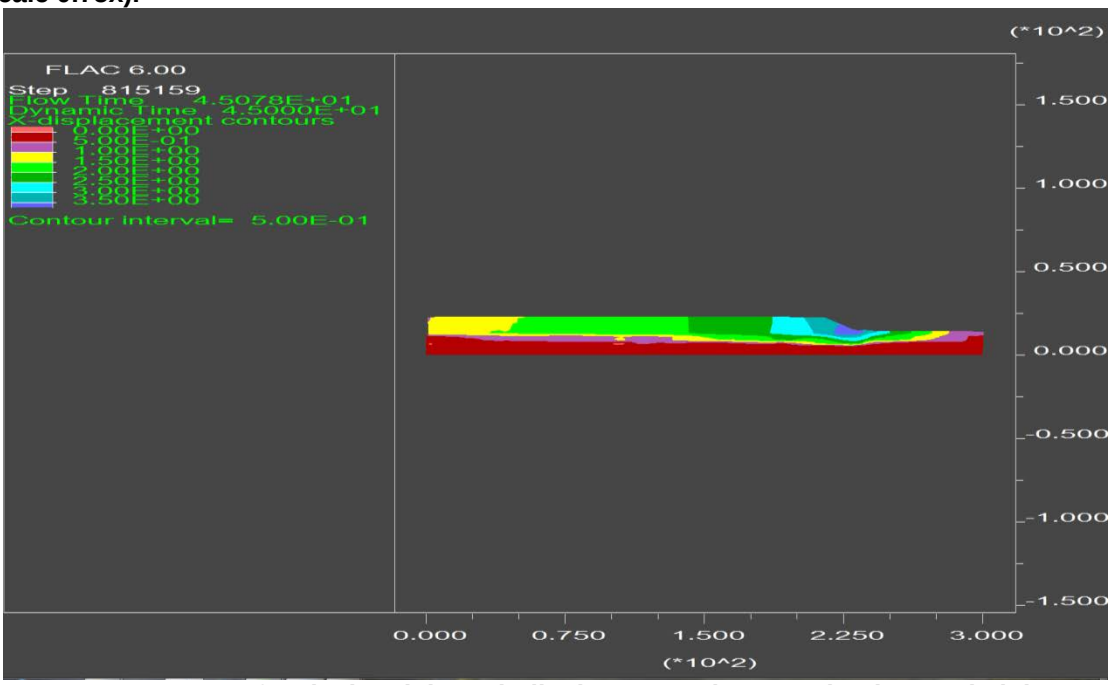

Figure B.12. Contours of calculated lateral displacement (9 m embankment height, 8 meter liquefiable sand layer, corrected $(N_1)_{60}$ blow count of 8, ground motion = 92 Landers Joshua Tree 090 Scale 1.5x).

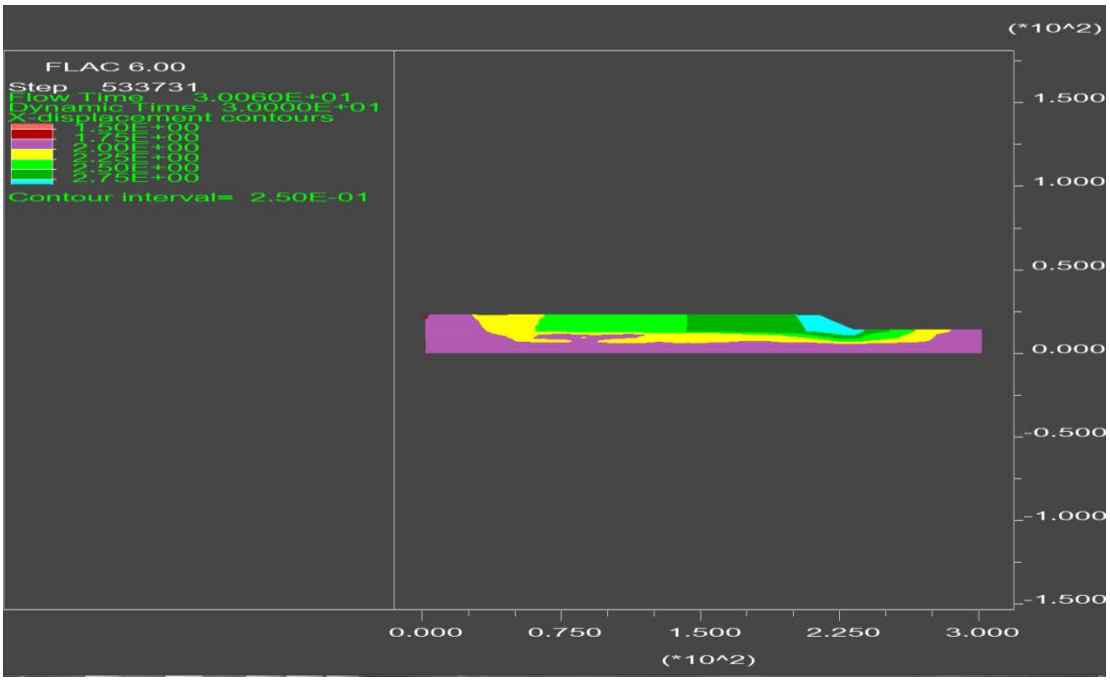

Figure B.13. Contours of calculated lateral displacement (9 m embankment height, 8 meter liquefiable sand layer, corrected $(N_1)_{60}$ blow count of 8, ground motion = 92 Landers Lucerne 260)

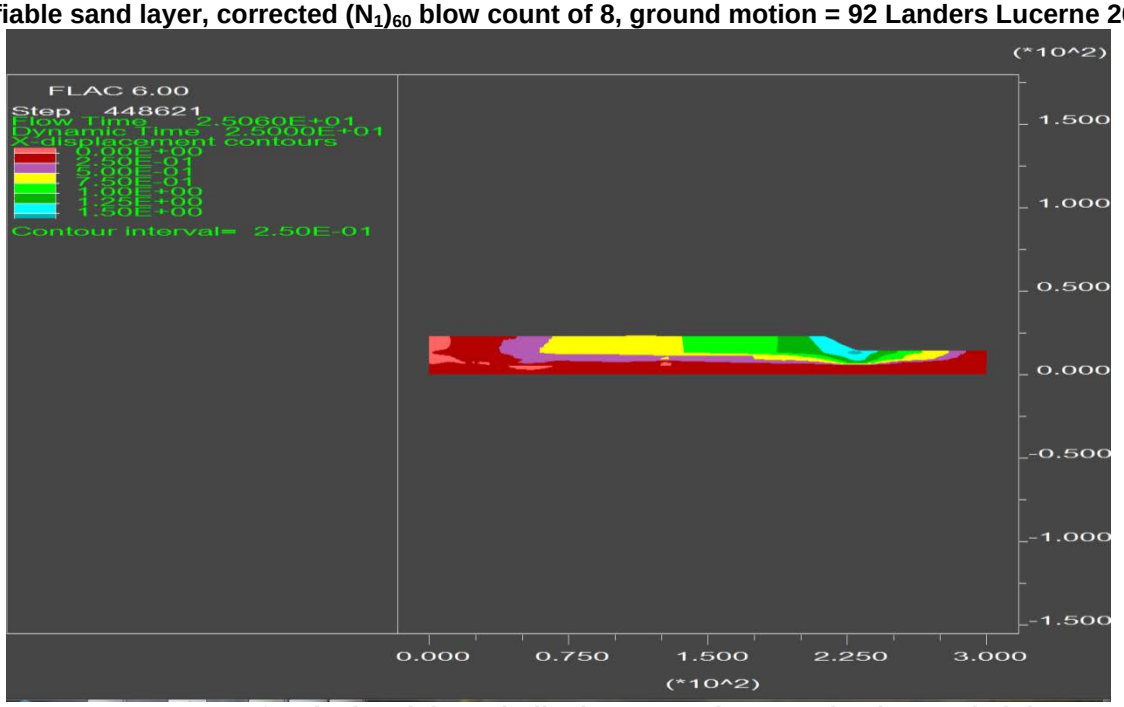

Figure B.14. Contours of calculated lateral displacement (9 m embankment height, 8 meter liquefiable sand layer, corrected $(N_1)_{60}$ blow count of 8, ground motion = 89 Loma Prieta LGPC 090)

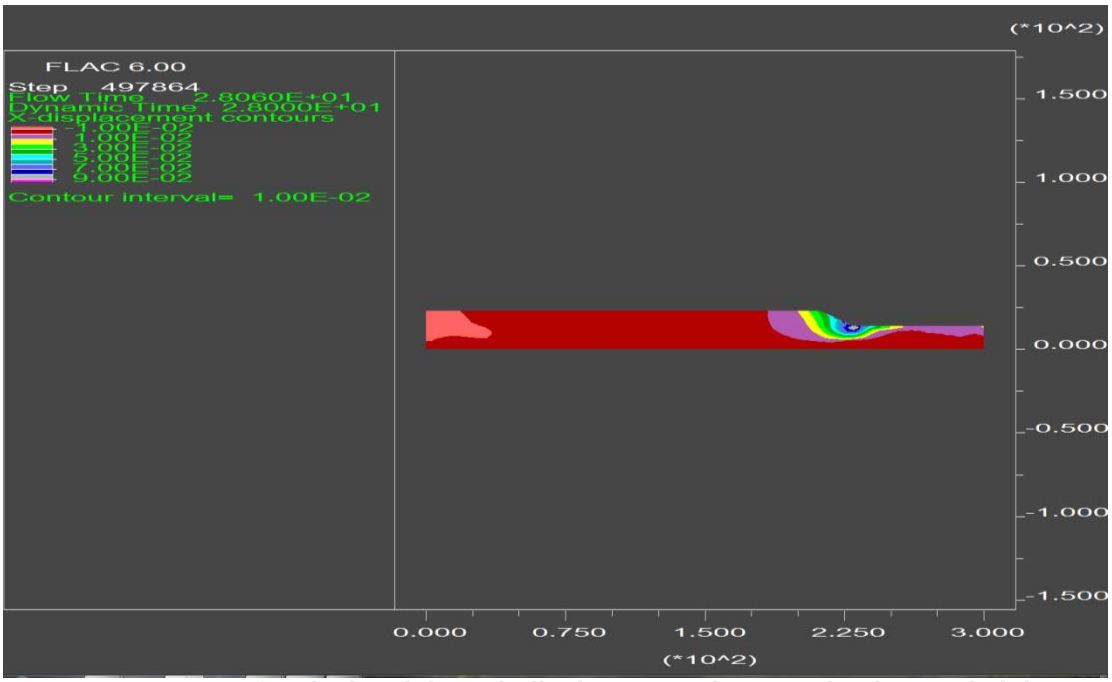

Figure B.15. Contours of calculated lateral displacement (9 m embankment height, 8 meter liquefiable sand layer, corrected $(N_1)_{60}$ blow count of 8, ground motion = 71 San Fernando LA Hollywood Stor Lot 180)

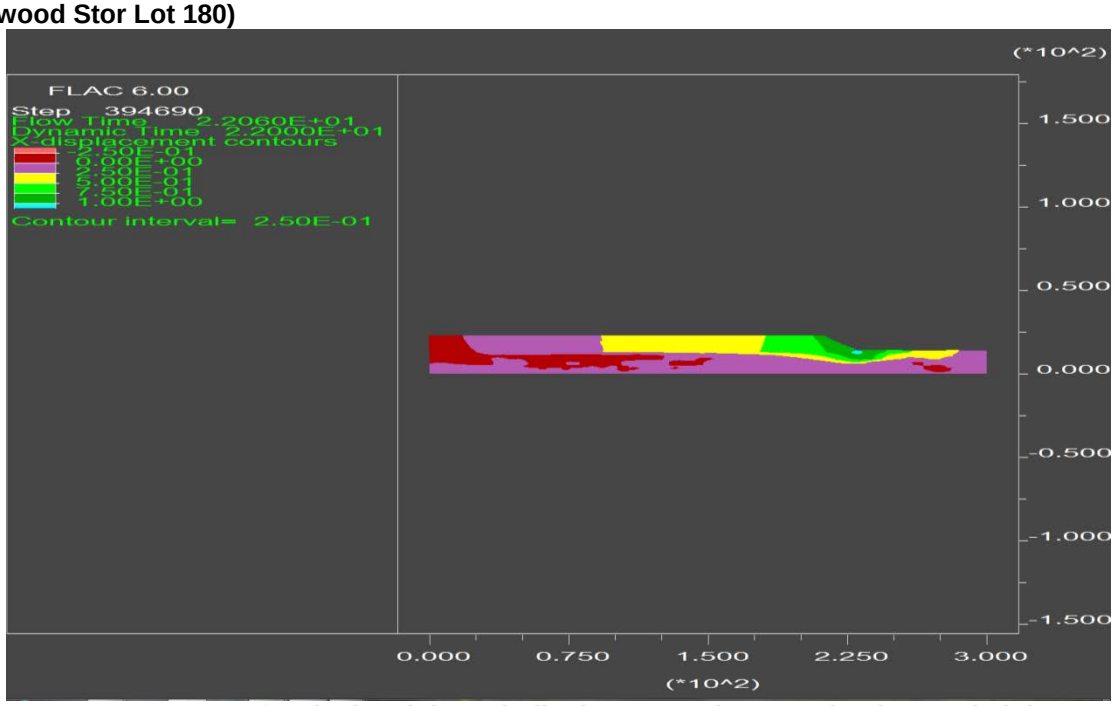

Figure B.16. Contours of calculated lateral displacement (9 m embankment height, 8 meter liquefiable sand layer, corrected $(N_1)_{60}$ blow count of 8, ground motion = 87 Superstition Hills Parachute T S 315)

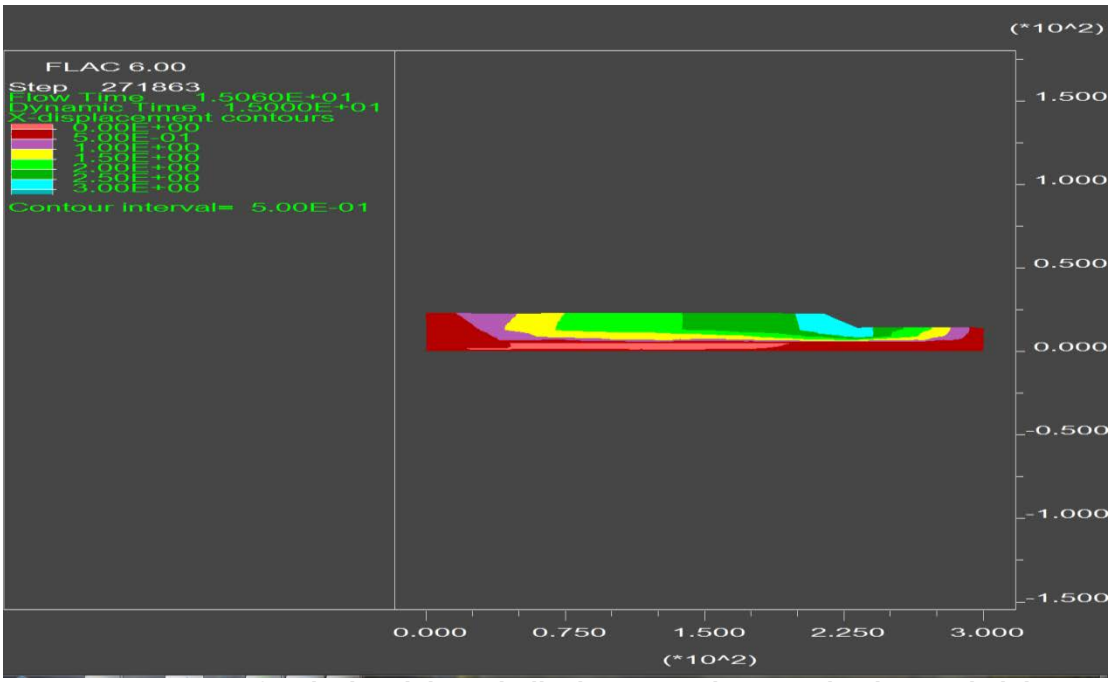

Figure B.17. Contours of calculated lateral displacement (9 m embankment height, 8 meter liquefiable sand layer, corrected $(N_1)_{60}$ blow count of 8, ground motion = 94 Northridge Rinaldi R Sta 228)

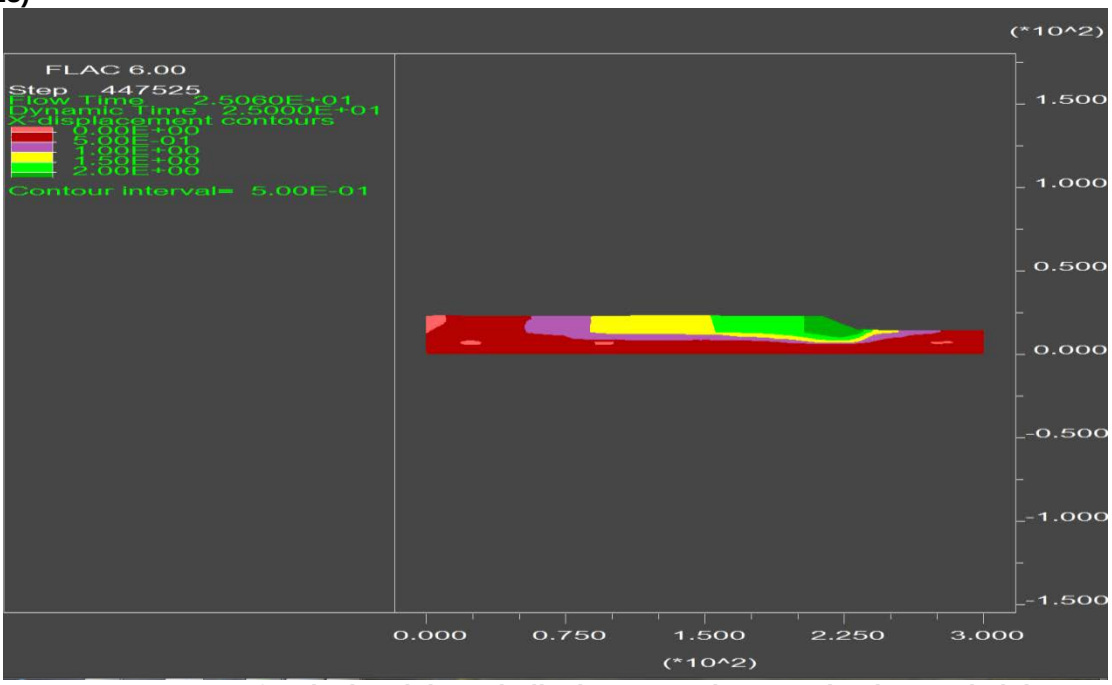

Figure B.18. Contours of calculated lateral displacement (9 m embankment height, 8 meter liquefiable sand layer, corrected $(N_1)_{60}$ blow count of 8, ground motion = 94 Northridge Sylmar - Conv Sta 052 Scale 0.5x)

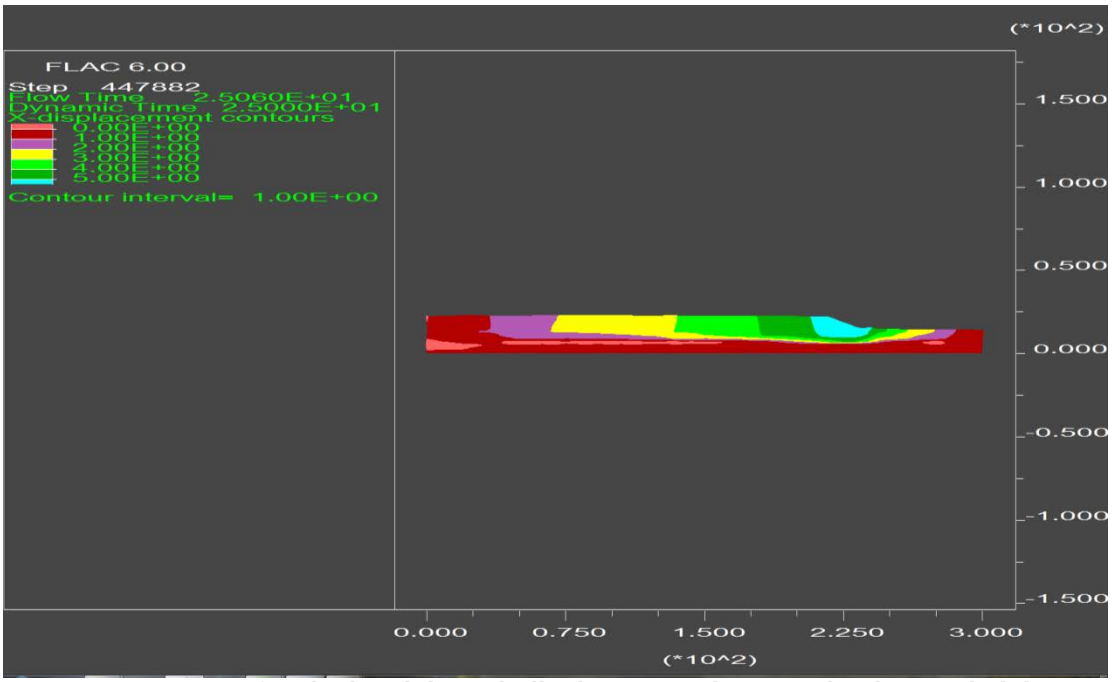

Figure B.19. Contours of calculated lateral displacement (9 m embankment height, 8 meter liquefiable sand layer, corrected $(N_1)_{60}$ blow count of 8, ground motion = 94 Northridge Sylmar - Conv Sta 052 Scale 1.25x)

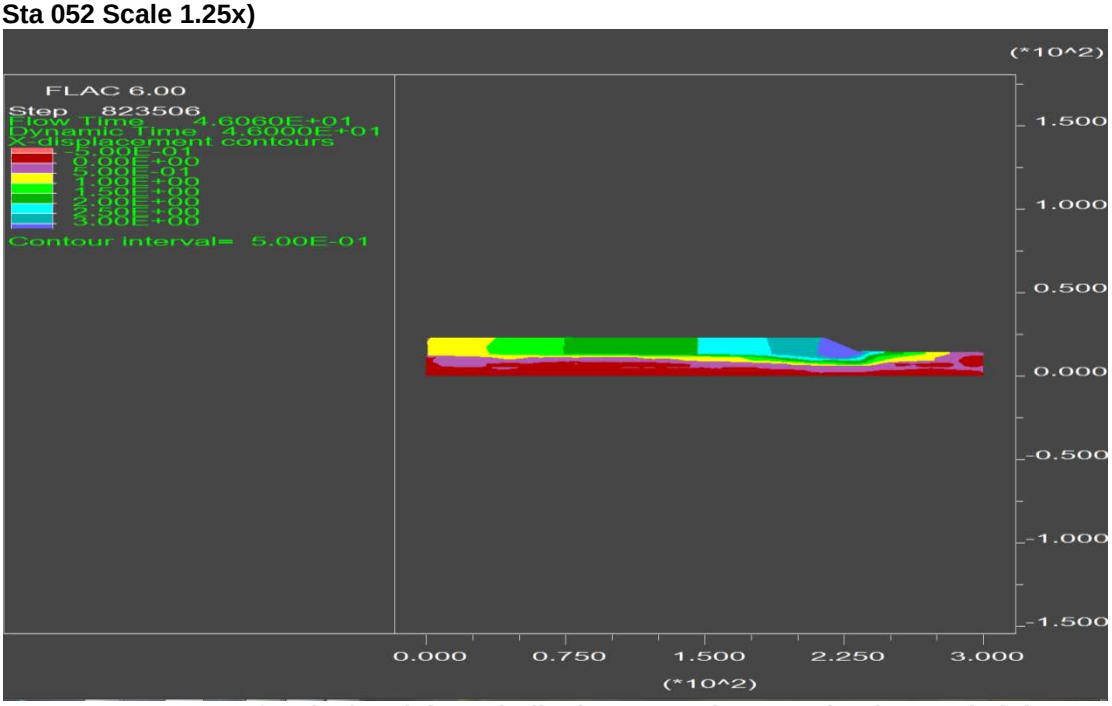

Figure B.20. Contours of calculated lateral displacement (9 m embankment height, 8 meter liquefiable sand layer, corrected $(N_1)_{60}$ blow count of 8, ground motion = 99 Chi Chi TCU078 270 (E))

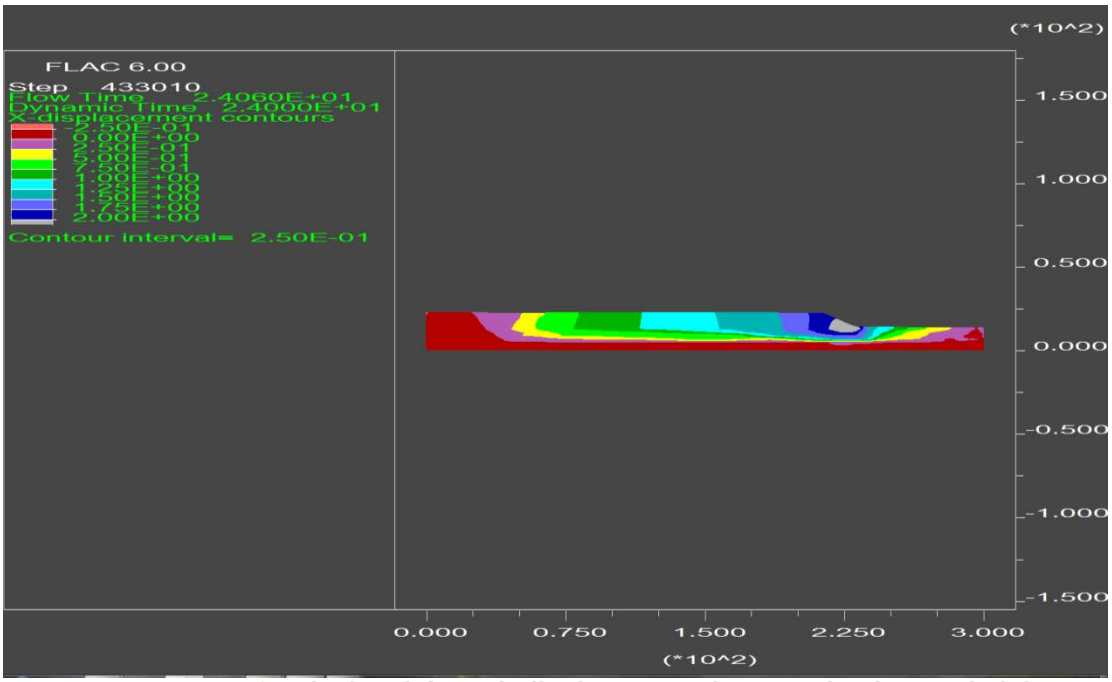

Figure B.21. Contours of calculated lateral displacement (9 m embankment height, 8 meter liquefiable sand layer, corrected $(N_1)_{60}$ blow count of 8, ground motion = 94 Northridge Newhall - W Pico Cany 046)

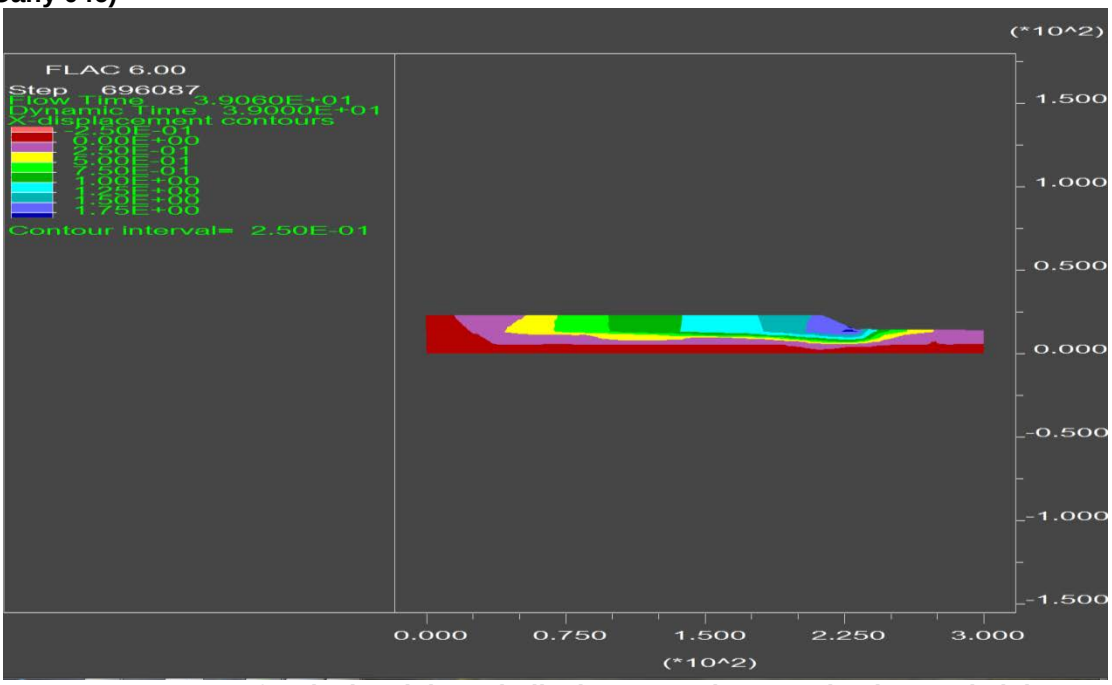

Figure B.22. Contours of calculated lateral displacement (9 m embankment height, 8 meter liquefiable sand layer, corrected $(N_1)_{60}$ blow count of 8, ground motion = 89 Loma Prieta Saratoga WV Coll 270)

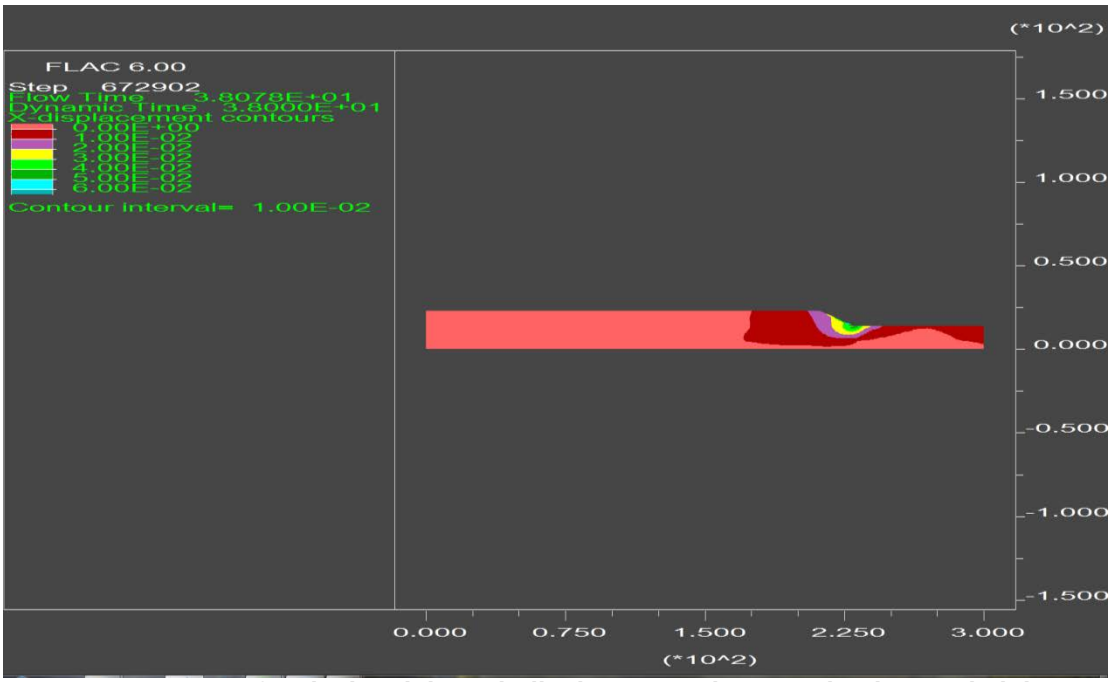

Figure B.23. Contours of calculated lateral displacement (9 m embankment height, 8 meter liquefiable sand layer, corrected $(N_1)_{60}$ blow count of 15, ground motion = 79 Imperial Valley Brawley Airport)

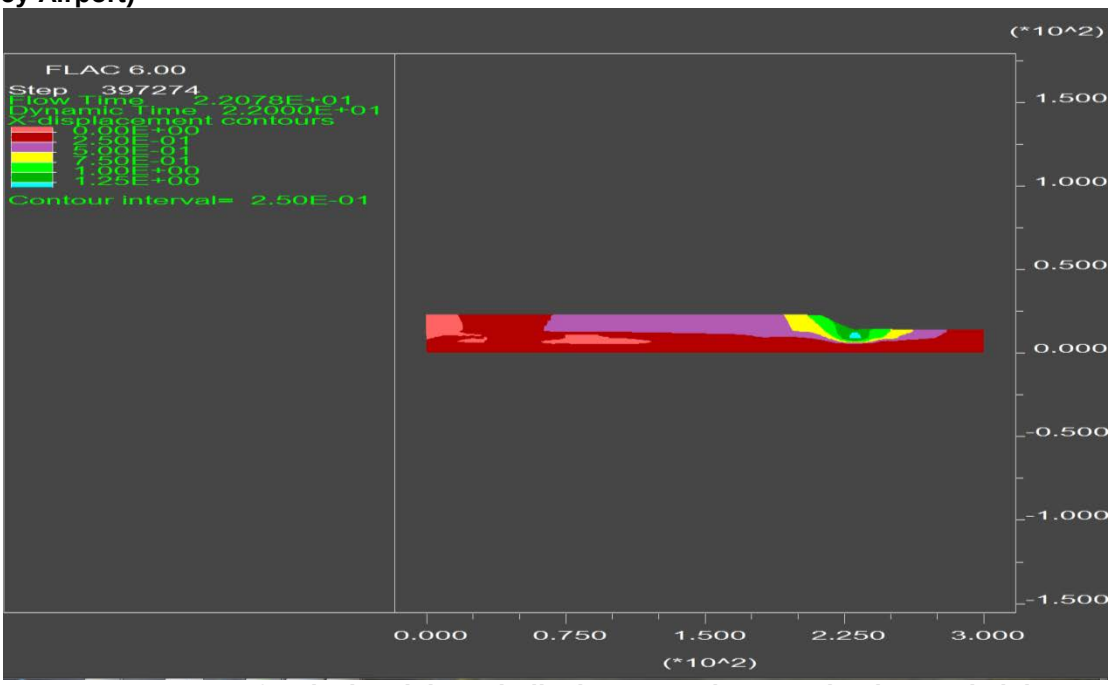

Figure B.24. Contours of calculated lateral displacement (9 m embankment height, 8 meter liquefiable sand layer, corrected $(N_1)_{60}$ blow count of 15, ground motion = 87 Superstition Hills Superstition Mtn Cam 045)

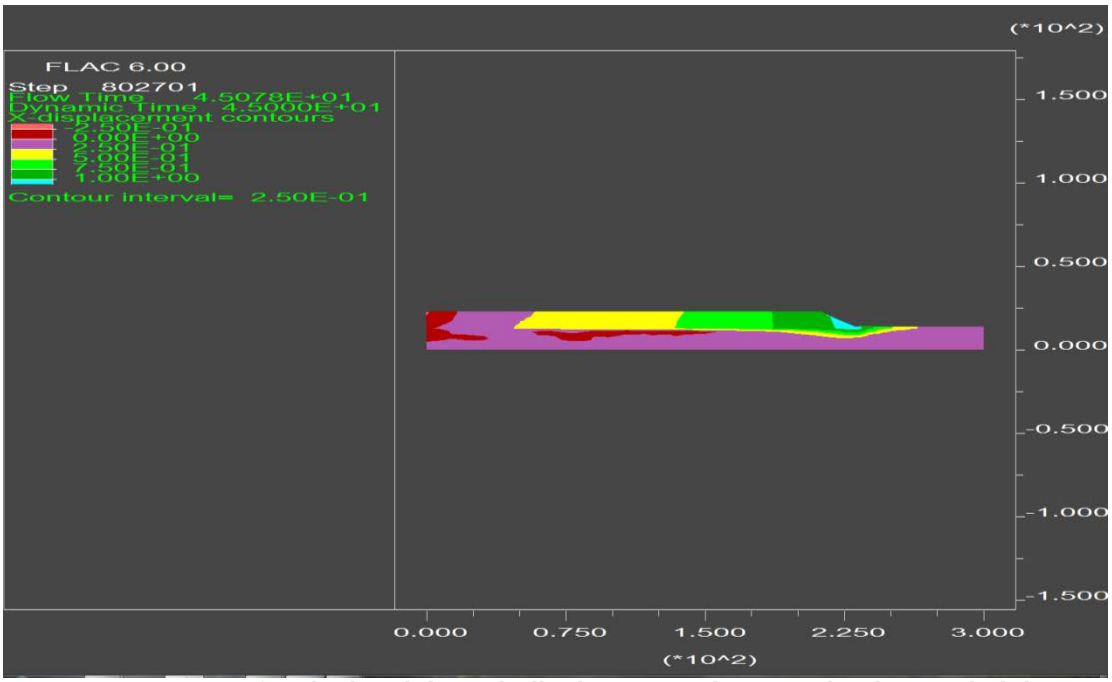

Figure B.25. Contours of calculated lateral displacement (9 m embankment height, 8 meter liquefiable sand layer, corrected $(N_1)_{60}$ blow count of 15, ground motion = 92 Landers Joshua Tree 090 Scale 0.75x).

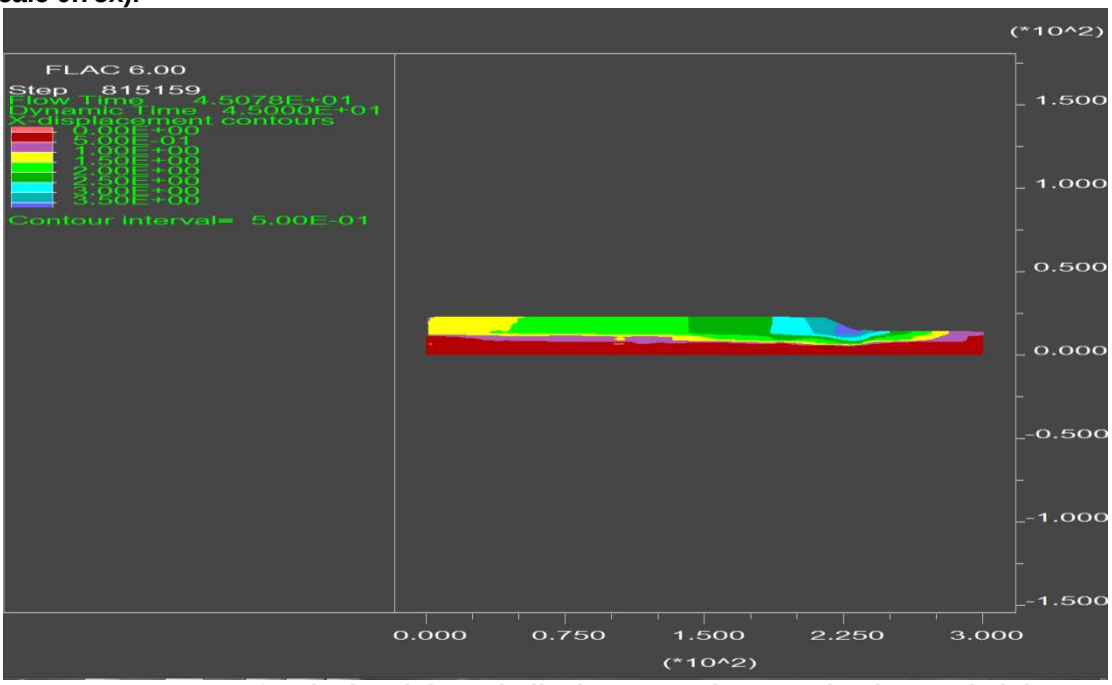

Figure B.26. Contours of calculated lateral displacement (9 m embankment height, 8 meter liquefiable sand layer, corrected $(N_1)_{60}$ blow count of 15, ground motion = 92 Landers Joshua Tree 090 Scale 1.5x).

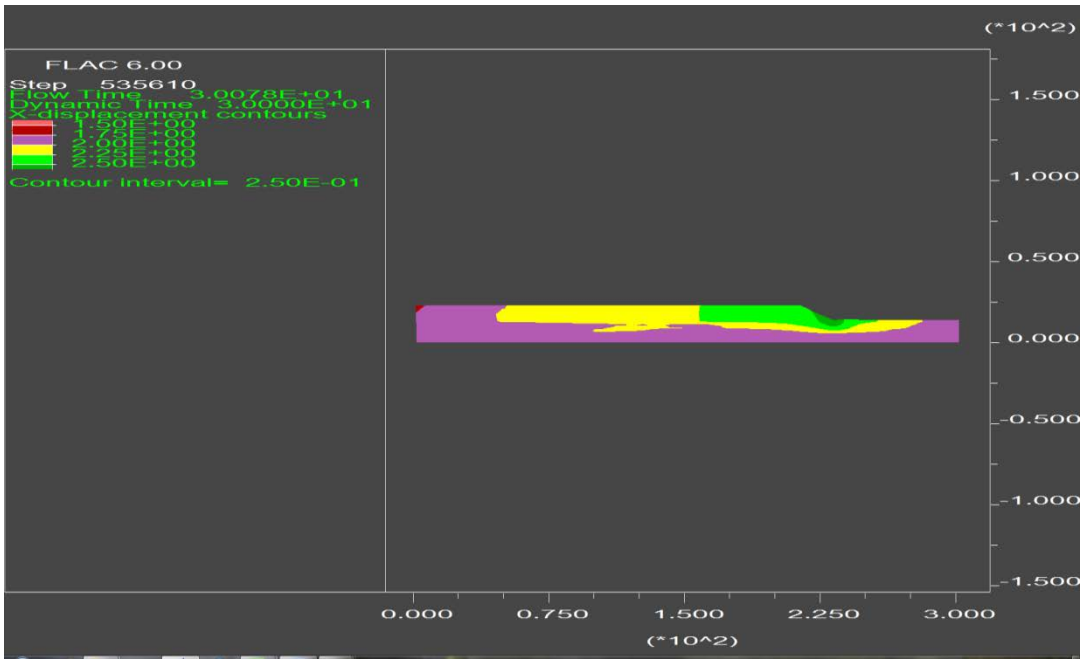

Figure B.27. Contours of calculated lateral displacement (9 m embankment height, 8 meter liquefiable sand layer, corrected $(N_1)_{60}$ blow count of 15, ground motion = 92 Landers Lucerne 260). Note that displacements shown are total displacements and include approximately 175 cm of fling step that can be subtracted out to obtain relative displacements.

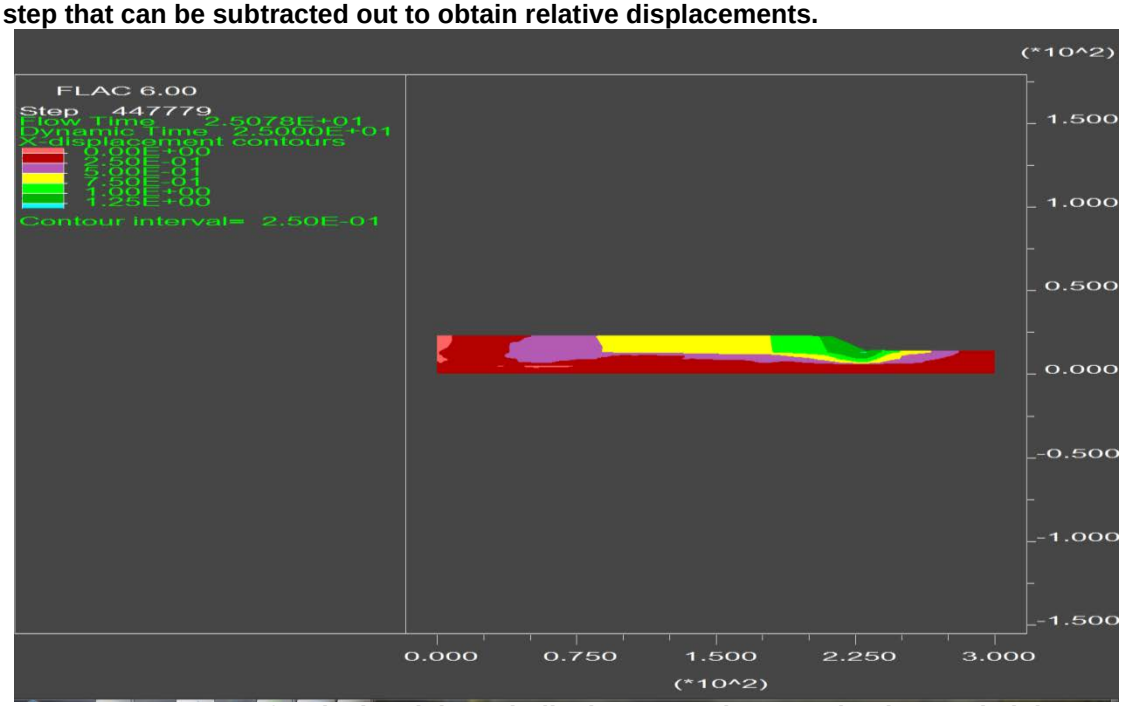

Figure B.28. Contours of calculated lateral displacement (9 m embankment height, 8 meter liquefiable sand layer, corrected $(N_1)_{60}$ blow count of 15, ground motion = 89 Loma Prieta LGPC 090)

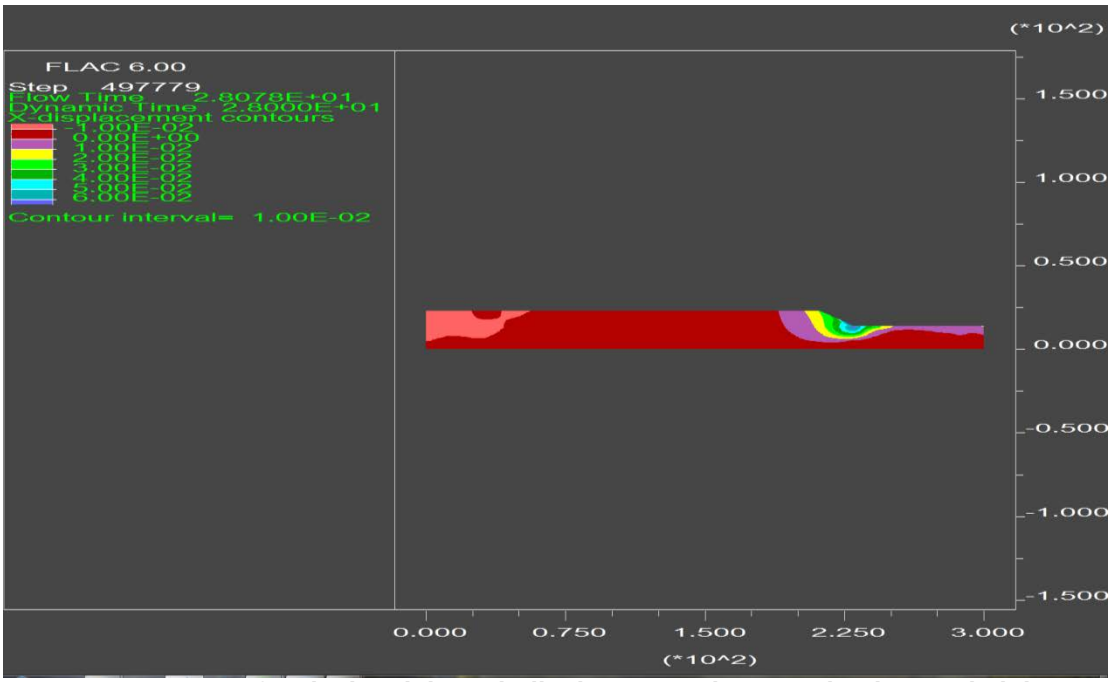

Figure B.29. Contours of calculated lateral displacement (9 m embankment height, 8 meter liquefiable sand layer, corrected $(N_1)_{60}$ blow count of 15, ground motion = 71 San Fernando LA Hollywood Stor Lot 180)

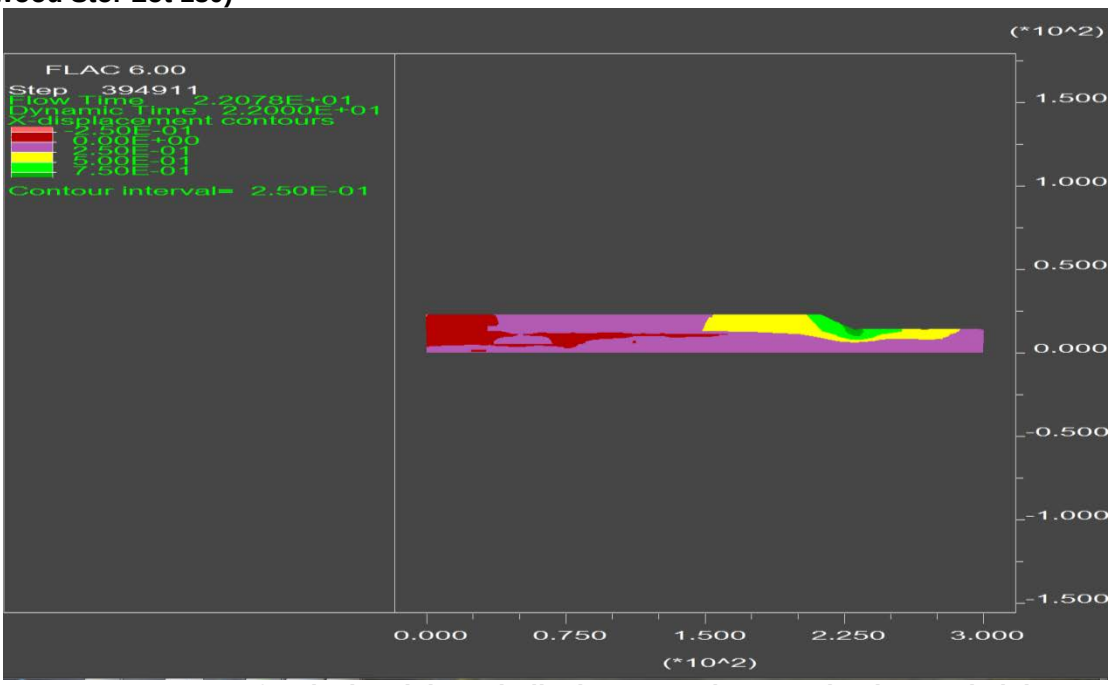

Figure B.30. Contours of calculated lateral displacement (9 m embankment height, 8 meter liquefiable sand layer, corrected $(N_1)_{60}$ blow count of 15, ground motion = 87 Superstition Hills Parachute T S 315)

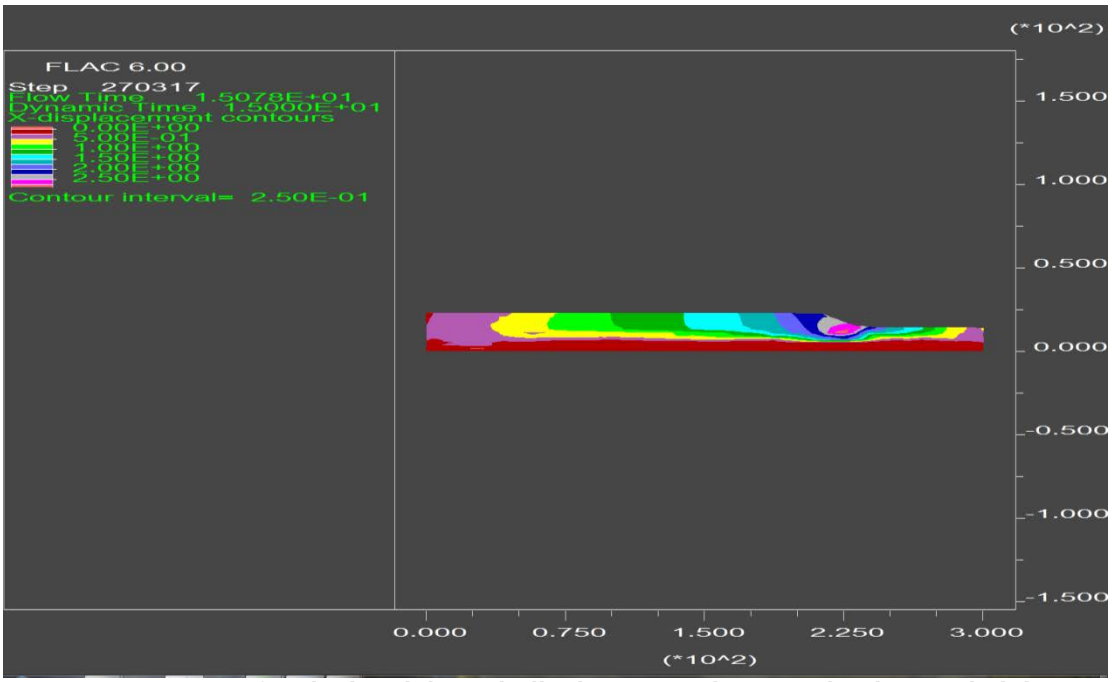

Figure B.31. Contours of calculated lateral displacement (9 m embankment height, 8 meter liquefiable sand layer, corrected $(N_1)_{60}$ blow count of 15, ground motion = 94 Northridge Rinaldi R Sta 228)

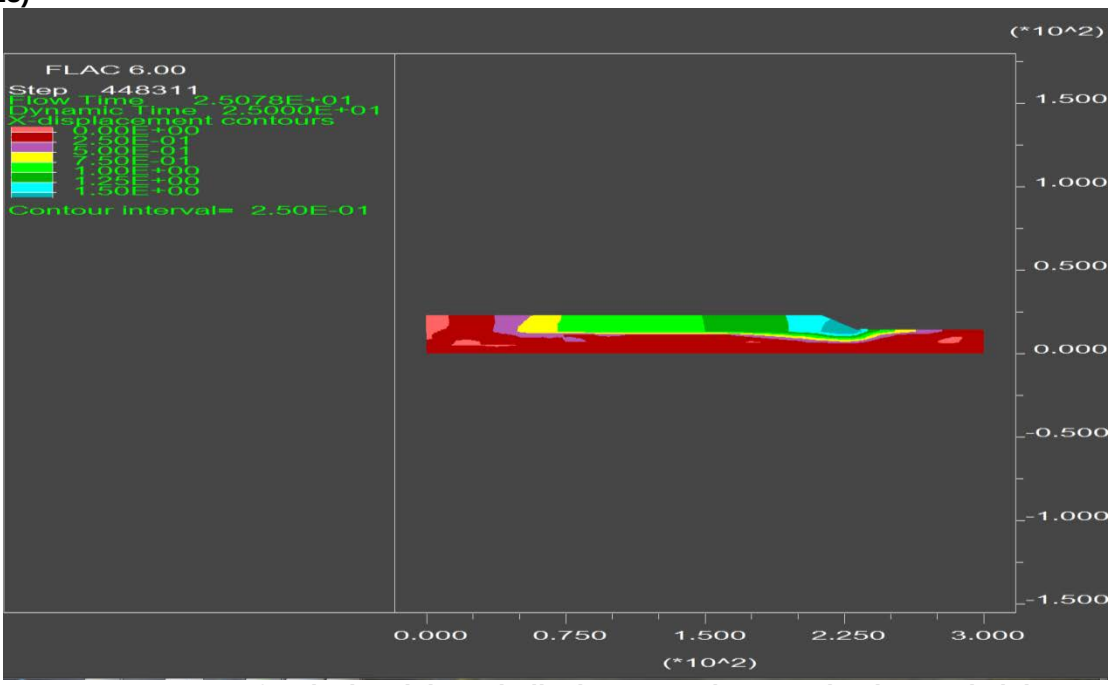

Figure B.32. Contours of calculated lateral displacement (9 m embankment height, 8 meter liquefiable sand layer, corrected $(N_1)_{60}$ blow count of 15, ground motion = 94 Northridge Sylmar - Conv Sta 052 Scale 0.5x)

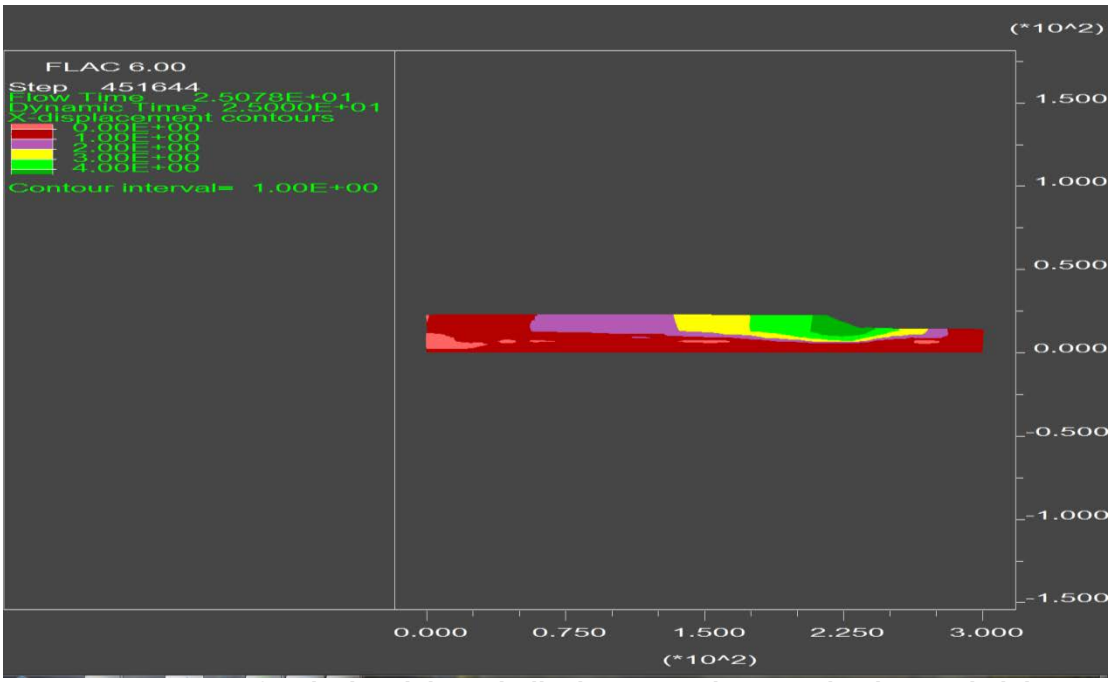

Figure B.33. Contours of calculated lateral displacement (9 m embankment height, 8 meter liquefiable sand layer, corrected $(N_1)_{60}$ blow count of 15, ground motion = 94 Northridge Sylmar - Conv Sta 052 Scale 1.25x)

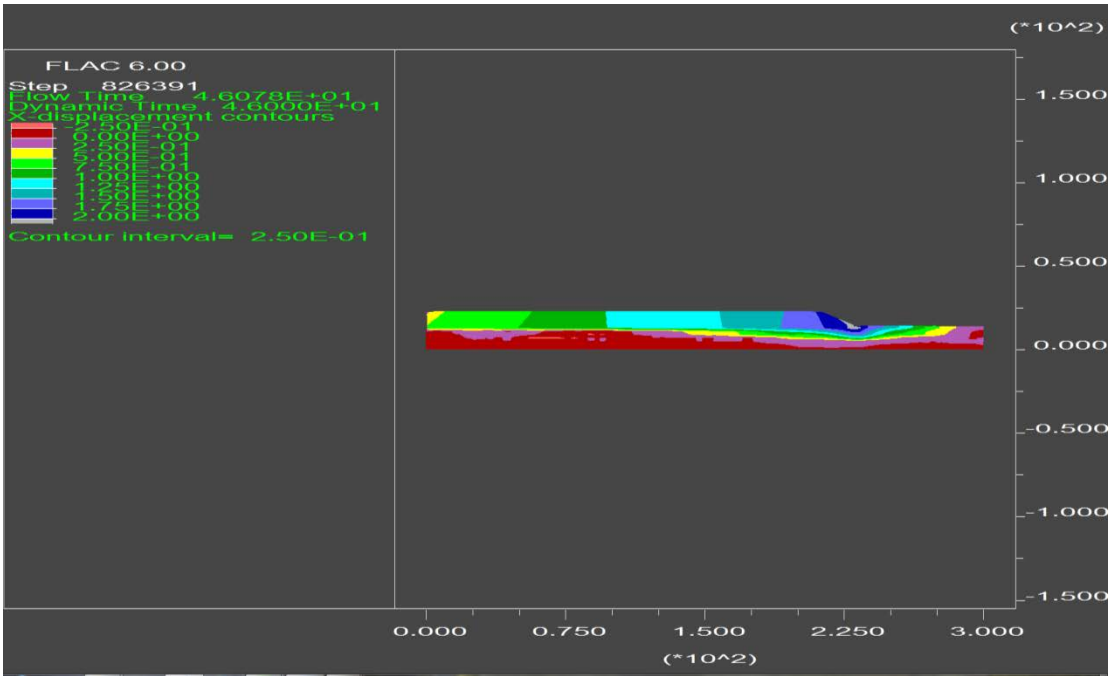

Figure B.34. Contours of calculated lateral displacement (9 m embankment height, 8 meter liquefiable sand layer, corrected $(N_1)_{60}$ blow count of 15, ground motion = 99 Chi Chi TCU078 270 (E))

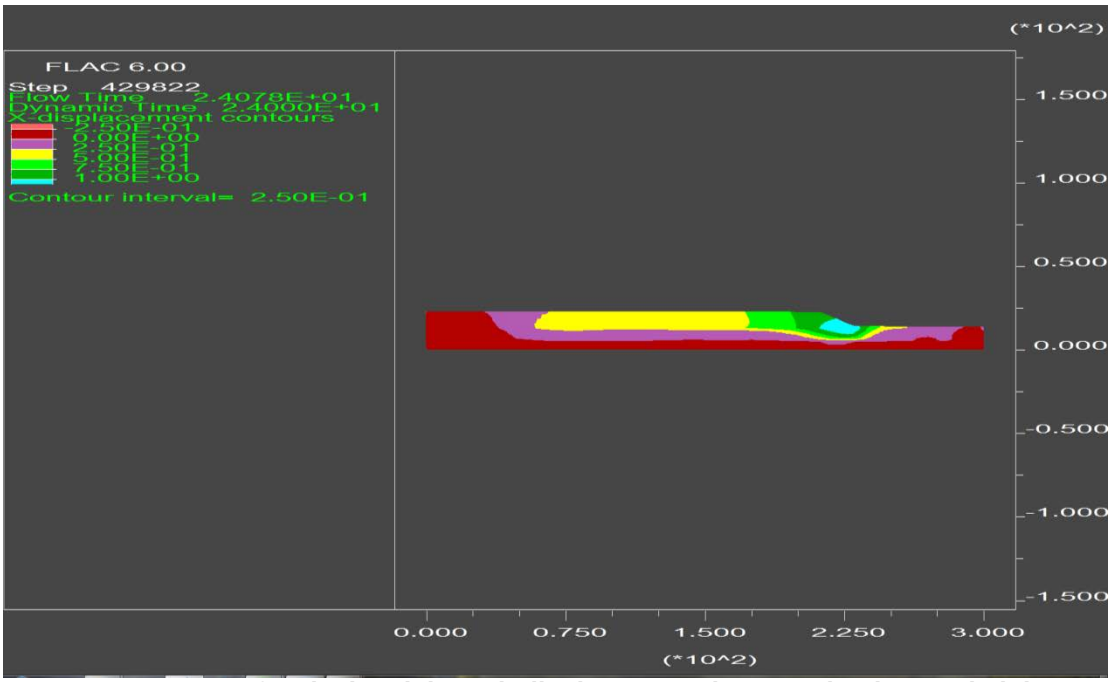

Figure B.35. Contours of calculated lateral displacement (9 m embankment height, 8 meter liquefiable sand layer, corrected $(N_1)_{60}$ blow count of 15, ground motion = 94 Northridge Newhall - W Pico Cany 046)

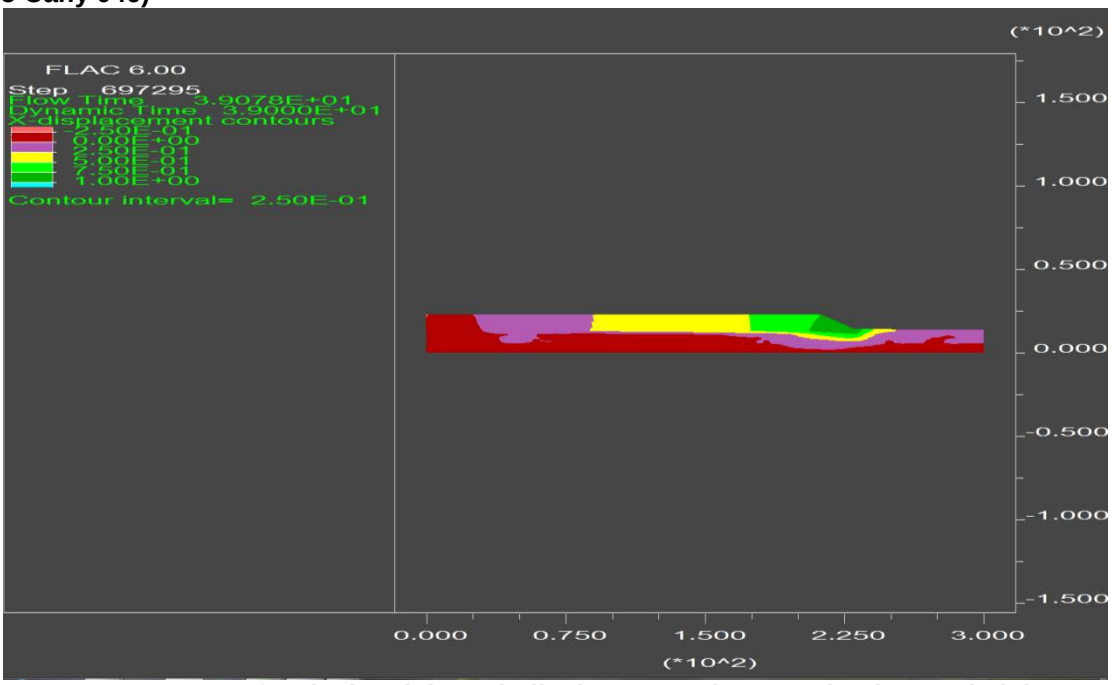

Figure B.36. Contours of calculated lateral displacement (9 m embankment height, 8 meter liquefiable sand layer, corrected $(N_1)_{60}$ blow count of 15, ground motion = 89 Loma Prieta Saratoga WV Coll 270)

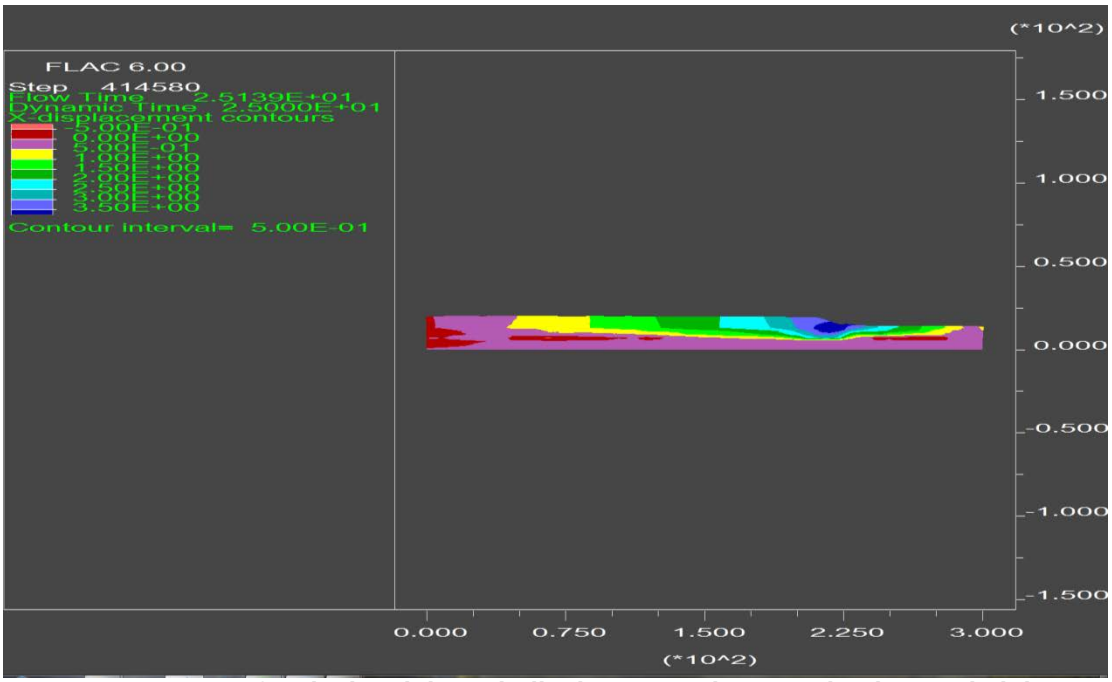

Figure B.37. Contours of calculated lateral displacement (6 m embankment height, 8 meter liquefiable sand layer, corrected $(N_1)_{60}$ blow count of 8, ground motion = 94 Northridge Sylmar - Conv Sta 052 Scale 1.0x).

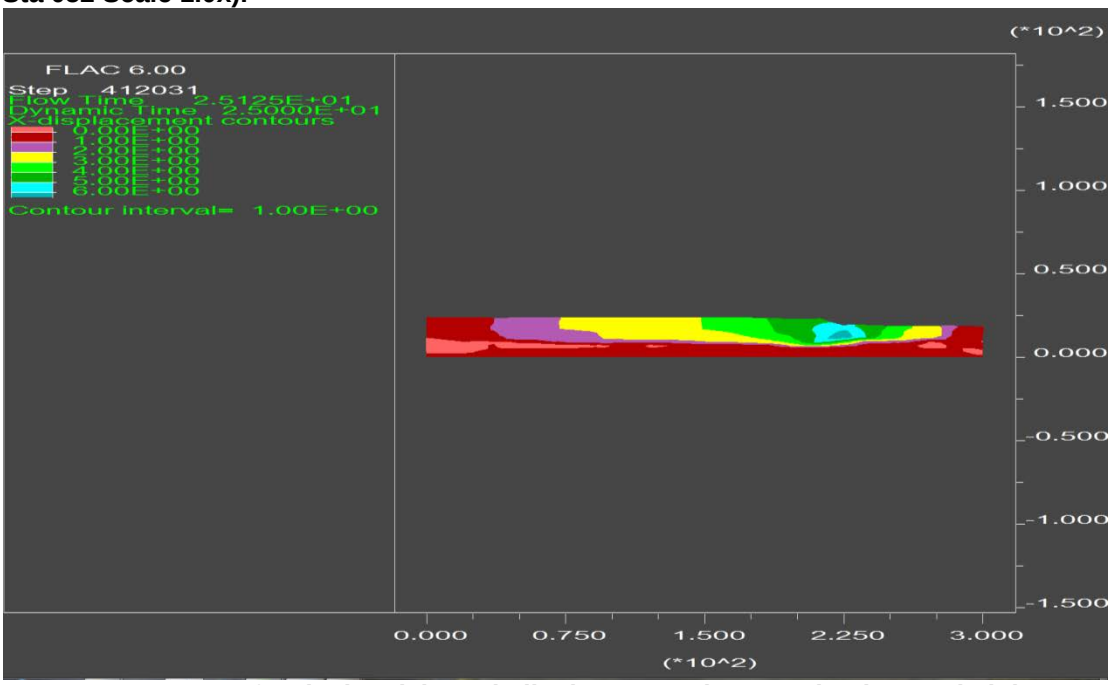

Figure B.38. Contours of calculated lateral displacement (6 m embankment height, 12 meter liquefiable sand layer, corrected $(N_1)_{60}$ blow count of 8, ground motion = 94 Northridge Sylmar - Conv Sta 052 Scale 1.0x).

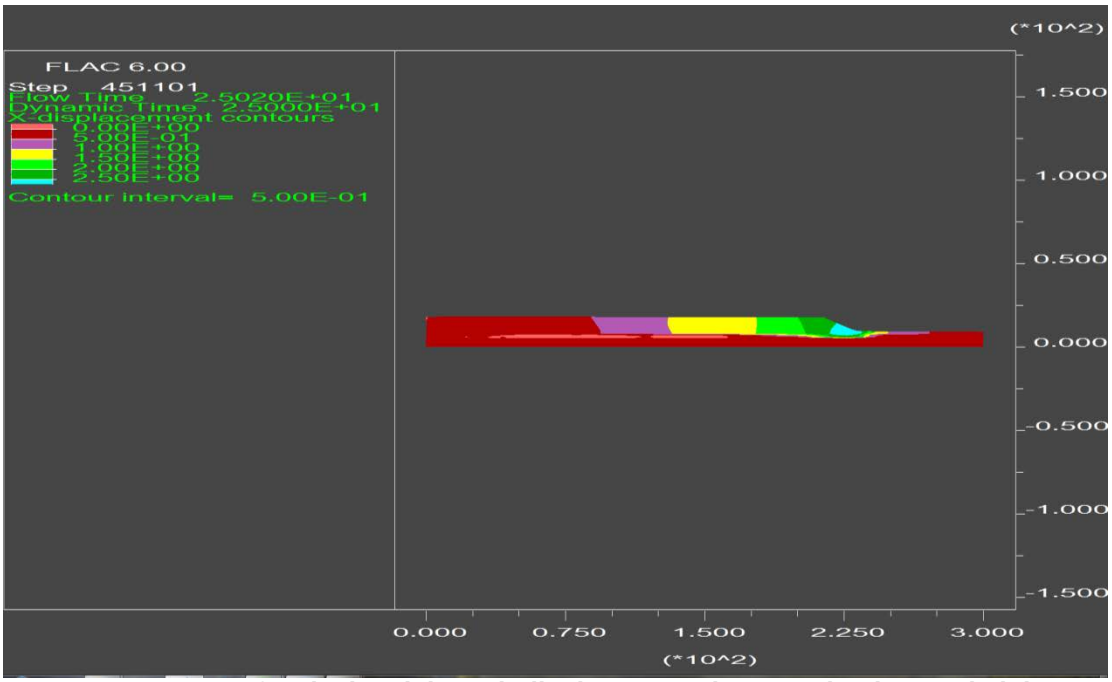

Figure B.39. Contours of calculated lateral displacement (9 m embankment height, 3 meter liquefiable sand layer, corrected $(N_1)_{60}$ blow count of 8, ground motion = 94 Northridge Sylmar - Conv Sta 052 Scale 1.0x).

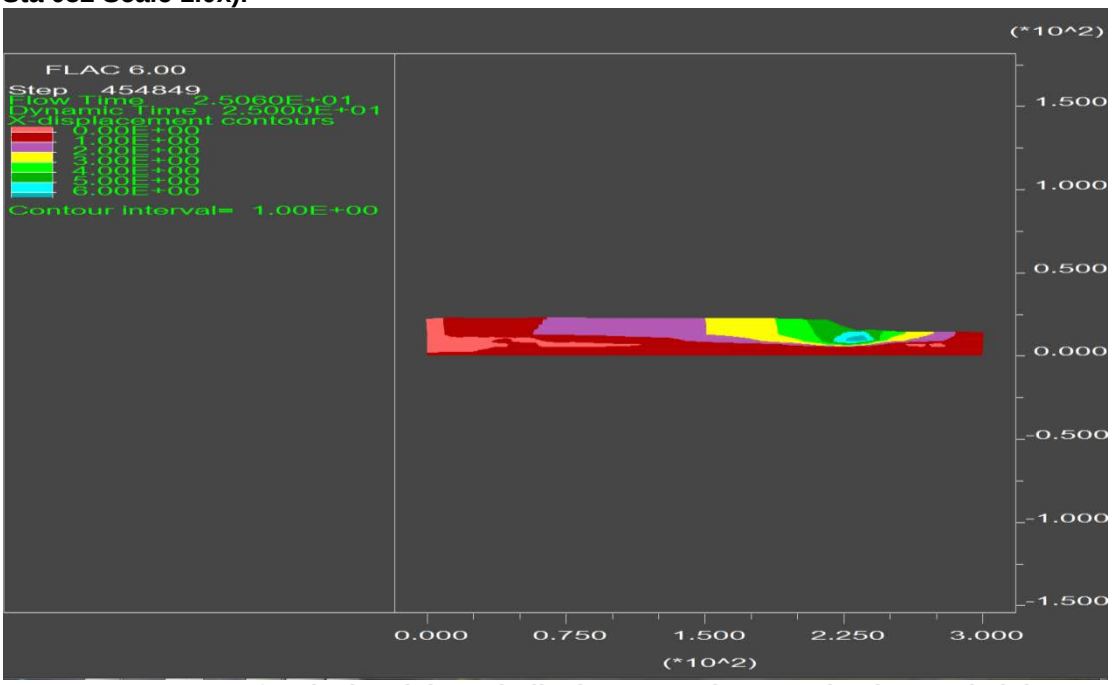

Figure B.40. Contours of calculated lateral displacement (9 m embankment height, 8 meter liquefiable sand layer, corrected $(N_1)_{60}$ blow count of 8, ground motion = 94 Northridge Sylmar - Conv Sta 052 Scale 1.0x).

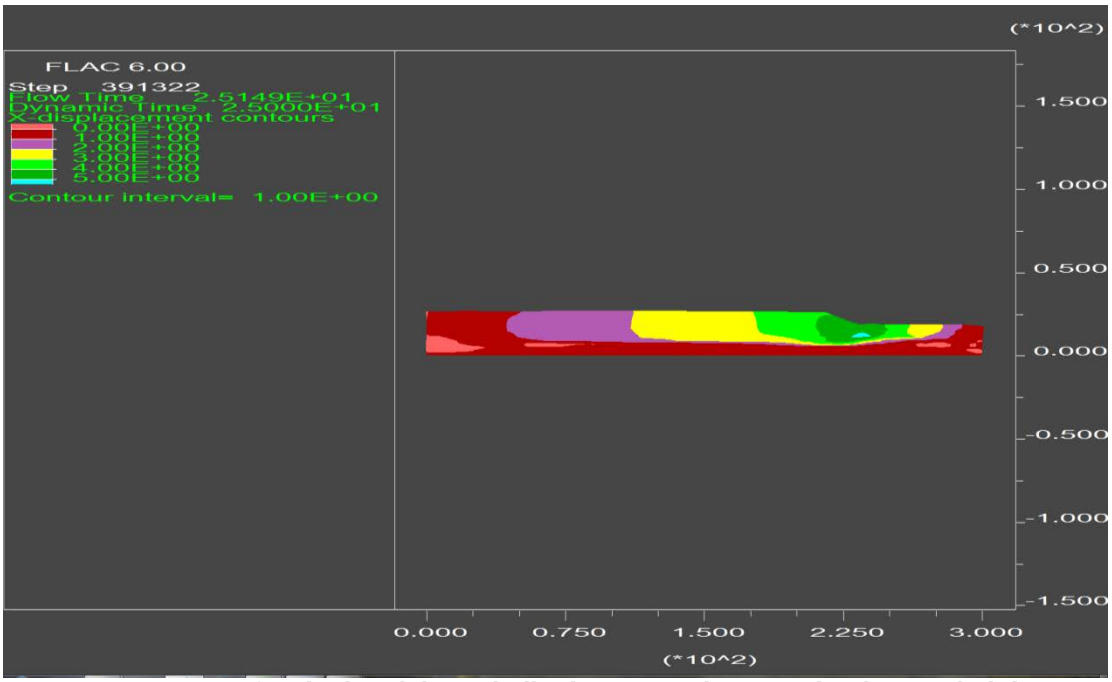

Figure B.41. Contours of calculated lateral displacement (9 m embankment height, 12 meter liquefiable sand layer, corrected $(N_1)_{60}$ blow count of 8, ground motion = 94 Northridge Sylmar - Conv Sta 052 Scale 1.0x).

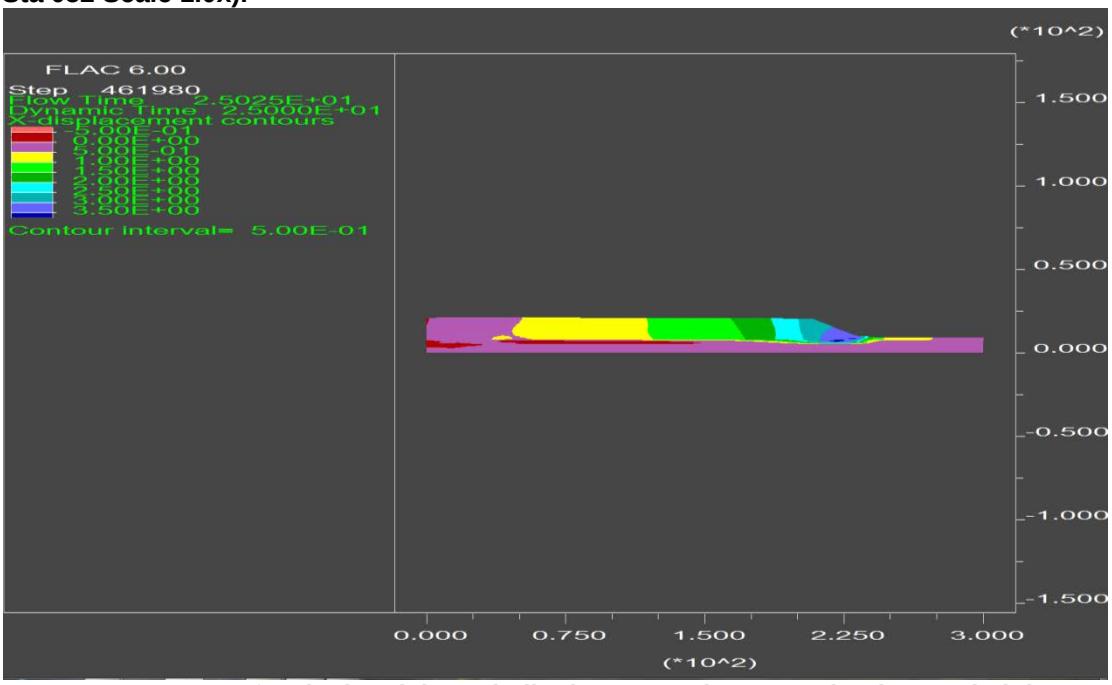

Figure B.42. Contours of calculated lateral displacement (12 m embankment height, 3 meter liquefiable sand layer, corrected $(N_1)_{60}$ blow count of 8, ground motion = 94 Northridge Sylmar - Conv Sta 052 Scale 1.0x).

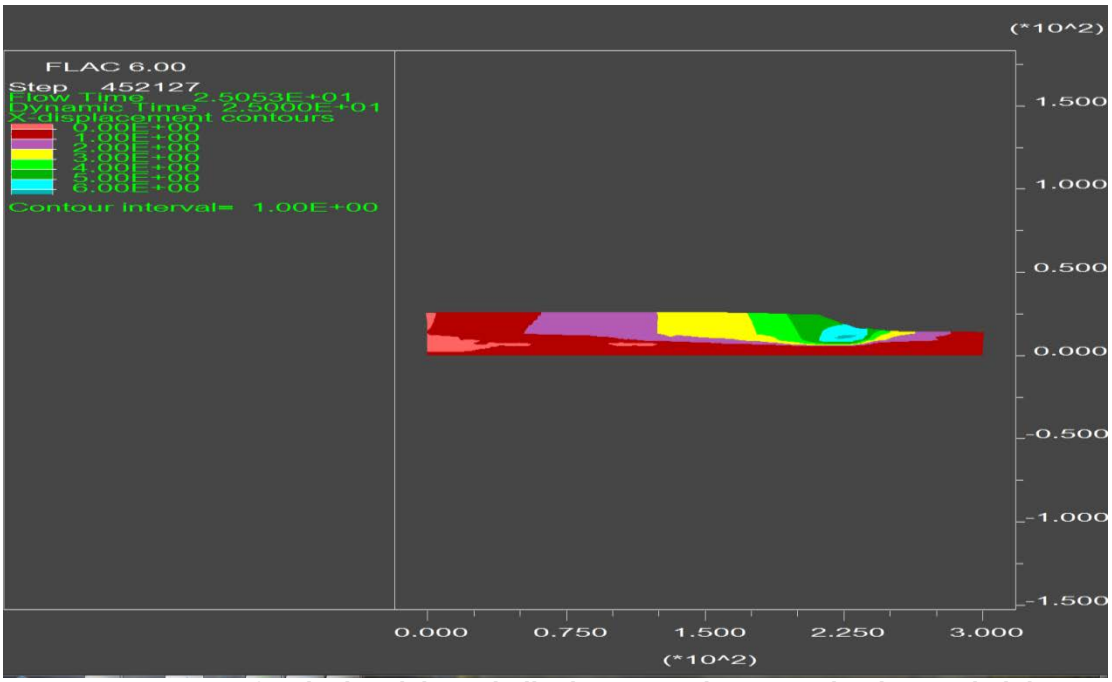

Figure B.43. Contours of calculated lateral displacement (12 m embankment height, 8 meter liquefiable sand layer, corrected $(N_1)_{60}$ blow count of 8, ground motion = 94 Northridge Sylmar - Conv Sta 052 Scale 1.0x).

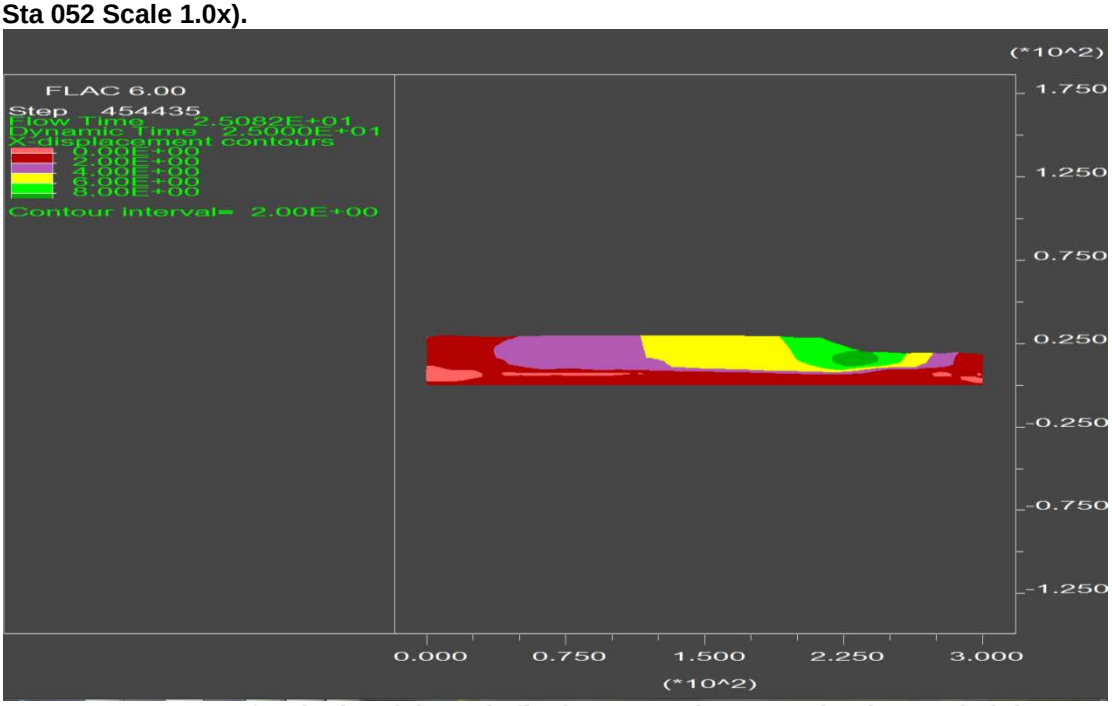

Figure B.44. Contours of calculated lateral displacement (12 m embankment height, 12 meter liquefiable sand layer, corrected $(N_1)_{60}$ blow count of 8, ground motion = 94 Northridge Sylmar - Conv Sta 052 Scale 1.0x).

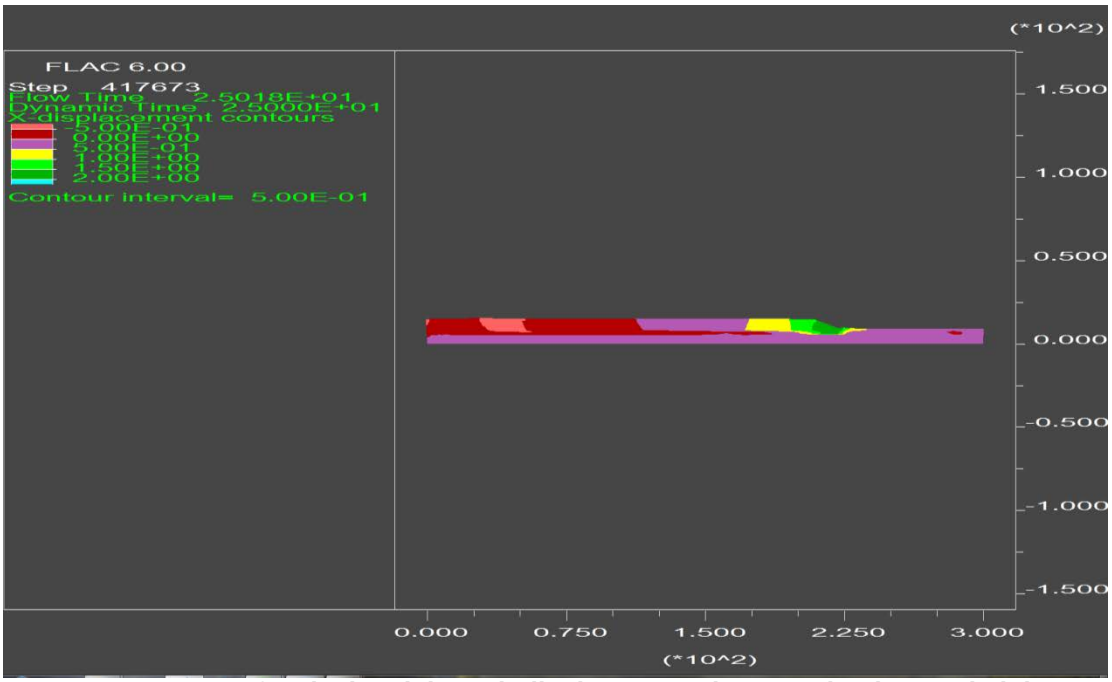

Figure B.45. Contours of calculated lateral displacement (6 m embankment height, 3 meter liquefiable sand layer, corrected $(N_1)_{60}$ blow count of 15, ground motion = 94 Northridge Sylmar - Conv Sta 052 Scale 1.0x).

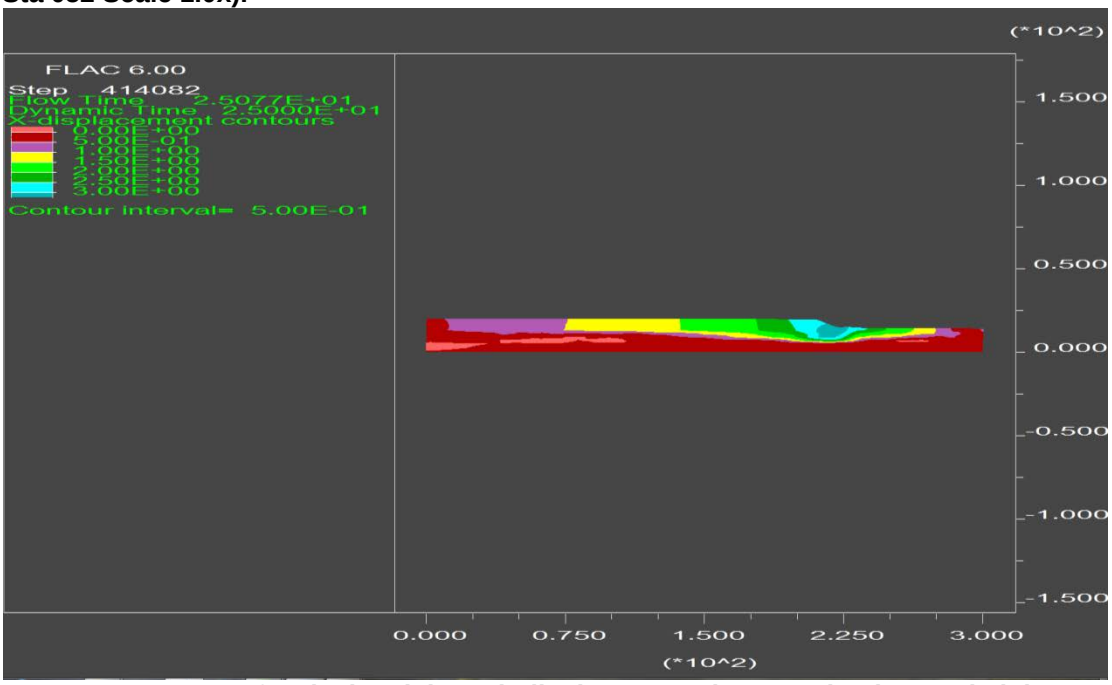

Figure B.46. Contours of calculated lateral displacement (6 m embankment height, 8 meter liquefiable sand layer, corrected $(N_1)_{60}$ blow count of 15, ground motion = 94 Northridge Sylmar - Conv Sta 052 Scale 1.0x).

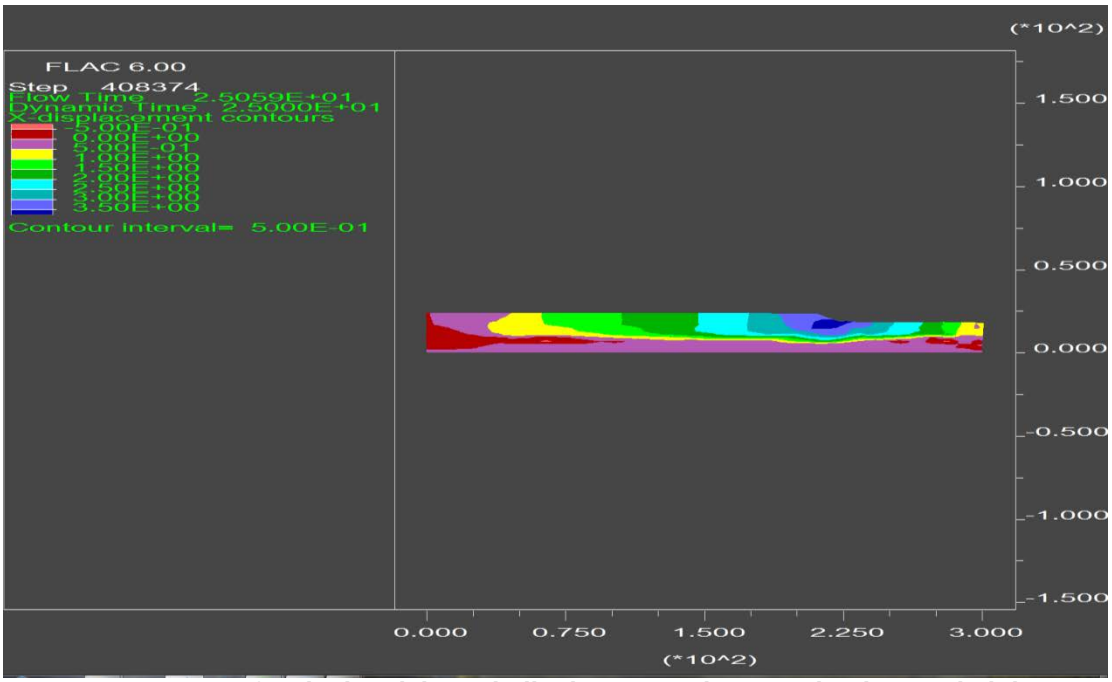

Figure B.47. Contours of calculated lateral displacement (6 m embankment height, 12 meter liquefiable sand layer, corrected $(N_1)_{60}$ blow count of 15, ground motion = 94 Northridge Sylmar - Conv Sta 052 Scale 1.0x).

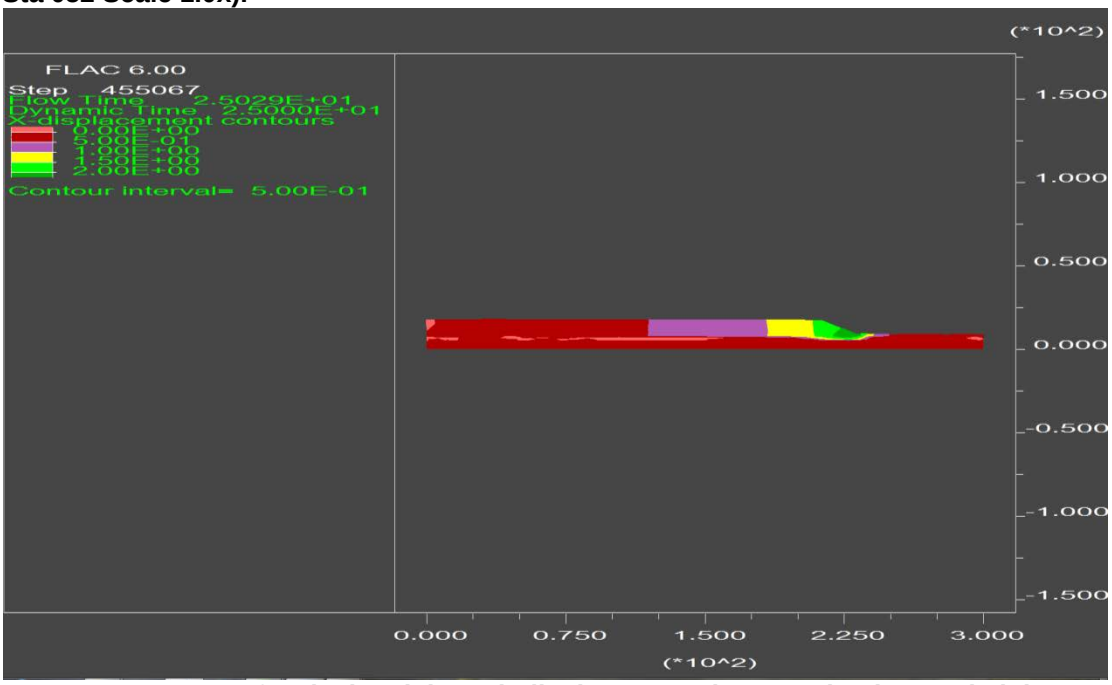

Figure B.48. Contours of calculated lateral displacement (9 m embankment height, 3 meter liquefiable sand layer, corrected $(N_1)_{60}$ blow count of 15, ground motion = 94 Northridge Sylmar - Conv Sta 052 Scale 1.0x).

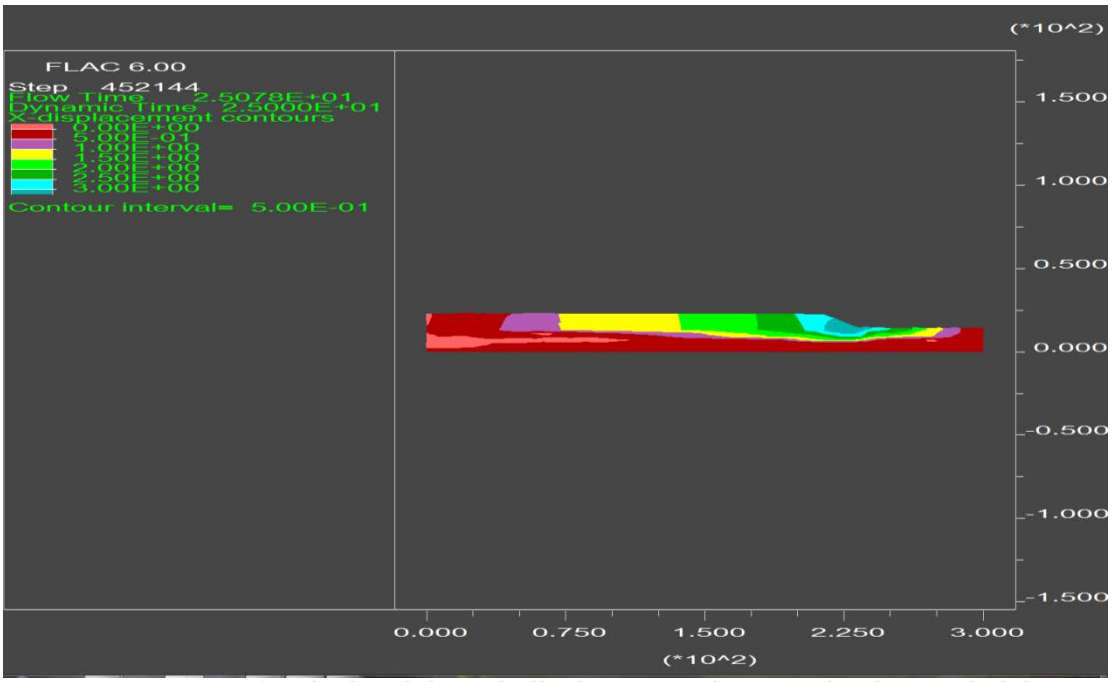

Figure B.49. Contours of calculated lateral displacement (9 m embankment height, 8 meter liquefiable sand layer, corrected $(N_1)_{60}$ blow count of 15, ground motion = 94 Northridge Sylmar - Conv Sta 052 Scale 1.0x).

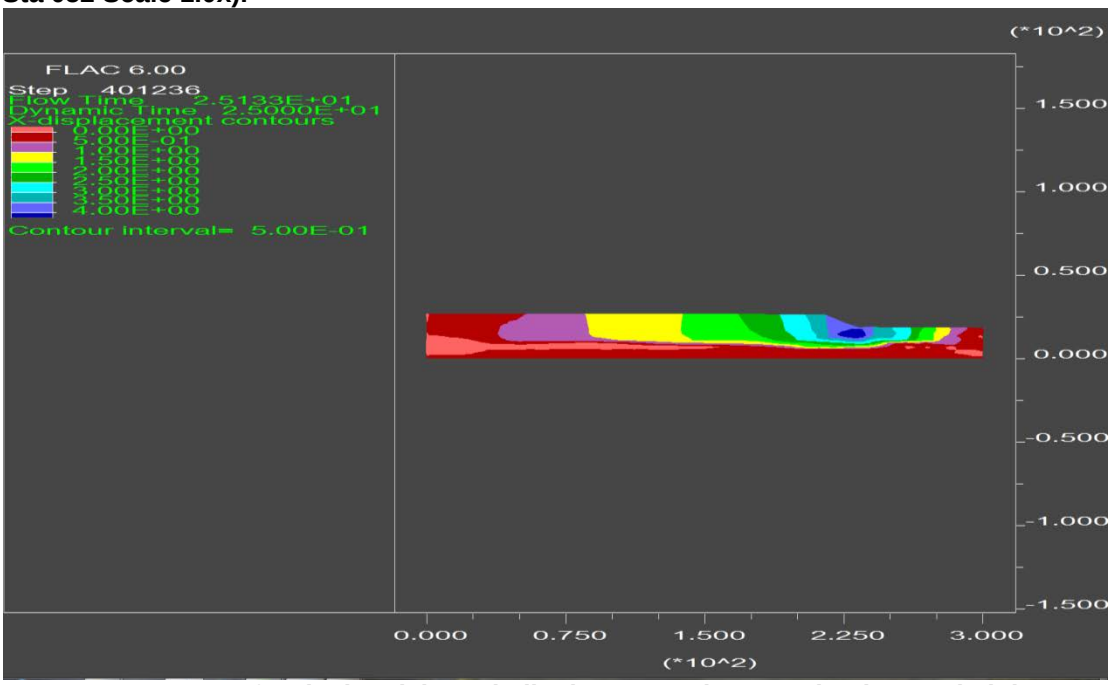

Figure B.50. Contours of calculated lateral displacement (9 m embankment height, 12 meter liquefiable sand layer, corrected $(N_1)_{60}$ blow count of 15, ground motion = 94 Northridge Sylmar - Conv Sta 052 Scale 1.0x).

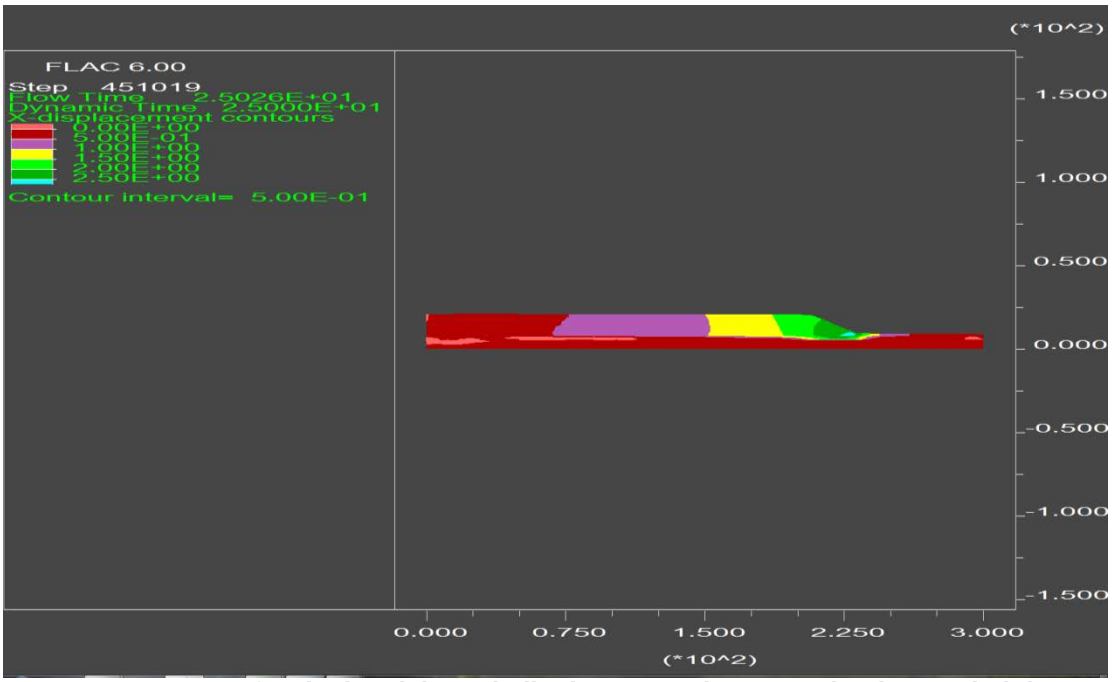

Figure B.51. Contours of calculated lateral displacement (12 m embankment height, 3 meter liquefiable sand layer, corrected $(N_1)_{60}$ blow count of 15, ground motion = 94 Northridge Sylmar - Conv Sta 052 Scale 1.0x).

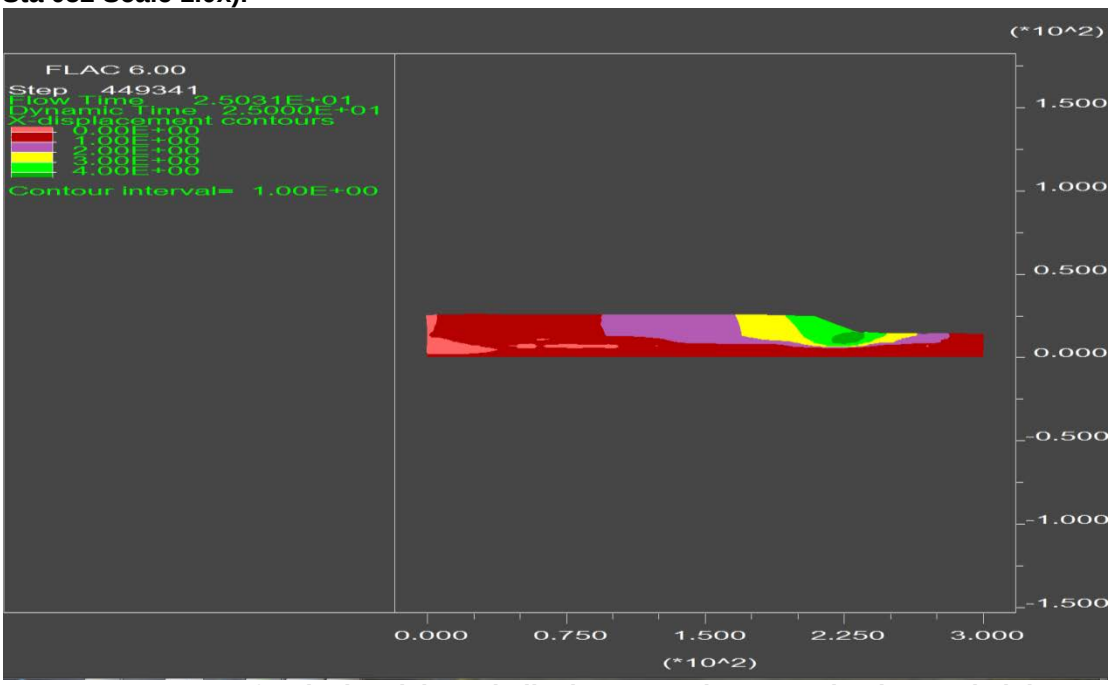

Figure B.52. Contours of calculated lateral displacement (12 m embankment height, 8 meter liquefiable sand layer, corrected $(N_1)_{60}$ blow count of 15, ground motion = 94 Northridge Sylmar - Conv Sta 052 Scale 1.0x).

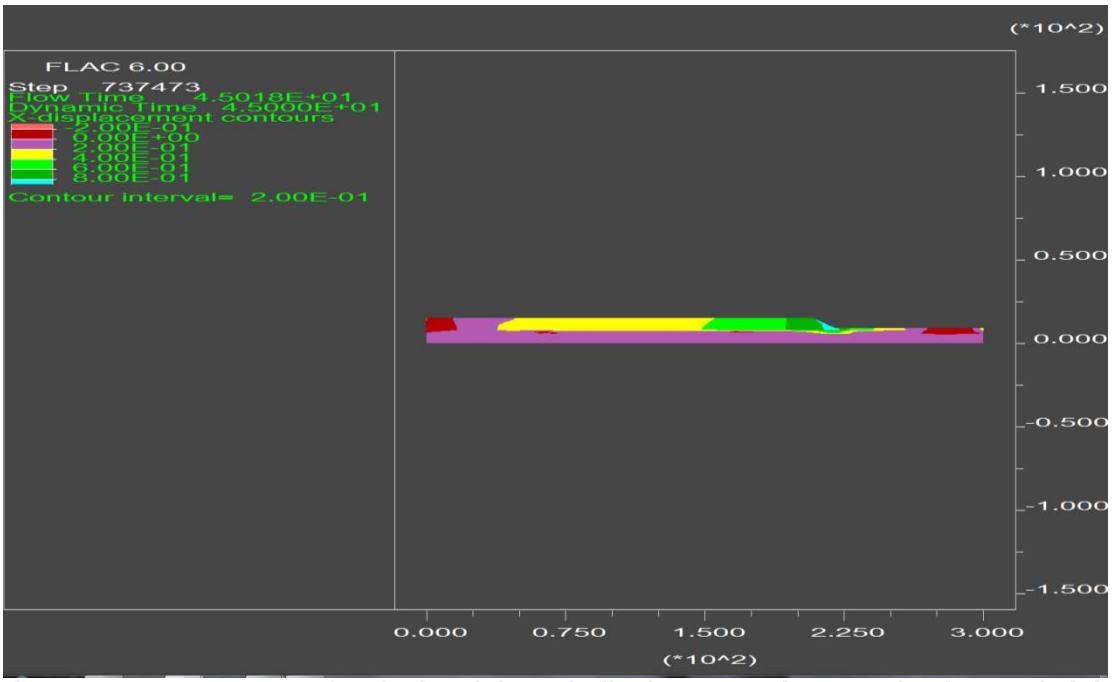

Figure B.53. Contours of calculated lateral displacement (6 m embankment height, 3 meter liquefiable sand layer, corrected $(N_1)_{60}$ blow count of 15, ground motion = 92 Landers Joshua Tree 090 Scale 1.0x).

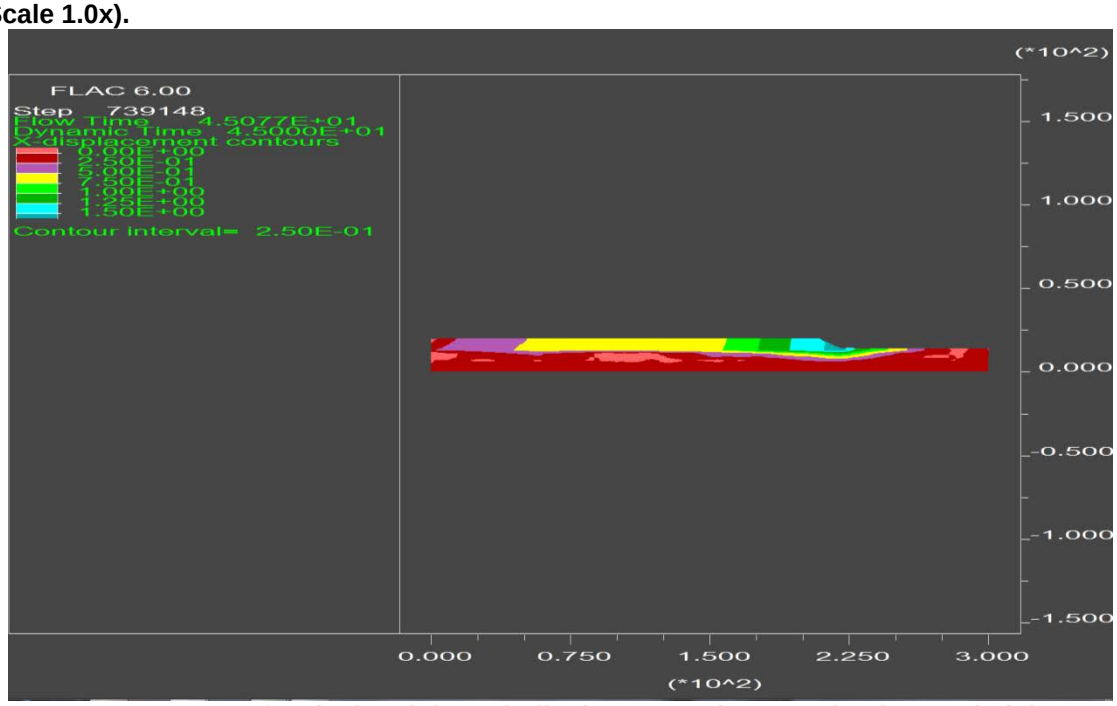

Figure B.54. Contours of calculated lateral displacement (6 m embankment height, 8 meter liquefiable sand layer, corrected $(N_1)_{60}$ blow count of 15, ground motion = 92 Landers Joshua Tree 090 Scale 1.0x).

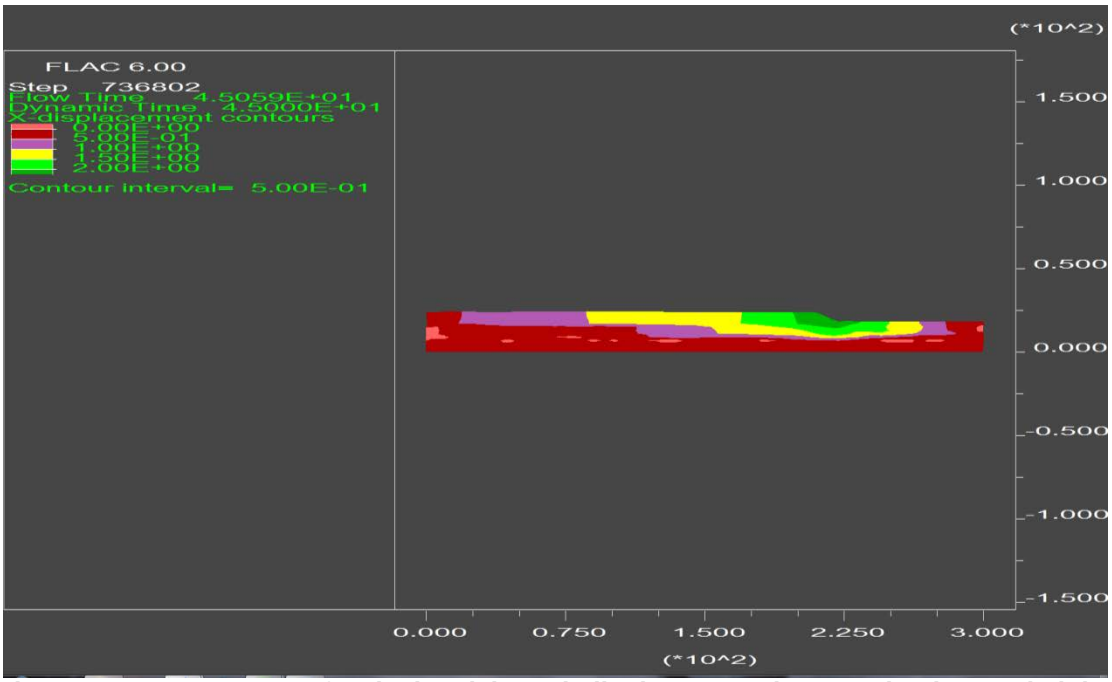

Figure B.55. Contours of calculated lateral displacement (6 m embankment height, 12 meter liquefiable sand layer, corrected $(N_1)_{60}$ blow count of 15, ground motion = 92 Landers Joshua Tree 090 Scale 1.0x).

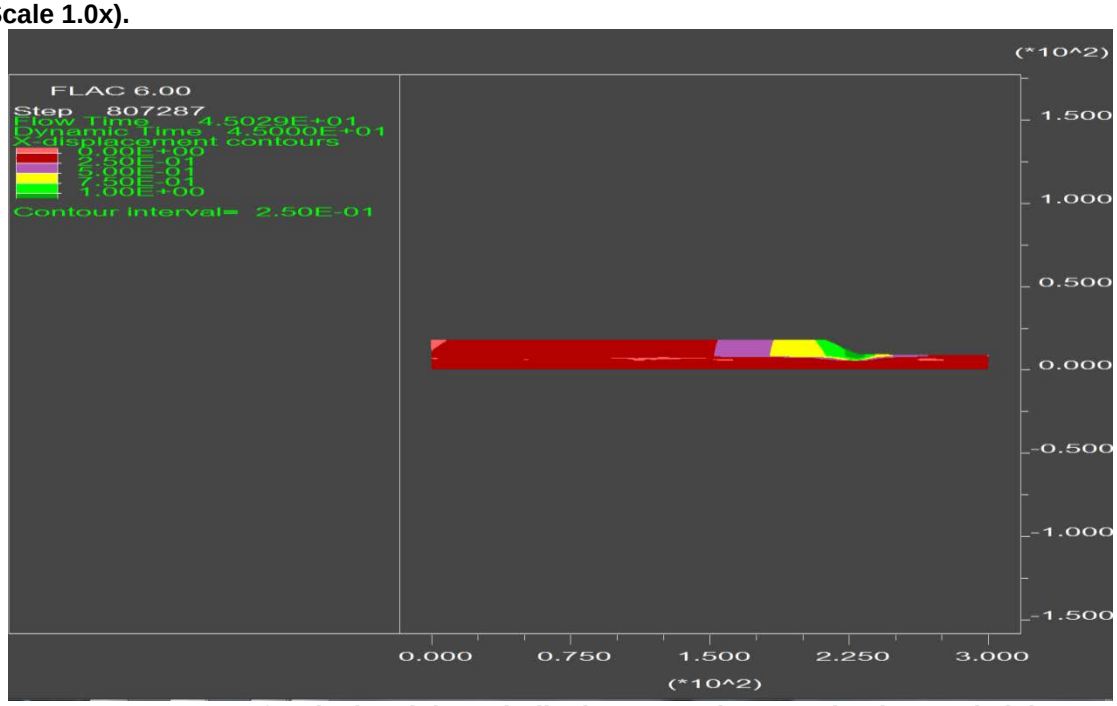

Figure B.56. Contours of calculated lateral displacement (9 m embankment height, 3 meter liquefiable sand layer, corrected $(N_1)_{60}$ blow count of 15, ground motion = 92 Landers Joshua Tree 090 Scale 1.0x).

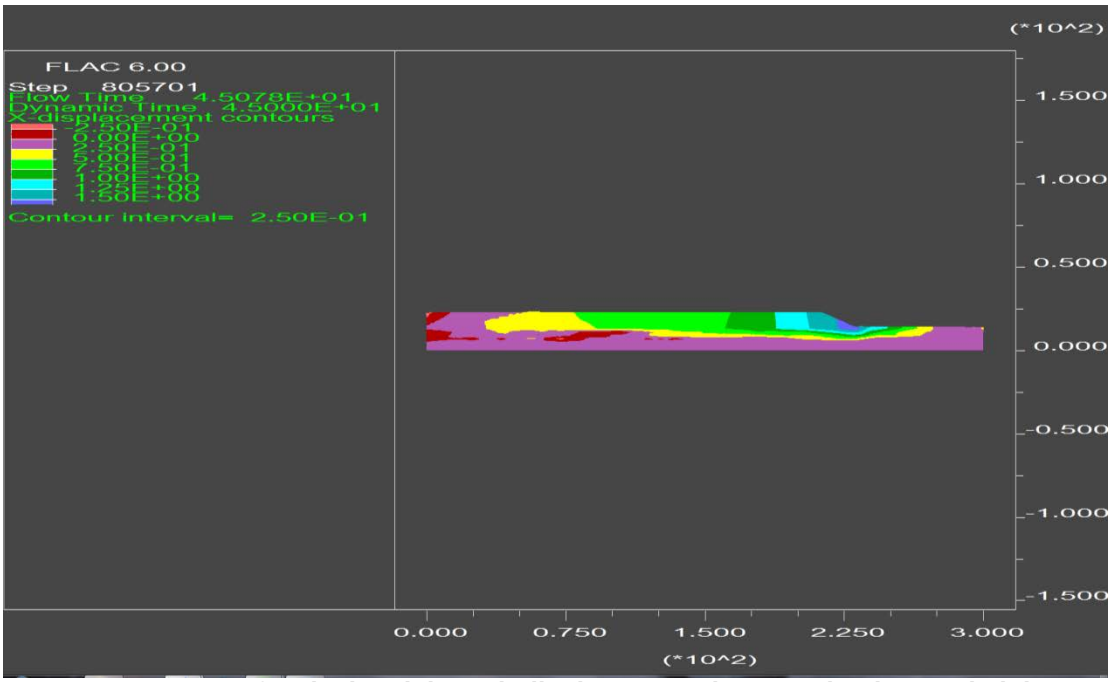

Figure B.57. Contours of calculated lateral displacement (9 m embankment height, 8 meter liquefiable sand layer, corrected $(N_1)_{60}$ blow count of 15, ground motion = 92 Landers Joshua Tree 090 Scale 1.0x).

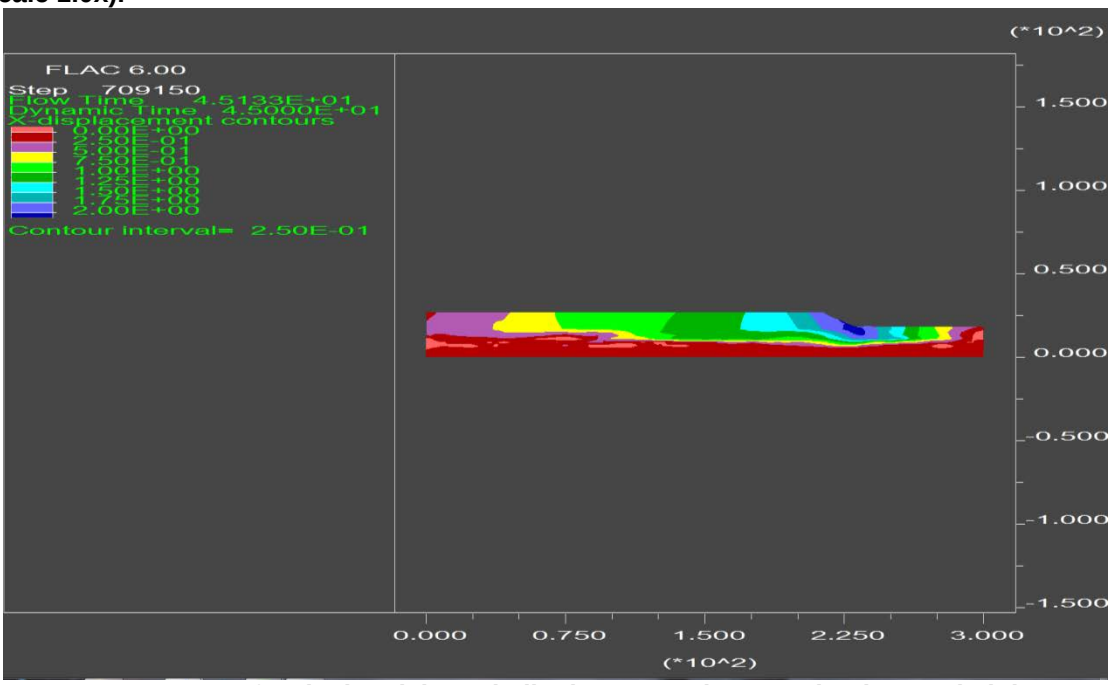

Figure B.58. Contours of calculated lateral displacement (9 m embankment height, 12 meter liquefiable sand layer, corrected $(N_1)_{60}$ blow count of 15, ground motion = 92 Landers Joshua Tree 090 Scale 1.0x).

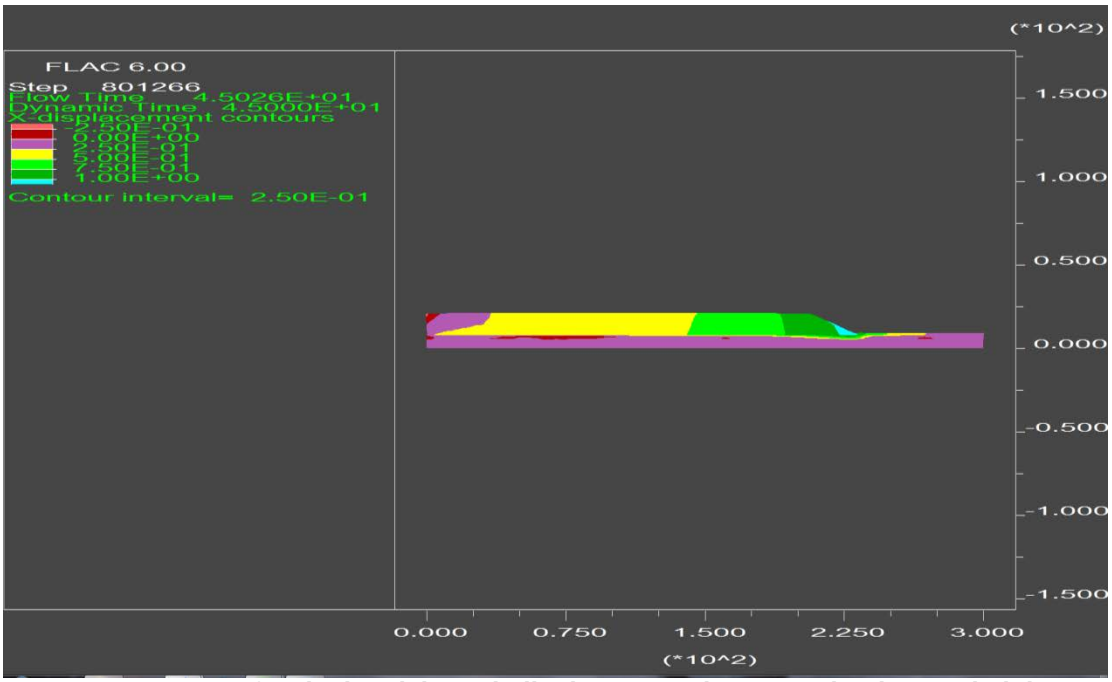

Figure B.59. Contours of calculated lateral displacement (12 m embankment height, 3 meter liquefiable sand layer, corrected $(N_1)_{60}$ blow count of 15, ground motion = 92 Landers Joshua Tree 090 Scale 1.0x).

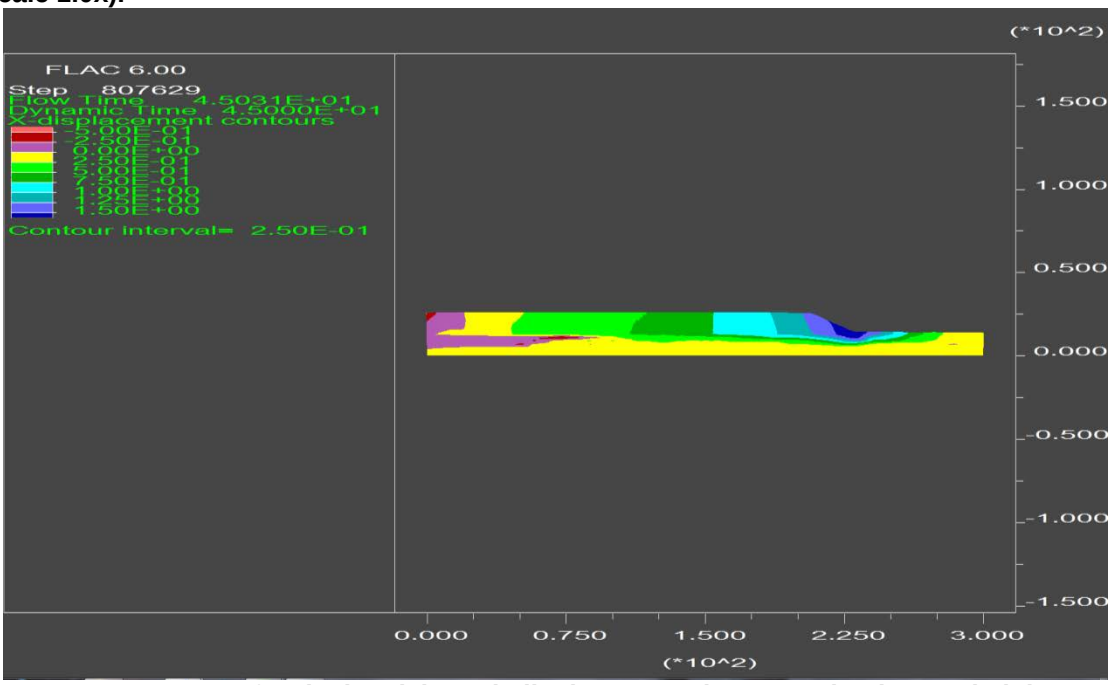

Figure B.60. Contours of calculated lateral displacement (12 m embankment height, 8 meter liquefiable sand layer, corrected $(N_1)_{60}$ blow count of 15, ground motion = 92 Landers Joshua Tree 090 Scale 1.0x).

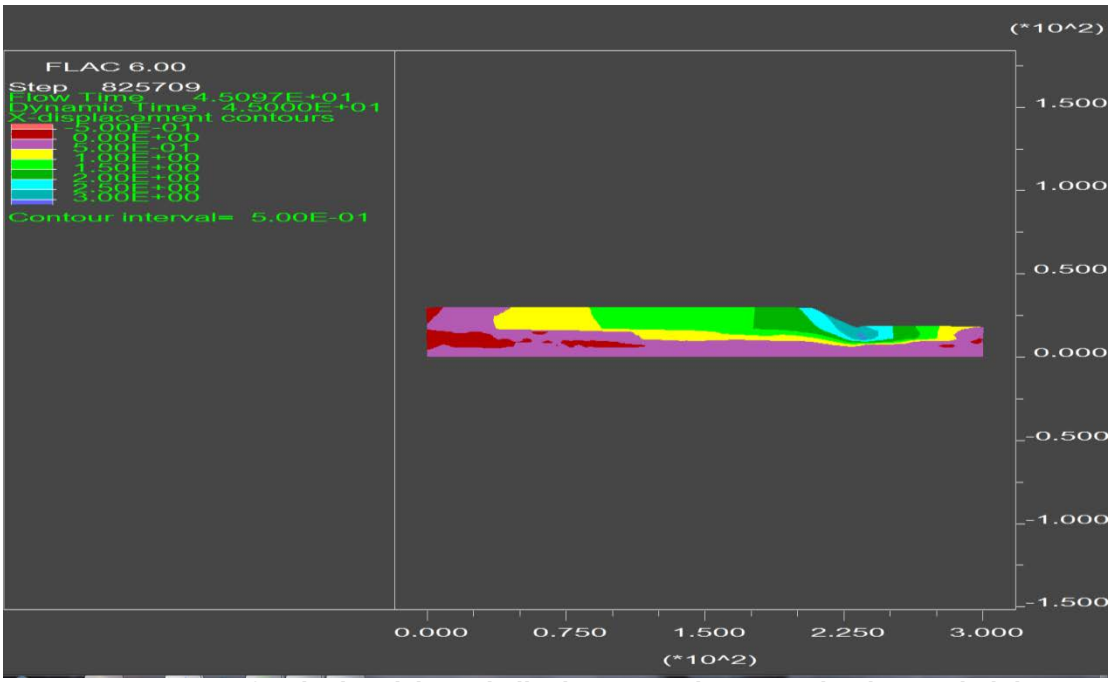

Figure B.61. Contours of calculated lateral displacement (12 m embankment height, 12 meter liquefiable sand layer, corrected $(N_1)_{60}$ blow count of 15, ground motion = 92 Landers Joshua Tree 090 Scale 1.0x).

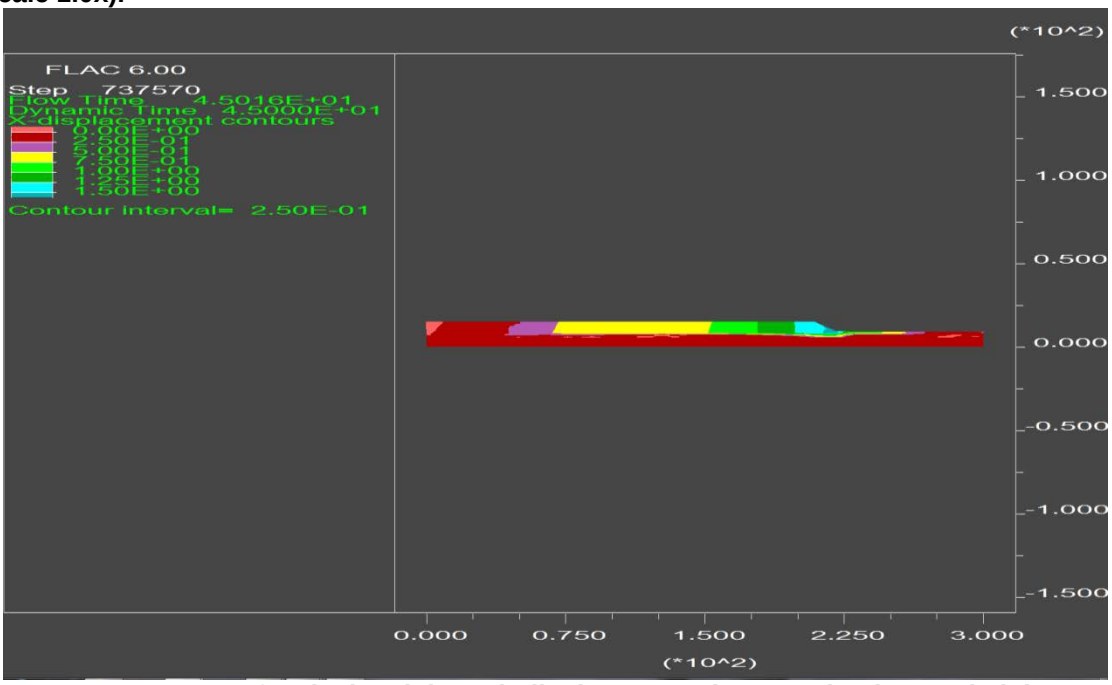

Figure B.62. Contours of calculated lateral displacement (6 m embankment height, 3 meter liquefiable sand layer, corrected $(N_1)_{60}$ blow count of 8, ground motion = 92 Landers Joshua Tree 090 Scale 1.0x).

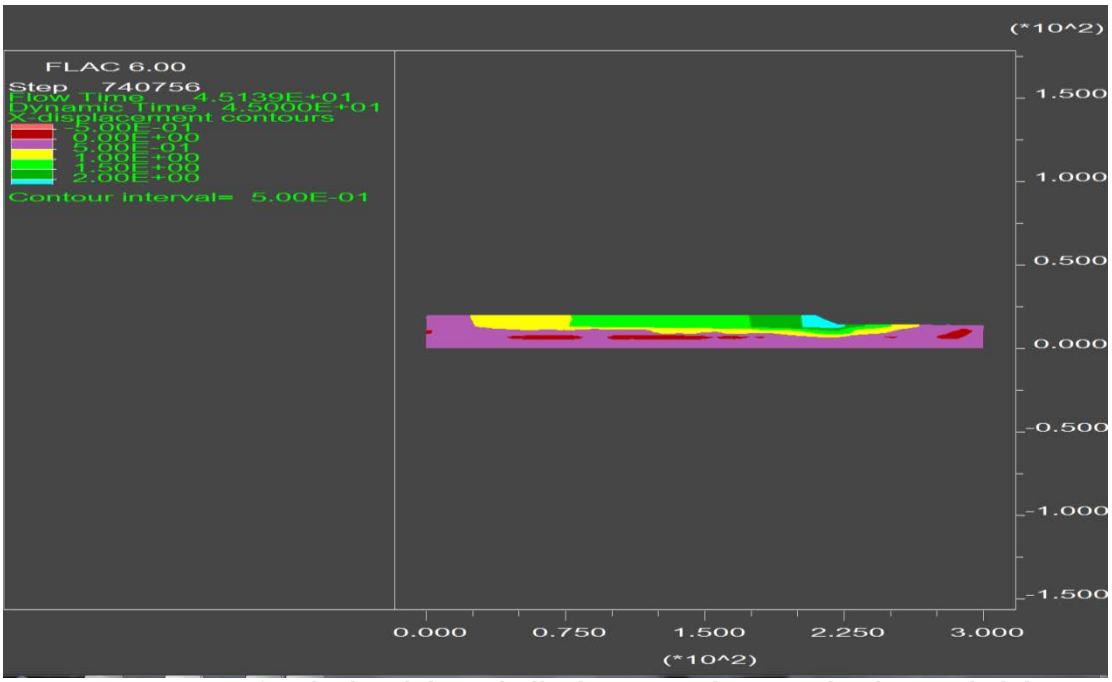

Figure B.63. Contours of calculated lateral displacement (6 m embankment height, 8 meter liquefiable sand layer, corrected $(N_1)_{60}$ blow count of 8, ground motion = 92 Landers Joshua Tree 090 Scale 1.0x).

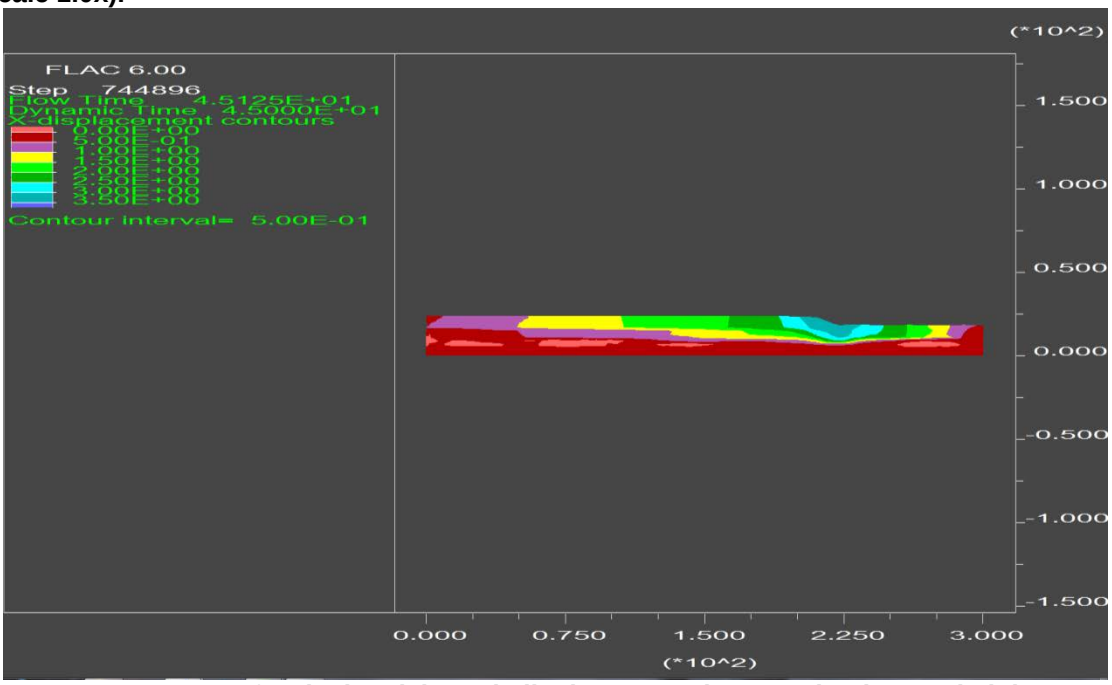

Figure B.64. Contours of calculated lateral displacement (6 m embankment height, 12 meter liquefiable sand layer, corrected $(N_1)_{60}$ blow count of 8, ground motion = 92 Landers Joshua Tree 090 Scale 1.0x).

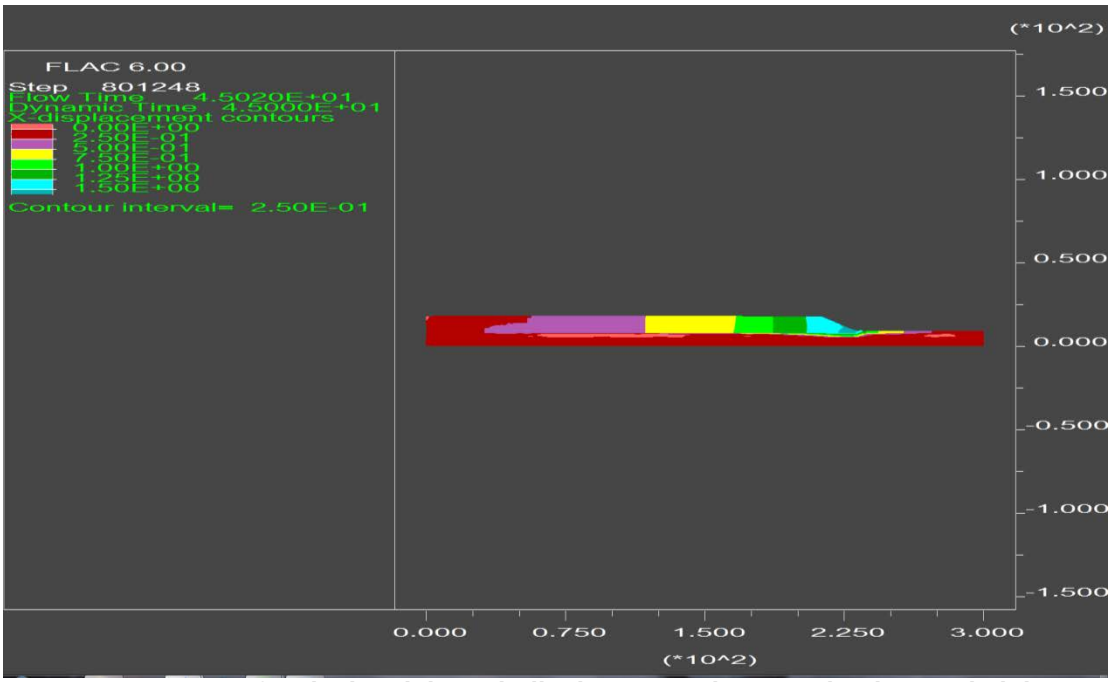

Figure B.65. Contours of calculated lateral displacement (9 m embankment height, 3 meter liquefiable sand layer, corrected $(N_1)_{60}$ blow count of 8, ground motion = 92 Landers Joshua Tree 090 Scale 1.0x).

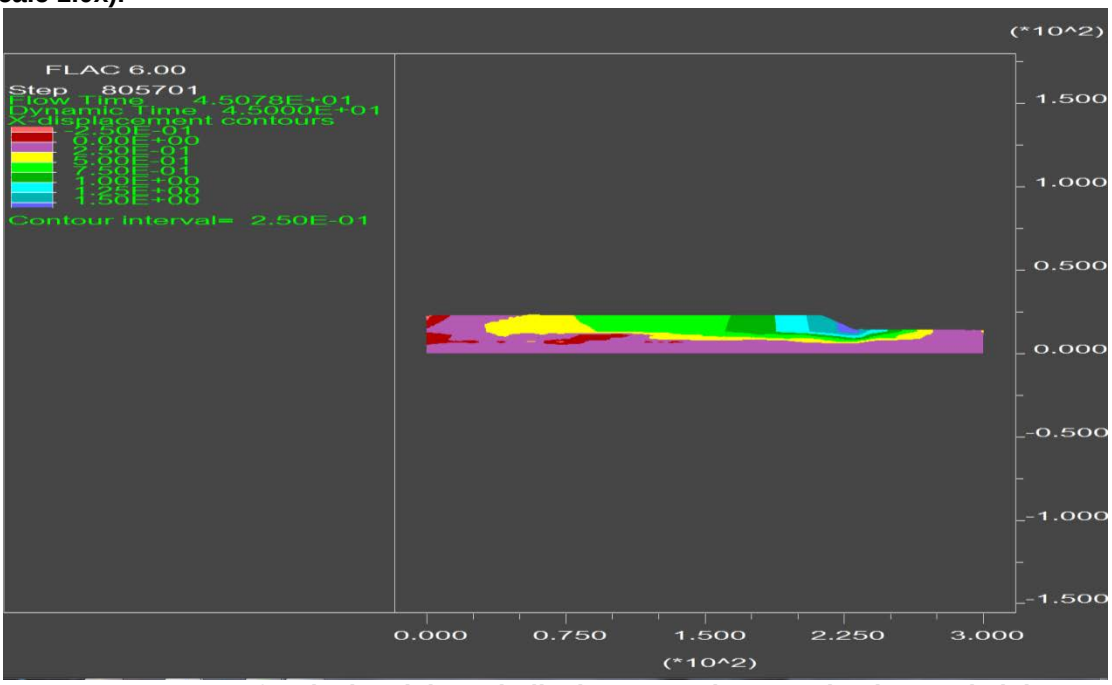

Figure B.66. Contours of calculated lateral displacement (9 m embankment height, 8 meter liquefiable sand layer, corrected $(N_1)_{60}$ blow count of 8, ground motion = 92 Landers Joshua Tree 090 Scale 1.0x).

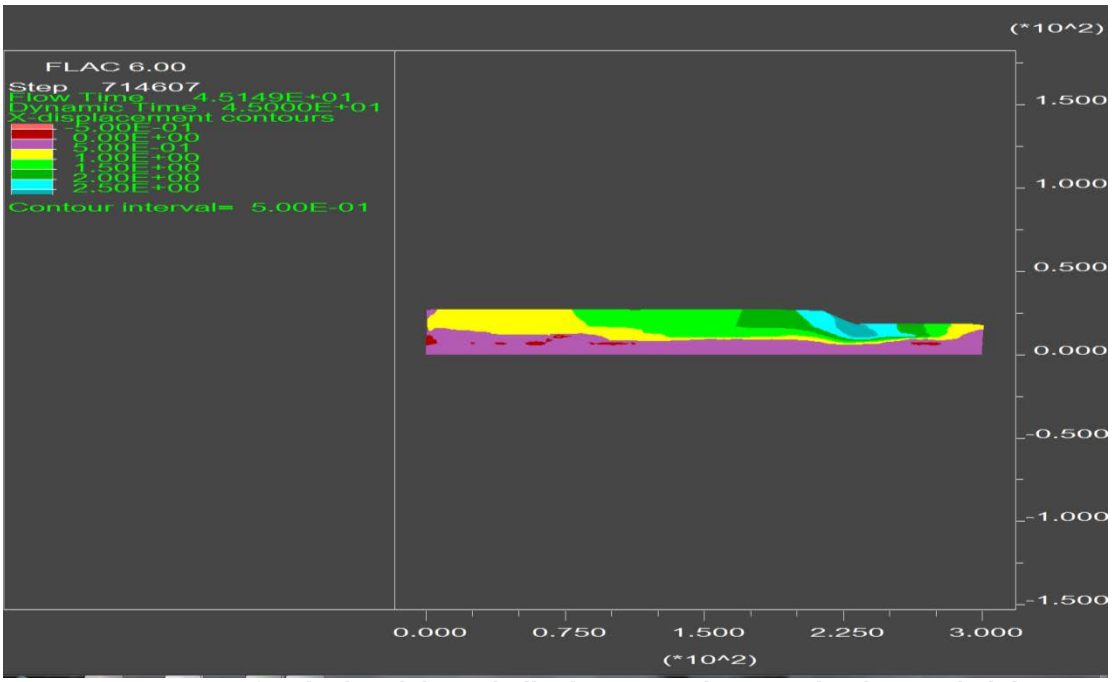

Figure B.67. Contours of calculated lateral displacement (9 m embankment height, 12 meter liquefiable sand layer, corrected $(N_1)_{60}$ blow count of 8, ground motion = 92 Landers Joshua Tree 090 Scale 1.0x).

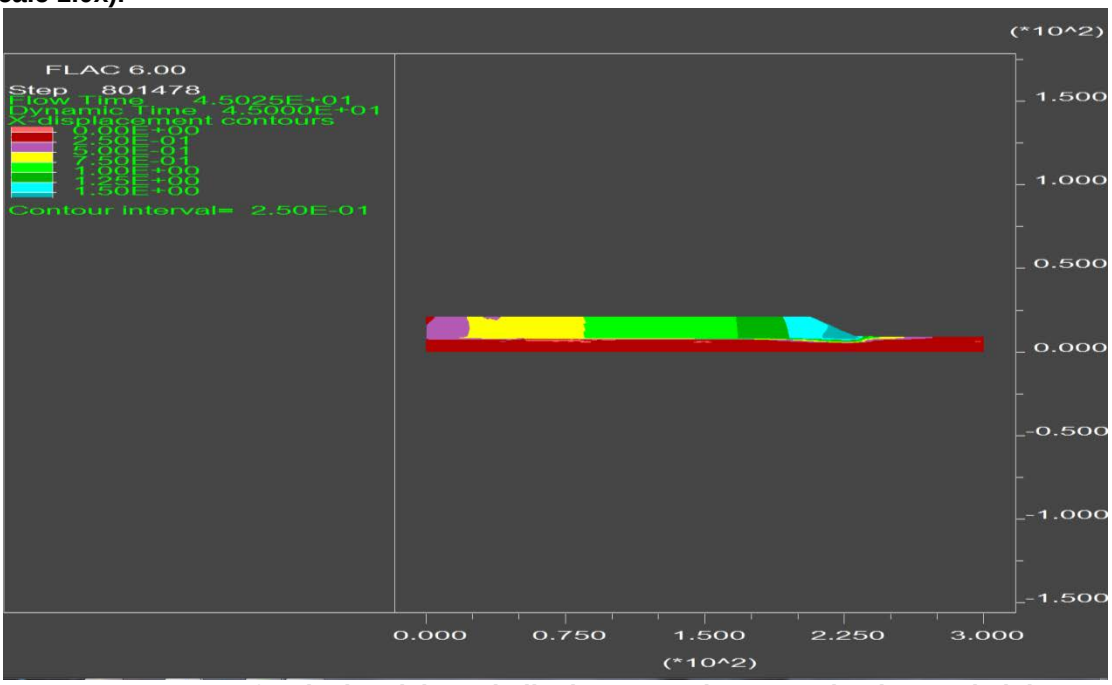

Figure B.68. Contours of calculated lateral displacement (12 m embankment height, 3 meter liquefiable sand layer, corrected $(N_1)_{60}$ blow count of 8, ground motion = 92 Landers Joshua Tree 090 Scale 1.0x).

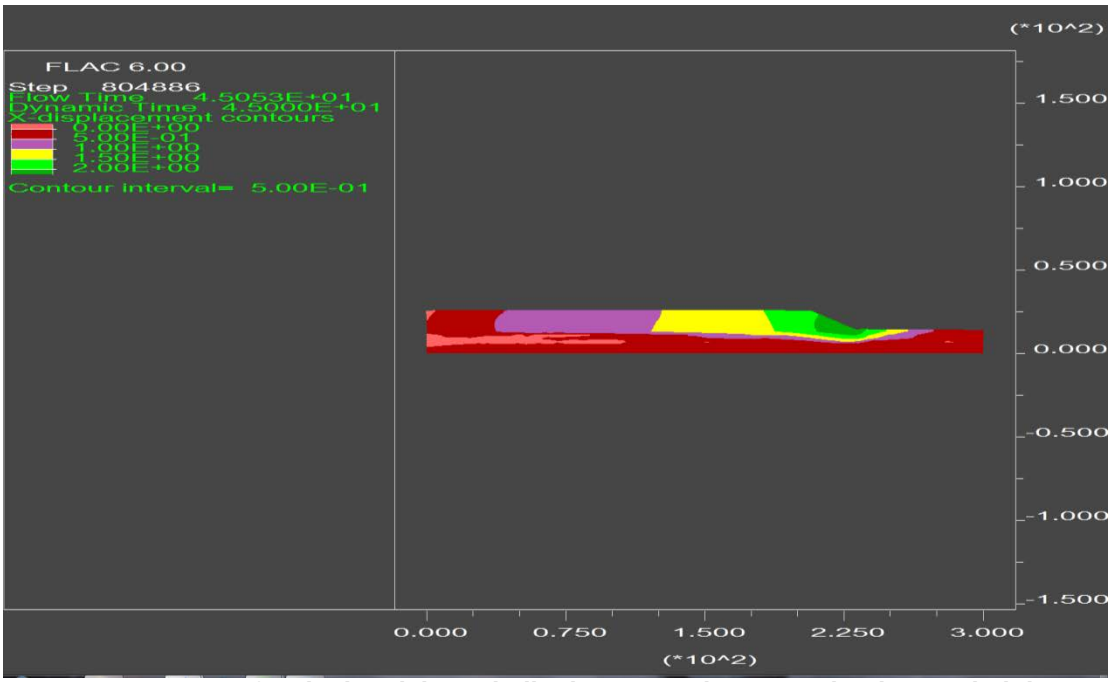

Figure B.69. Contours of calculated lateral displacement (12 m embankment height, 8 meter liquefiable sand layer, corrected $(N_1)_{60}$ blow count of 8, ground motion = 92 Landers Joshua Tree 090 Scale 1.0x).

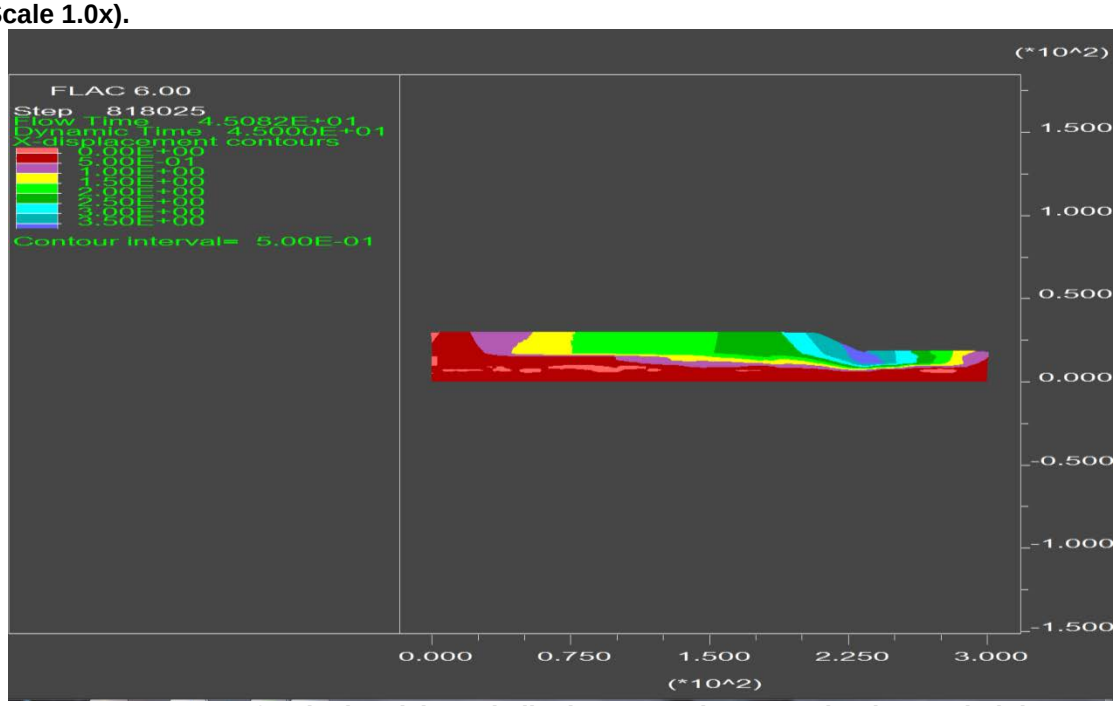

Figure B.70. Contours of calculated lateral displacement (12 m embankment height, 12 meter liquefiable sand layer, corrected $(N_1)_{60}$ blow count of 8, ground motion = 92 Landers Joshua Tree 090 Scale 1.0x).

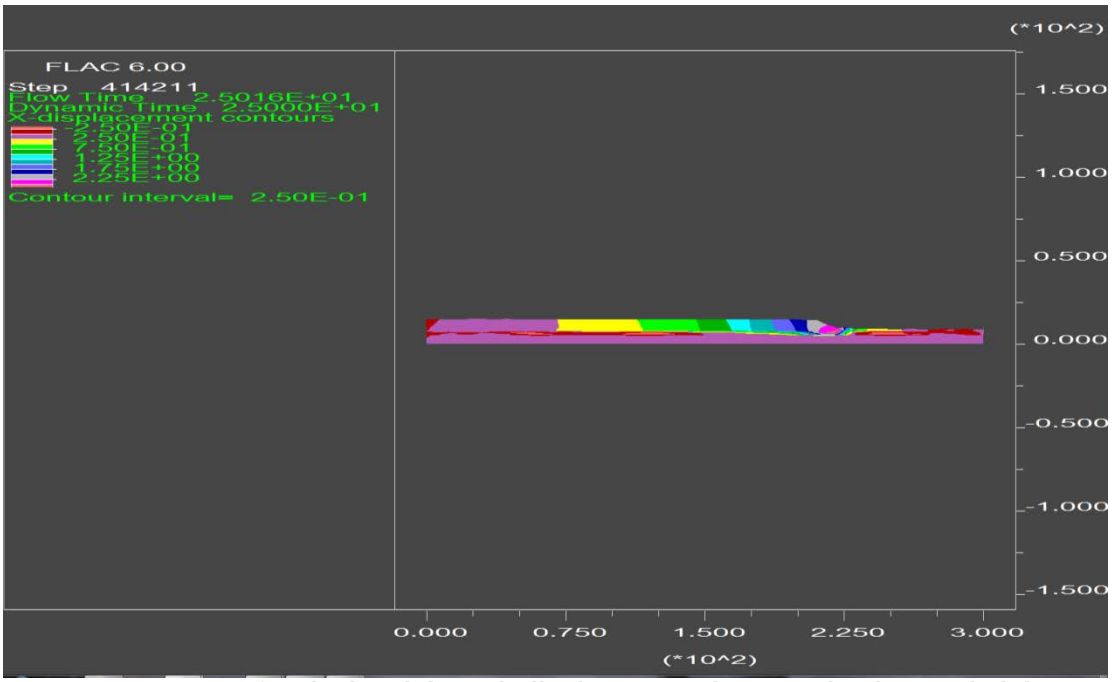

Figure B.71. Contours of calculated lateral displacement (6 m embankment height, 3 meter liquefiable sand layer, corrected $(N_1)_{60}$ blow count of 8, ground motion = 94 Northridge Sylmar - Conv Sta 052 Scale 1.0x).